

[www.aecenar.com/institutes/iap](http://www.aecenar.com/institutes/iap)

## Ground Based IAP-Observatory

Report 1 (2013-2019)

- IAP-SWRDA (Radio Astronomy HI Line Sensor): Basics, Design, Realization
- IAP-OSM (Optical Spectrometer): Basics, Design
- IAP-IRS (Infrared Sensor): Basics, Design, Manufacturing Plan

Initial document: Ras Masqa/Tripoli, 01 October 2018

Last update: 25.08.2019

Editor: Samir Mourad

With contributions of:

Samir Mourad, Suheeb Kassar, Maysaa Kamareddine, Siham Aisha, Ihab Wahbe

# Content

<b>CONTENT</b> .....	<b>2</b>
<b>INSTITUTE FOR ASTROPHYSICS (IAP) PROJECT MANAGEMENT</b> .....	<b>I</b>
IAP Organisation.....	i
Working Packages and Time Plan.....	i
<b>IAP-SWRDA</b> .....	<b>I</b>
Abstract.....	ii
Master Thesis Task.....	iii
Presentation (May 2015).....	iv
Table of contents.....	xviii
List of figures.....	xix
List of Keywords.....	xix
<b>1 INTRODUCTION TO SWRDA</b> .....	<b>21</b>
1.1 BACKGROUND.....	21
1.2 THE SRWDA PROJECT .....	21
1.1 OBJECTIVES .....	21
1.2 OUTLINE .....	21
<b>2 BASICS</b> .....	<b>22</b>
2.1 21-CM RADIO ASTRONOMY BASICS .....	22
2.2 RADIO WAVE RECEIVING.....	23
2.3 SOFTWARE DESIGNED RADIO.....	23
2.4 BASIC SDR RECEIVER ARCHITECTURE.....	24
<b>3 SYSTEM DESIGN</b> .....	<b>26</b>
<b>4 HARDWARE CONCEPTION</b> .....	<b>28</b>
4.1 PLATFORM SELECTION.....	28
4.1.1 <i>Hackrf platform</i> .....	28
4.1.2 <i>BladeRF Platform</i> .....	29
4.1.3 <i>Ettus Research's USRP B100</i> .....	29
4.1.4 <i>Rtl_SDR (RTL2832+ E4000)</i> .....	30
<b>5 HARDWARE REALIZATION</b> .....	<b>31</b>
5.1 HARDWARE OF RTL SDR (RTL2832+E4000):.....	31
5.1.1 <i>RTL2832</i> .....	31
5.1.2 <i>Tuner E4000</i> .....	31
5.2 HARDWARE OF USRP .....	33
5.2.1 <i>USRP B100 as motherboard</i> .....	33
5.2.2 <i>WBX 50-2200 MHz Rx/Tx as daughterboard</i> .....	34
5.2.3 <i>FPGA</i> .....	35
5.2.4 <i>ADC converter</i> .....	37
5.3 LOW NOISE AMPLIFIER LNA .....	37
5.4 HYDROGEN LINE FILTER .....	38
5.5 PREAMPLIFIER:.....	40
5.6 ANTENNA AND FEED HORN .....	41
<b>6 SOFTWARE</b> .....	<b>43</b>
6.1 GNU RADIO .....	43
6.2 GNU RADIO ARCHITECTURE .....	44
6.3 GNU RADIO COMPANION (GRC).....	45
6.4 BASIC BLOCKS .....	47
6.4.1 <i>RTL SDR source</i> .....	47
6.4.2 <i>WX GUI blocks</i> .....	47

6.5	SOFTWARE DESIGN .....	48
6.6	SOFTWARE IMPLEMENTATION .....	48
6.6.1	RTL Source.....	49
6.6.2	FFT filter.....	50
6.7	TEST AND MEASUREMENTS.....	50
<b>7</b>	<b>FUTURE WORK .....</b>	<b>52</b>
<b>8</b>	<b>LITERATURE .....</b>	<b>53</b>
<b>9</b>	<b>APPENDIX .....</b>	<b>54</b>
A.1	SOFTWARE .....	54
	Python code.....	54
A.2	HARDWARE.....	63
	SDR RTL 2382+4000.....	63
	IF Amplifier.....	63
	Low noise amplifier.....	64
	Motherboard USRP B100 .....	65
A.3	LIST OF OFF-THE-SHELF ELECTRONIC COMPONENTS AND ASSEMBLIES .....	68
A.4	MECHANICAL COMPONENTS .....	69
	<b>IAP-OSM (OPTICAL SPECTROMETER) .....</b>	<b>LXXI</b>
<b>1</b>	<b>BASICS .....</b>	<b>72</b>
1.3	SPECTROSCOPY .....	72
1.3.1	Theory.....	72
1.3.2	Type of radiative energy.....	73
1.3.3	Nature of the interaction.....	74
1.3.4	Type of materials.....	75
1.4	SPECTROMETER.....	76
1.4.1	Types of spectrometer .....	77
1.4.1.1	Optical spectrometer .....	77
1.4.1.2	Spectroscopes .....	78
1.4.1.3	Mass spectrometer .....	79
1.4.1.4	Time-of-flight spectrometer.....	79
1.4.1.5	Magnetic spectrometer.....	79
1.5	TYPES OF OPTICAL SPECTROMETERS .....	79
1.5.1	General dispersive spectrometer design .....	80
1.6	CCD DETECTOR .....	82
1.6.1	Overview .....	82
1.6.2	Driving a linear CCD .....	82
1.6.3	CCD output handling.....	82
1.6.4	Driving the CCD with a microcontroller .....	84
1.6.5	Communication interfaces .....	85
1.6.5.1	Comparison of different interfaces .....	85
1.6.5.2	Hardware for USB communication.....	85
1.6.6	Brief description of USB protocol.....	86
<b>2</b>	<b>DESIGN AND REALIZATION OF A SPECTROMETER PROTOTYPE .....</b>	<b>88</b>
2.1	OPTICAL SETUP .....	88
2.1.1	Diffraction grating source.....	90
2.1.1.1	Microcontroller circuit.....	90
2.1.2	Supply circuit.....	92
2.1.3	Spectrometer casing.....	92
2.2	MINIMAL CIRCUIT BETWEEN USB AND MICROCONTROLLER .....	93
2.3	MICROCONTROLLER FIRMWARE.....	94
2.4	CCD DRIVING .....	96
2.4.1	USB communication.....	98

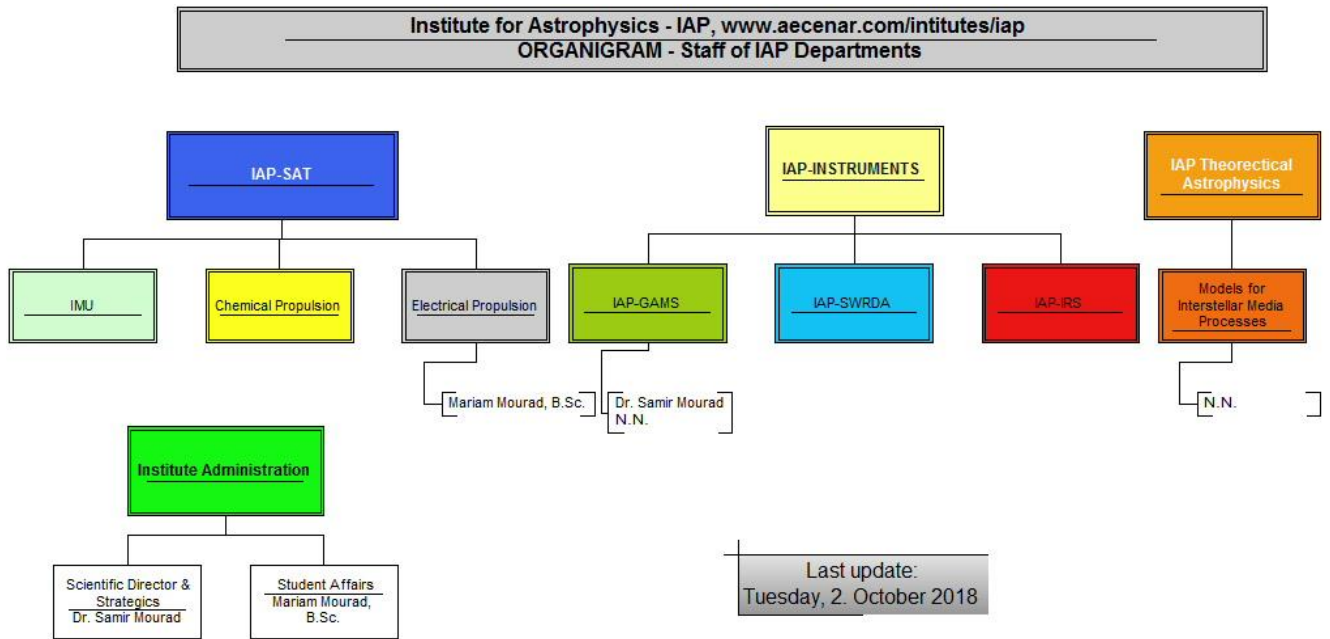
2.5	THE MAIN LOOP.....	101
2.6	COMPUTER SOFTWARE.....	103
2.6.1	<i>Command line backend for USB communication</i> .....	103
2.6.2	<i>Data preprocessing according to calibration</i> .....	104
2.6.3	<i>Python module backend</i> .....	104
2.6.4	<i>Graphical user interface</i> .....	104
2.6.5	<i>Calibration</i> .....	106
2.7	RESULTS.....	107
2.8	CONCLUSION.....	108
<b>3</b>	<b>DESIGN OF IAP-OSM.....</b>	<b>110</b>
3.1	OPTICAL SETUP.....	111
3.2	MATERIALS FOR OPTICAL SETUP.....	111
3.3	SCHEMATIC OF SPARKFUN TRIAD SPECTROSCOPY SENSOR - AS7265X (QWIIC).....	112
3.4	SOFTWARE DESIGN CONSIDERATIONS AND ARDUINO.....	112
3.5	REFERENCES.....	114
	<b>IAP-IRS.....</b>	<b>115</b>
	Project Status at Beginning of actual project phase.....	<b>Fehler! Textmarke nicht definiert.</b>
<b>1</b>	<b>BASICS OF INFRARED SCIENCE &amp; TECHNOLOGY.....</b>	<b>117</b>
1.1	INFRARED ASTRONOMY (NEAR INFRARED, MID INFRARED, FAR INFRARED).....	117
1.1.1	<i>NEAR INFRARED</i> .....	118
1.1.2	<i>MID INFRARED</i> .....	119
1.1.3	<i>FAR INFRARED</i> .....	120
1.2	DEFINITION OF INFRARED AND THE ORIGIN OF THE INFRARED RADIATION.....	120
1.2.1	<i>The definition of the infrared band</i> .....	121
1.3	INSTRUMENTATION / SENSORS TECHNOLOGY.....	124
1.3.1	IRAS.....	124
1.3.1.1	The most important results of IRAS.....	125
1.4	INFRARED SATELLITE OBSERVATORIES.....	126
1.4.1	<i>Infrared Space Observatory (ISO)</i> .....	127
1.4.1.1	Scientific instruments and observing strategy.....	128
1.4.1.2	Most important results.....	129
<b>2</b>	<b>IAP-IRS UNIT DESIGN (PBS DETECTOR) OVERVIEW (PRESENTATION).....</b>	<b>132</b>
<b>3</b>	<b>BASICS.....</b>	<b>143</b>
3.1	INTRODUCTION TO LEAD SALT INFRARED DETECTORS (KONDAS, FEBRUARY 1993).....	144
3.2	STRUCTURE.....	145
3.3	THEORETICAL BACKGROUND.....	146
3.3.1	<i>Basic principle</i> .....	147
3.3.2	<i>Biasing</i> .....	147
3.3.3	<i>Noise</i> .....	147
<b>4</b>	<b>OVERVIEW (WILLIAM V. CUMMINGS JR., 1951).....</b>	<b>149</b>
<b>5</b>	<b>IR PHOTOCONDUCTIVE DETECTORS.....</b>	<b>151</b>
5.1	PHOTOCONDUCTORS VS. PHOTODIODES.....	151
5.2	USAGE NOTES.....	151
5.3	THEORY OF OPERATION.....	151
5.4	FREQUENCY RESPONSE.....	152
5.5	TEMPERATURE CONSIDERATIONS.....	153
5.6	TYPICAL PHOTOCONDUCTOR AMPLIFIER CIRCUIT.....	153
5.7	SIGNAL TO NOISE RATIO.....	154
5.8	NOISE EQUIVALENT POWER.....	154
5.9	DARK RESISTANCE.....	154
5.10	DETECTIVITY (D) AND SPECIFIC DETECTIVITY (D*).....	154

<b>6</b>	<b>ROOM-TEMPERATURE, THIN-FIL, PBS PHOTOCONDUCTIVE DETECTOR HARDENED AGAINST LASER DAMAGE .....</b>	<b>156</b>
<b>7</b>	<b>PBS SYNTHESIS .....</b>	<b>163</b>
7.1	PREPARE REACTANTS .....	163
7.2	DEGAS THE MIXTURE .....	163
7.3	INJECTION .....	163
7.4	CLEANING .....	163
7.5	PBS/POLYMER NANOCOMPOSITE OPTICAL MATERIALS WITH HIGH REFRACTIVE INDEX .....	164
<b>8</b>	<b>CONCLUSION.....</b>	<b>165</b>
	Heat sink: .....	168
	Sapphire window overview: .....	168
	Substrate quartz: .....	169
	Thermoelectric cooler .....	171
<b>9</b>	<b>THERMOELECTRICALLY COOLED IR DETECTORS BEAT THE HEAT .....</b>	<b>176</b>
9.1	THERMOELECTRIC COOLERS .....	176
9.2	CHOOSING A COOLER .....	177
9.3	NEAR-INFRARED DETECTORS .....	178
9.4	PRINCIPLE OF THERMOELECTRIC COOLING .....	179
9.4.1	<i>Peltier effect</i> .....	180
<b>10</b>	<b>LEAD SULFIDE QUANTUM DOTS SYNTHESIS .....</b>	<b>181</b>
10.1	OVERVIEW .....	181
10.2	SIGNIFICANCE .....	181
10.3	PROCEDURE .....	181
10.4	PBS/POLYMER NANOCOMPOSITE OPTICAL MATERIALS WITH HIGH REFRACTIVE INDEX .....	182
<b>11</b>	<b>SYNTHESIS AND OPTICAL PROPERTIES OF THE SEMICONDUCTOR PBS NANOBELTS .....</b>	<b>184</b>
11.1	INTRODUCTION.....	184
11.2	EXPERIMENTAL SECTION .....	184
11.2.1	<i>Reagents &amp; Equipments:</i> .....	184
11.3	RESULTS AND DISCUSSIONS .....	186
11.4	CONCLUSION .....	188
<b>12</b>	<b>MATERIALS .....</b>	<b>190</b>
<b>13</b>	<b>REFERENCES TO IAP-IRS .....</b>	<b>191</b>
13.1	REFERENCES AND FURTHER READING TO THE 2.6.....	191
13.2	FOR PBS SENSOR .....	192
	<b>SUPPLIERS DATA .....</b>	<b>I</b>
	Electronics, Control.....	i
	Satellite Parts.....	i
	CNC Fine Mechanics (2D).....	i
	3D Printing (Plastics) .....	ii
	CNC .....	ii
	<b>TABLE OF FIGURES</b>	
	FIGURE 1: HYDROGEN EMISSION .....	22
	FIGURE 2: SPAIN MECHANISMS.....	23
	FIGURE 3: RADIO SYSTEM .....	23
	FIGURE 4: MODEL OF SOFTWARE RADIO [1] .....	24
	FIGURE 5: BLOCK SCHEME OF TYPICAL SDR RECEIVER.....	25
	FIGURE 6: OVERVIEW AND COMPARISON OF DIFFERENT PLATFORMS .....	28
	FIGURE 7:USRP INSTANT SDR KIT .....	33

FIGURE 8: ARCHITECTURE OF B100 .....	34
FIGURE 9: RF FRONT-END DIAGRAM .....	34
FIGURE 10: RECEIVER BLOCKS .....	35
FIGURE 11: DDC BLOCK .....	36
FIGURE 12: SCHEMATIC AND PLATINE OF LNA.....	37
FIGURE 13: TEST OF LNA.....	38
FIGURE 14: OUTPUT SIGNAL OF LNA.....	38
FIGURE 15 OUTPUT @ 2DB.....	38
FIGURE 16.....	39
FIGURE 17 FREQUENCY RESPONSE .....	40
FIGURE 18 IF AMPLIFIER .....	40
FIGURE 19 FREQUENCY RESPONSE OF IF AMP .....	41
FIGURE 20 FUNCTIONALITY OF GNURADIO.....	44
FIGURE 21 SOFTWARE ARCHITECTURE.....	45
FIGURE 22 SOFTWARE ARCHITECTURE.....	45
FIGURE 23: IMPLEMENTATION OF DIAL_TONE EXAMPLE WITHIN GNU RADIO COMPANION .....	45
FIGURE 24 RTL SDR DRIVER IN GNURADIO .....	47
FIGURE 25 MOCK UP MODEL .....	52
FIGURE 26 IMPORT RECEIVER ON MOCKUP MODEL .....	52
FIGURE 1: ANALYSIS OF WHITE LIGHT BY DISPERSING IT WITH A PRISM IS AN EXAMPLE OF SPECTROSCOPY. ....	72
FIGURE 2: A HUGE DIFFRACTION GRATING AT THE HEART OF THE ULTRA-PRECISE ESPRESSOSPECTROGRAPH. ....	74
FIGURE 3: GRATING SPECTROMETER SCHEMATIC.....	77
FIGURE 4: SPECTRUM OF LIGHT EMITTED BY A DEUTERIUM LAMP IN THE UV VISIBLE AND NEAR INFRARED PART OF THE ELECTROMAGNETIC SPECTRUM. ....	78
FIGURE 5: HORIZONTAL SCHEMATICS AND LIGHT PATHS.....	81
FIGURE 6: VERTICAL SCHEMATICS AND LIGHT PATHS .....	81
FIGURE 7: : ONE OF THE FIRST MEASUREMENTS OF THE CCD OUTPUT ON AN OSCILLOSCOPE. ON THE SCREEN, THERE ARE TWO CONSECUTIVE READ OUTS OF CCD. THE DETECTOR WINDOW WAS COVERED BY FOUR THIN PAPER STRIPES. NOTE THE END OF REGISTER SIGNAL IN THE MIDDLE OF THE SCREEN AND THE BLOOMING WHICH SLIGHTLY OVERLAPS THE LESS ILLUMINATED AREAS. ....	83
FIGURE 8: : A) PINS ON THE USB B CONNECTOR; B) MINIMAL CIRCUIT FOR CONNECTING ATMEGA8 TO USB.....	86
FIGURE 9: DETAIL OF THE CCD MOUNT AND THE ADJUSTABLE CYLINDRICAL MIRRO .....	89
FIGURE 10: THE MICROCONTROLLER CIRCUIT. AT ITS LEFT SIDE IT IS CONNECTED TO THE SUPPLY CIRCUIT, AT RIGHT TO THE CCD DETECTOR.....	91
FIGURE 11: THE SUPPLY CIRCUIT. AT ITS LEFT SIDE IT IS CONNECTED TO THE COMPUTER VIA USB CABLE.....	92
FIGURE 12: A VIEW OF THE ASSEMBLED SPECTROMETER WITHOUT TOP COVER AND PAPER LIGHT SHIELDING. THE LIGHT PASSES THROUGH THE INPUT SLIT AT THE TOP RIGHT AND FOLLOWS THE PATH INDICATED AT FIG. 5. AT THE LEFT, THERE ARE THE CONVERTER AND MICROCONTROLLER CIRCUITS AND USB OUTPUT.....	93
FIGURE 13:PROPERTIES OF COLORS .....	93
FIGURE 14: A SCREENSHOT OF THE GRAPHICAL USER INTERFACE, SHOWING THE ORANGE-RED FLUORESCENCE OF A HIGHLIGHTER PEN ILLUMINATED BY A GREEN LASER POINTER, WHOSE REFLECTION MANIFESTS AS THE NARROW PEAK AT 532 NM. NOTE ALSO THE WEAK COMPONENT AT $\approx 810$ NM COMING FROM THE LASER DIODE PUMPING THE Nd:YVO4 CRYSTAL.....	105
FIGURE 15: EMISSION OF A COMPACT FLUORESCENT LAMP, 5 S AFTER COLD START (BLACK) AND $\approx 60$ S LATER (BLUE). THE HORIZONTAL AXIS IS THE WAVELENGTH IN NANOMETER.....	106
FIGURE 16: TRANSMISSION OF PURE WATER (BLACK LINE); OF WATER WITH $\approx 10$ $\mu$ MOL/L SOLUTION OF KMNO4 (RED LINE) AND OF WATER WITH $\approx 100$ $\mu$ MOL/L SOLUTION THEREOF (GREEN LINE). THE HORIZONTAL AXIS IS THE WAVELENGTH IN NANOMETERS .....	108
FIGURE 1:SCHEMATIC OF A PHOTOCONDUCTIVE DETECTOR .....	143
FIGURE 2: TYPICAL LEAD SALT DETECTOR .....	143
FIGURE 3: TYPES OF INFRARED DETECTORS.....	144
FIGURE 4:A SINGLE ELEMENT LEAD SALT DETECTOR.....	145
FIGURE 5: PHOTOCONDUCTIVE DETECTOR BIAS CIRCUIT.....	147
FIGURE 6: SPECTRAL RESPONSE CURVES OF VARIOUS PHOTOCELLS .....	149
FIGURE 7: THE SR540 OPTICAL BEAM CHOPPER FROM STANFORD RESEARCH SYSTEMS.....	152

# Institute for Astrophysics (IAP) Project Management

## IAP Organisation



## Working Packages and Time Plan

WP No.	Working package content	Time span, costs	Development environment (HW, SW)	Responsible	Status





**IAP-SWRDA**

Based on

**Prototype for a base station for supernova remnant HI line  
radio wave detector and analyzer (SRWDA)**

Master Thesis

by  
Suheeb Kassar

Supervisor: M.Sc. M.Eng. Samir Mourad, *IAP (AECENAR)*



Main Referee: Prof. Dr. rer. nat. Wilhelm Stork, *ITIV (KIT)*



provide flexibility in technical point of view (Software) respectively market challenges. The advantages of SDR as multiband, multicarrier, multimode, Multirate and variable bandwidth enable to scan a wide range of frequencies with modified channel (modulation). On the other hand SDR concept can be implemented in different reconfigurable Hardware such as FPGA und DSP which means that replacing another analog elements for example antenna in Hardware can be effected using software design concept in reprogrammable und reconfigurable Systems .

This thesis describes the design and implementation of radio wave detector and analyzer (SRWDA) for processing supernova radio signals collected using four antennas which gives also direction information of the signals. The implemented Hardware in Software reduce the cost of station and at same time the right choice for accelerated digital signal processing. The detected signal can be displayed on GUI to observe a desired signals. The project was carried out in corporation with the Institute for Astrophysics (IAP). Some of the work was carried out in the IAP facility in Ras Nhache/Batroun/Lebanon.

## Master Thesis Task

Basmillah

10.9.2013









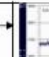



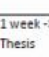
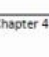

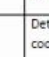
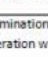
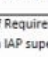
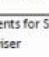
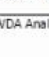
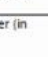


**The SRWD project**

The radio astronomical IAP project supernova radio wave detector and analyzer (SRWDA) aims to detect and analyze radio signals from supernovas. At the base station a set of antennas, which gives also direction information of the signals, is aimed to be connected to a computer which acts as Software Defined Radio (SDR). Afterwards an analyzing program is aimed to be installed.

Later the detectors are planned to be installed on satellites to improve the resolution and to suppress disturbing signals from earth stations.

Master Thesis

**Initial Prototype for a base station for supernova radio wave detector and analyzer (SRWDA)**

																																																																																																																																																																																																																																																														
---	---	---	---	---	---	---	---	---	---	---	---	---	--	---	---	---	---	---	---	---	---	---	---	---	---	---	---	---	---	---	---	---	---	---	---	---	---	---	---	---	---	---	---	---	---	---	---	---	---	---	---	---	---	---	---	---	---	---	---	---	---	---	---	---	---	---	---	---	---	---	---	---	---	---	---	---	---	---	---	---	---	---	---	---	---	---	---	---	---	---	---	---	---	---	---	---	---	---	---	---	---	---	---	---	---	---	---	---	---	---	---	---	---	---	---	---	---	---	---	---	---	---	---	---	---	---	---	---	---	---	---	---	---	---	---	---	---	---	---	---	---	---	---	---	---	---	---	---	---	---	---	---	---	---	--	--	--	--	--	--	--	--	--	--	--	--	--	--	--	--	--	--	--	--	--	--	--	--	--	--	--	--	--	--	--	--	--	--	--	--	--	--	--	--	--	--	--	--	--	--	--	--	--	--	--	--	--	--	--	--	--	--	--	--	--	--	--	--	--	--	--	--	--	--	--	--	--	--	--	--	--	--	--	--	--	--	--	--	--	--	--	--	--	--	--	--	--	--	--	--	--	--	--	--

## Presentation (May 2015)



Institut für Technik der  
Informationsverarbeitung



# MasterThesis

cand. el. **Suheeb Kassar**

### Directors

Prof. Dr.-Ing. Dr.h.c. J. Becker (speaker)

Prof. Dr.-Ing. K. D. Müller-Glaser

Prof. Dr. rer. nat. W. Stork

### Supervising Tutors

M.Sc. M.Eng. Samir Mourad

Institut für Technik der Informationsverarbeitung (ITIV)

## Prototype for a base station for supernova remnant HI line radio wave detector and analyser (SRWDA)

KIT – University of the State of Baden-Wuerttemberg and  
National Laboratory of the Helmholtz Association

[www.kit.edu](http://www.kit.edu)

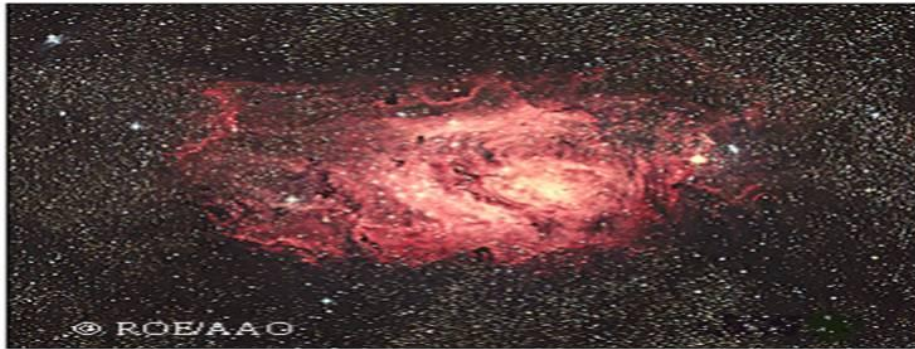
## Contents



- Thesis motivation
- Background
  - Radio astronomy and Hydrogen line1 (HL1)
  - Software defined radio(SDR) for detection HL1
- System design
- Hardware
  - Antenna
  - Analog filtering
  - SDR platform for digital processing
- Software
  - Design
  - Implementation
- Measurement
- System import on Mock-up modell

## Motivation

- Design and implementation of radio wave (Hydrogen line1) detector and analyser (SRWDA)
- Integration SRWDA with IAP Mockup model

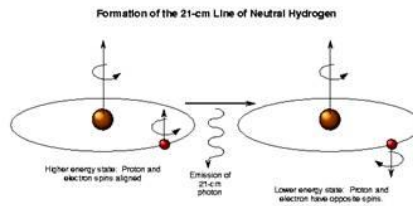
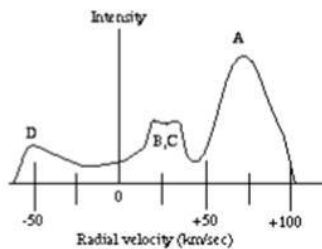


## Background

- What Radio Astronomy
  - Radio astronomy studies celestial objects at radio frequencies
  - The discovery of the cosmic microwave background radiation
  - Observation of new classes of objects (quasars, pulsars)
- Astronomical radio source
  - The Sun
  - Supernova remnants
  - Pulsars
  - Primordial black holes
  - .....

## Hydrogen line 1 (HL1)

- Electromagnetic radiation spectral line (1420 MHz, 21 cm)
- HL1 is created by a change in the energy state of neutral hydrogen atoms.
- The HL1 provides the best way to map the structure of the Galaxy
- Calculate the mass of galaxies



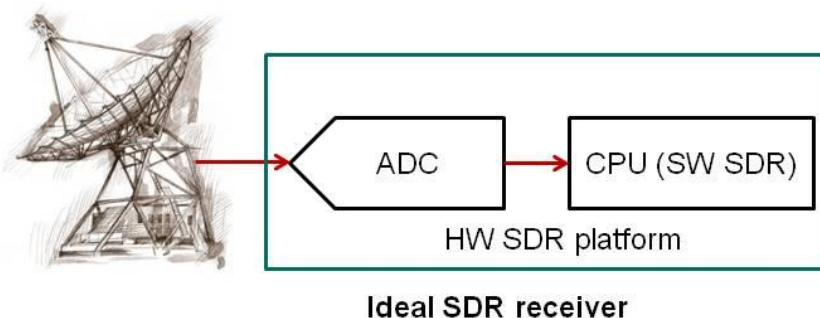
5

17.08.2019 cand.el. [Suheeb Kassab] – [SRWDA]

Institut für Technik der Informationsverarbeitung (ITIV)

## Software Defined Radio(SDR) for Detection HL

- Idea of SDR: hardware components (e.g. mixers, filters etc.) are implemented by means of software
- Radio telescope for HL can be designed using SDR
- The challenge for detection HL is a weakness of signal



**Ideal SDR receiver**

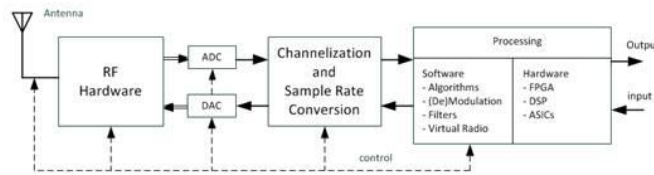
6

17.08.2019 cand.el. [Suheeb Kassab] – [SRWDA]

Institut für Technik der Informationsverarbeitung (ITIV)

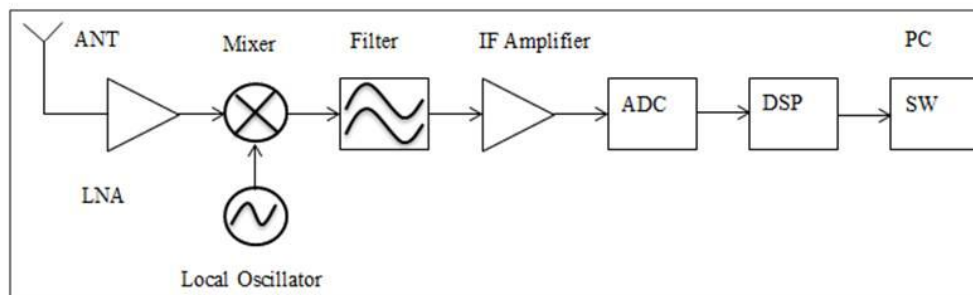
## Why SDR?

- Design flexibility
- Reliability
- Upgradability
- Reusability
- Reconfigurability
- Enhanced Functionality
- Lower Cost

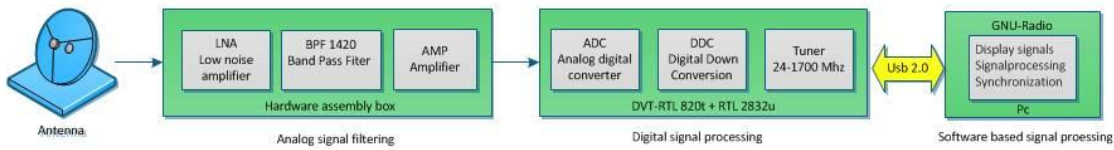


## Basic SDR heterodyne receiver architecture

- The most used radio receivers use the architecture of super heterodyne receiver
- Received signal has been converted to a fixed intermediate frequency
- which can be more processed than the original radio carrier frequency.



## Telescope design



## Real system



## Antenna + Feeder

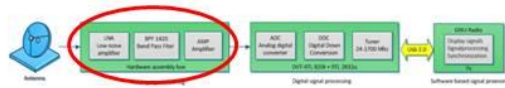


- Parabolic reflector antenna
- Ratio  $F/D = 0.5$ 
  - F : Focal distance.  $f = 55$  cm
  - D : Antenna diameter ie.  $d = 110$  cm
- Feed: dipole or crossdipole
- Feed horn  $D = 15$  cm,  $L = 20$  cm

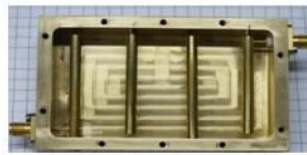
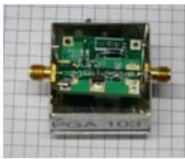




# Analog hardware



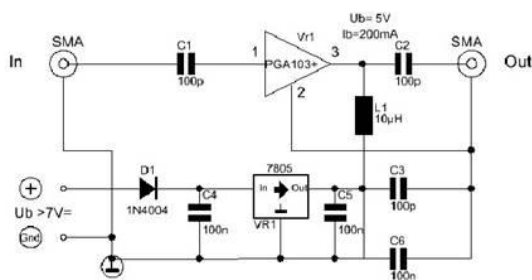
- Low noise amplifier (LNA)
- Band pass filter
- IF main amplifier & Attenuator



# Low noise amplifier (LNA)

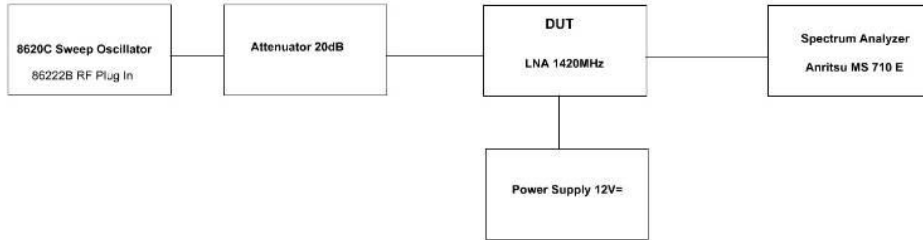


- Low noise amplifier (LNA)
  - Noise figure 12 dB
  - Gain 12 dB at 1420 MHz
  - IP1dB, 22.3dBm @ 2 GHz



## Low noise amplifier (LNA)

### ■ Test setup for LNA

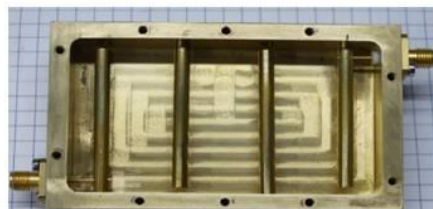


### ■ Frequency response



## Hydrogen filter 1420 MHz

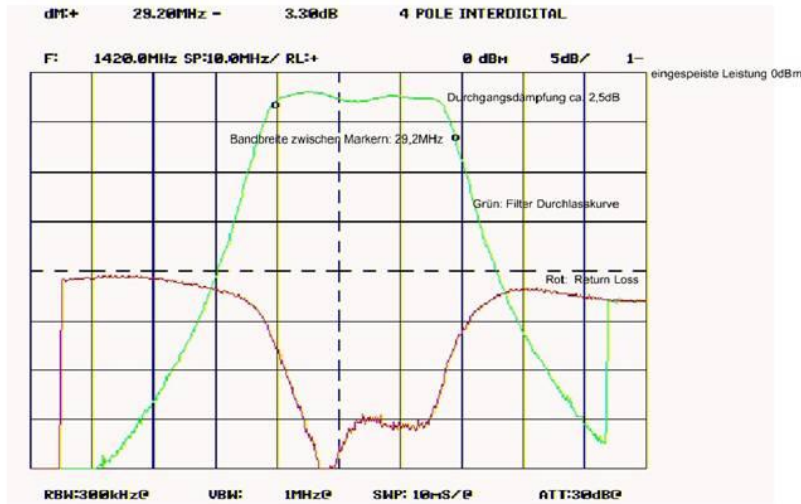
- Interdigital 4 Pole Filter
- frequency domain (3 dB): 1405 to 1437 MHz
- Insertion Loss: 1 dB typ.
- Input / Output impedance: 50 Ohms



# Hydrogen filter 1420 MHz



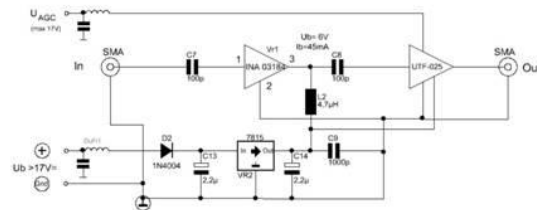
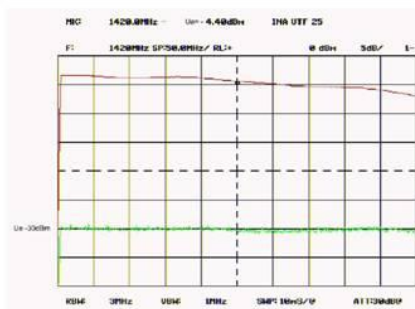
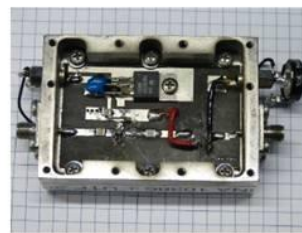
- Frequency response



# IF Amp



- IF main amplifier & Attenuator
- Bandwidth 10 -1800 MHz
- Gain 26 dB @1.5 GHz



## Digital Hardware (SDR Platform)



Criteria for selecting a suitable platform:

- The frequency range up to 1.70 GHz.
- Suitable for low-cost experimentation
- Reprogramability
- Fully open source platform (hardware, software)
- High resolution
- Sufficient bandwidth

## Overview of SDR platform

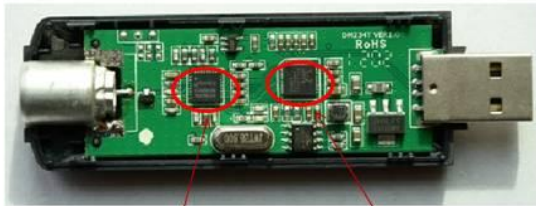
SDR Platform	Hackrf	BladeRF	USRP (B100)	Rtl_SDR(E4000)
Frequency range	30 MHz – 6 GHz	300 MHz – 3.8 GHz	50 MHz – 2.2 GHz	52 – 2200 MHz
Bandwidth	20 MHz	28 MHz	16 MHz	3.57MHz
Simple size (ADC-DAC)	8 bit	12 bit	12 bit/14 bit	8 bit
Simple rate (ADC-DAC)	20 Msps	40 Msps	64 Msps/128 Msps	3.2Msps
Transmit?	Yes	Yes	Yes	No
Interface speed	USB 2 (480Mbit)	USB 3(5 gigabit)	USB 2 (480Mbit)	USB (480Mbit)
Open source	Everything (SW+HW)	HDL + Code Schematics	HDL + Code Schematics	Open source
Supported software	Gnu radio	Gnu radio	Gnu-radio/ Matlab	Gnu radio
Price	\$300	\$420	\$675	\$20



# SDR (RTL2832U-E4000)

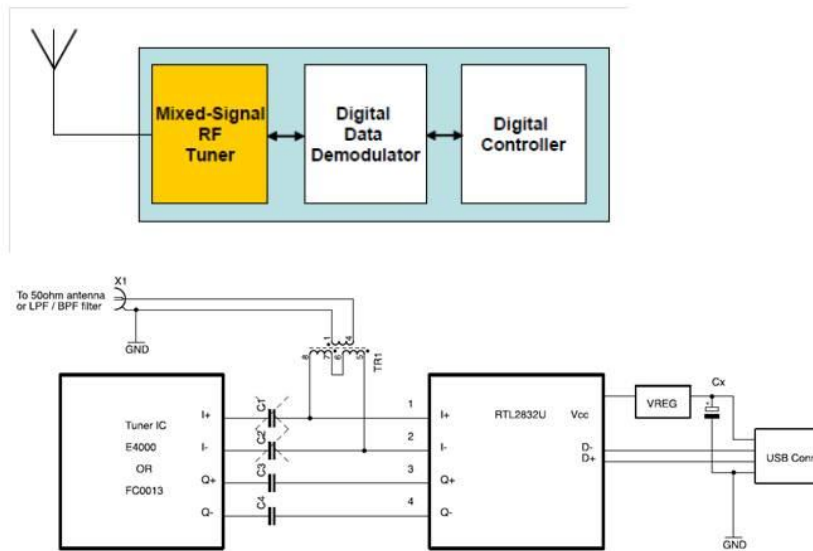


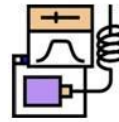
- Filtered signal is down sampled
- Frequency selecting done by The E4000 tunerchip
- Analog to digital converter (RTL2832U)
- Downconversion from IF to BF
- Output is sent to the computer by USB2.0



E4000                  RTL2832u

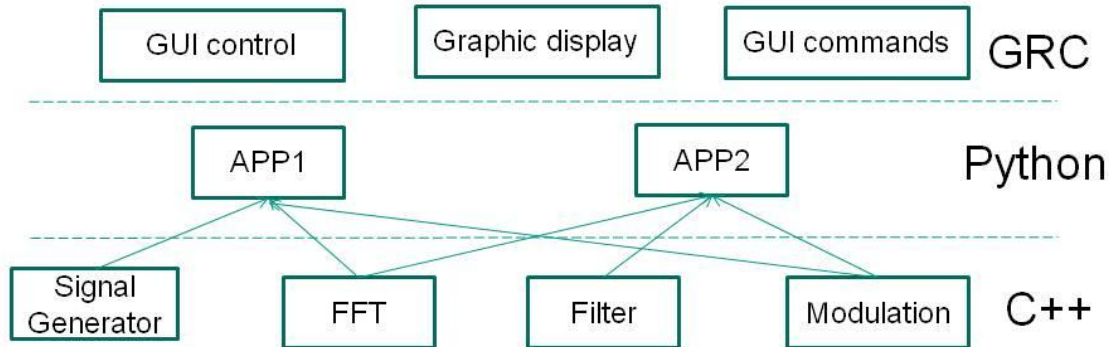
# SDR (RTL2832U-E4000)





## Software Design

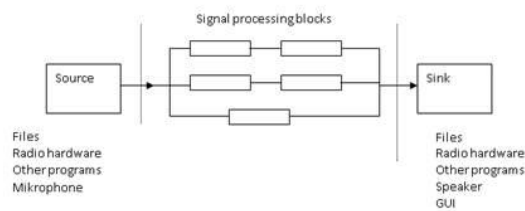
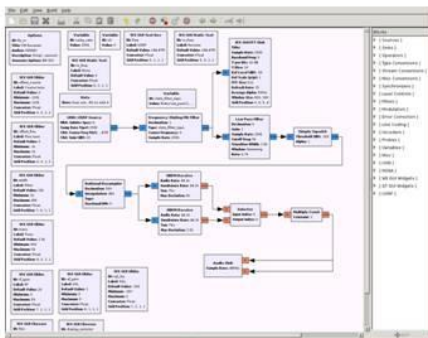
- GNU radio is an open source, Python-based architecture for building SDR projects
- C++ written signal processing blocks and python written connectors
- Available on Linux, Mac OS and Windows



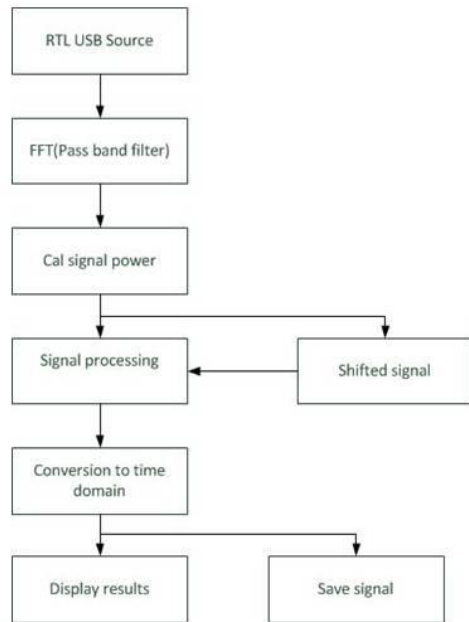
## GNU Radio Companion



- A graphical tool that Create signal flow graphs & Generate flow-graph source code

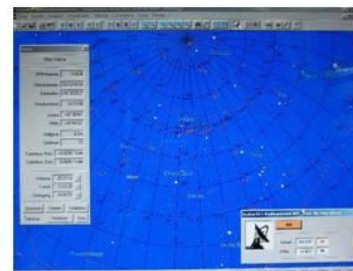
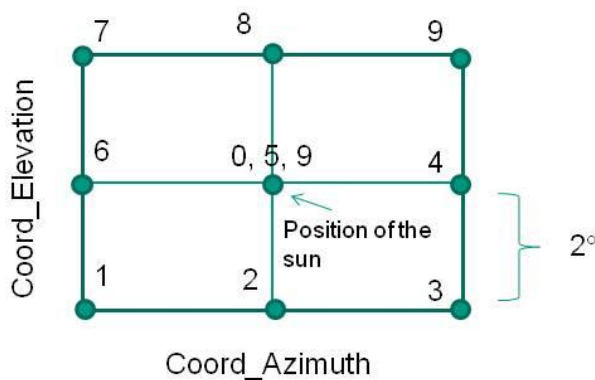


# Software Implementation



# Software Implementation

- Scan(movement of the antenna) of area of
- Time transmission takes 2 sec between each 2 nodes
- Scanning starts from sun position(Easy Sky) and ends there
- Center of the matrix is tested 3 times



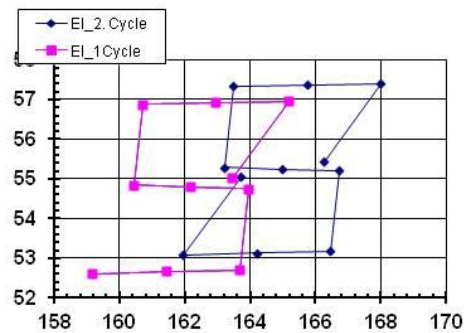
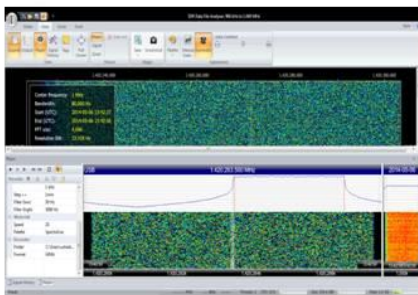
Easy Sky software

## Measurement

### ■ First scenario



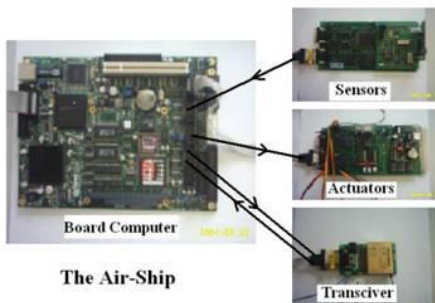
### ■ Second scenario



## Mock-up model of IAP-satellite (future work)

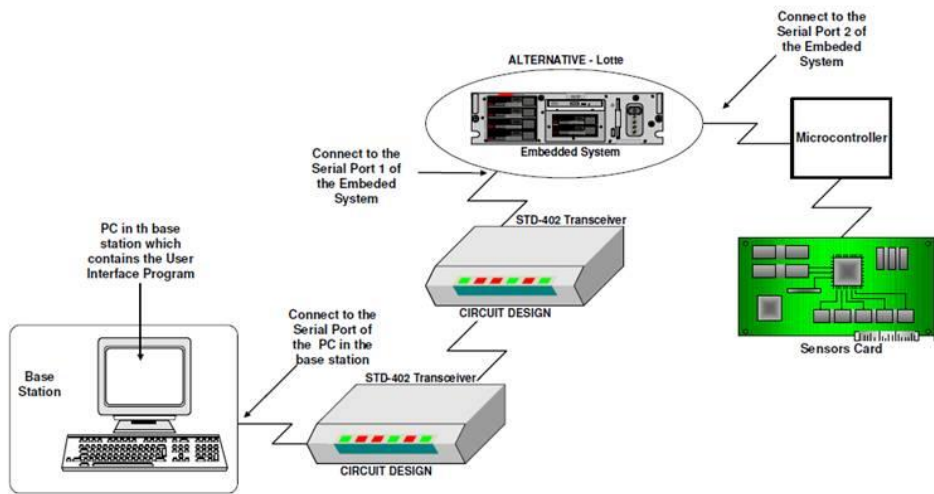
### ■ Mock-up is prototype model of IAP satellite

- Linux embedded Board computer
- Sensor card (temperature, camera,...)
- Transceiver card
- RTL SDR
- Antenna





# Communication system on Mock-up model



# Integration receiver model on Mock-up

- Import GnuRadio Model on embedded board
  - Operating system: Linux
  - Generated python\_code(GnuRadio) is compiled to C code by compiler
  - C-code will be sent by transceiver to ground station



**Table of contents**

<b>ABSTRACT</b> .....	<b>II</b>
<b>TABLE OF CONTENTS</b> .....	<b>XVIII</b>
<b>LIST OF FIGURES</b> .....	<b>XIX</b>
<b>LIST OF TABLES</b> .....	<b>FEHLER! TEXTMARKE NICHT DEFINIERT.</b>
<b>LIST OF FORMULAS</b> .....	<b>FEHLER! TEXTMARKE NICHT DEFINIERT.</b>
<b>LIST OF KEYWORDS</b> .....	<b>XIX</b>
<b>1 INTRODUCTION</b> .....	<b>21</b>
1.1 BACKGROUND .....	21
1.2 MOTIVATION .....	21
1.3 OBJECTIVES.....	<b>FEHLER! TEXTMARKE NICHT DEFINIERT.</b>
1.4 OUTLINE.....	21
<b>2 BASICS</b> .....	<b>22</b>
2.1 21-CM RADIO ASTRONOMY BASICS .....	22
2.2 RADIO WAVE RECEIVING .....	23
2.3 SOFTWARE DESIGNED RADIO .....	23
2.4 BASIC SDR RECEIVER ARCHITECTURE.....	24
<b>3 SYSTEM DESIGN</b> .....	<b>26</b>
<b>4 MECHANICS</b> .....	<b>FEHLER! TEXTMARKE NICHT DEFINIERT.</b>
4.1 MECHANICAL DESIGN .....	<b>FEHLER! TEXTMARKE NICHT DEFINIERT.</b>
<b>5 HARDWARE CONCEPTION</b> .....	<b>28</b>
5.1 PLATFORM SELECTION .....	28
5.1.1 <i>Hackrf platform</i> .....	28
5.1.2 <i>BladeRF Platform</i> .....	29
5.1.3 <i>Ettus Research's USRP B100</i> .....	29
5.1.4 <i>Rtl_SDR(820)</i> .....	30
<b>6 HARDWARE REALIZATION</b> .....	<b>31</b>
6.1 HARDWARE OF USRP .....	33
6.1.1 <i>USRP B100 as motherboard</i> .....	33
6.1.2 <i>WBX 50-2200 MHz Rx/Tx as daughterboard</i> .....	34
6.1.3 <i>FPGA</i> .....	35
6.1.4 <i>ADC converter</i> .....	37
6.2 LOW NOISE AMPLIFIER LNA .....	37
6.3 LINE AMPLIFIER.....	40
6.4 ANTENNA .....	40
<b>7 SOFTWARE</b> .....	<b>43</b>
7.1 SOFTWARE DESIGN .....	<b>FEHLER! TEXTMARKE NICHT DEFINIERT.</b>
7.2 SOFTWARE IMPLEMENTATION .....	48
<b>8 INTEGRATION</b> .....	<b>FEHLER! TEXTMARKE NICHT DEFINIERT.</b>
<b>9 INTEGRATION TEST</b> .....	<b>FEHLER! TEXTMARKE NICHT DEFINIERT.</b>
<b>10 FUTURE WORK</b> .....	<b>52</b>
<b>11 LITERATURE</b> .....	<b>53</b>
<b>12 APPENDIX</b> .....	<b>54</b>

A.1	SOFTWARE .....	54
A.1.1	System Software .....	<b>Fehler! Textmarke nicht definiert.</b>
A.1.1.1	Example.c .....	<b>Fehler! Textmarke nicht definiert.</b>
A.2	HARDWARE .....	63
A.2.1	Layout motherboard USRP B100 .....	63
A.3	LIST OF OFF-THE-SHELF ELECTRONIC COMPONENTS AND ASSEMBLIES .....	68
A.4	MECHANICAL COMPONENTS .....	69

## List of figures

FIGURE 1: HYDROGEN EMISSION .....	22
FIGURE 2: SPAIN MECHANISMS.....	23
FIGURE 3: RADIO SYSTEM .....	23
FIGURE 4: MODEL OF SOFTWARE RADIO [1] .....	24
FIGURE 5: BLOCK SCHEME OF TYPICAL SDR RECEIVER.....	25
FIGURE 8: OVERVIEW AND COMPARISON OF DIFFERENT PLATFORMS .....	28
FIGURE 9:USRP INSTANT SDR KIT.....	33
FIGURE 10: ARCHITECURE OF B100 .....	34
FIGURE 11: RF FRONT-END DIAGRAM .....	34
FIGURE 12: RECEIVER BLOCKS .....	35
FIGURE 13: DDC BLOCK .....	36
FIGURE 14: SCHEMATIC AND PLATINE OF LNA.....	37
FIGURE 15: TEST OF LNA .....	38
FIGURE 16: OUTPUT SIGNAL OF LNA.....	38
FIGURE 17.....	39
FIGURE 18.....	<b>FEHLER! TEXTMARKE NICHT DEFINIERT.</b>
FIGURE 19: IMPLEMENTATION OF DIAL_TONE EXAMPLE WITHIN GNU RADIO COMPANION.....	45

## List of Keywords

**ADC** Analog-to-Digital converter

**AF** Audio Frequency

**AGC** Automatic Gain Control

**AM** Amplitude Modulation

**BFO** Beat Frequency Oscillator

**CW** Continuous Wave

**DAB** Digital Audio Broadcasting

**DVB-T** Digital Video Broadcasting - Terrestrial

**RTL-SDR** Software Defeind Radio Dongle

**FFT** Fast Fourier Transform

**FM** Frequency Modulation

**FPGA** Field Programmable Gate Array

**FSF** Free Software Foundation

**GRC** GNU Radio Companion

**IF** Intermediate Frequency

**IAP** Institute for AstroPhysics

**I/O** Input/output

**ISO** International Organization for Standardization

**LNA** Low Noise Amplifier

**RDS** Radio Data System

**RF** Radio Frequency

**SRD** Software Defined Radio

**SRWDA** supernova radio wave detector and analyzer.

**USB** Universal Serial Bus

# **1 Introduction to SWRDA**

## **1.1 Background**

The gained information about the universe has been interpreted using radio frequency electromagnetic signals that can be detected through radio digital receiver. One of the most important beams is HI line 21cm that carry information about hydrogen atoms in space to get different astronomic parameters of hydrogen atom as speed, direction or distance within the galaxy etc. The rotation curve of our galaxy has also been calculated using the 21-cm hydrogen line. It is then possible to use the plot of the rotation curve and the velocity to determine the distance to a certain point within the galaxy [1].

The digital technology in communication scope made possible to measurement a spectrum line and processes to get clean signals.

## **1.2 The SRWDA Project**

The radio astronomical IAP project supernova radio wave detector and analyser (SRWDA) aims to detect and analyze HI radio signals from supernova remnants. At the base station a set of antennas, which gives also direction information of the signals, is aimed to be connected to a computer which acts as Software Defined Radio (SDR). Afterwards an analysing program is aimed to be installed.

Later the detectors are planned to be installed on satellites in the IAP SRWDA-SAT project [9] to improve the resolution and to suppress disturbing signals from earth stations.

### **1.1 Objectives**

In this thesis it is aimed to build a first prototype for a ground station for SRWDA.

### **1.2 Outline**

This thesis presents the design and implementation of SDR (Software Defined Radio) receiver to detect spectral line 21 cm of hydrogen atom for radio astronomy using reconfigurable platform and open source software for implementing Digital signal processing.

Chapter 2 gives some scientific and technical background information.

Chapters 3 until the last chapter describe the successive development process of the prototype according to the V model.

## 2 Basics

### 2.1 21-cm Radio Astronomy Basics

The hydrogen gas is one important of the main materials that can be found in throughout of the space. The 1420 MHz radiation form hydrogen pass through the Earth's atmosphere and gives us a more complete map of the hydrogen than that of the stars themselves since their visible light won't penetrate the dust clouds. The radiation comes from the transition between the two levels of the hydrogen 1s ground state, slightly split by the interaction between the electron spin and the nuclear spin. In this procedure hydrogen in its lower state will absorb 1420 MHz.

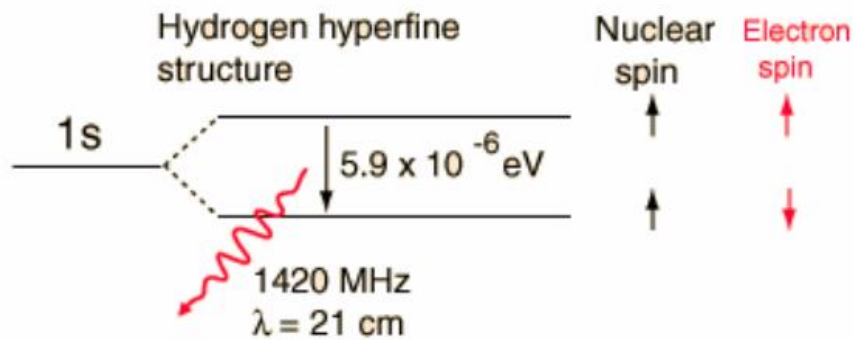


Figure 1: hydrogen emission

The electron moving around the proton can have a spin in the same direction as the proton's spin (i.e., parallel) or spin in the direct opposite direction as the proton's spin (i.e., anti-parallel). The energy state of an electron spinning antiparallel is slightly lower than the energy state of a parallel-spin. Since atoms always want to be in the lowest energy state possible, the electron will eventually flip to the anti-parallel spin direction if it were in the parallel spin direction. The energy difference is very small, so a hydrogen atom can wait on average a few million years before it undergoes this transition. The advantage for detecting the 21cm signal is to calculate the mass of galaxies, to put limits on any changes over time of the universal gravitational constant and to study dynamics of individual galaxies and to plot the rotation curve of our galaxy respectively the velocity [1].

This splitting of the hydrogen ground state is extremely small compared to the ground state energy of  $-13.6 \text{ eV}$ , only about two parts in a million. The two states come from the fact that both the electron and nuclear spins are  $1/2$  for the proton, so there are two possible states, spin parallel and spin antiparallel. The state with the spins parallel is slightly higher in energy (less tightly bound).

In visualizing the transition as a spin-flip, it should be noted that the quantum mechanical property called "spin" is not literally a classical spinning charge sphere. It is a description of the behaviour of quantum mechanical angular momentum and does not have a definitive classical analogy. The observation of the 21cm line of hydrogen marked the birth of spectral-line radio astronomy. It was first observed in 1951 by Harold Ewen and Edward M. Purcell at Harvard, followed soon afterward by observers in Holland and Australia.

The prediction that the 21 cm line should be observable in emission was made in 1944 by Dutch astronomer H. C. van de Hulst [2]. A radio telescope is powerful tool, which can “see” radio waves emitted by radio sources in throughout the space.

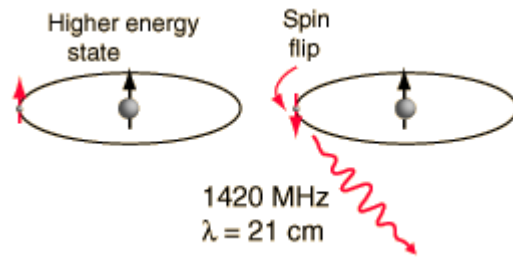


Figure 2: Spin mechanisms

## 2.2 Radio Wave Receiving

Firstly we want to present the simple radio system diagram and explain their components to get better understanding for complete system.

The electromagnetic signal has been received by an antenna and then converted into an electrical signal. This signal is normally very weak and disturbed because of many factors as atmosphere ... etc. therefor the noise must be removed from a signal amplified before it processing later. That will be happened in the next stage (RFF) that processes a signal for ADC converter. RFF consists of filter, amplifier und mixer to convert the radio frequency to lower frequency. The resulted analog signal from RFF has to be digitized using *Analog -Digital converter* for further processing in suitable hardware components as Digital Signal Processing (DSP), Field Programmable Gate Array (FPGA) or microprocessor [2].

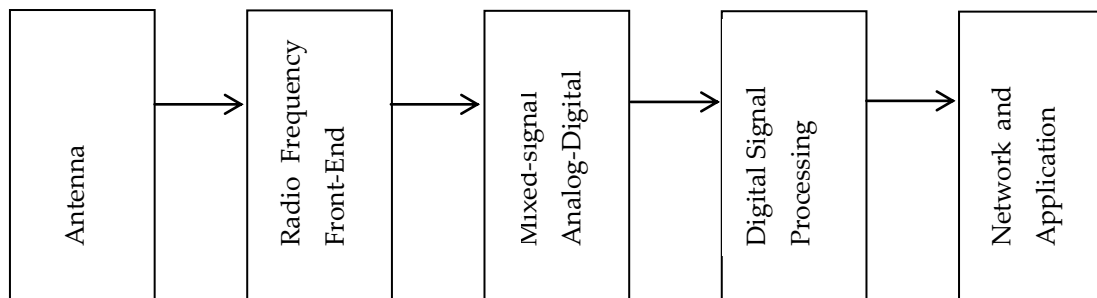


Figure 3: Radio system

Finally

a

processed radio signal can interface in modern system to a network or an application.

## 2.3 Software Designed Radio

The definition software radio was Joe Mitola in 1991 to refer to the class of reprogrammable or reconfigurable radios [3]. That means, the same hardware components can execute different functions at different times. However, a radio defines in software its modulation, error correction, and encryption processes, exhibits some control over the RF hardware, and can be reprogramed is clearly a software radio.

SDR is defined as a described radio in Software and whose physical layer behaviour can be significantly altered through changes to its software in which the receive digitization is performed at some stage downstream from the antenna, typically after wideband filtering, low noise amplification, and down conversion to a lower frequency in subsequent stages – with a reverse process occurring for the transmit digitization. Digital signal processing in flexible and reconfigurable functional blocks defines the characteristics of the radio [4].

Hardware components of the traditionally radio system consists of the mixers, filters, amplifiers and oscillators are replaced by software in SDR as indicated in the Figure 2.2. The hardware for signal processing should be selected for high speed signal processing for example as GGP, FPGA or DSP. The main advantage of an SDR is reconfigurability and customizable. The implementing radio functions in software are more flexible than in hardware for a radio device to be reconfigured for different use cases rather needing to redesign the hardware to support new functionality. With the rapid evolution of wireless protocols and standards, a hardware radio could be made obsolete due to the inability to conform to new standards or protocols. An SDR, however, could be reconfigured to support new standards that may not have existed at the time the device was built. Such flexibility is attractive to the manufacturers of the devices as it enables them to update their SDR product through software and not necessarily need to change the hardware of the radio. Such flexibility is helpful to fast update suchlike systems and allows manufacturer to redesign the system without changing the hardware architecture.

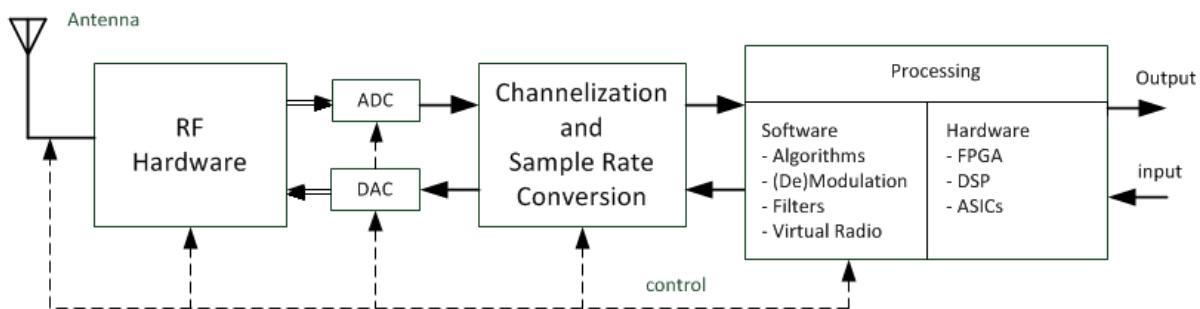


Figure 4: Model of Software Radio [1]

## 2.4 Basic SDR Receiver Architecture

The most used radio receivers use the architecture of super heterodyne receiver, in which a received signal has been converted to a fixed intermediate frequency, which can be more processed than the original radio carrier frequency. A detected signal is picked up via the antenna, mixed with local oscillator to reduce frequency of an incoming signal to intermediate frequency (IF) for further processing, filtered due unwanted signals filtered using low pass filter and finally amplified with a low noise amplifier (LNA) for accommodation to ADC converter.

The digitized IF signal repeat oneself as spectral harmonic that can be placed near the baseband frequency, helping frequency translation and digitization to be carried out simultaneously. For next processing digital filtering and downconversion of sample rate (for receiving) are needed to change a sampled signal from high frequency to lower frequency allowing a hardware as DSP or FPGA to process it with suitable sample rate without loss of the information.



Typical SDR receivers have a simple and cheap direct-conversion or low intermediate frequency architecture. The ideal SDR receiver would have all the radio-frequency bands and modes defined software-wise, meaning it would consist only of an antenna, ADC and a programmable processor. Typically, RF front-end of a SDR will consist of antenna circuitry, amplifiers, filters, local oscillators and ADCs. When the signal is received, it is amplified and its carrier frequency downconverted to a low-intermediate frequency in order for ADC to perform digitization.

The processing is done by some of the computational resources at our disposition – mainly, General Purpose Processors (GPPs), Digital Signal Processors (DSPs) and Field Programmable Gate Arrays (FPGAs), whereas some of the future resources may include a combination of the aforementioned, thus extending the computational capacity. One of the most important aspects when deciding on a computational resource that is to be used in the system is its reprogrammability (important for implementation of new waveforms), therefore dedicated-purpose circuitry is generally avoided in SDRs.

The basic receiving process is illustrated in Figure 2.3 with its principle design constraints will be explained in this chapter.

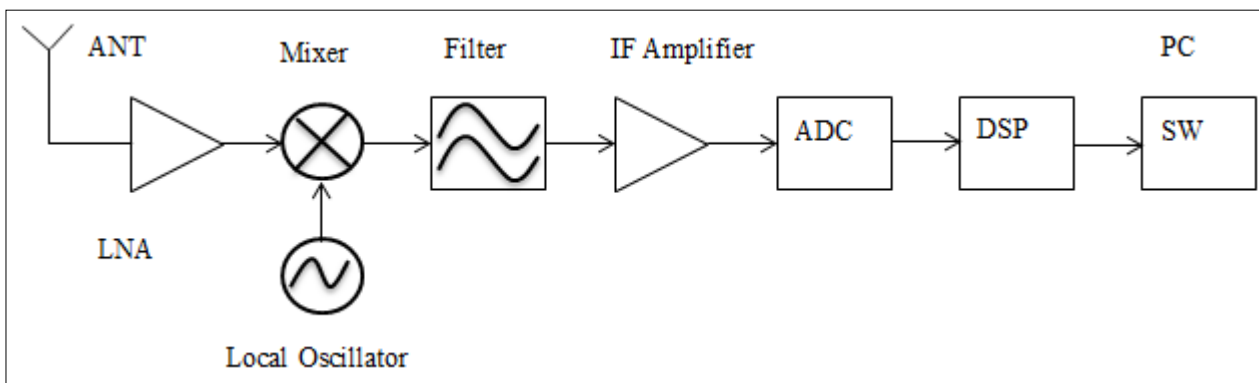


Figure 5: Block scheme of typical SDR receiver

The important design parameters that have to be considered during design SDR receiver system are: input sensitivity, maximum expected input signal and blocker specifications.

### 3 System Design

The HI spectrum signal will be detected by the antenna which converts the electromagnetic signal to analog signal to process with SDR system (Hardware and Software). Because of the weakness of the incoming HI spectrum signal we have to use a low noise amplifier for filtering the incoming signals and amplifying the hydrogen line signal at 1420 MHz. The filtered signal is then available for further processing phase. It is important to integrate a line amplifier in the design taking into account the signal line loss by using coaxial cable. For further high signal processing SDR platform (SDR-hardware and-software) were needed to realize **SRWDA** model. Two designs have been developed in IAP institute. The figures 6 und 7 give both alternative designs explained.

A software-defined radio (SDR) system is a hardware and software co-design system which can tune to any frequency band and preform different communication functions (modulation, demodulation, etc.) by means of a programmable hardware, which is controlled by software. SDR platform software performs various amounts of digital signal processing in PC [1]. SDR has evolved with advancement in computing machines and high-speed analog-digital (A/D) and digital-analog (D/A) converters. Thus SDR allows a single device to support a wide range of capabilities previously available only through multiple products [1].

As explained signals received by an antenna should be digitized so that SDR may processes these digitized samples at RF frequencies (around GHz frequencies) to perform further signal processing steps (IF conversion, filtering, baseband conversion etc). But due to certain limitations like unavailability of A/D converters at very high frequencies (starting from a few GHz) and very high speed general purpose computers, digitization takes place after the IF or baseband demodulator stage. That typically means that hardware is still required to convert the signals of interest into and out of the “baseband” frequencies in the digital domain, but all of the complex processing performed at baseband is handled in the digital software domain [1]. Yet, such hardware is usually fairly simple comprising of a local oscillator and mixer, and a pair of low-pass filters.

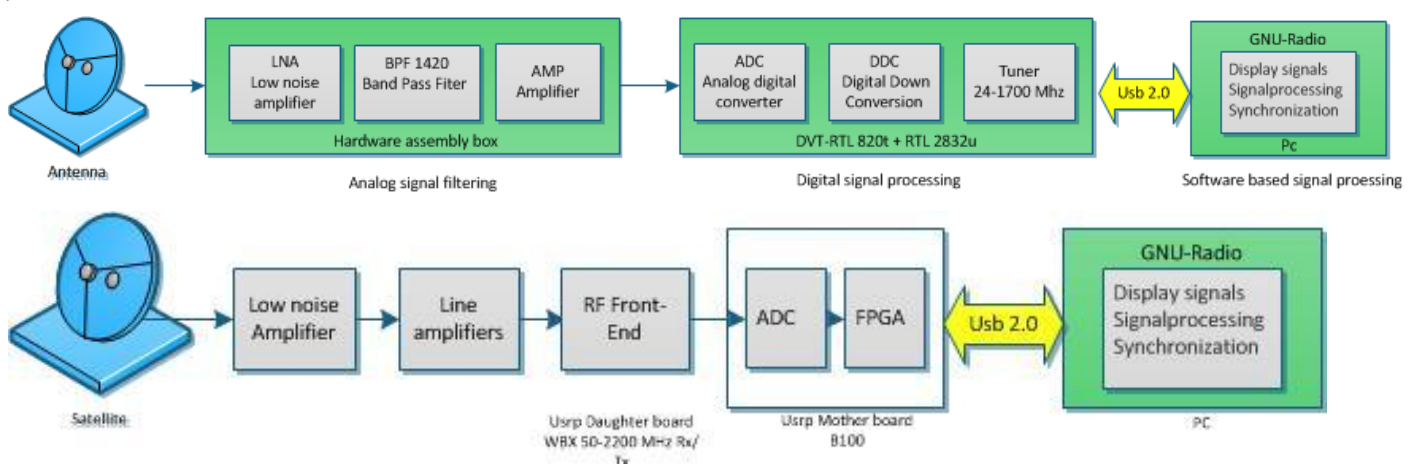


Figure 6: 1.System design overview

The digital signal will be sent via usb2.0 to host pc which software *Gnu-Radio* uses to control SDR hardware platform and transmit and receive data. GNU Radio is an open-source software toolkit. that, connected with hardware equipment such as USRP, allows for building Software Defined

Radios connect with hardware. We will later go into details also hardware components and software respectively.

## 4 Hardware Conception

### 4.1 Platform Selection

This chapter describes the core idea for selecting receiver components to implement our system and the desired environment work. These are the criteria which have to be fulfilled by a suitable platform:

The receiver system operates in 1420 MHz.

Suitable for low-cost experimentation.

Reprogrammability.

Fully open source platform (hardware, software).

Couple of weeks of research narrowed the options down to the following SDR platforms:

SDR Platform	Hackrf	BladeRF	USRP(B100)	Rtl_SDR(E4000)
Frequency range	30 MHz - 6 GHz	300 MHz - 3.8 GHz	50 MHz - 2.2 GHz	52 - 2200 MHz
Bandwidth	20 MHz	28 MHz	16 MHz	3.57MHz
Simple size (ADC-DAC)	8 bit	12 bit	12 bit/14 bit	8 bit
Simple rate (ADC-DAC)	20 Msps	40 Msps	64 Msps/128 Msps	3.2Msps
Transmit?	Yes	Yes	Yes	No
Interface speed	USB 2 (480Mbit)	USB 3(5 gigabit)	USB 2 (480Mbit)	USB (480Mbit)
Open source	Everything (SW+HW)	HDL + Code Schematics	HDL + Code Schematics	-----
Supported OS	Linux, OS X, Windows	Linux, OS X, Windows	Linux, OS X, Windows	Linux, OS X, Windows
Supported software	Gnu radio	Gnu radio	Gnu-radio/ Labview	Gnu radio
Price	\$300	\$420	\$675	\$20

Figure 6: Overview and comparison of different platforms

#### 4.1.1 Hackrf platform

Hackrf is open source hardware to build SDR system that has been developed by Michael Ossmann. HackRF operates from 30 MHz to 6 GHz, a wider range than any SDR peripheral available today. This range includes the frequencies used by most of the digital radio systems on Earth. It can operate at even lower frequencies in the MF and HF bands when paired with the Ham It Up RF upconverter. HackRF can be used to transmit or receive radio signals. It operates in half-duplex mode: it can

transmit or receive but can't do both at the same time. However, full-duplex operation is possible if you use two HackRF devices.

HackRF is designed primarily for use with a USB-attached host computer, but it can also be used for stand-alone applications with Jared's HackRF PortaPack, an add-on that gives HackRF an LCD screen, directional buttons, and audio ports

HackRF was designed to be the most widely useful SDR peripheral that can be manufactured at a low cost. The estimated future retail price of HackRF is \$300, but you can get one for even less by backing the Kickstarter project today. The most important goal of the HackRF project is to produce an open source design for a widely useful SDR peripheral. All hardware designs and software source code are available under an open source license. The hardware designs are produced in KiCad, an open source electronic design automation tool.

#### **4.1.2 BladeRF Platform**

bladeRF is a Software Defined Radio (SDR) platform make possible to enable a community of hobbyists, and professionals to explore and experiment with the multidisciplinary facets of RF communication. By providing source code modern radio systems will be simplified by covering everything from the RF, analog, and digital hardware design to the firmware running on the ARM MCU and FPGA to Linux kernel device drivers.

The bladeRF can tune from 300MHz to 3.8GHz without the need for extra boards. The current open source drivers provide support for GNURadio among other things, allowing the bladeRF to be placed into immediate use. This gives the bladeRF the flexibility to act as a custom RF modem, a GSM and LTE pico cell, a GPS receiver, an ATSC transmitter or a combination Bluetooth/WiFi client without the need for any expansion cards.

The bladeRF was designed to be highly integrated and fully reprogrammable. This means more than just providing source code to modify the host software. The USB 3.0 (Cypress FX3) microcontroller firmware is available to modify, as is the Altera Cyclone IV FPGA VHDL, bringing developers as close to the RF transceiver as possible.

#### **4.1.3 Ettus Research's USRP B100**

The Universal Software Radio Peripheral (USRP) is a digital acquisition (DAQ) system containing four 64 MS/s, 12-bit A/D converters (ADCs), four 128 MS/s, 14-bit D/A converters (DACs), and supports USB 2.0 interface or Ethernet(USRP N210). The USRP is capable of processing signals with 16 MHz of bandwidth.

The USRP takes daughter-cards to map the frequency ranges of interest into the "baseband" that is visible by the A/D hardware. The USRP is a most widespread SDR's in academic environments, Ettus products still count as the best-buy platforms for research. Ettus Research offers several platforms – USRP, USRP2 and USRP N210 that differ in the level of instantaneous bandwidth they can process; reprogrammability of the FPGA; type of interface to the computer (USB or Ethernet) and, of course, price..

#### 4.1.4 Rtl\_SDR (RTL2832+ E4000):

RTL-SDR is a very cheap software defined radio, that uses a DVB-T TV tuner dongle based on the RTL2832U chipset (USB devices intended to allow you to watch over-the-air DVB-T broadcast television) ,had a special “mode” that allow them to be used as crude SDR receivers. In this mode, the digital base-band samples bypass the DVB-T demodulator/decoder in the RTL2832U chip, and are sent over USB. Normally, these devices send partially-decoded MPEG transport frames over the USB, but in this “SDR” mode, they send raw I/Q base-band samples instead.

These “dongles” are typically shipped with one of two or three different tuner chips, and the most popular ones, E4000 tuner allows tuning to the hydrogen-line frequency of 1420Mhz.

A driver library was quickly produced<sup>3</sup> based on the information gleaned from datasheets and a bit of reverse engineering. The driver library can be used stand-alone, or in concert with a “plug in” for GnuRadio that allows Gnu Radio applications to use the RTLSDR devices. The disadvantages by using Rtl\_SDR outweigh his advantages because of the following reasons:

Dynamic range is quite limited, due to use of an 8-bit ADC, roughly 45dB SFDR.

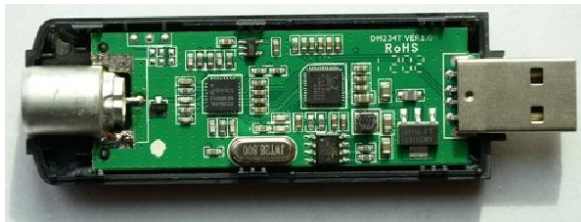
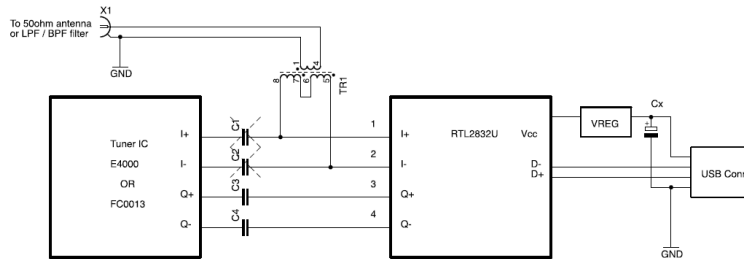
Temperature stability is poor, leading to gain drift, and frequency drift.

Phase and amplitude balance is quite poor, leading to image problems.

The total cost was 30 \$.

## 5 Hardware Realization

### 5.1 Hardware of RTL SDR (RTL2832+E4000):



#### 5.1.1 RTL2832

The RTL2832U is a high-performance DVB-T COFDM demodulator that supports a USB 2.0 interface. The RTL2832U complies with NorDig Unified 1.0.3, D-Book 5.0, and EN300 744 (ETSI Specification). It supports 2K or 8K mode with 6, 7, and 8MHz bandwidth. Modulation parameters, e.g., code rate, and guard interval, are automatically detected.

The RTL2832U supports tuners at IF (Intermediate Frequency, 36.125MHz), low-IF (4.57MHz), or Zero-IF output using a 28.8MHz crystal, and includes FM/DAB/DAB+ Radio Support. Embedded with an advanced ADC (Analog-to-Digital Converter), the RTL2832U features high stability in portable reception.

The state-of-the-art RTL2832U features Realtek proprietary algorithms (patent-pending), including superior channel estimation, co-channel interference rejection, long echo channel reception, and impulse noise cancellation, and provides an ideal solution for a wide range of applications for PC-TV, such as USB dongle and MiniCard/USB, and embedded system via USB interface.

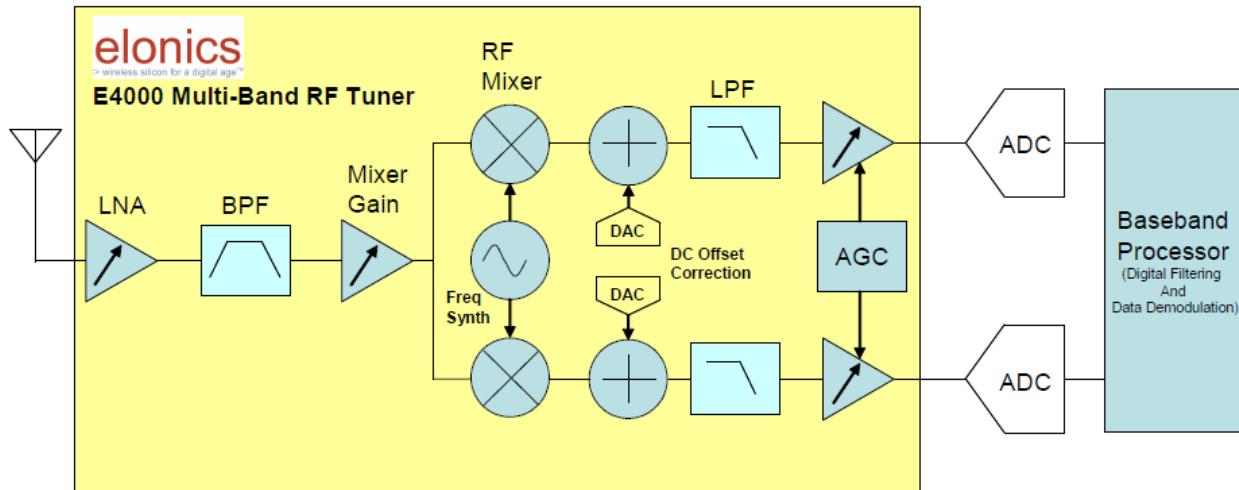
#### 5.1.2 Tuner E4000

The Elonics DigitalTune™ architecture provide solution around the ability to optimize each part of the tuner signal chain from input to output. The tuner must be able to cover the complete frequency spectrum required by the product, and output the

desired channel of interest all under control of the system controller. However, behind this apparently simple concept lies a hugely complex and challenging design problem. In order to provide such a solution, each stage in the RF tuner signal chain must be capable of being

modified to optimize the signal path characteristics for downstream processing, dependent on the broadcast standard and the desired signal characteristics chosen by the system designer.

Figure 4 shows the internal block diagram of the E4000 multi-standard RF tuner. Although the signal path looks conventional, the E4000 using the DigitalTune™ architecture provides unique flexibility at each stage in the process from input to output.



#### Benefits of Tuner E4000

- A single re-configurable RF tuner front
- Parametric performance comparable to single function tuners
- Low system power
- Small PCB
- Few external components
- Low system cost

#### Zero IF Architecture

A zero IF architecture is part of the DigitalTune™ concept. A homodyne or zero IF architecture as shown in Figure 7 employs a single stage to down convert the RF signal using a single sideband mixer to a baseband signal centred at DC. A subsequent low pass filter removes the higher frequency mixing products and attenuates unwanted out of band signals.

This filtered signal can then be digitised directly by a fast sampling ADC that has enough dynamic range to absorb both the wanted and unwanted signals. Final fine tune filtering can then be performed digitally.

The mixer output contains the sum and difference of the input signal frequencies to the mixer.

The advantages of a zero IF architecture are numerous if the intrinsic problems can be overcome.



There is no image because the signal is mixed to baseband, and therefore no image filter is needed. Because there is no intermediate IF stage, there is also no requirement for a bandpass IF filter. Finally power consumption is reduced, not only due to the simplification of the signal chain but also because the signal amplification is done at lower frequencies

## 5.2 Hardware of USRP

The Universal Software Radio Peripheral (USRP) is a low-cost SDR system developed by Ettus Research. The system consists of a motherboard with FPGA, 2 pairs of DACs and ADCs, digital downconverters and upconverters with programmable interpolation rates, and a the second part of the system is daughterboard which serve as RF front-end. The connection to the PC is done via USB2.0. Ettuscompany offers a SDR kit containing of USRP B100 as motherboard, WBX 50-2200 MHz as daughterboard which is suitable for low cost-experiment. The total price costs 590 euro. For mor details see appendix A6.



*Figure 7:USRP Instant SDR Kit*

### 5.2.1 USRP B100 as motherboard

A USRP motherboard is the heart of software defined system provides subsystems where can be built reconfigurable structure for many application in wireless communication systems. The B100-hardware provides low-cost RF processing capability, and up to 16 MS/s of signal streaming through the USB 2.0 host interface. As shown in figure 3.2 the B100 consists of FPGA, ADC, DAC and a USB interface.

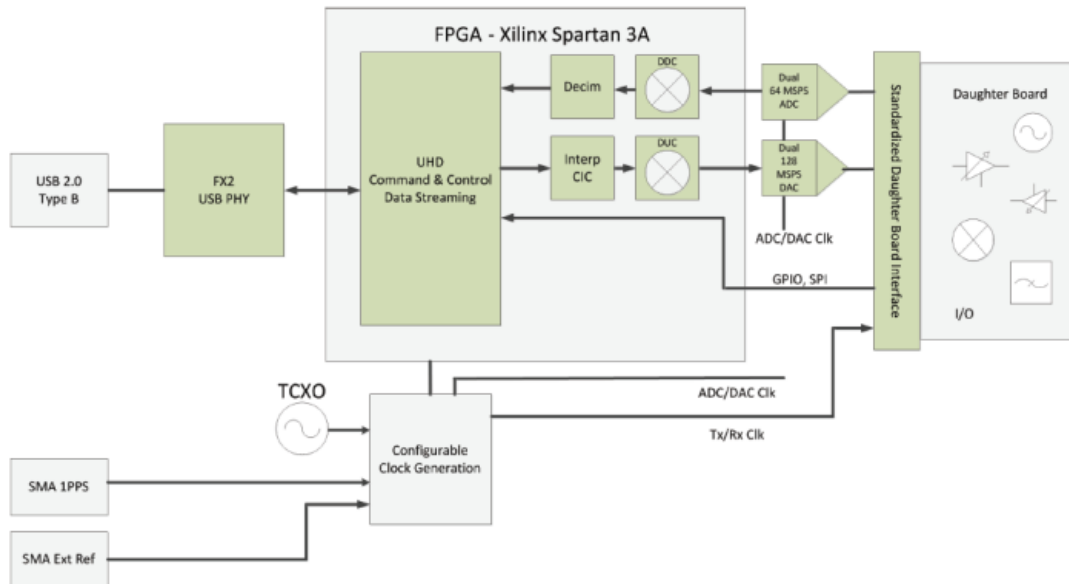


Figure 8: Architecture of B100

### 5.2.2 WBX 50-2200 MHz Rx/Tx as daughterboard

A new front-end circuit is used for analog operations such as up/down-conversion, filtering, and other signal conditioning. This modularity allows the USRP to serve applications that operate between DC and 6 GHz. The main function of RF Front-End is to reject undesired signal using filtering it after taking the signal from antenna and then converting the signal to a center frequency with an amplitude compatible for the analog digital conversion process. The Ettus research has developed many boards as RF so called daughterboard<sup>1</sup> which achieve our requirements and cover different frequency bands. For the project, receiver boards operating in 1.4 GHz (HL spectrum line) frequency band were needed, therefore two WBX 50-2200 MHz Rx/Tx daughterboard were chosen.

The WBX is a wide bandwidth transceiver that provides up to 100 mW of output power and a noise figure of 5 dB. The LO's for the receive and transmit chains operate independently, but can be synchronized for MIMO operation. The WBX provides 40 MHz of bandwidth capability and is ideal for applications requiring access to a number of different bands within its range - 50 MHz to 2.2 GHz [5]. This receiver architecture, shown in Figure 3.3, is implemented on the daughterboard WBX.

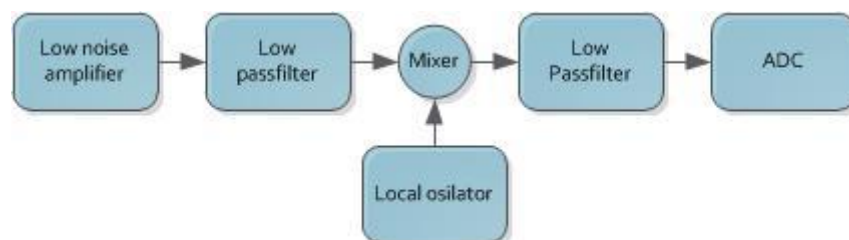


Figure 9: RF Front-End diagram

<sup>1</sup>Ettus Research Company offers different boards for various application areas. For selecting a suitable combination of boards Ettus Company recommends new users evaluate their application requirements against the specifications USRP devices.

### 5.2.3 FPGA

The FPGA plays an important role in the Radio system, providing digital signal processing, as well as timing logic for clock, chip rate and time slot synthetization . The main functionality of FPGA is to perform high bandwidth math, and to reduce the data rates to something you can squirt over USB2.0. The FPGA connects to a USB2 interface chip, the Cypress FX2. Everything (FPGA circuitry and USB Microcontroller) is programmable over the USB2 bus.

USRP B100 is powered by Xilinx Spartan 3A-1400 FPGA[5] and has the following characteristics:

Configurable Logic Blocks (CLBs) contain flexible Look-Up Tables (LUTs) that implement logic plus storage elements used as flip-flops or latches. CLBs perform a wide variety of logical functions as well as store data.

Input/output Blocks (IOBs) control the flow of data between the I/O pins and the internal logic of the device. IOBs support bidirectional data flow plus 3-state operation. Supports a variety of signal standards, including several high-performance differential standards. Double Data-Rate (DDR) registers are included.

Block RAM provides data storage in the form of 18-Kbit dual-port blocks.

Multiplier Blocks accept two 18-bit binary numbers as inputs and calculate the product.

Digital Clock Manager (DCM) Blocks provide self-calibrating, fully digital solutions for distributing, delaying, multiplying, dividing, and phase-shifting clock signals.

The standard FPGA configuration includes digital down converters (DDC) implemented with cascaded integrator-comb (CIC) filters. CIC filters are very high-performance filters using only adds and delays. The FPGA implements 4 digital down converters (DDC). This allows 1, 2 or 4 separate RX channels. The receiver side includes 4 ADCs and 4 DDCs as shown in figure 3. Each DDC has two inputs I and Q. Each of the 4 ADCs can be routed to either of I or the Q input of any of the 4 DDCs.

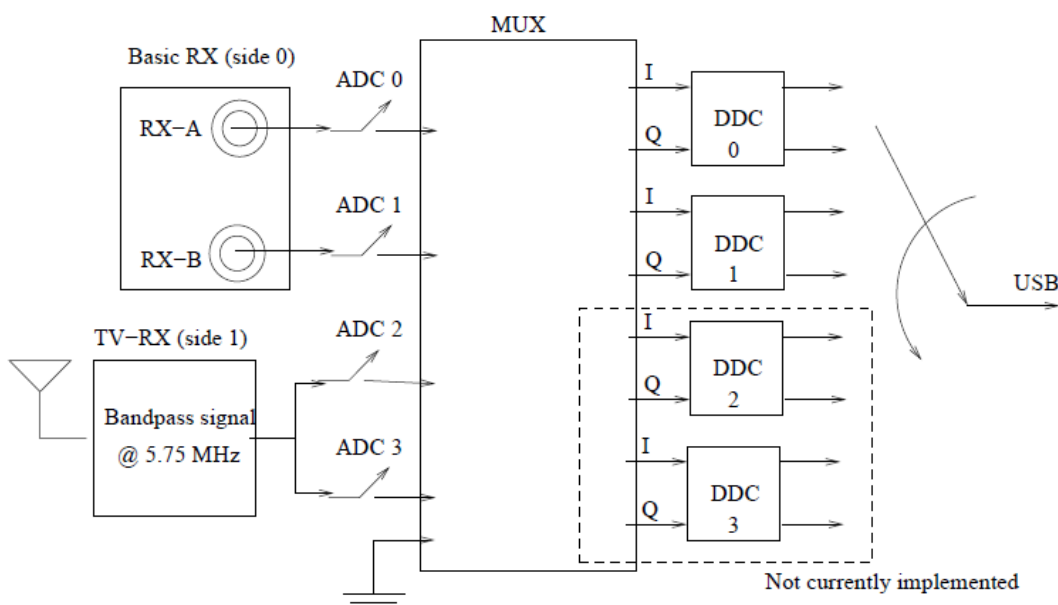


Figure 10: Receiver Blocks

The MUX is like a router or a circuit switcher. It determines which ADC (or constant zero) is connected to each DDC input. There are 4 DDCs. Each has two inputs. We can control the MUX using `usrp.set_mux()` method in Python [6].

Each input (I0, Q0, I1 ... I3, Q3) can be connected with which ADC by using 4 bits (0, 1, 2, 3 or 0xf). For most real sampling applications, the Q input of each DDC is constant zero. So quite often we don't need to modify the standard configuration of the FPGA. Actually it is anticipated that the majority of USRP users will never need to use anything other than the standard FPGA configuration.

The platform contains two digital downconverters with programmable decimation rates, in charge of mixing, filtering and decimating arriving signals in the FPGA. Digital downconverters shift the frequency band of the incoming high sampling rate digitized signal to the baseband and lower the sampling rate without any information loss. First, the digitized stream is mixed with a digitized cosine (for I channel) and digitized sine (for Q channel), producing the sum and the difference components. These outputs are then put through the identical digital filters, filtering unwanted components. At this point, because the bandwidth of the signals we want to process has been reduced, sampling frequency can be loss lessly decimated. The DDC converts down the signal from the IF band to the base band. Second, it decimates the signal so that the data rate can be adapted by the USB 2.0 and is reasonable for the computers' computing capability. The Figure 3.4 shows the block diagram of the DDC. The complex input signal (IF) is multiplied by the constant frequency (usually also IF) exponential signal. The resulting signal is also complex and centered at 0. Then we decimate the signal with a factor  $N$ . Note that when there are multiple channels (up to 4), the channels are interleaved. For example, with 4 channels, the sequence sent over the USB would be I0 Q0 I1 Q1 I2 Q2 I3 Q3 I0 Q0 I1 Q1, etc. The FPGA's configuration data is stored externally in PROM or some other non-volatile medium, either on or off the board. After applying power, the configuration data is written to the FPGA.

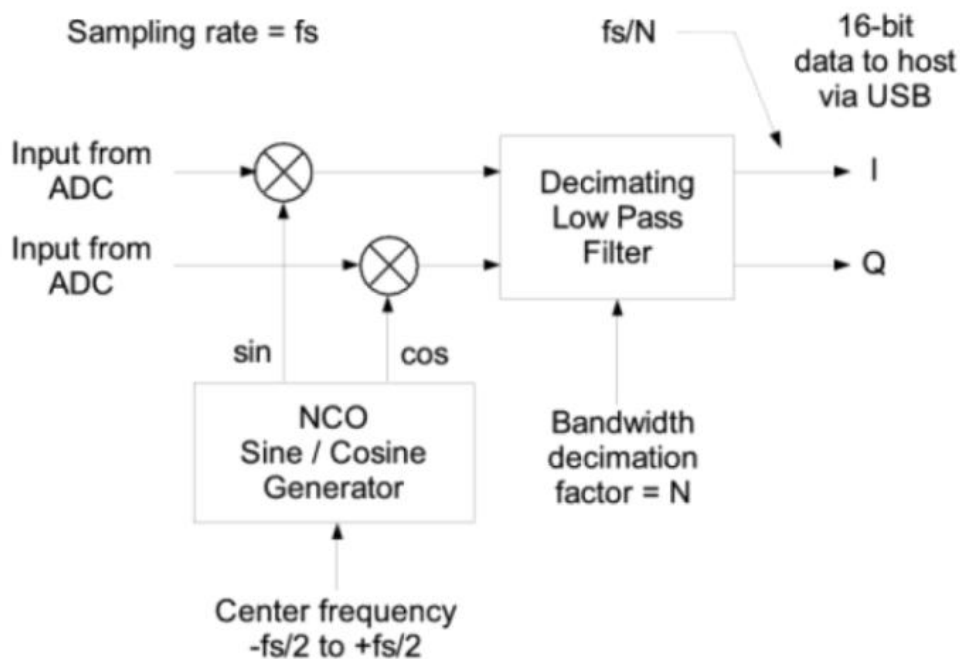


Figure 11: DDC Block

Finally I/Q complex signal enters the computer via the USB. Here starts the software fabric with signal processing.

### 5.2.4 ADC converter

In SDR system, the acquiring data via antenna has to be digitalized immediately in the receiver chain. The B100 contains two 12 bit analog digital converters with sampling rate 64 MS/s. B100 ADC's full range is 2V peak-to-peak with the input 50 ohms impedance. ADC performs sampling and quantization of incoming signal at a certain sampling rate.

### 5.3 Low Noise Amplifier LNA

In wireless communications system, low noise amplifier (LNA) plays a significant role as the critical interface between the antenna and the electronic circuits. An LNA can be considered as front-end of the receiver channel. The noise of the total receive side is reduced by using an LNA which capture and amplify a very weak signal received by antenna in addition to associated random noise which the antenna presents to it. The main parameter of LNA is noise figure (NF) that defines the degradation of the signal-to-noise ratio (SNR) due to effect of atmosphere, thermal and other sources

Low noise amplifier has been developed in the Institute IAP with typical noise figure values 0.7 dB und gain 12 dB. The figure 7 shows a schematic of an LNA using monolithic amplifier „PGA-103+“ which is characterized through high dynamic range over a broad frequency range and with low noise figure [1]. In addition, the PGA-103+ has good input and output return loss over a broad frequency range without the need for external matching components and has demonstrated excellent reliability.

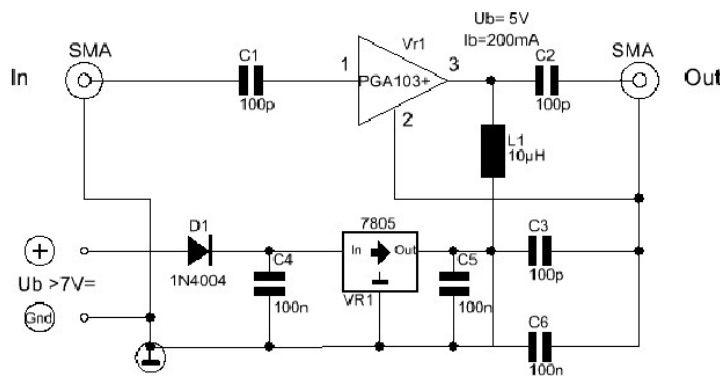


Figure 12: Schematic and platine of LNA

Furthermore, an LNA has been tested using 8620C Sweep Oscillator and the results are to see on Spectrum Analyzer (Anritsu MS 710E) as depicted in a figure 8

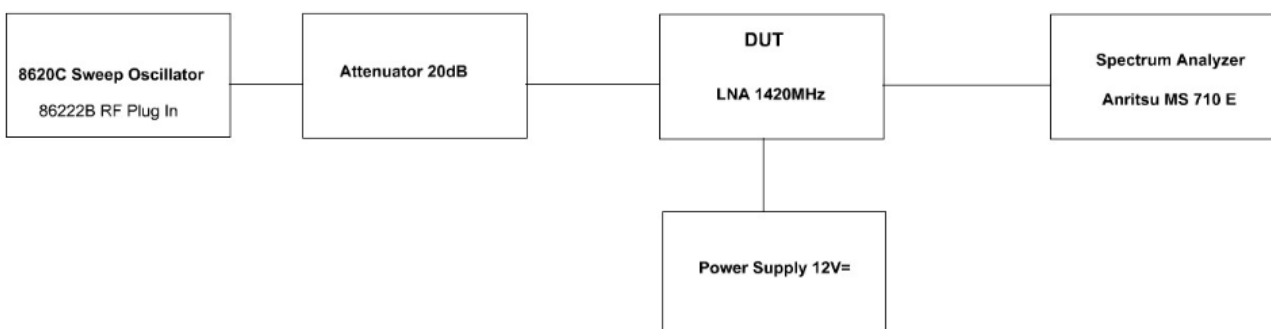


Figure 13: Test of LNA

The output signal of our test bed is to show in figure 9

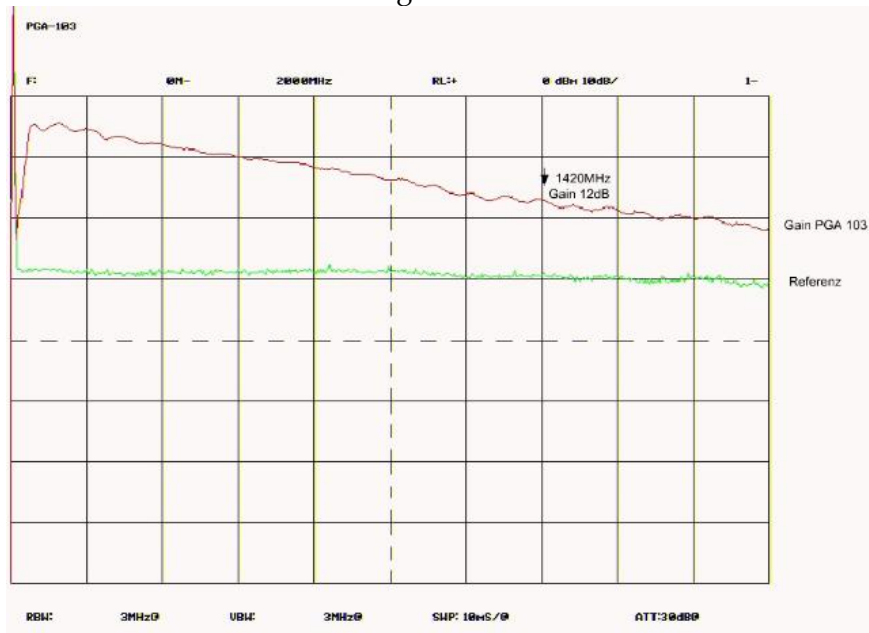


Figure 14: Output signal of LNA

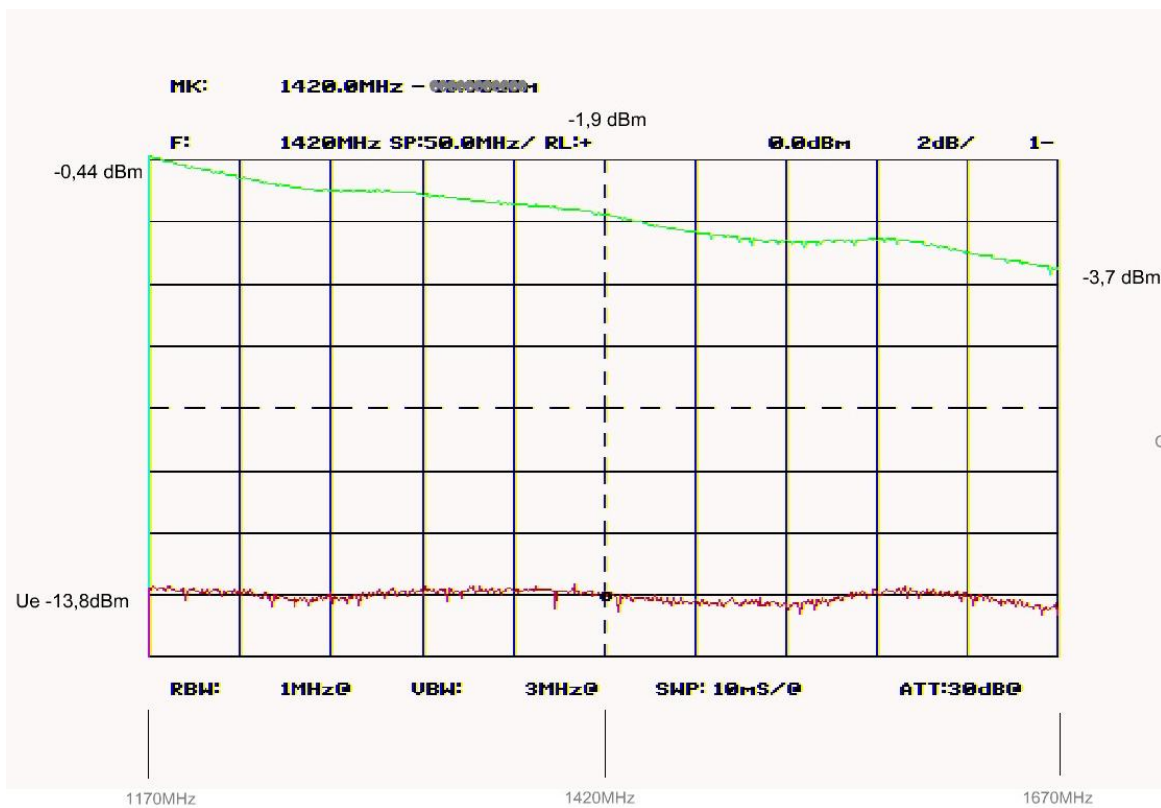
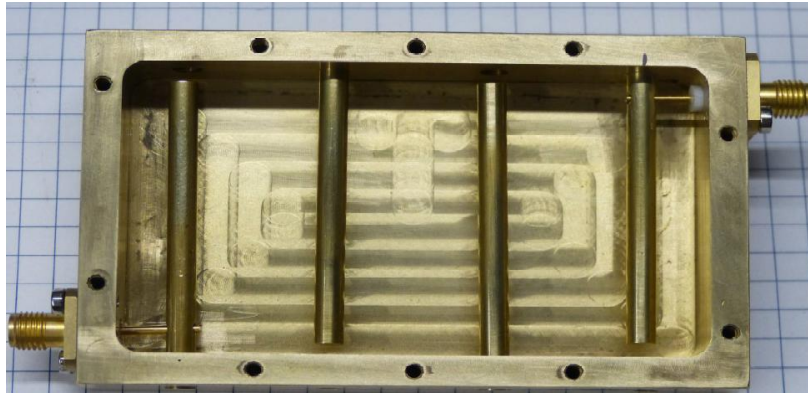


Figure 15 Output @ 2db

## 5.4 Hydrogen line filter

The frequency band to the observation of the hydrogen line which is worldwide exclusively at the radio astronomy's disposal suffices from 1400 to 1435 MHz. On the upper and lower side of this narrow frequency range strong transmitters work, such as L-band radar, mobile telephones etc.. The antennas and preamplifiers don't have the selectivity to attenuate these strong signals. This was the reason for the development of this filter. Only the frequency range around 1420 MHz passes the filter. All other frequencies become effectively attenuated. This filter is a must to prevent interferences in an H-Line receiver.

The installation of the filter should if possible be at the receiver systems input. The insertion loss



worsens however the complete noise figure of the radio astronomical receiver. The filter behind the

*Figure 16*

preamplifier therefore is as recommended in the figure 8 shown commitments. Only if strong, disturbing transmitters lead to doubtful results, the filter should be used in front of the preamplifier. Please take care furthermore that no mechanical loads on the filter and his SMA connectors work. The filter must be installed in normal atmospheric humidity at a dry place, because the filter is not water protected. The preferred mounting place is in a temperature-stabilized case direct with the preamplifier at the feed of the antenna.

The following figure shows the frequency response of hydrogen filter

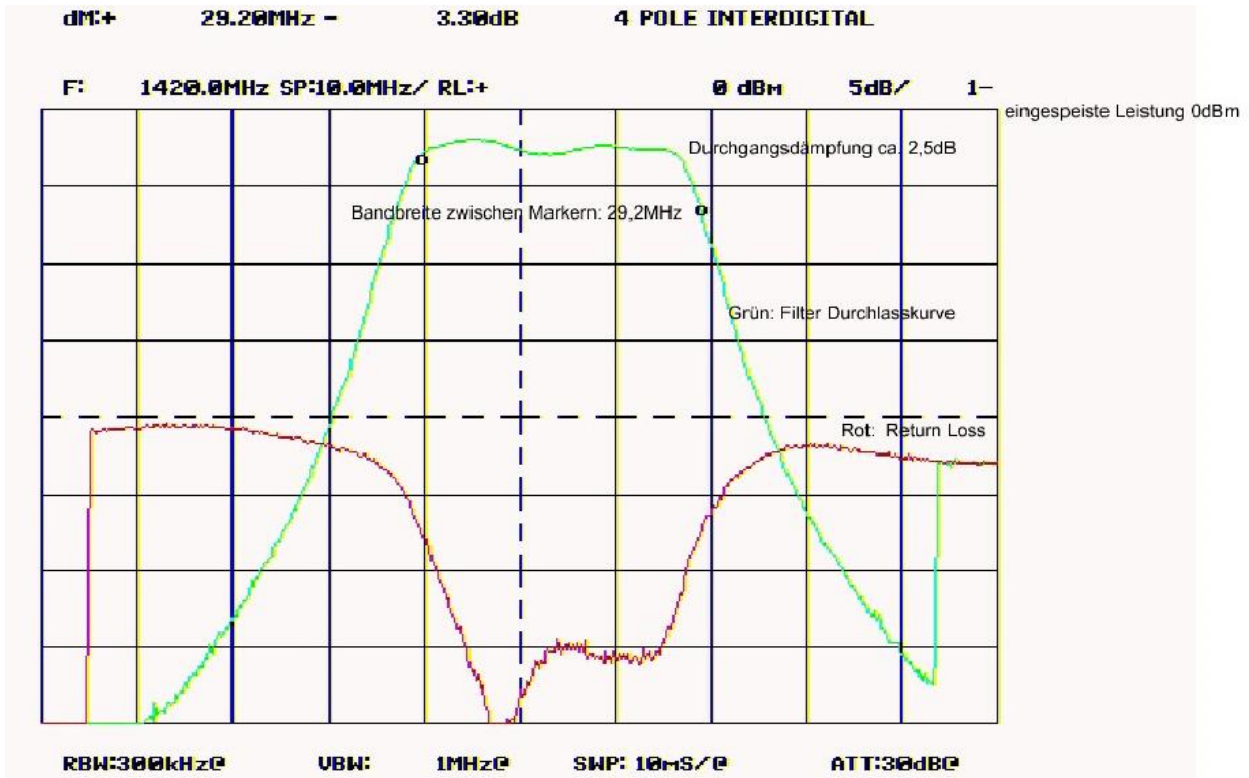


Figure 17 frequency response

## 5.5 Preamplifier:

The IF amplifier serves as adjustment the output of analog hardware with digital hardware so that adc converter can be able to work with high resolution. The next figures display the frequency response and hardware parts



Figure 18 IF amplifier

The bandwidth of IF is 10- 1800 MHz.



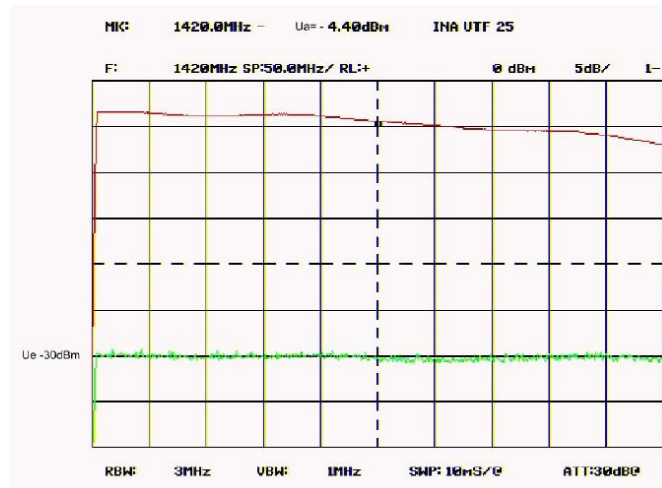


Figure 19 frequency response of IF amp

The feed horn is a corrugated aperture-controlled horn in which the phase variation over the aperture is small. By referring the design graph in [4, page 339], the directivity was calculated to be about 6 dB.

## 5.6 Antenna and Feed horn

Two parabolic mesh-surface reflector antennas were used in this project. The first antenna was thought for fixed receiver system without tracing the sun position having the diameter of 1.1 meters. Following is the parabola arc of the reflector. The F/D ratio was calculated to be about 0.5.



## 6 Software

### 6.1 Gnu radio

Radio is a free & open-source software development toolkit developed by Eric Blossom that is designed to couple PC host with hardware equipment (SDR platform) such as USRP, allowing for building SDR systems. GNU radio operates as stand-alone software package and provides signal processing blocks to implement software radios [3]. It can be used with readily-available low-cost external RF hardware to create software-defined radios, or without hardware in a simulation-like environment. Optimal operating system for building GNU Radio is Linux, but it can also be built on MS Windows using one of Linux-like environments such as Cygwin or MinGW/MSYS.

Most of GNU Radio's applications are written in Python as communicator function between functional blocks, whereas every block is programmed in C++ for implementing signal processing blocks. Python commands are used to control all of platform for software software-defined parameters, such as transmit power, gain, frequency, antenna selection, etc., some of which can be modified while the application is being executed. That means developer can implement real time radio systems in this development environment.

GNU Radio has been structured on two main levels: signal processing blocks and flow graphs. Blocks are designed to have a certain number of input and output ports, consisting of small Signal processing components. When the blocks are appropriately connected, a flow graph is made.

GNU Radio it is very straightforward to modulate and simulate SDR systems. It has a same principle as Matlab/Simulink and can be categorized as sinks, sources, filters and other functional blocks.

- Sources blocks consist of outputs have no inputs and are used as the first element in building the flow graph.
- Sinks consist of inputs and have no outputs and are typically the last element in building the flow graph.
- Filters are all the in between blocks and consist of both inputs and outputs.
- Flow-graph: the application is based on a flow-graph. Every flow-graph consists of intermediate blocks along with source and sink blocks.
- Scheduler: It is created for each active block, which is based on steady stream of data flow between the blocks. It is responsible for transferring data through the flow-graph- it monitors each block for sufficient data at I/p and O/p buffers so as to trigger processing function for those blocks.

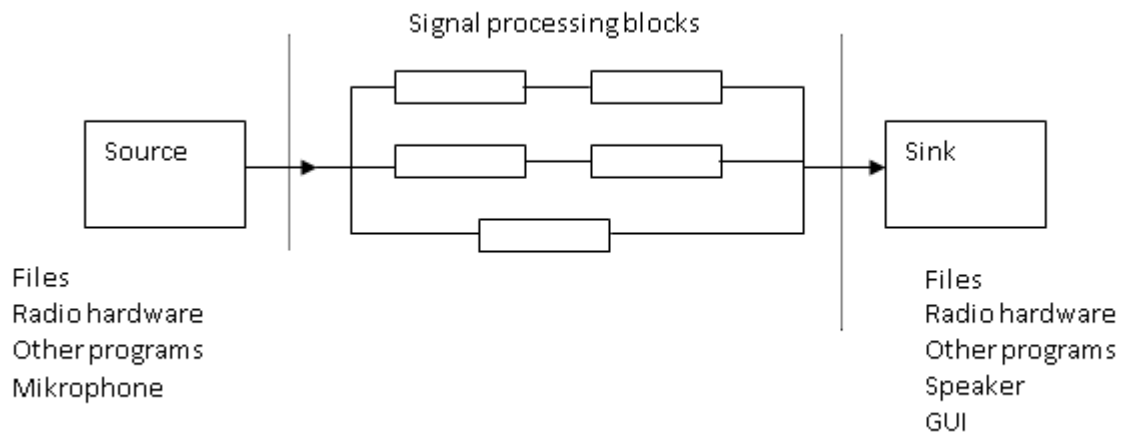


Figure 20 functionality of gnuradio

Various blocks such as different modulation/demodulation, filter, signal indicators, signal generator and widgets, .etc. are written in C++ and already integrated within GNU Radio, while it is also possible to write and add new blocks. Graphical interfaces are such as FFT sink and oscilloscope supported in GNU Radio.

Two kinds of Flow graphs are available in GNU Radio either as hierarchical blocks or as top blocks. Top blocks are top level flow graphs that contain all other flow graphs and have no input/output (IO) ports.

Hierarchical blocks, on the other hand, contain a certain number of IO ports (used to connect to other blocks). All of the basic signal processing blocks are connected within hierarchical blocks and can that way be used as one block. Communication between blocks is achieved using data streams considering to be connected together using same data type. It means that data types between output of one block and input of the next have to be adequately set. GNU Radio supports different data types such as byte, short, integer, float and complex (8 float byte).

## 6.2 Gnu Radio Architecture

The basic architecture of Gnuradio shows in following figure 18 containing a complex flow-graph that consists of blocks modules and low-level algorithms. Every Block or algorithm is implemented in C++ and offers various signal processing functions (Channel Coding, Filters, Modulations technique etc). These functions can be converted (generated) automatically into python modules using python "wrapper"(Simplified Wrapper) and it serves as the interface compiler allowing the integration between C++ and Python language. As mentioned, the signal processing blocks are written in C++ so that script language python connects the blocks together to form the flow graph [1]. The generated blocks are used to build a flow-graph model with the help of python. The python framework is responsible for communication of data through module buffers and creates a simple scheduler that helps to run blocks in a sequential order for signal iteration [1]

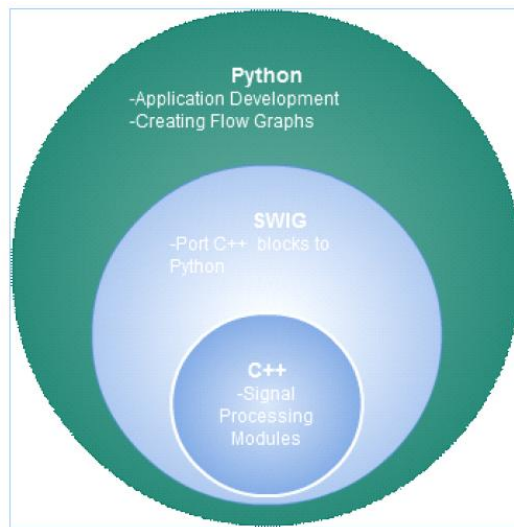


Figure 21 Software architecture

### 6.3 Gnu Radio Companion (GRC)

GNU Radio Companion is a graphical user interface for GNU Radio that allows building flow graphs by simply connecting visually-presented blocks. GRC is highly intuitive interface suitable for GNU Radio beginners that resembles Matlab Simulink's one, so anyone with some background in working with Simulink shouldn't have problems learning GRC as well.

From the Ubuntu terminal, GRC is started with command:

`gnuradio-companion .`

The dial\_tone example can be considered as “Hello world” of GNU Radio can be done using GRC as explained in Figure xx

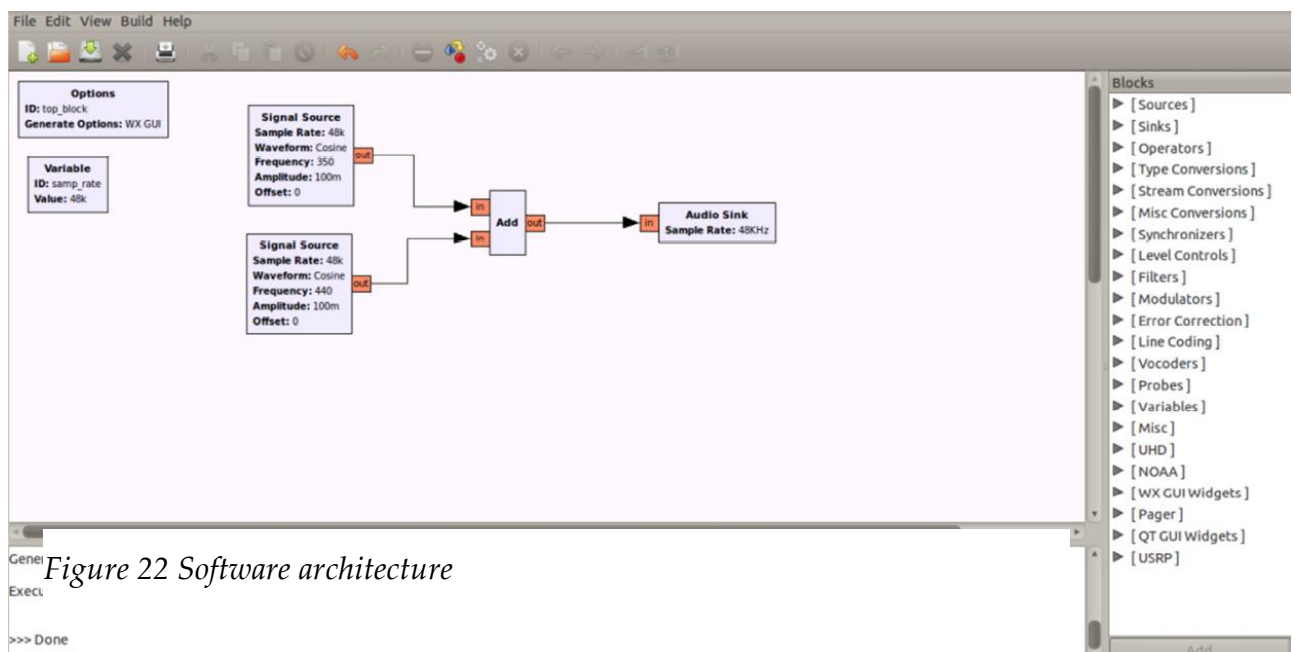




Figure 22 Software architecture

Figure 23: Implementation of dial\_tone example within Gnu Radio Companion

*Dial\_tone* example generates two sine waves of the same amplitude at frequencies 350 Hz and 440 Hz, which corresponds to the sound of US dial tone, and outputs them to the sound card.

One can translate this graph into the correspondent python code by pressing on the button “generate the flow graph ”. The  generated code will be saved in the Linux Ubuntu under home/bin and then can be executed through the button „execute the flow graph ”.

The created code source of the *dial\_tone* exsample is given and explained below.

```
#!/usr/bin/env python
from gnuradio import gr
from gnuradio import audio

def build_graph ():
    sampling_freq = 48000
    ampl = 0.1
    fg = gr.flow_graph ()
    src0 = gr.sig_source_f (sampling_freq, gr.GR_SIN_WAVE, 350, ampl)
    src1 = gr.sig_source_f (sampling_freq, gr.GR_SIN_WAVE, 440, ampl)
    dst = audio.sink (sampling_freq)
    fg.connect ((src0, 0), (dst, 0))
    fg.connect ((src1, 0), (dst, 1))
    return fg

if __name__ == '__main__':
    fg = build_graph ()
    fg.start ()
    raw_input ('Press Enter to quit: ')
    fg.stop ()
```

The first line, `#!/usr/bin/env python`, points python to the location of python executable, and is a line that has to be added to every program that we want to run directly from terminal (as an executable).

Then, we define which modules to import – in this case, *gr*, which is always imported, and *audio*, which allows us to use audio sink.

After that, sampling frequency is set according to sound card’s specifications (48 kHz is the sampling frequency of majority of modern sound-cards), and the amplitude to 0.1.

*gr.sig\_source\_f* is used to create sine waves at the frequencies of 350 Hz and 440 Hz, where *\_f* extension, as previously explained, indicates that the produced data is of type float.

Then, the audio sink that writes received data to the sound card is created. It is worth mentioning that audio sink only accepts float data as an input.

*fg.connect* connects the flow graph’s blocks – the first sine wave is connected to the port 0 of the audio sink, while the second sine wave is connected to port 1.

## 6.4 Basic Blocks

### 6.4.1 RTL SDR source

The purpose of the Master thesis is converting a big part of the Hardware from receiver for registration of the HL 21 cm spectrum into software using GnuRadio platform. So many algorithms for signal processing and hardware functionality (filter, modulation etc..) can be made in GRC (*gnuradio-companion*). The RTL SDR Usb(2382u) conduces as Front-End to detect HI Signal and convert it to digital signal. GnuRadio recognizes the incoming data from RTL SDR using driver implemented by Osmsann [1] in GRC in order to receive IQ data so one inputs the desired parameters as center frequency, gain, decimation etc.. through the graphic user interface driver to tune the desired frequency. The RTL driver in GRC is given and explained as follows in Figure 18.

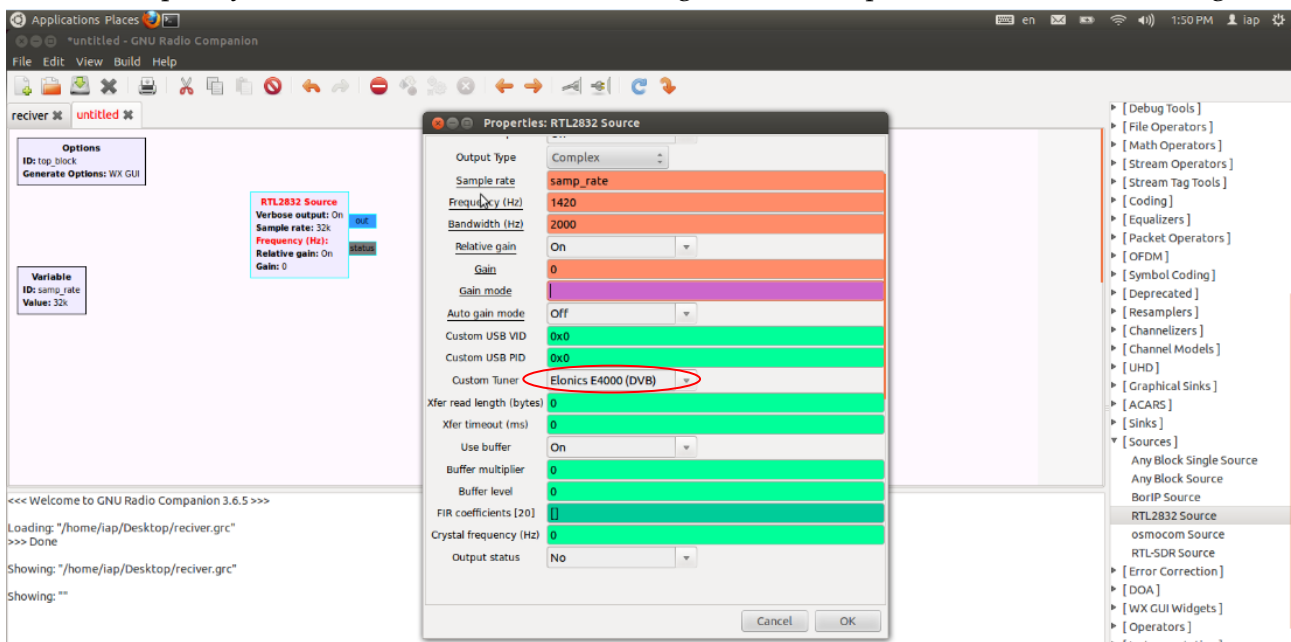


Figure 24 RTL SDR driver in GnuRadio

In the properties window of RTL2832 (our source hardware) one can select too tuner which RTL Usb contains (Elonics E4000 DVB).

### 6.4.2 WX GUI blocks

The WX GUI functions is very powerful tools to display and analyze a signal is to display in time domain and frequency domain. This block made us easy to measure and analyzes a hydrogen line 1 graphically. The python framework provides such wonderful tools in Gunradio to construct GUI tools. We used the following WX GUI blocks:

#### - FFT sink block

The function of FFT is used just as the signal sink ,based on fast Fourier transformation (FFT). It is defined in the module in python interface "wxgui.fftsink.py". The function "make\_fft\_sink\_c()" helps as the interface to create an instance of the FFT sink.

#### - Scope sink block

WX GUI scope is very useful tools in Gnu Radio to display the waveforms in the time domain. It seems as software oscillograph.

## 6.5 Software design

The HI 21 cm signals with other signals were obtained directly from RTL SDR Usb. The incoming digital data was filtered with FFT band-pass filter which filter the signal in frequency domain to get better removing frequently noise, whereas the parameter of this filter can be connected with GUI and then parameters of filter (center frequency, bandwidth, gain etc...) can be entered through it. Hereafter the filtered signal has been converted back to time domain then the power spectrum calculated and integrated to get average power. The averaging process ensures removing the random noise from the signal as much as possible.

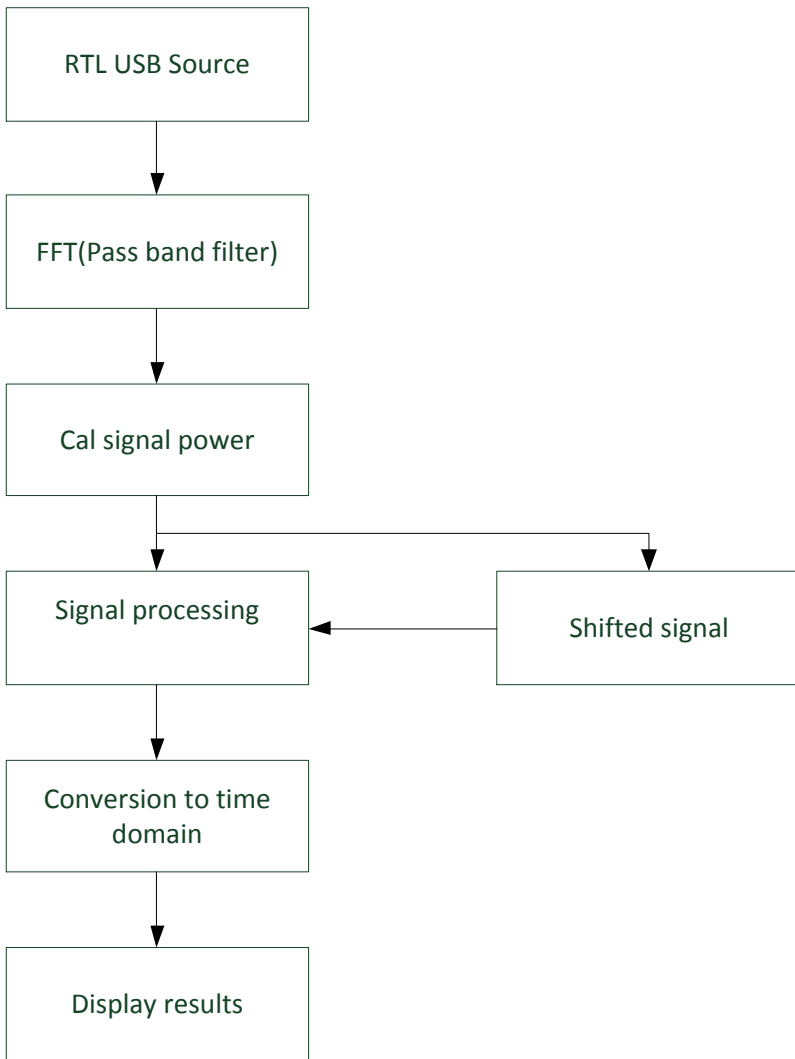
To make the signal detectable within desired range and probable noise a signal processing technique is performed. The main idea of this technique is comparing the spectrum at Hydrogen line with calculated spectrum created from shift the Hydrogen line signal a few Mhz. The exact spectrum is calculated and stored for a certain period of time. The help signal comes into existence using changing the local oscillator frequency of the mixer (IF stage) to a few MHz away from Hydrogen line and then spectrum is calculated at that frequency. The Spectrum at the Hydrogen line is named Signal and spectrum at some offset frequency from Hydrogen line is named Help.

## 6.6 Software Implementation

The RF signal coming from Satellite, amplified through LNA, pass-filtered using interdigital 4 pole filter for passing signal 21 cm with bandwidth 20 Mhz finally through PGA circuit pre-amplified, is fed into RTL SDR which has E4000 chip as tuner and a RTL 2382 u chip that contains an IF stage for converting RF into IF and then baseband with a maximum bandwidth of 4 MHz This baseband signal is available through usb2.0 interface to GnuRadio running on a PC for further processing. The software for filters and FFT analyze are implemented in GnuRadio to calculate the power spectrum. In order to have two slightly different frequency signals (Signal and Reference), frequency switching is used. Instead, the whole band consisting of the signal as well as the reference was obtained for processing. In our case this was as follows Signal at 1420.4 MHz with 2.5 MHz bandwidth (1419.15 – 1421.65) MHz.

Reference at 1417.9 MHz with 2.5 MHz bandwidth (1416.65 – 1419.15) MHz. Total bandwidth comprising of Signal and Reference thus became 5 MHz. The signal and reference signals are then filtered through separate filters, their FFT is calculated, averaged and finally the above mathematical equation is applied to detect the required signal.





### 6.6.1 RTL Source

The HL signal was acquired using determining the signal's parameters. The software diagram begins always with signal source (hardware, software). The important parameters are listed as follows.

Output type: IQ (In-phase and Quadrature) is used in signal kind of the typical kind signal in wireless communication

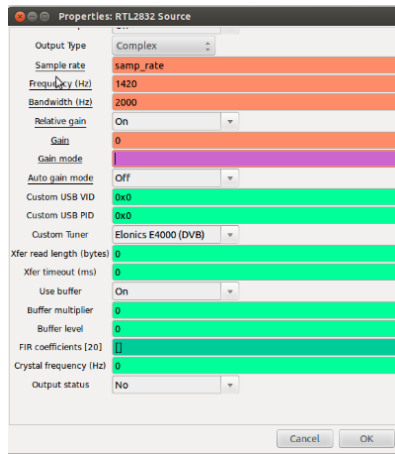
Frequency: Frequency: This is the frequency which will be down-converted to 0 Hz (baseband). It was set to the center of Reference frequency band i.e. 1417.9 MHz.

Sample rate:

Bandwidth: 4 MHz

Gain: 10 dB

Customer Tuner : Elonics E 4000 (DVB) is built on RTL SDR



### 6.6.2 FFT filter

As explained the goal of using FFT filter is to remove noise in frequency domain. The suitable pass band filter was implemented in FFT block.

## 6.7 Test and Measurements

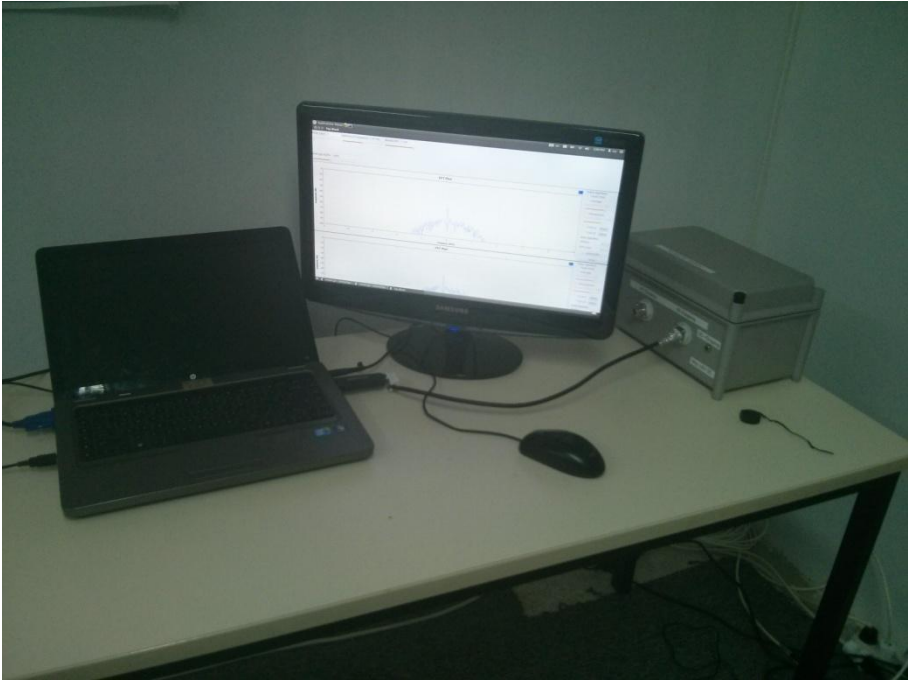
The setup of total system was realized on the high mountains for testing the whole system for HL1 detection. This testing in real environment would be validating that all the components are placed in the right order. (antenna, LNA, power supply etc).

Many experiments were carried out for the first test in different directions and then power values of the signal were measured. As next step the antenna was orient in the direction of the sun and power spectrum has been observed and that noted whereby the power values was shifted compared to spectrum taken form many astronomical observatory in Heppenheim Germany [1] and in offline environment (simulation) therefore power spectrum has been recorded regarding to changing of preamplifier gain (hardware) and filters parameters (software). The results were relative acceptable as expected. Then the antenna has scanned the sky for many angle values inclusive in the direction of hydrogen line source. Figures 3-10, 3-12, 3-13 show the setup and the difference in the spectrum of (sig-ref/ref) without and with the antenna pointed towards the Hydrogen line source respectively. It can be seen from the figures 3-12 and 3-13 that the receiver worked properly as the signal is differentiable from noise.

Comparing the spectrum taken with the old configuration of SALSA ([11], figure 3-11) pointed toward the same direction of the galactic plane (Galactic longitude  $l=120$  degrees, Galactic latitude  $b = 0$ ) and the spectrum (figure 3-13), obtained with the upgraded digital software receiver pointing in the same direction, clearly shows the functionality of the upgraded digital receiver. The difference is spectrum can be explained by the approximate pointing during our experiment, but it certainly looks like a detection! It would also have been useful to observe in a slightly larger or shifted (towards right) band [11].

The observed spectrum range seems far wider than the actual spectrum band needed to observe (within red circle in figure 3-13). This is due to the FFT Scope block of the GnuRadio, where no zooming on a particular section of the spectrum is possible; hence we have to see the whole band which is being translated from analog to digital domain through sampling. To observe only a small

part of spectrum, one could decimate the (SIGNAL-REFERENCE)/REFERENCE signal to a point where the bandwidth is half the decimated sampling rate (Nyquist Theorem). Actually, a small decimation is performed here if we compare figures 3-13 and 3-9 to see the difference.



## 7 Future Work

Parts of the system are planned to be put on a satellite in a further step in the IAP SRWDA-SAT project [9]. The Gnu Radio receiver model will be converted to python code then stored on memory of board computer



*Figure 26 Import Receiver on Mockup model*



*Figure 25 Mock up model*

## 8 Literature

- [1] K. Rohlfs, Tools of radio astronomy, 2004.
- [2] E. Grayver, Implementing software defined radio, 2013.
- [3] I. Joseph Mitola, Software Radio Architecture: Object Oriented Approaches to Wireless Systems Engineering., John Wiley and Sons, 2000.
- [4] W. Tuttlebee, Software Defined Radio, England, 2002.
- [5] E. Comany, „<https://www.ettus.com/product/details/WBX>“.
- [6] Xilinx, „[http://www.xilinx.com/support/documentation/data\\_sheets/ds529.pdf](http://www.xilinx.com/support/documentation/data_sheets/ds529.pdf)“.
- [7] D. Shen, „The USRP Board,“ p. 7, Augst 2005.
- [9] IAP SRWDA-SAT project, see [www.aecenar.com/research](http://www.aecenar.com/research)

[www.astronomynotes.com](http://www.astronomynotes.com)

[www.aao.gov.au](http://www.aao.gov.au)

## 9 Appendix

### A.1 Software

#### Python code

```
#!/usr/bin/env python
#####
# Gnuradio Python Flow Graph
# Title: Top Block
# Generated: Tue May 6 15:46:55 2014
#####

from gnuradio import blocks
from gnuradio import eng_notation
from gnuradio import fft
from gnuradio import filter
from gnuradio import gr
from gnuradio import window
from gnuradio.eng_option import eng_option
from gnuradio.filter import firdes
from gnuradio.gr import firdes
from gnuradio.wxgui import fftsink2
from gnuradio.wxgui import forms
from grc_gnuradio import wxgui as grc_wxgui
from optparse import OptionParser
import ConfigParser
import baz
import wx

class top_block(grc_wxgui.top_block_gui):

    def __init__(self):
        grc_wxgui.top_block_gui.__init__(self, title="Top Block")
        _icon_path = "/usr/share/icons/hicolor/32x32/apps/gnuradio-
grc.png"
        self.SetIcon(wx.Icon(_icon_path, wx.BITMAP_TYPE_ANY))

        #####
        # Variables
        #####
        self._variable_config_0_config = ConfigParser.ConfigParser()
        self._variable_config_0_config.read("default")
        try: variable_config_0 =
self._variable_config_0_config.getfloat("main", "key")
        except: variable_config_0 = 0
        self.variable_config_0 = variable_config_0
        self.samp_rate = samp_rate = 10000000
        self.low_cutoff = low_cutoff = 0.125
        self.high_cutoff = high_cutoff = 0.375
        self.gui_onoff = gui_onoff = False
        self.gain = gain = 1
        self.fft_size = fft_size = 1024
        self.dec = dec = 10
        self.avg_alpha = avg_alpha = 0.1
        self.Sig_minus_Ref = Sig_minus_Ref = 2500000
        self.Sig_freq = Sig_freq = 1420400000
        self.Ref_freq = Ref_freq = 1417900000
```

```

self.N = N = 1024
self.BW = BW = 2500000

#####
# Blocks
#####
_gain_sizer = wx.BoxSizer(wx.VERTICAL)
self._gain_text_box = forms.text_box(
    parent=self.GetWin(),
    sizer=_gain_sizer,
    value=self.gain,
    callback=self.set_gain,
    label="Filter Gain",
    converter=forms.float_converter(),
    proportion=0,
)
self._gain_slider = forms.slider(
    parent=self.GetWin(),
    sizer=_gain_sizer,
    value=self.gain,
    callback=self.set_gain,
    minimum=1,
    maximum=32,
    num_steps=100,
    style=wx.SL_HORIZONTAL,
    cast=float,
    proportion=1,
)
self.GridAdd(_gain_sizer, 0, 0, 1, 1)
_avg_alpha_sizer = wx.BoxSizer(wx.VERTICAL)
self._avg_alpha_text_box = forms.text_box(
    parent=self.GetWin(),
    sizer=_avg_alpha_sizer,
    value=self.avg_alpha,
    callback=self.set_avg_alpha,
    label="Average Alpha",
    converter=forms.float_converter(),
    proportion=0,
)
self._avg_alpha_slider = forms.slider(
    parent=self.GetWin(),
    sizer=_avg_alpha_sizer,
    value=self.avg_alpha,
    callback=self.set_avg_alpha,
    minimum=0.001,
    maximum=0.25,
    num_steps=100,
    style=wx.SL_HORIZONTAL,
    cast=float,
    proportion=1,
)
self.GridAdd(_avg_alpha_sizer, 3, 0, 1, 3)
_BW_sizer = wx.BoxSizer(wx.VERTICAL)
self._BW_text_box = forms.text_box(
    parent=self.GetWin(),
    sizer=_BW_sizer,
    value=self.BW,
    callback=self.set_BW,
    label="Bandwidth",

```

```
        converter=forms.float_converter(),
        proportion=0,
    )
self._BW_slider = forms.slider(
    parent=self.GetWin(),
    sizer=_BW_sizer,
    value=self.BW,
    callback=self.set_BW,
    minimum=500000,
    maximum=2500000,
    num_steps=100,
    style=wx.SL_HORIZONTAL,
    cast=float,
    proportion=1,
)
self.GridAdd(_BW_sizer, 0, 4, 1, 1)
self.wxgui_fftsink2_0_0_0 = fftsink2.fft_sink_c(
    self.GetWin(),
    baseband_freq=0,
    y_per_div=10,
    y_divs=10,
    ref_level=0,
    ref_scale=2.0,
    sample_rate=samp_rate,
    fft_size=1024,
    fft_rate=15,
    average=False,
    avg_alpha=None,
    title="FFT Plot",
    peak_hold=False,
)
self.Add(self.wxgui_fftsink2_0_0_0.win)
self.wxgui_fftsink2_0_0 = fftsink2.fft_sink_c(
    self.GetWin(),
    baseband_freq=0,
    y_per_div=10,
    y_divs=10,
    ref_level=0,
    ref_scale=2.0,
    sample_rate=samp_rate,
    fft_size=1024,
    fft_rate=15,
    average=False,
    avg_alpha=None,
    title="FFT Plot",
    peak_hold=False,
)
self.Add(self.wxgui_fftsink2_0_0.win)
self.wxgui_fftsink2_0 = fftsink2.fft_sink_c(
    self.GetWin(),
    baseband_freq=0,
    y_per_div=10,
    y_divs=10,
    ref_level=0,
    ref_scale=2.0,
    sample_rate=samp_rate,
    fft_size=1024,
    fft_rate=15,
    average=False,
```



```

        avg_alpha=None,
        title="FFT Plot",
        peak_hold=False,
    )
    self.Add(self.wxgui_fftsink2_0.win)
    self.single_pole_iir_filter_xx_0_0 =
filter.single_pole_iir_filter_ff(0.1, 1024)
    self.single_pole_iir_filter_xx_0 =
filter.single_pole_iir_filter_ff(0.1, 1024)
    self.rtl2832_source_0 = baz.rtl_source_c(defer_creation=True,
output_size=gr.sizeof_gr_complex)
    self.rtl2832_source_0.set_verbose(True)
    self.rtl2832_source_0.set_vid(0x0)
    self.rtl2832_source_0.set_pid(0x0)
    self.rtl2832_source_0.set_tuner_name("e4k")
    self.rtl2832_source_0.set_default_timeout(0)
    self.rtl2832_source_0.set_use_buffer(True)
    self.rtl2832_source_0.set_fir_coefficients([])

    self.rtl2832_source_0.set_read_length(0)

    if self.rtl2832_source_0.create() == False: raise
Exception("Failed to create RTL2832 Source: rtl2832_source_0")

    self.rtl2832_source_0.set_sample_rate(samp_rate)

    self.rtl2832_source_0.set_frequency(1420000000)

    self.rtl2832_source_0.set_auto_gain_mode(False)
    self.rtl2832_source_0.set_relative_gain(True)
    self.rtl2832_source_0.set_gain(27)

    self._gui_onoff_check_box = forms.check_box(
        parent=self.GetWin(),
        value=self.gui_onoff,
        callback=self.set_gui_onoff,
        label="check to parameter",
        true=True,
        false=False,
    )
    self.Add(self._gui_onoff_check_box)
    self.freq_xlating_fir_filter_xxx_0 =
filter.freq_xlating_fir_filter_ccc(1,
(gr.firdes.complex_band_pass(gain,samp_rate,low_cutoff,high_cutoff,BW, 0
,beta=6.76)), -2500000, samp_rate)
    self.fft_vxx_0_0_0_0 = fft.fft_vcc(1024, True,
(window.hamming(N)), False, 1)
    self.fft_vxx_0_0_0 = fft.fft_vcc(1024, True,
(window.blackmanharris(1024)), True, 1)
    self.fft_vxx_0_0 = fft.fft_vfc(1024, True,
(window.blackmanharris(1024)), 1)

```

```

        self.fft_filter_xxx_0_0_0 = filter.fft_filter_ccc(1,
(gr.firdes.complex_band_pass(gain,samp_rate,low_cutoff,high_cutoff,BW, 0
,beta=6.76)), 1)
        self.fft_filter_xxx_0_0 = filter.fft_filter_ccc(1,
(gr.firdes.complex_band_pass(gain,samp_rate,low_cutoff,high_cutoff,BW, 0
,beta=6.76)), 1)
        self.fft_filter_xxx_0 = filter.fft_filter_ccc(1,
(gr.firdes.complex_band_pass(gain,samp_rate,low_cutoff,high_cutoff,BW, 0
,beta=6.76)), 1)
        self.blocks_vector_to_stream_0 =
blocks.vector_to_stream(gr.sizeof_gr_complex*1, 1024)
        self.blocks_stream_to_vector_0_0 =
blocks.stream_to_vector(gr.sizeof_gr_complex*1, 1024)
        self.blocks_stream_to_vector_0 =
blocks.stream_to_vector(gr.sizeof_gr_complex*1, 1024)
        self.blocks_keep_one_in_n_0 =
blocks.keep_one_in_n(gr.sizeof_gr_complex*1, 5)
        self.blocks_divide_xx_0 = blocks.divide_ff(1024)
        self.blocks_conjugate_cc_0 = blocks.conjugate_cc()
        self.blocks_complex_to_mag_squared_1_0 =
blocks.complex_to_mag_squared(1024)
        self.blocks_complex_to_mag_squared_1 =
blocks.complex_to_mag_squared(1024)
        self.blocks_add_const_vxx_0 = blocks.add_const_vff(([-1]*N))
        _Ref_freq_sizer = wx.BoxSizer(wx.VERTICAL)
        self._Ref_freq_text_box = forms.text_box(
            parent=self.GetWin(),
            sizer=_Ref_freq_sizer,
            value=self.Ref_freq,
            callback=self.set_Ref_freq,
            label="Reference frequency",
            converter=forms.float_converter(),
            proportion=0,
        )
        self._Ref_freq_slider = forms.slider(
            parent=self.GetWin(),
            sizer=_Ref_freq_sizer,
            value=self.Ref_freq,
            callback=self.set_Ref_freq,
            minimum=1417400000,
            maximum=1418400000,
            num_steps=100,
            style=wx.SL_HORIZONTAL,
            cast=float,
            proportion=1,
        )
        self.GridAdd(_Ref_freq_sizer, 0, 1, 1, 3)

#####
# Connections
#####
        self.connect((self.fft_vxx_0_0_0_0, 0),
(self.blocks_complex_to_mag_squared_1, 0))
        self.connect((self.blocks_add_const_vxx_0, 0),
(self.fft_vxx_0_0, 0))
        self.connect((self.blocks_divide_xx_0, 0),
(self.blocks_add_const_vxx_0, 0))
        self.connect((self.single_pole_iir_filter_xx_0, 0),
(self.blocks_divide_xx_0, 1))

```

```

        self.connect((self.blocks_keep_one_in_n_0, 0),
(self.wxgui_fftsink2_0, 0))
        self.connect((self.fft_vxx_0_0, 0),
(self.blocks_vector_to_stream_0, 0))
        self.connect((self.blocks_complex_to_mag_squared_1, 0),
(self.single_pole_iir_filter_xx_0, 0))
        self.connect((self.blocks_conjugate_cc_0, 0),
(self.freq_xlating_fir_filter_xxx_0, 0))
        self.connect((self.blocks_vector_to_stream_0, 0),
(self.blocks_conjugate_cc_0, 0))
        self.connect((self.single_pole_iir_filter_xx_0_0, 0),
(self.blocks_divide_xx_0, 0))
        self.connect((self.blocks_complex_to_mag_squared_1_0, 0),
(self.single_pole_iir_filter_xx_0_0, 0))
        self.connect((self.fft_vxx_0_0_0, 0),
(self.blocks_complex_to_mag_squared_1_0, 0))
        self.connect((self.fft_filter_xxx_0, 0),
(self.blocks_keep_one_in_n_0, 0))
        self.connect((self.freq_xlating_fir_filter_xxx_0, 0),
(self.fft_filter_xxx_0, 0))
        self.connect((self.rtl2832_source_0, 0),
(self.fft_filter_xxx_0_0, 0))
        self.connect((self.fft_filter_xxx_0_0, 0),
(self.wxgui_fftsink2_0_0, 0))
        self.connect((self.rtl2832_source_0, 0),
(self.fft_filter_xxx_0_0_0, 0))
        self.connect((self.fft_filter_xxx_0_0_0, 0),
(self.wxgui_fftsink2_0_0_0, 0))
        self.connect((self.fft_filter_xxx_0_0_0, 0),
(self.blocks_stream_to_vector_0, 0))
        self.connect((self.blocks_stream_to_vector_0, 0),
(self.fft_vxx_0_0_0_0, 0))
        self.connect((self.fft_filter_xxx_0_0, 0),
(self.blocks_stream_to_vector_0_0, 0))
        self.connect((self.blocks_stream_to_vector_0_0, 0),
(self.fft_vxx_0_0_0, 0))

```

```

def get_variable_config_0(self):
    return self.variable_config_0

```

```

def set_variable_config_0(self, variable_config_0):
    self.variable_config_0 = variable_config_0

```

```

def get_samp_rate(self):
    return self.samp_rate

```

```

def set_samp_rate(self, samp_rate):
    self.samp_rate = samp_rate

```

```

self.freq_xlating_fir_filter_xxx_0.set_taps((gr.firdes.complex_band_p
ass(self.gain,self.samp_rate,self.low_cutoff,self.high_cutoff,self.BW, 0
,beta=6.76)))

```

```

self.fft_filter_xxx_0.set_taps((gr.firdes.complex_band_pass(self.gain
,self.samp_rate,self.low_cutoff,self.high_cutoff,self.BW, 0 ,beta=6.76)))

```

```

self.fft_filter_xxx_0_0_0.set_taps((gr.firdes.complex_band_pass(self.

```

```
gain,self.samp_rate,self.low_cutoff,self.high_cutoff,self.BW, 0
,beta=6.76)))
    self.rtl2832_source_0.set_sample_rate(self.samp_rate)

    self.fft_filter_xxx_0_0.set_taps((gr.firdes.complex_band_pass(self.gai
in,self.samp_rate,self.low_cutoff,self.high_cutoff,self.BW, 0 ,beta=6.76)))
    self.wxgui_fftsink2_0.set_sample_rate(self.samp_rate)
    self.wxgui_fftsink2_0_0_0.set_sample_rate(self.samp_rate)
    self.wxgui_fftsink2_0_0.set_sample_rate(self.samp_rate)

def get_low_cutoff(self):
    return self.low_cutoff

def set_low_cutoff(self, low_cutoff):
    self.low_cutoff = low_cutoff

    self.freq_xlating_fir_filter_xxx_0.set_taps((gr.firdes.complex_band_p
ass(self.gain,self.samp_rate,self.low_cutoff,self.high_cutoff,self.BW, 0
,beta=6.76)))

    self.fft_filter_xxx_0.set_taps((gr.firdes.complex_band_pass(self.gain
,self.samp_rate,self.low_cutoff,self.high_cutoff,self.BW, 0 ,beta=6.76)))

    self.fft_filter_xxx_0_0_0.set_taps((gr.firdes.complex_band_pass(self.
gain,self.samp_rate,self.low_cutoff,self.high_cutoff,self.BW, 0
,beta=6.76)))

    self.fft_filter_xxx_0_0.set_taps((gr.firdes.complex_band_pass(self.gai
in,self.samp_rate,self.low_cutoff,self.high_cutoff,self.BW, 0 ,beta=6.76)))

def get_high_cutoff(self):
    return self.high_cutoff

def set_high_cutoff(self, high_cutoff):
    self.high_cutoff = high_cutoff

    self.freq_xlating_fir_filter_xxx_0.set_taps((gr.firdes.complex_band_p
ass(self.gain,self.samp_rate,self.low_cutoff,self.high_cutoff,self.BW, 0
,beta=6.76)))

    self.fft_filter_xxx_0.set_taps((gr.firdes.complex_band_pass(self.gain
,self.samp_rate,self.low_cutoff,self.high_cutoff,self.BW, 0 ,beta=6.76)))

    self.fft_filter_xxx_0_0_0.set_taps((gr.firdes.complex_band_pass(self.
gain,self.samp_rate,self.low_cutoff,self.high_cutoff,self.BW, 0
,beta=6.76)))

    self.fft_filter_xxx_0_0.set_taps((gr.firdes.complex_band_pass(self.gai
in,self.samp_rate,self.low_cutoff,self.high_cutoff,self.BW, 0 ,beta=6.76)))

def get_gui_onoff(self):
    return self.gui_onoff

def set_gui_onoff(self, gui_onoff):
    self.gui_onoff = gui_onoff
    self._gui_onoff_check_box.set_value(self.gui_onoff)

def get_gain(self):
    return self.gain
```

```

def set_gain(self, gain):
    self.gain = gain
    self._gain_slider.set_value(self.gain)
    self._gain_text_box.set_value(self.gain)

    self.freq_xlating_fir_filter_xxx_0.set_taps((gr.firdes.complex_band_p
ass(self.gain,self.samp_rate,self.low_cutoff,self.high_cutoff,self.BW, 0
,beta=6.76)))

    self.fft_filter_xxx_0.set_taps((gr.firdes.complex_band_pass(self.gain
,self.samp_rate,self.low_cutoff,self.high_cutoff,self.BW, 0 ,beta=6.76)))

    self.fft_filter_xxx_0_0_0.set_taps((gr.firdes.complex_band_pass(self.
gain,self.samp_rate,self.low_cutoff,self.high_cutoff,self.BW, 0
,beta=6.76)))

    self.fft_filter_xxx_0_0.set_taps((gr.firdes.complex_band_pass(self.ga
in,self.samp_rate,self.low_cutoff,self.high_cutoff,self.BW, 0 ,beta=6.76)))

def get_fft_size(self):
    return self.fft_size

def set_fft_size(self, fft_size):
    self.fft_size = fft_size

def get_dec(self):
    return self.dec

def set_dec(self, dec):
    self.dec = dec

def get_avg_alpha(self):
    return self.avg_alpha

def set_avg_alpha(self, avg_alpha):
    self.avg_alpha = avg_alpha
    self._avg_alpha_slider.set_value(self.avg_alpha)
    self._avg_alpha_text_box.set_value(self.avg_alpha)

def get_Sig_minus_Ref(self):
    return self.Sig_minus_Ref

def set_Sig_minus_Ref(self, Sig_minus_Ref):
    self.Sig_minus_Ref = Sig_minus_Ref

def get_Sig_freq(self):
    return self.Sig_freq

def set_Sig_freq(self, Sig_freq):
    self.Sig_freq = Sig_freq

def get_Ref_freq(self):
    return self.Ref_freq

def set_Ref_freq(self, Ref_freq):
    self.Ref_freq = Ref_freq
    self._Ref_freq_slider.set_value(self.Ref_freq)
    self._Ref_freq_text_box.set_value(self.Ref_freq)

```

```
def get_N(self):
    return self.N

def set_N(self, N):
    self.N = N
    self.blocks_add_const_vxx_0.set_k((-1)*self.N)

def get_BW(self):
    return self.BW

def set_BW(self, BW):
    self.BW = BW

    self.freq_xlating_fir_filter_xxx_0.set_taps((gr.firdes.complex_band_pass(self.gain,self.samp_rate,self.low_cutoff,self.high_cutoff,self.BW, 0 ,beta=6.76)))

    self.fft_filter_xxx_0.set_taps((gr.firdes.complex_band_pass(self.gain,self.samp_rate,self.low_cutoff,self.high_cutoff,self.BW, 0 ,beta=6.76)))
    self._BW_slider.set_value(self.BW)
    self._BW_text_box.set_value(self.BW)

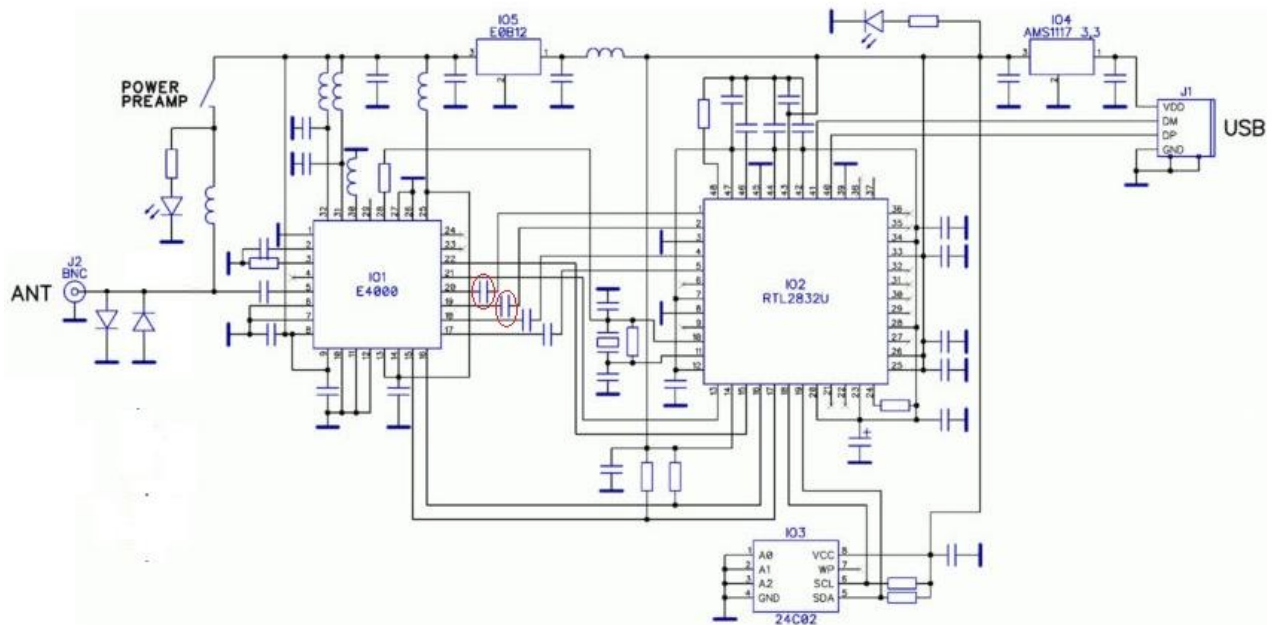
    self.fft_filter_xxx_0_0_0.set_taps((gr.firdes.complex_band_pass(self.gain,self.samp_rate,self.low_cutoff,self.high_cutoff,self.BW, 0 ,beta=6.76)))

    self.fft_filter_xxx_0_0.set_taps((gr.firdes.complex_band_pass(self.gain,self.samp_rate,self.low_cutoff,self.high_cutoff,self.BW, 0 ,beta=6.76)))

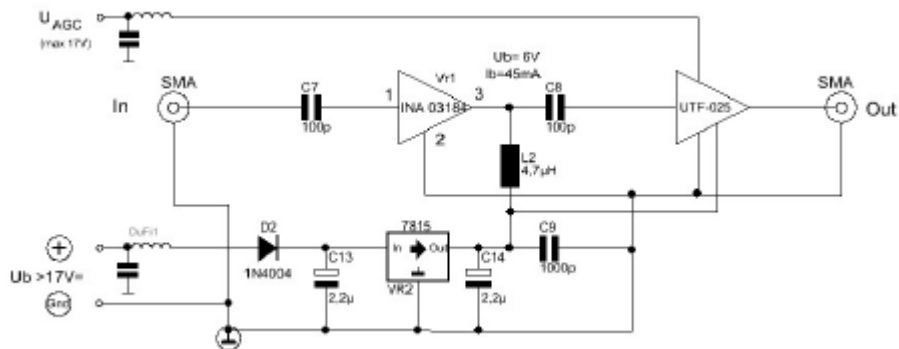
if __name__ == '__main__':
    parser = OptionParser(option_class=eng_option, usage="%prog:
[options]")
    (options, args) = parser.parse_args()
    tb = top_block()
    tb.Run(True)
```

## A.2 Hardware

### SDR RTL 2382+4000



### IF Amplifier



# Low noise amplifier

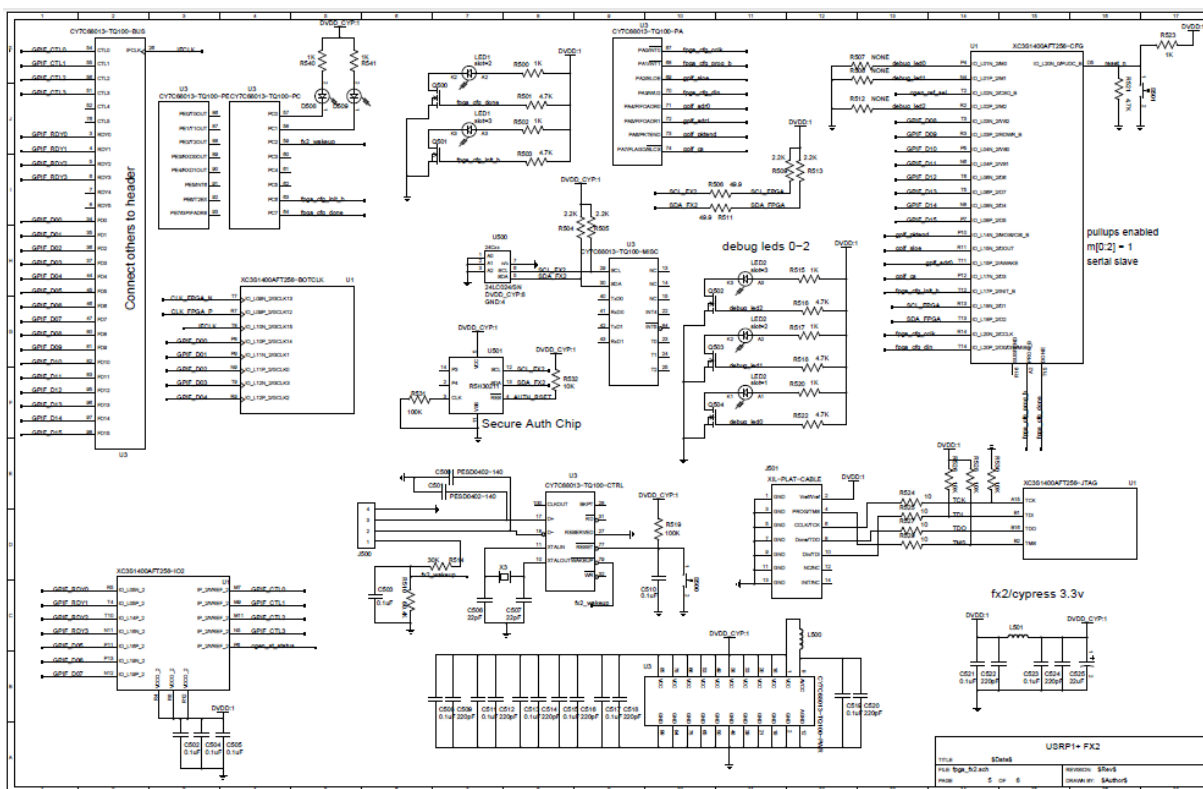
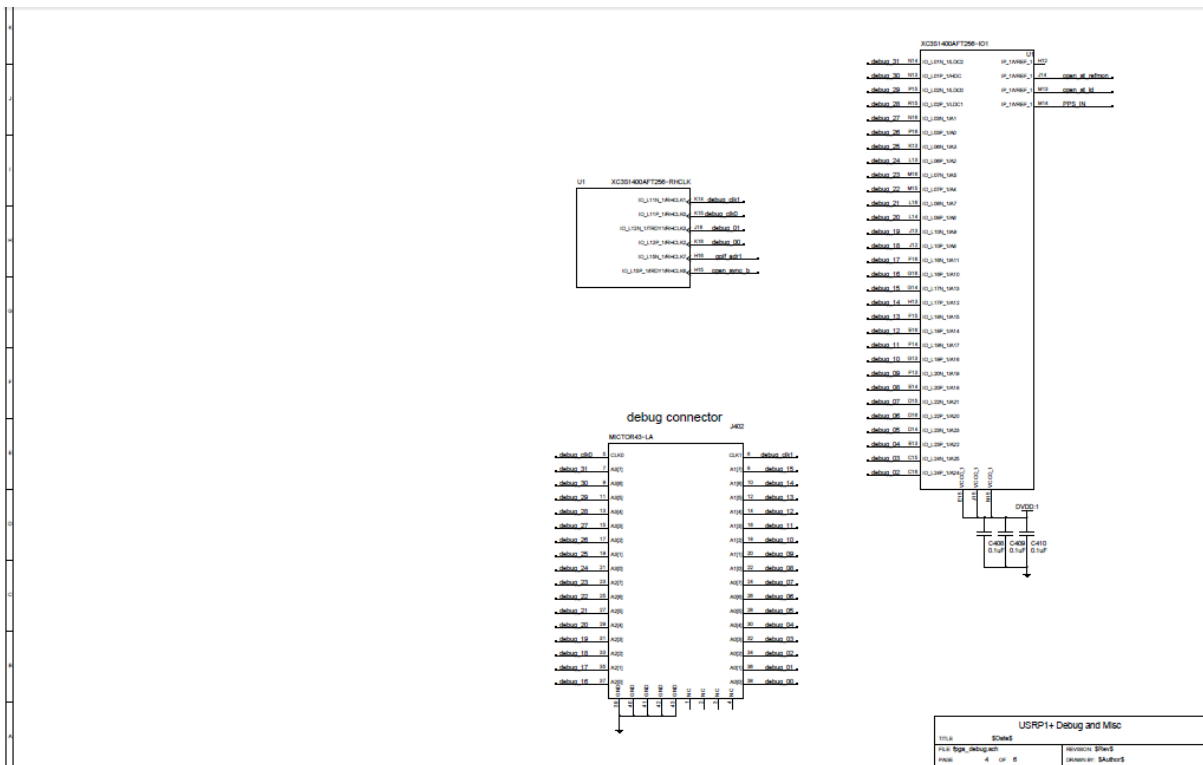
	A	B	C	D	E	F
1	<div style="display: flex; justify-content: space-between;"> <div style="width: 45%;"> <p style="margin-top: 20px;">Low Noise Amplifier PGA 103+                      Gain @1400 MHz 12dB                      Noise Figure @1400MHz 0,7 dB                      P1dB 22,5dBm typ. @ 2 GHz @5V                      High IP3, 45dBm typ. @2GHz, 5V</p> </div> <div style="width: 50%;"> <p style="text-align: right; margin-top: 10px;">Verstärkeroberseite</p> <p style="text-align: right; margin-top: 10px;">Verstärkerunterseite</p> </div> </div>					
2						
3						
4						

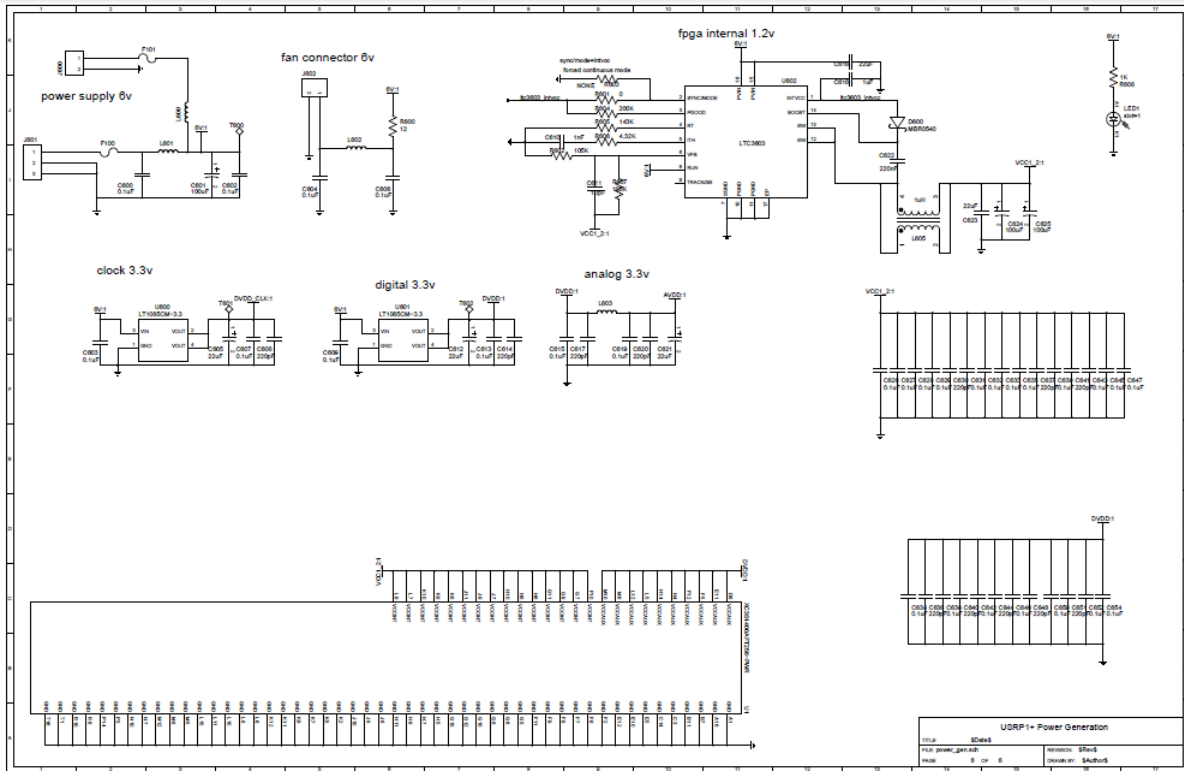
Änderungen		Datum	Name	Bezeichnung:	Blattzahl:
Datum	Name	gez.:		LNA PG103+	Blatt-Nr.:
		gepr.:			
				Zeichnungs-Nr.:	











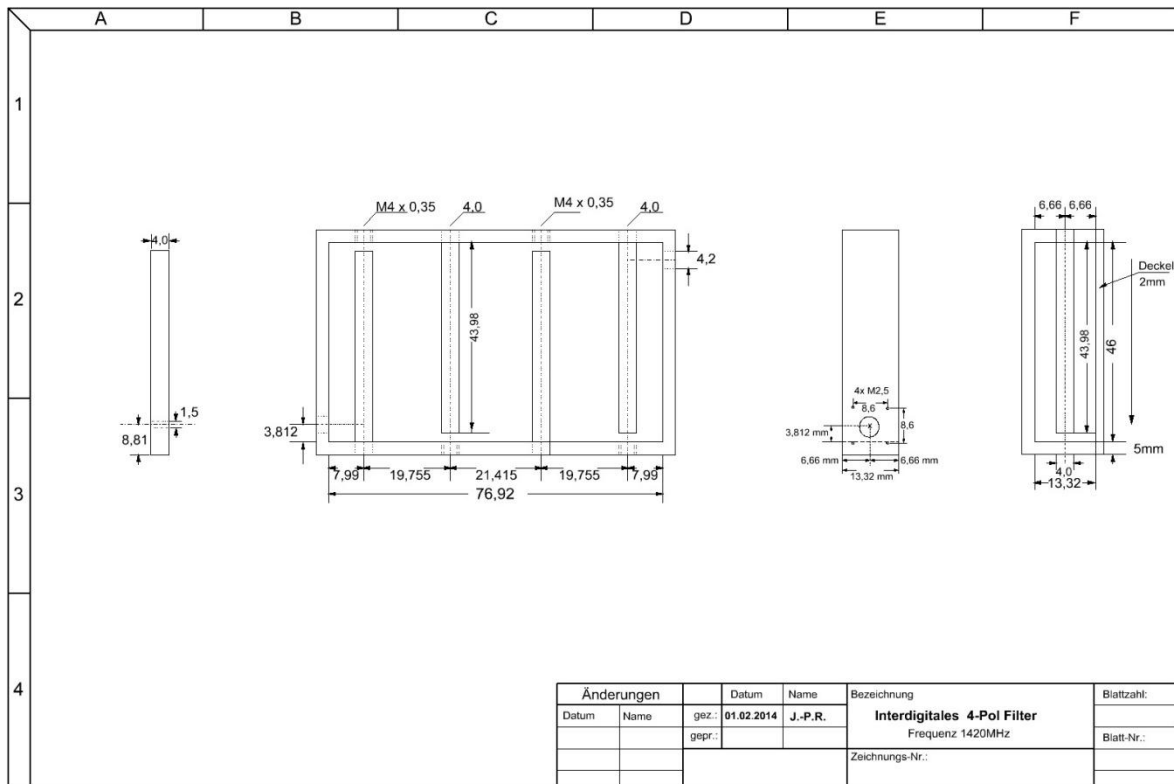
### A.3 List of off-the-shelf electronic components and assemblies

Receiver box		250 €
Hydrogen filter		
Power supply		22 €
Low noise Amplifier		120 €
Line Amplifier		3.80 €

Antenna		120 €
---------	---	-------

## A.4 Mechanical Components

### Hydrogen Filter





# IAP-OSM (Optical Spectrometer)



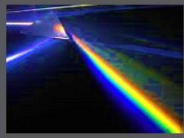
بِسْمِ اللَّهِ الرَّحْمَنِ الرَّحِيمِ



## Spectroscope for Visual Data

### 1-Definition of spectroscopy

Spectroscopy is the study of the interaction between matter and electromagnetic radiation. Historically, spectroscopy originated through the study of visible light dispersed according to its wavelength by a prism. Later the concept was expanded greatly to include any interaction with radiative energy as a function of its wavelength or frequency.



التحليل الطيفي هو دراسة التفاعل بين المادة والإشعاع الكهرومغناطيسي. تاريخياً، نشأ التحليل الطيفي من خلال دراسة الضوء المرئي المشتت وفقاً لطول الموجة، بواسطة المنشور. في وقت لاحق تم توسيع المفهوم إلى حد كبير ليشمل أي تفاعل مع الطاقة الإشعاعية كدالة لطول الموجة.

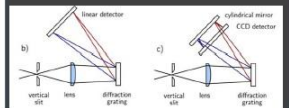
### 2-Spectrometer

A spectrometer is a scientific instrument used to separate and measure spectral components of a physical. The capability of spectroscopy to determine chemical composition drove its advancement and continues to be one of its primary uses. Much of our knowledge of the chemical makeup of the universe comes from spectroscopy.

المطياف هو أداة علمية تستخدم لفصل وقياس المكونات الطيفية. يعتبر بقدرة التحليل الطيفي لتحديد التركيب الكيميائي الأساسية الكثير من معرفتنا للتركيب الكيميائي للكون يأتي من دراسة معرفة الأطياف.

### 3-Principle:

In the horizontal plane, the incoming light must be spatially limited by a vertical slit. Then the spatial limitation is converted to angular limitation using a concave mirror or a convex lens. Ideally, we obtain a parallel beam of white light. Its width is limited either by the size of the mirror or lens used, or by the angle of the beam passing through the slit. The light components of different wavelengths separate after being reflected into different angles by a diffraction grating, delivered to the CCD. Finally, the angular separation might be converted back to spatial separation using another lens or mirror. However, this would require a big lens with diameter similar to the length of CCD. The spatial difference would be proportional to its focal length, probably resulting in a small spatial separation.



### 4-The charge coupled device, CCD:

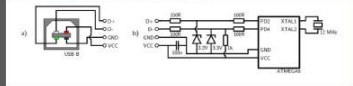
was originally designed not to be an optical detector but a memory instead. It should work as an analog shift register, storing arbitrary charge in each of its cells and reading them sequentially. Soon it was discovered that illumination causes internal photoelectric effect in the silicon substrate and fills up each memory cell with additional charge proportional to the incident light intensity.



Although CCD was rarely used as a memory, it found widespread application as a sensitive optical detector both in consumer electronics and in high-end scientific instruments such as astronomical telescopes. It should use NEA µPD3799 CCD detector.

### 5-Electronic setup

A common microcontroller The Atmega8-16PU version has 28 pins, of which 4 were occupied by DC supply, 2 by USB, 2 by oscillator, 4 by CCD driving signals and one for ADC input. The most demanding task is the USB communication.



The microcontroller should be equipped by a sufficient internal analog-to-digital converter (ADC). Many contemporary microcontrollers have an internal 10-bit converter able to perform at least 10,000 samples per second, which is sufficient for this application. The microcontroller was programmed via the serial programming interface using a USB-to-UART hardware programmer and the avrdude program. The firmware code was compiled on Linux (Ubuntu 10.04) in avr-gcc compiler and it was loaded into the microcontroller flash memory with commands.

### Properties of colors

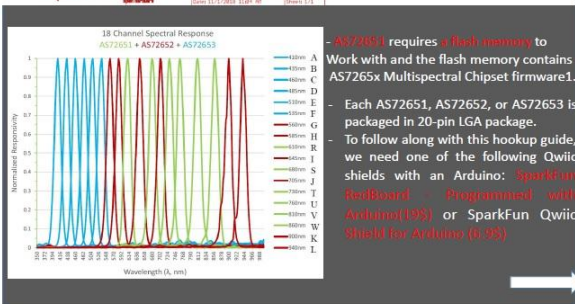
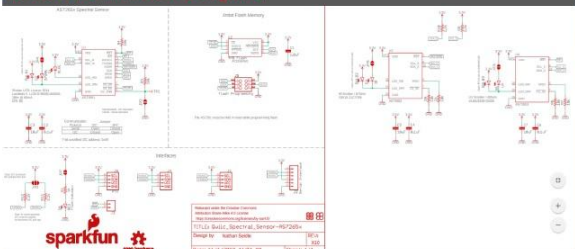
Color	Wavelength	Frequency	Photon energy
Violet	380-450 nm	668-789 THz	2.75-3.26 eV
Blue	450-495 nm	606-668 THz	2.50-2.75 eV
Green	495-570 nm	526-606 THz	2.17-2.50 eV
Yellow	570-590 nm	508-526 THz	2.10-2.17 eV
Orange	590-620 nm	484-508 THz	2.00-2.10 eV
Red	620-750 nm	400-484 THz	1.65-2.00 eV

### 6-Materials for optical setup

1. A standard aluminium L-profile 25 mm high, 2 mm thick and with 12 mm long foot.
2. The input slit was made of two razor blade segments, 15 mm long.
3. The collimating lens had 14 mm diameter, focal length  $f = 30$  mm, Plano-convex geometry.
4. The cylindrical mirror was obtained from a scrap photocopier. It is a polished metal rectangle, 42x15 mm in size. Its focal length is approximately 30 mm.
5. a blazed diffraction grating with 500 - 1000 grooves/mm, with size at least 8x8 mm.

### 7-Schematic of SparkFun Triad Spectroscopy Sensor - AS7265x (Qwiic)

AS7265x Multispectral Chipset consists of AS72651, AS72652, and AS72653 devices and each device has 6 optical filters so that AS7265x Multispectral Chipset have total 18 channels for spectral identification from 400nm to 1000nm with FWHM of 20nm. AS72651 is the main device with the smart interface to a microcontroller. The microcontroller gets the sensors data including AS72652 and AS72653 through AS72651 AT commands at I2C registers.



- AS72651 requires a flash memory to work with and the flash memory contains AS7265x Multispectral Chipset firmware.
- Each AS72651, AS72652, or AS72653 is packaged in 20-pin LGA package.
- To follow along with this hookup guide, we need one of the following Qwiic shields with an Arduino: SparkFun RedBoard Programmed with Arduino (19\$) or SparkFun Qwiic Shield by Arduino (6.9\$)

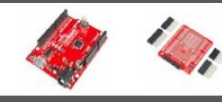
### 8-Software Design Considerations

In most of system designs, AS72651 is controlled by a microcontroller. With the UART interface, the controller could configure the devices and get the sensors data through some AT commands. The software of microcontroller design would be simple.

The following sections would focus on I2C interface and the software of microcontroller design should satisfy both I2C specification and AS7265x Multispectral Chipset register structure.



- Accessories:
- Qwiic Cable - Breadboard Jumper (4-pin) \$1.50
  - Qwiic Cable - 100mm \$1.50
  - SparkFun Qwiic Shield for Arduino \$6.95
  - SparkFun Qwiic HAT for Raspberry Pi \$5.95
  - SparkFun Qwiic Mux Breakout - 8 Channel \$11.95

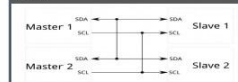


### 9-Arduino

- A computer (Windows, Mac, or Linux)
- An Arduino-compatible microcontroller (anything from this guide should work)
- A USB A-to-B cable, or another appropriate way to connect your Arduino-compatible microcontroller to your computer.
- 1-Installing Arduino IDE: <http://arduino.cc/en/Main/arduinoSoftwareIde>
- 2-The Inter-integrated Circuit (I2C) Protocol is a protocol intended to allow multiple "slave" digital integrated circuits ("chips") to communicate with one or more "master" chips. Like the Serial Peripheral Interface (SPI), it is only intended for short distance communications within a single device. Like Asynchronous Serial Interfaces (such as RS-232 or UARTs), it only requires two signal wires to exchange information.

#### I2C/Qwiic Interface:

The sensors are 3.3V compatible so don't use with a 5V Arduino Uno without proper conversion (use the Qwiic shield instead!). If you're using a 3.3V development platform that doesn't have a Qwiic connector, consider using the Qwiic Breadboard Cable.



# 1 Basics

In order to study the intensity of waves of stars ,we eleaborate this work to built a station that facilate the detection of waves .

## 1.3 Spectroscopy<sup>2</sup>

Spectroscopy is the study of the interaction between matter and electromagnetic radiation. Historically, spectroscopy originated through the study of visible light dispersed according to its wavelength, by a prism. Later the concept was expanded greatly to include any interaction with radiative energy as a function of its wavelength or frequency, predominantly in the electromagnetic spectrum, though matter waves and acoustic waves can also be considered forms of radiative energy; recently, with tremendous difficulty, even gravitational waves have been associated with a spectral signature in the context of LIGO and laser interferometry. Spectroscopic data are often represented by an emission spectrum, a plot of the response of interest as a function of wavelength or frequency.

Spectroscopy, primarily in the electromagnetic spectrum, is a fundamental exploratory tool in the fields of physics, chemistry, and astronomy, allowing the composition, physical structure and electronic structure of matter to be investigated at atomic scale, molecular scale, macro scale, and over astronomical distances. Important applications arise from biomedical spectroscopy in the areas of tissue analysis and medical imaging.



Figure 27: Analysis of white light by dispersing it with a prism is an example of spectroscopy.

Spectroscopy and spectrography are terms used to refer to the **measurement of radiation intensity as a function of wavelength** and are often used to describe experimental spectroscopic methods. Spectral measurement devices are referred to as spectrometers, spectrophotometers, spectrographs or spectral analyzers.

### 1.3.1 Theory

One of the central concepts in spectroscopy is a resonance and its corresponding resonant frequency. Resonances were first characterized in mechanical systems such as pendulums. Mechanical systems that vibrate or oscillate will experience large amplitude oscillations when they are driven at their

---

<sup>2</sup> from <https://en.wikipedia.org/wiki/Spectroscopy>



resonant frequency. A plot of amplitude vs. excitation frequency will have a peak centered at the resonance frequency. This plot is one type of spectrum, with the peak often referred to as a spectral line, and most spectral lines have a similar appearance.

In quantum mechanical systems, the analogous resonance is a coupling of two quantum mechanical stationary states of one system, such as an atom, via an oscillatory source of energy such as a photon. The coupling of the two states is strongest when the energy of the source matches the energy difference between the two states. The energy ( $E$ ) of a photon is related to its frequency  $E=h\nu$ ,  $h$  is Planck's constant, and so a spectrum of the system response vs. photon frequency will peak at the resonant frequency or energy. Particles such as electrons and neutrons have a comparable relationship, the de Broglie relations, between their kinetic energy and their wavelength and frequency and therefore can also excite resonant interactions.

Spectra of atoms and molecules often consist of a series of spectral lines, each one representing a resonance between two different quantum states. The explanation of these series, and the spectral patterns associated with them, were one of the experimental enigmas that drove the development and acceptance of quantum mechanics. The hydrogen spectral series in particular was first successfully explained by the Rutherford-Bohr quantum model of the hydrogen atom. In some cases spectral lines are well separated and distinguishable, but spectral lines can also overlap and appear to be a single transition if the density of energy states is high enough. Named series of lines include the principal, sharp, diffuse and fundamental series.

### 1.3.2 Type of radiative energy

The types of spectroscopy are distinguished by the type of radiative energy involved in the interaction. In many applications, the spectrum is determined by measuring changes in the intensity or frequency of this energy. The types of radiative energy studied include:

- Electromagnetic radiation was the first source of energy used for spectroscopic studies. Techniques that employ electromagnetic radiation are typically classified by the wavelength region of the spectrum and include microwave, terahertz, infrared, near-infrared, ultraviolet-visible, x-ray, and gamma spectroscopy.
- Particles, because of their de Broglie waves, can also be a source of radiative energy. Both electron and neutron spectroscopy are commonly used. For a particle, its kinetic energy determines its wavelength.
- Acoustic spectroscopy involves radiated pressure waves.
- Dynamic mechanical analysis can be employed to impart radiating energy, similar to acoustic waves, to solid materials.

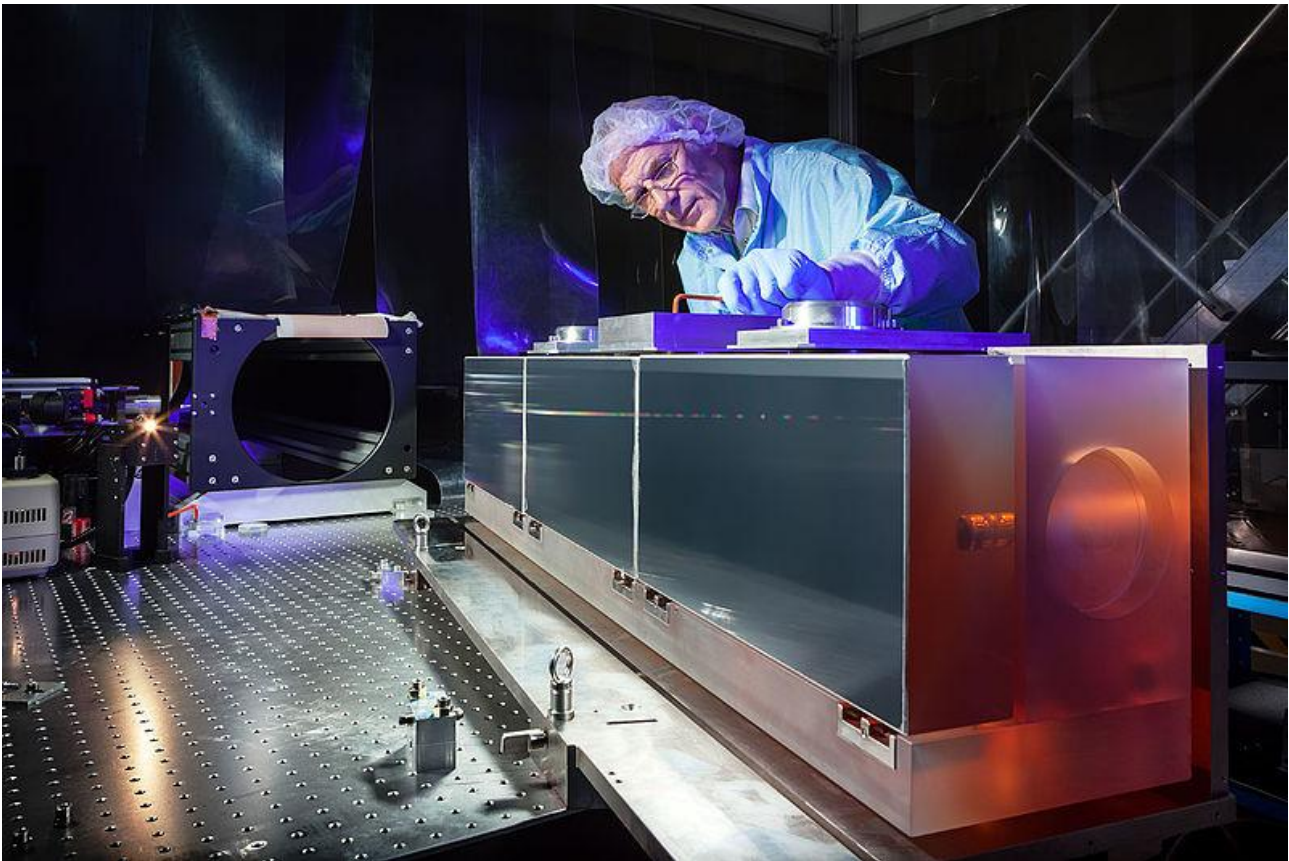


Figure 28: A huge diffraction grating at the heart of the ultra-precise ESPRESSO spectrograph.

### 1.3.3 Nature of the interaction

The types of spectroscopy also can be distinguished by the nature of the interaction between the energy and the material. These interactions include:<sup>[1]</sup>

- Absorption spectroscopy: Absorption occurs when energy from the radiative source is absorbed by the material. Absorption is often determined by measuring the fraction of energy transmitted through the material, with absorption decreasing the transmitted portion.
- Emission spectroscopy: Emission indicates that radiative energy is released by the material. A material's blackbody spectrum is a spontaneous emission spectrum determined by its temperature. This feature can be measured in the infrared by instruments such as the atmospheric emitted radiance interferometer.<sup>[4]</sup> Emission can also be induced by other sources of energy such as flames or sparks or electromagnetic radiation in the case of fluorescence.
- Elastic scattering and reflection spectroscopy determine how incident radiation is reflected or scattered by a material. Crystallography employs the scattering of high energy radiation, such as x-rays and electrons, to examine the arrangement of atoms in proteins and solid crystals.

- Impedance spectroscopy: Impedance is the ability of a medium to impede or slow the transmittance of energy. For optical applications, this is characterized by the index of refraction.
- Inelastic scattering phenomena involve an exchange of energy between the radiation and the matter that shifts the wavelength of the scattered radiation. These include Raman and Compton scattering.
- Coherent or resonance spectroscopy are techniques where the radiative energy couples two quantum states of the material in a coherent interaction that is sustained by the radiating field. The coherence can be disrupted by other interactions, such as particle collisions and energy transfer, and so often require high intensity radiation to be sustained. Nuclear magnetic resonance (NMR) spectroscopy is a widely used resonance method, and ultrafast laser spectroscopy is also possible in the infrared and visible spectral regions.

#### 1.3.4 Type of materials

spectroscopic studies are designed so that the radiant energy interacts with specific types of matter.

- Atoms

Atomic spectroscopy was the first application of spectroscopy developed. Atomic absorption spectroscopy and atomic emission spectroscopy involve visible and ultraviolet light. These absorptions and emissions, often referred to as atomic spectral lines, are due to electronic transitions of outer shell electrons as they rise and fall from one electron orbit to another. Atoms also have distinct x-ray spectra that are attributable to the excitation of inner shell electrons to excited states.

Atoms of different elements have distinct spectra and therefore atomic spectroscopy allows for the identification and quantitation of a sample's elemental composition. After inventing the spectroscope, Robert Bunsen and Gustav Kirchhoff discovered new elements by observing their emission spectra. Atomic absorption lines are observed in the solar spectrum and referred to as Fraunhofer lines after their discoverer. A comprehensive explanation of the hydrogen spectrum was an early success of quantum mechanics and explained the Lamb shift observed in the hydrogen spectrum, which further led to the development of quantum electrodynamics.

Modern implementations of atomic spectroscopy for studying visible and ultraviolet transitions include flame emission spectroscopy, inductively coupled plasma atomic emission spectroscopy, glow discharge spectroscopy, microwave induced plasma spectroscopy, and spark or arc emission spectroscopy. Techniques for studying x-ray spectra include X-ray spectroscopy and X-ray fluorescence.

- Molecules

The combination of atoms into molecules leads to the creation of unique types of energetic states and therefore unique spectra of the transitions between these states. Molecular spectra can be obtained due to electron spin states (electron paramagnetic resonance), molecular rotations, molecular vibration, and electronic states. Rotations are collective motions of the atomic nuclei and typically lead to spectra in the microwave and millimeter-wave spectral regions. Rotational spectroscopy and microwave spectroscopy are synonymous. Vibrations are relative motions of the atomic nuclei and are studied by both infrared and Raman spectroscopy. Electronic excitations are studied using visible and ultraviolet spectroscopy as well as fluorescence spectroscopy.

Studies in molecular spectroscopy led to the development of the first maser and contributed to the subsequent development of the laser.

- Crystals and extended materials

The combination of atoms or molecules into crystals or other extended forms leads to the creation of additional energetic states. These states are numerous and therefore have a high density of states. This high density often makes the spectra weaker and less distinct, i.e., broader. For instance, blackbody radiation is due to the thermal motions of atoms and molecules within a material. Acoustic and mechanical responses are due to collective motions as well. Pure crystals, though, can have distinct spectral transitions, and the crystal arrangement also has an effect on the observed molecular spectra. The regular lattice structure of crystals also scatters x-rays, electrons or neutrons allowing for crystallographic studies.

- Nuclei

Nuclei also have distinct energy states that are widely separated and lead to gamma ray spectra. Distinct nuclear spin states can have their energy separated by a magnetic field, and this allows for nuclear magnetic resonance spectroscopy.

## 1.4 Spectrometer

A spectrometer is a scientific instrument used to separate and measure spectral components of a physical phenomenon. Spectrometer is a broad term often used to describe instruments that measure a continuous variable of a phenomenon where the spectral components are somehow mixed. In visible light a spectrometer can for instance separate white light and measure individual narrow bands of color, called a spectrum, while a mass spectrometer measures the spectrum of the masses of the atoms or molecules present in a gas. The first spectrometers were used to split light into an array of separate colors. Spectrometers were developed in early studies of physics, astronomy, and chemistry. The capability of spectroscopy to determine chemical composition drove its advancement and continues to be one of its primary uses. Spectrometers are used in astronomy to analyze the

chemical composition of stars and planets, and spectrometers gather data on the origin of the universe.

Examples of spectrometers are devices that separate particles, atoms, and molecules by their mass, momentum, or energy. These types of spectrometers are used in chemical analysis and particle physics.

### 1.4.1 Types of spectrometer

#### 1.4.1.1 Optical spectrometer

An **optical spectrometer** (**spectrophotometer**, **spectrograph** or **spectroscope**) is an instrument used to measure properties of light over a specific portion of the electromagnetic spectrum, typically used in spectroscopic analysis to identify materials. The variable measured is most often the light's intensity but could also, for instance, be the polarization state. The independent variable is usually the wavelength of the light or a unit directly proportional to the photon energy, such as reciprocal centimeters or electron volts, which has a reciprocal relationship to wavelength.

A spectrometer is used in spectroscopy for producing spectral lines and measuring their wavelengths and intensities. Spectrometers may also operate over a wide range of non-optical wavelengths, from gamma rays and X-rays into the far infrared. If the instrument is designed to measure the spectrum in absolute units rather than relative units, then it is typically called a spectrophotometer. The majority of spectrophotometers are used in spectral regions near the visible spectrum.

Spectrometers are used in many fields. For example, they are used in astronomy to analyze the radiation from astronomical objects and deduce chemical composition. The spectrometer **uses a prism or a grating to spread the light from a distant object into a spectrum**. This allows astronomers to detect many of the chemical elements by their characteristic spectral fingerprints. If the object is glowing by itself, it will show spectral lines caused by the glowing gas itself. These lines are named for the elements which cause them, such as the hydrogen alpha, beta, and gamma lines. Chemical compounds may also be identified by absorption. Typically, these are dark bands in specific locations in the spectrum caused by energy being absorbed as light from other objects passes through a gas cloud. Much of our knowledge of the chemical makeup of the universe comes from spectra.

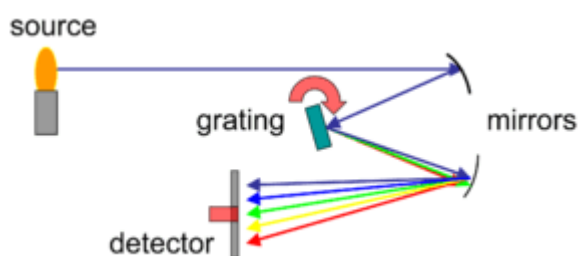


Figure 29: Grating spectrometer schematic

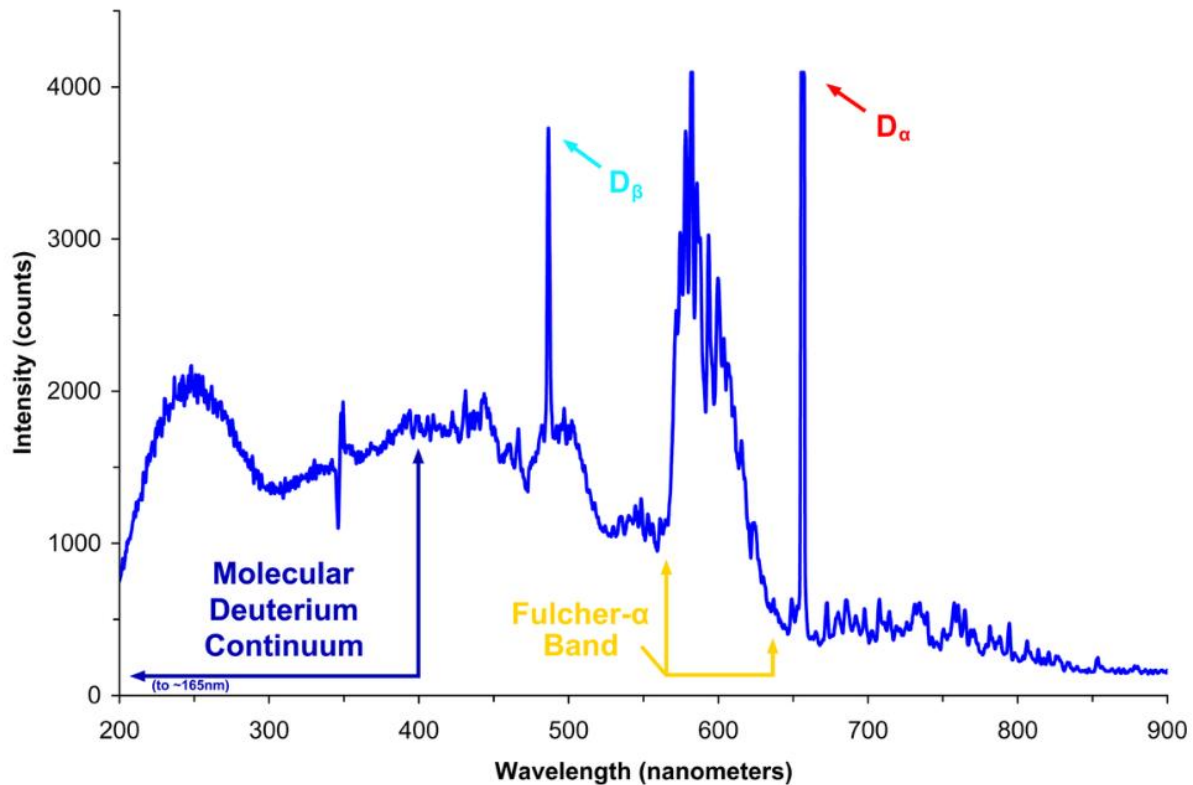


Figure 30: Spectrum of light emitted by a deuterium lamp in the UV visible and near infrared part of the electromagnetic spectrum.

#### 1.4.1.2 Spectroscopes

Spectroscopes are often used in astronomy and some branches of chemistry. Early spectroscopes were simply prisms with graduations marking wavelengths of light. Modern spectroscopes generally use a diffraction grating, a movable slit, and some kind of photodetector, all automated and controlled by a computer.

Joseph von Fraunhofer developed the first modern spectroscope by combining a prism, diffraction slit and telescope in a manner that increased the spectral resolution and was reproducible in other laboratories. Fraunhofer also went on to invent the first diffraction spectroscope.[2] Gustav Robert Kirchhoff and Robert Bunsen discovered the application of spectroscopes to chemical analysis and used this approach to discover caesium and rubidium.[3][4] Kirchhoff and Bunsen's analysis also enabled a chemical explanation of stellar spectra, including Fraunhofer lines.[5]

When a material is heated to incandescence it emits light that is characteristic of the atomic makeup of the material. Particular light frequencies give rise to sharply defined bands on the scale which can be thought of as fingerprints. For example, the element sodium has a very characteristic double yellow band known as the Sodium D-lines at 588.9950 and 589.5924 nanometers, the color of which will be familiar to anyone who has seen a low pressure sodium vapor lamp.

In the original spectroscope design in the early 19th century, light entered a slit and a collimating lens transformed the light into a thin beam of parallel rays. The light then passed through a prism (in hand-held spectroscopes, usually an Amici prism) that refracted the beam into a spectrum because different wavelengths were refracted different amounts due to dispersion. This image was then

viewed through a tube with a scale that was transposed upon the spectral image, enabling its direct measurement.

With the development of photographic film, the more accurate spectrograph was created. It was based on the same principle as the spectroscope, but it had a camera in place of the viewing tube. In recent years, the electronic circuits built around the photomultiplier tube have replaced the camera, allowing real-time spectrographic analysis with far greater accuracy. Arrays of photosensors are also used in place of film in spectrographic systems. Such spectral analysis, or spectroscopy, has become an important scientific tool for analyzing the composition of unknown material and for studying astronomical phenomena and testing astronomical theories.

In modern spectrographs in the UV, visible, and near-IR spectral ranges, the spectrum is generally given in the form of photon number per unit wavelength (nm or  $\mu\text{m}$ ), wavenumber ( $\mu\text{m}^{-1}$ ,  $\text{cm}^{-1}$ ), frequency (THz), or energy (eV), with the units indicated by the abscissa. In the mid- to far-IR, spectra are typically expressed in units of Watts per unit wavelength ( $\mu\text{m}$ ) or wavenumber ( $\text{cm}^{-1}$ ). In many cases, the spectrum is displayed with the units left implied (such as "digital counts" per spectral channel).

#### 1.4.1.3 Mass spectrometer

A mass spectrometer is an analytical instrument that is used to identify the amount and type of chemicals present in a sample by measuring the mass-to-charge ratio and abundance of gas-phase ions.<sup>[2]</sup>

#### 1.4.1.4 Time-of-flight spectrometer

The energy spectrum of particles of known mass can also be measured by determining the time of flight between two detectors (and hence, the velocity) in a time-of-flight spectrometer. Alternatively, if the velocity is known, masses can be determined in a time-of-flight mass spectrometer.

#### 1.4.1.5 Magnetic spectrometer

when a fast charged particle (charge  $q$ , mass  $m$ ) enters a constant magnetic field  $B$  at right angles, it is deflected into a circular path of radius  $r$ , due to the Lorentz force. The momentum  $p$  of the particle is then given by:

$$p = mv = qBr,$$

### 1.5 Types of optical spectrometers

Most optical spectrometers that produce a spectral waveform spanning over a selected region of wavelengths may be divided by their principle of operation into 3 most important groups:

1. Fourier-transform spectrometers use Michelson interferometer to measure how the interference signal oscillates when one of the mirrors moves. The interference function is later digitally processed to get the intensity spectrum. They can achieve very high spectral resolution and can measure even far-infrared spectra, assuming IR optics and detector are used.
2. Spectrometers with a monochromatic usually utilize rotating diffraction grating. They are simpler and less sensitive to environment, as no interference fringes are measured. The Czerny Turner setup

is often used, but other different setups may suit a particular purpose better. For example, to replace the rotating grating by a prism with moving mirror may be favorable for UV spectroscopy or when higher diffraction orders are to be eliminated.

3. The latter setup can be modified to obtain a spectrometer with multi-channel detector and no moving components. The grating is then fixed and the spectrum is projected on a broadband detector, which is usually a CCD.

The spectrometers in this category largely differ by sensitivity, resolution, application, size and price. For instance, the High Accuracy Radial Velocity Planet Searcher at La Silla Observatory in Chile is able to detect 1 m/s velocity difference in star's movement, enabling to indirectly search for extrasolar planets. On the other hand, spectrometers of this type can be made very compact and they are optimal for applications where resolution and sensitivity is not critical. Some models are available as a PCI card fitting into a computer.

This research project focuses on building a simple, cheap and compact spectrometer meeting following objectives:

1. The spectral resolution ( $\Delta\lambda$ ) should be better than 5 nm.
2. No moving components should be used.
3. The device and supplied software should be easy to use so that anybody with basic knowledge of spectroscopy can use it immediately.
4. The supplied software must run on most major operating systems with dependence on freely available programs only.
5. Except for initial calibration, no further maintenance would be required. Each device built will store its own calibration data in its permanent memory to prevent the need for recalibration when another model is connected.
6. Communication with computer and electrical supply should be performed via single USB cable.

The purpose of this research project is to decide whether such device can be built at a substantially lower price and yet remain suitable for practical tasks, as well as to present a possible way of doing that.

Additionally, the computer software is released under free license, allowing the aforementioned modifications and scripting. Last but not least, the data acquisition, processing and displaying techniques can be reused in many other applications involving measurement automation.

### 1.5.1 General dispersive spectrometer design

A diffraction grating design with a CCD detector was used. This section describes how the light components are separated and delivered to the CCD. In the horizontal plane, the incoming light must be spatially limited by a vertical slit. Then the spatial limitation is converted to angular limitation using a concave mirror or a convex lens. Ideally, we obtain a parallel beam of white light. Its width is limited either by the size of the mirror or lens used, of by the angle of the beam passing through the slit. The light components of different wavelengths separate after being reflected into different angles by a diffraction grating. Finally, the angular separation might be converted back to spatial separation



using another lens or mirror as drawn in Fig. 5a. However, this would require a big lens with diameter similar to the length of CCD. The spatial difference would be proportional to its focal length, probably resulting in a small spatial separation. Fortunately, the second lens is not necessary, as the first lens can be shifted several millimeters away from the slit to create a real image in arbitrary distance from the grating (Fig. 5b). The beam incident on the diffraction grating becomes slightly convergent when a single lens is used. This results in nonuniform angular difference even for single wavelength and the projected image of the slit becomes slightly blurred. However, for the sharp angle of convergence this effect can be neglected.

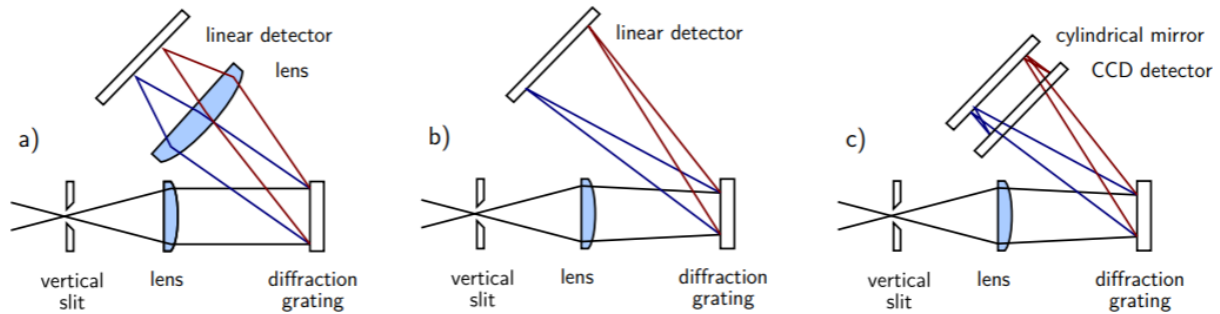


Figure 31: Horizontal schematics and light paths

There are several other phenomena limiting the spectral resolution of this setup, but assuming an ideal diffraction grating is used, the nonzero width of the input slit dominates. In the vertical projection, a single point in the slit plane is projected onto another point on the sensor as shown at Fig. 6a. As the CCD sensor is very narrow, the spectrometer would be sensitive in only one point at the slit, not depending on the incident angle. This would be optimal if either a thin optical fiber or a point source are measured. However, it was expected that the incident light would mostly be cover some area on the slit and that the spectrometer should be sensitive at nonzero length along the slit. Therefore a cylindrical mirror was inserted near to the focal plane to concentrate each spectral line (image of the input slit) into a much shorter line at the detector (Fig. 5c, 2b). If the light entered the slit at a single point and this point slightly moved in vertical axis, its image would move in vertical axis, too. When a cylindrical mirror is used, the point image would still be projected onto the CCD, albeit under different angle. The detector could not be put directly in the focal plane of this mirror, because the horizontal focus given by the lens must be maintained. Nonetheless, the sensitivity to the light entering the slit was substantially improved.

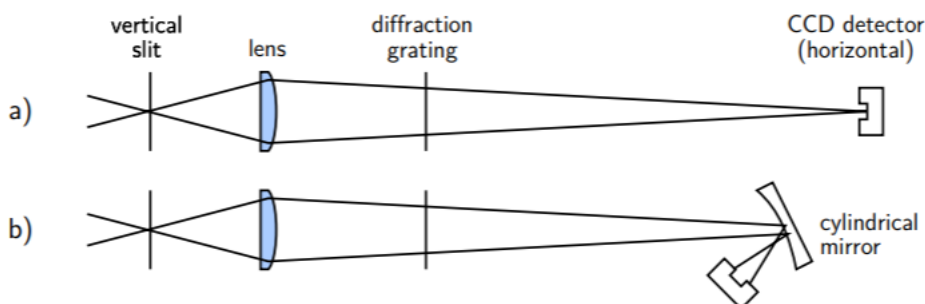


Figure 32: Vertical schematics and light paths

## 1.6 CCD detector<sup>3</sup>

### 1.6.1 Overview

The charge coupled device, CCD, was originally designed not to be an optical detector, but a memory instead. It should work as an analog shift register, storing arbitrary charge in each of its cells and reading them sequentially. Soon it was discovered that illumination causes internal photoelectric effect in the silicon substrate and fills up each memory cell with additional charge proportional to the incident light intensity. Although CCD was rarely used as a memory, it found widespread application as a sensitive optical detector both in consumer electronics and in high-end scientific instruments such as astronomical telescopes. CCD detectors may be divided into two groups: linear CCDs, where one row of pixels is shifted to the output, and matrix CCDs, where the bottom row is fully shifted out always when all columns are shifted down by one pixel. For this project, a linear CCD was chosen over a matrix CCD because only a linear detector several centimeters long was needed. Still, it would be possible to build a custom matrix CCD driver, too [1]. Another option, a CMOS sensor, was not used because of worse availability.

### 1.6.2 Driving a linear CCD

Although the internal design of the particular components may differ, the basic principle of CCD operation should remain similar. In the CCD register itself, a silicon substrate is covered by a thin layer of insulator and the electrodes. When a voltage is applied to an electrode, the electrons get trapped under the layer of insulator. By changing the voltage distribution on the surface, the charge packet can be moved with negligible loss.

In a common two-phase driven CCD, there are two electrodes on the insulating layer over each pixel. The geometry of electrodes is asymmetrical, dragging the electron packet nearer to one end of electrode. Therefore, a two-phase only signal is needed to transport the charge to the next pixel. The two phase crossing must be nearly symmetrical, which requires them to be switched at once<sup>1</sup>. The silicon surface can integrate the charge produced by internal photoelectric effect, but this is rarely used now. Instead, contemporary sensors contain an array of photodiodes, which are much more sensitive than the actual CCD register. When a transfer gate impulse comes, the charge is transferred to each corresponding pixel in the CCD register. This also eliminates blur of the image when the charges are shifted [4]. At the end of the analog register, the charge is coupled out to a pre-amplifier.

### 1.6.3 CCD output handling

Depending on the particular design, **the two CCD phases and additional one to three inputs need to be activated by an impulse so that each pixel is read. After correct pixel driving signals are input, the CCD shifts the pixel's charge to its internal preamplifier and the corresponding voltage signal occurs at one pin.** Sometimes is the output voltage stored in a sample-and-hold circuit. The CCD detector output shall depend on the illumination linearly, but the signal is inverted, at least in the CCD detectors considered, e. g., for the CCD used in this project (NEC  $\mu$ PD3799): Under no illumination, the output is approximately +7 V, whereas under full saturation the output drops to +2.4

---

<sup>3</sup> from [https://www.fzu.cz/~dominecf/electronics/usb-spect/usb\\_spectrometer\\_dominec.pdf](https://www.fzu.cz/~dominecf/electronics/usb-spect/usb_spectrometer_dominec.pdf)

V. The influence of incident light on the CCD register itself and its supporting circuitry, along with thermal electrons, can interfere with measurement.

- **Blooming:** occurs when excess charge concentrates in one cell and it leaks into neighbouring cells. It manifests as a flat, fully saturated regions with sharp edges, effectively obscuring the signal in the vicinity of the intensively illuminated spot. Most modern CCDs address this by electronic design, but the simple linear CCDs used in this project do not. Overexposed areas must be avoided by either reducing the light intensity or integration time. For instance, the saturation exposure of the used linear CCD is lower than  $0.5 \text{ lx}\cdot\text{s}$  [4].

- **Charge volatility:** The stored charge decays over time. This is expected to be caused by both thermal electrons and incident light. At room temperature, it was experimentally proven that the CCD must be read in  $\approx 0.5 \text{ s}$  after gate transfer to avoid this. This presents a time constraint to the data acquisition and transmitting time. When the CCD is read in bursts, a sawtooth-like additive bias will occur.

- **Oversaturation:** When the CCD is illuminated by common daylight for a while ( $> 10 \text{ lx}\cdot\text{s}$ ), the chip becomes so oversaturated that several full read-outs are needed to drain the integrated charge. Otherwise the output voltage may drop even under the saturation voltage. Sometimes this manifested as a step transition from saturation of one colour component in the middle of CCD reading, even when the CCD has been in dark for the last integration period.

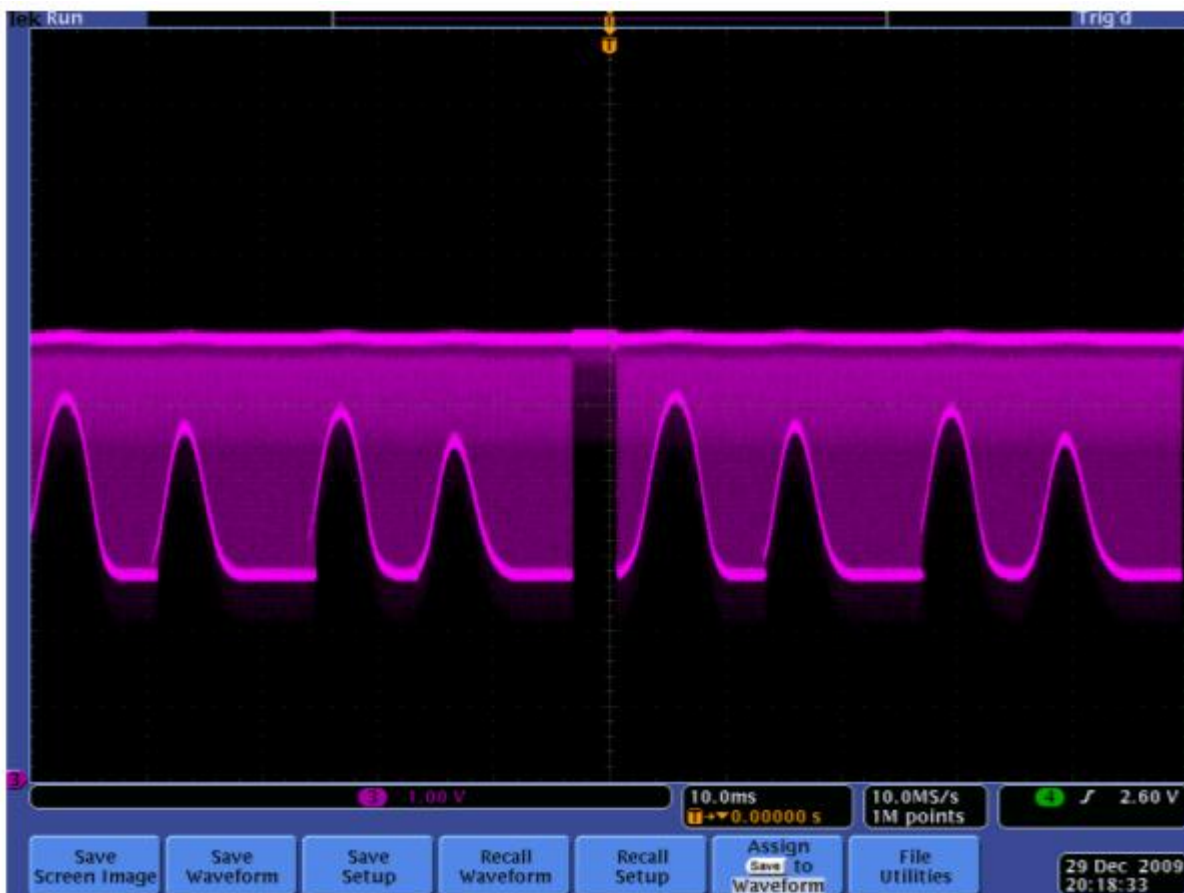


Figure 33: : One of the first measurements of the CCD output on an oscilloscope. On the screen, there are two consecutive read outs of CCD. The detector window was covered by four thin paper stripes.

Note the end of register signal in the middle of the screen and the blooming which slightly overlaps the less illuminated areas.

- **Thermal noise**

is caused by random thermal electron-hole pairs. It is probably lower than electronic noise in the sampling circuit used. Some of the mentioned issues can be addressed by thermoelectrical cooling of the sensor, as a 20 °C temperature drop is expected to effectively suppress the thermal noise and conductivity. No cooling was used in this design because of rather high power requirements of a Peltier cell. When a colour CCD is used, the red, green and blue signals must be averaged to obtain sensitivity covering the whole spectrum to be measured. This was done by inserting a 10 kΩ resistor at each channel and by connecting their second terminals together. The resulting spectral sensitivity is inhomogeneous, which was later addressed by amplitude calibration.

#### 1.6.4 Driving the CCD with a microcontroller

The proper CCD driving, analogue to digital conversion and consequent data transmission would require complicated circuitry if constructed from discrete components or TTL logic. Even such designs were constructed but most of these tasks can be easily handled by a common microcontroller of middle class. The most demanding task is the USB communication, which determines the minimum MCU computational power to approximately 12 MIPS at least. This topic is discussed later. **The microcontroller should be equipped by a sufficient internal analog-to-digital converter (ADC). Usage of an external ADC would present additional cost and complexity. Many contemporary microcontrollers have an internal 10-bit converter able to perform at least 10,000 samples per second, which is sufficient for this application.** Additionally, the need to avoid the mentioned sawtooth bias requires that the whole CCD is read at once and the spectral curve is stored in the memory until it is transmitted to the computer. Many microcontrollers come with fairly limited amount of internal RAM, which ranges from tens of bytes to 1 kB in the middle class. Taking into account that about 100 bytes are allocated by various program 10 data and that each pixel occupies 10 bits, there remains room for approximately 720 pixels if 1 kB of RAM was used. This severely limits the theoretical spectral resolution of 5300 pixels. The real spectral resolution in this case is, however, more limited by imprecise optics, and therefore the 1 kB of RAM was considered sufficient. If higher optical resolution was achieved and consequently bigger data buffer was appropriate, microcontrollers with 2 kB or 4 kB of RAM are available for approximately 5 Euro and 8 Euro, respectively. A cheaper solution would be an external RAM. As of 2010, the market is saturated by cheap parallel static RAM circuits with capacity in tens of kB. However, most of these circuits use more than 20 pins for addressing and data transmission, which would occupy all available pins of the cheaper microcontroller. The SRAM circuits communicating over the serial line are much less available, although there are plenty of rather cheap serial EEPROM circuits, which have limited number of write cycles. Possible candidates could be Microchip 23K640 and 23K256 models with 8 and 32 kB, respectively. Anyway, the use of external RAM would make the device more complicated and error prone. **Therefore no external RAM was used in this design.** As 1 kB of RAM was considered sufficient, the Atmel Atmega8 microcontroller was found to fulfill all aforementioned requirements. Moreover, this MCU supports in system

programming, which was very handy to develop and debug communication with both CCD and computer. **The Atmega8-16PU version has 28 pins, of which 4 were occupied by DC supply, 2 by USB, 2 by oscillator, 4 by** CCD driving signals and one for ADC input. There remained enough pins and capacity for a 7-segment display and simple user controls on the device, but later it was considered impractical and only the computer control was left. As for 2010, Atmega8-16PU circuit is still one of the most cost effective microcontrollers on the market, with price of about 1.5 Euro. 2.4

## 1.6.5 Communication interfaces

### 1.6.5.1 Comparison of different interfaces

Several different interfaces are commonly used to transfer data between a computer and external instruments.

- The serial port (RS232) can use 3 wires only, one wire for each direction and a ground. The data rate must be set on both sides. Serial line is often used in industrial applications and for older computer peripherals. **The microcontroller used in this project has hardware circuit for asynchronous serial communication, which could make this option favorable.** However, RS232 begins to disappear from newer computers and it requires the user to set the serial port options manually, too.
- The parallel port would probably require writing an own driver for data transfer and it would be too bulky for this project.
- The GPIB interface is often used to communicate with scientific instruments, but is rarely available at standard computers, let alone notebooks. Moreover, it shares the disadvantages of parallel port.
- The ethernet interface uses complicated, high-level protocol, which probably could not be processed by the microcontroller unit (MCU) and would increase the device complexity.

The Universal Serial Bus interface remains to be the most advantageous option, providing decent data rate, excellent availability and sufficient power supply. In the low-speed mode, the signalling speed is 1.5 Mb/s. This data rate can be processed by the MCU firmware, although the MCU has no hardware acceleration for USB communication. For higher data rate in full-speed mode of 12 Mb/s, a dedicated USB to RS232 converter may be used. An example is the Future Technology FT232BM circuit. According to the datasheet, it should be able to communicate with computer via USB, handle all USB protocol messages and communicate with the MCU via serial port. In this case the maximum data rate over serial port should be 2 Mb/s. [9] This may not seem as an advantage over firmware USB driver until one realizes that it is the USB protocol in the low-speed mode what presents the bottleneck, limiting the average data rate to less than one tenth of the signalling speed. Likewise, when the MCU communicates using the USART (Universal Synchronous and Asynchronous serial Receiver and Transmitter) subcircuit, less time is spent by the driver routines used to handle the messages. The USB-RS232 converter was not used here in order to keep the device simple.

### 1.6.5.2 Hardware for USB communication

As no clock signal is sent over USB and the USB specification requires 1.5 % maximum tolerance for the timing, the MCU clock shall be timed precisely. Typically, the firmware drivers require oscillator whose frequency would be a multiple of 1.5 MHz. The minimum clock frequency is limited by the particular driver; mostly at least 8 processor steps per bit are required. A 12 MHz quartz crystal was

used in this project. **The USB cable contains 4 wires, which are listed in the table 1. The pins of the USB-B connector, used on the device side, are drawn in Fig. 8a.** The logical one voltage should fall between 2.7 and 3.6 V [16], therefore the 5 V TTL output of the MCU must be limited by Zener diodes. Additionally, the D- line must have logical one when the MCU is reset, which is ensured by the 1 k $\Omega$  pull-up resistor (Fig. 8b).

*Table 1: USB cable wires*

Wire label	Usual colour	Purpose
GND	black	ground
$U_{CC}$	red	DC power (up to 500 mA at 5 V)
D+	green	half-duplex, differential data line
D-	white	<i>dtto</i>

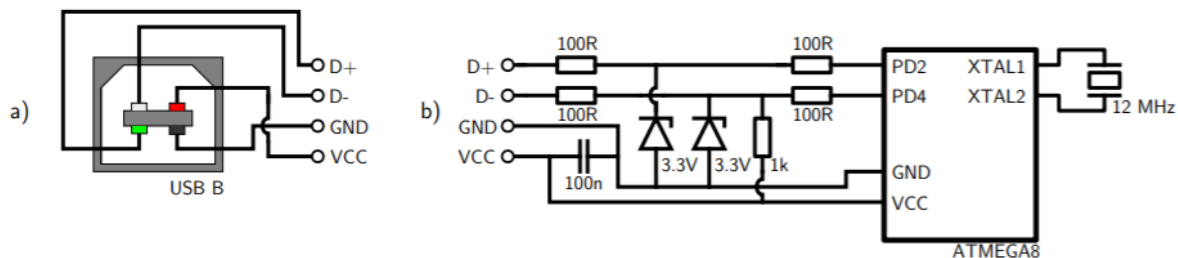


Figure 34: : a) Pins on the USB B connector; b) Minimal circuit for connecting ATMEGA8 to USB

The USB datasheet has some stricter requirements, e. g. for the device resistance, but the circuit from Fig. 8 worked flawlessly. Similar schematics are used in many other projects.

### 1.6.6 Brief description of USB protocol

The data sent over USB are encoded using non-return-to-zero format: when a "0" bit is transmitted, the D- and D+ differential lines switch their state. When a "1" bit is transmitted, no change occurs. However, when more than 6 consecutive "1" bits are to be transmitted, one "0" bit is stuffed after them to enable the receiver to synchronize its clock at an edge of incoming signal. The data lines do not have to be always differential. For several low-level signals, e. g. end of packet, the D- and D+ lines may go both to logical "0" or "1". All data are sent in packets. The packet contains an initial sync sequence, the packet identification number and optionally payload or control data along with its checksum. Some packets transmit payload data, while other packets are used for handshake and identification only. Three packets, token, data and handshake, usually form a transaction. The USB protocol, mostly in a simplified, yet working form, is handled fully by the firmware driver. After being requested by the host, each USB device identifies itself by a vendor number and an USB class. Most devices fall into the human interface device or mass storage classes. Each class is handled slightly differently by the computer. The human interface device class was chosen due to its simplicity and widespread universal drivers [16]. USB protocol is rather complicated and its more

detailed description is beyond the scope of this document. There are several software implementations of the USB protocol for AVR microcontrollers. This project utilizes the V-USB driver by Christian Starkjohan [13] because of its good documentation and numerous practical examples. The driver is licensed under GNU GPL for noncommercial use. All these drivers use a hardware interrupt, which is triggered by incoming USB packet. At 1.5 Mbit/s signalling speed and 12 MHz main oscillator, only 8 clock cycles remain to receive, convert and store each bit. This requires that the microcontroller completely halts all another operation when any USB packet is received or transmitted. Besides, the USB protocol has the master-slave topology, and accordingly the MCU stops to receive or transmit packets asynchronously with its operation, which has to be taken into account when programming real-time tasks.

## 2 Design and Realization of a spectrometer prototype<sup>4</sup>

Based on:

Czech Technical University in Prague, Faculty of Nuclear Sciences and Physical Engineering  
Department of Physical Electronics, *"Design and construction of a digital CCD spectrometer"*, Research project, Author: Filip Dominec, Supervisor: Ing. Jaroslav Pavel, Academic year: 2009/2010

([https://www.fzu.cz/~dominecf/electronics/usb-spect/usb\\_spectrometer\\_dominec.pdf](https://www.fzu.cz/~dominecf/electronics/usb-spect/usb_spectrometer_dominec.pdf))

Please note that this USB spectrometer project has a new HTML page, which may contain updates and further information: <http://www.fzu.cz/~dominecf/spek2/index.html>

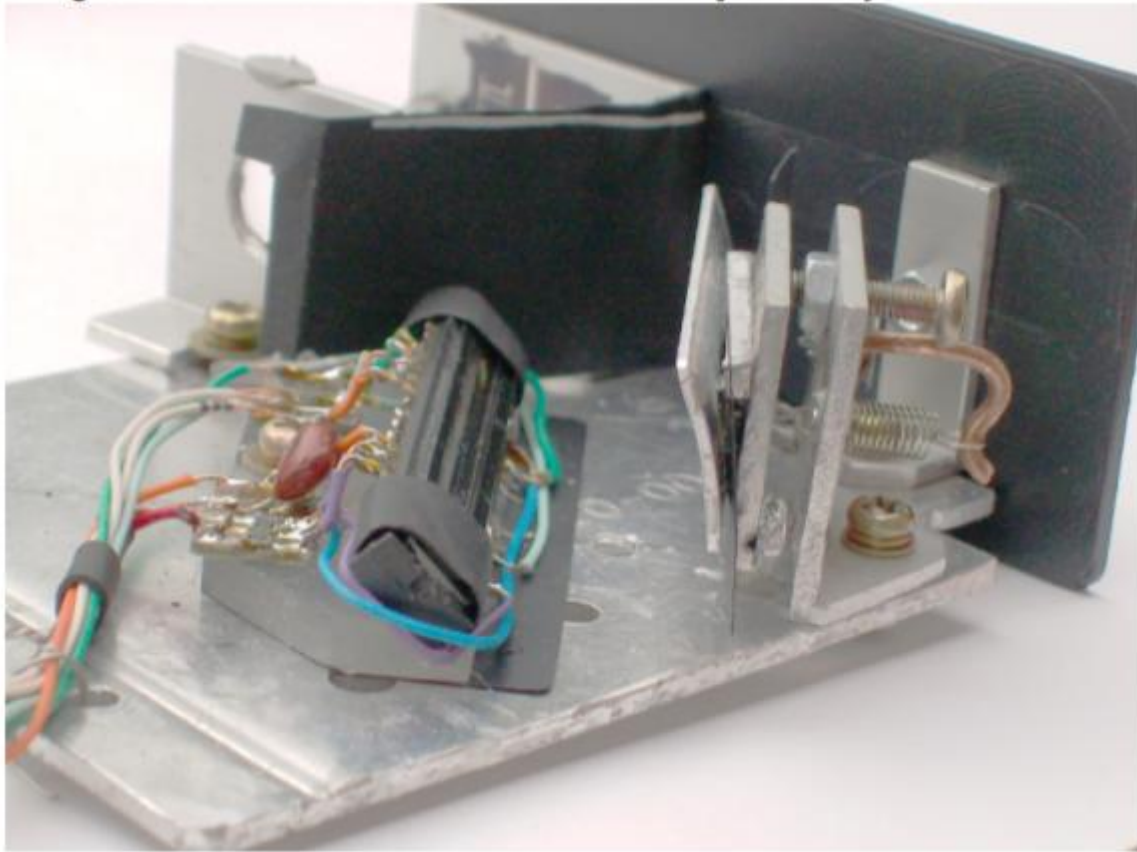
### 2.1 Optical setup

- The optical components holders were made of a standard aluminium L-profile 25 mm high, 2 mm thick and with 12 mm long foot. The beam path axis was chosen to be 14 mm above the base surface. This provided optimal vertical room for the beam, maintaining enough room between the light path and the base for bolts etc.
- The input slit was made of two razor blade segments, 15 mm long. One of the segments was glued onto the inner side of the L-profile to cover half of the input hole. Its sharp edge was adjusted to be perpendicular to the base. The second segment was clamped next to it by a short screw with a spring bushing. This makes adjusting the slit width possible. In the final setup, the slit width of 50  $\mu\text{m}$  – 100  $\mu\text{m}$  appeared to be appropriate
- The collimating lens had 14 mm diameter, focal length  $f \approx 30$  mm, plano-convex geometry and standard anti-reflex coating. (Generally, any common small lens of similar  $f$  may be used.) It was glued at the edges to a hole of similar diameter, keeping its axis at the beam axis. At the base of the L-profile, a notch instead of a hole was grinded to enable focusing.
- The reflective diffraction grating was attached nearly perpendicular to the incident beam. For the first prototype, a 20×20 mm segment cut from the outer edge of a blank CD-R was used. Notes to this solution are discussed later. The grating was rotated so that the most desired spectral range in the first diffraction order is projected on the CCD.
- The cylindrical mirror was obtained from a scrap photocopier. It is a polished metal rectangle, 42×15 mm in size. Its focal length is approximately 30 mm. The mirror was attached to a metal chip, which had a groove at the bottom. The groove fitted to two spikes in the bottom of the L-profile. At the top, an M3 screw allows to adjust the vertical angle of the mirror.
- The CCD detector was glued to a low profile PMMA slab. Its pins were shortened not to obscure any passing light and soldered to the controller circuit. The slab had a notch for the bolt. The output signal from three colour channels was averaged by three 10 k $\Omega$  resistors near the CCD and it was connected using a thin shielded cable to eliminate noise from the digital wires. Between the supply voltage and ground, a 100 nF capacitor was inserted.

---

<sup>4</sup> from [https://www.fzu.cz/~dominecf/electronics/usb-spect/usb\\_spectrometer\\_dominec.pdf](https://www.fzu.cz/~dominecf/electronics/usb-spect/usb_spectrometer_dominec.pdf)





*Figure 35: Detail of the CCD mount and the adjustable cylindrical mirror*

The optical setup was mounted (by M3 bolts and nuts) to a 2 mm thick aluminium plate, of approximately 70×90 mm in size. It provided a decently rigid, yet light base. There remained 6 degrees of freedom, that had to be precisely adjusted to obtain effective and narrow spectral lines projected on the CCD.

1. The input slit width The second razor segment should limit the light entrance to an uniform, thin line.
2. The longitudinal position of the collimating lens should focus the slit onto the CCD in the horizontal plane.
3. The vertical grooves orientation of the diffraction grating should be parallel to the slit.
4. The horizontal angle of the diffraction grating: The whole desired spectral range should be projected onto the CCD.
5. The cylindrical mirror and CCD should be perpendicular to the beam coming from diffraction grating, which illuminates the center of CCD.
6. The vertical angle of cylindrical mirror and the corresponding position of the CCD detector: Along with previous setting, it should focus the spectral lines to illuminate the narrow CCD line the most effectively. The coarse setting was done visually using the light from a standard fluorescent lamp. The fine tuning of the lens position was performed when the device was connected to computer and the spectral lines were optimised to be as narrow as possible.

### 2.1.1 Diffraction grating source

The reflection diffraction grating of suitable parameters prove to be the component, that was the hardest to obtain for this project, maintaining the low price criterion. Ideally, a blazed diffraction grating with 500 – 1000 grooves/mm, with size at least 8×8 mm and with optimum efficiency in the visible range should be used. As of 2010, there is likely no shop in the Czech Republic where such gratings could be bought easily, according to the search on Internet. Future models can use a **professional grating**, which would probably cost **at least 50 Euro** [8] . This price is not limiting, however it would spoil one of the objective of minimizing the device's cost. Maybe several gratings could be replicated after one professional grating is bought. Alternatively, there is a proof that a reasonable diffraction grating may be manufactured using a nearly home-built ruling engine, taking into account the contemporary availability of MCUs, lasers and stepping motors [10]. Anyway, the precision requirements for such ruling engine are very tight. To achieve 1 nm spectrometer resolution at the 500 nm wavelength, the RMS error of groove spacing must be at most few nanometers. This limits the groove spacing error to less than 10 diameters of silver atoms! For the first prototype, the CD-R slab worked quite well. The cheapest CD-R had unexpectedly low stray light and no apparent Rowland ghosts coming from low-frequency modulation of the grating. Apart from non-optimal efficiency and fragile metallic coating on the surface, the biggest problem was caused by the grooves curvature. A monochromatic beam limited by the slit is projected into a crescent shape in the focal plane of the collimating lens. Instead, a vertical line is required, as the cylindrical mirror focuses the beam in the vertical plane.

#### 2.1.1.1 Microcontroller circuit

Aside from the CCD detector and the supply circuit mentioned later, the electronics do not require many components. The MCU is clocked by a **12.000 MHz quartz oscillator**. Some designs suppose to couple each oscillator input to **ground by two 30 pF capacitors**, but this has proven not to be necessary. The CCD driving signals use **the TTL levels**, hence the CCD inputs may be connected directly to the MCU pins. **For the used NEC  $\mu$ PD3799 CCD detector four signal wires are needed:** the phase 1 and phase 2 signals, the RB (reset gate) and the TG (transfer gate) signals. When another CCD is used, additional driving signals may have to be added, e. g., for NEC  $\mu$ PD3797, additional CLB (reset feed-through level clamp clock) negative impulse must be included after the RB impulse. According to the particular datasheet, both the firmware routines and hardware wiring can be easily modified to accomplish this. Note that one MCU clock takes only 83 ns and some minimum pulse length and delay must be maintained according to the CCD datasheet. As was noted in the 1.4.3 section, the output signal of CCD is too high to be directly connected to the analog-to-digital converter (ADC) of the MCU. **The output must be linearly inverted, amplified and shifted before passing to the ADC, which measures in the range of 0 to 5 V.** There is an older project of Paul Stoffregen, who accomplished this transformation using five operational amplifiers, of which two act as a sample-and-hold circuits, storing the two voltage levels of dark and saturated signal [14]. A circuit of two potentiometers and only one operational amplifier was used here instead, as both the dark and the saturated voltage levels both prove to be relatively stable. If only one colour component becomes saturated, the output signal gets distorted and therefore unusable. Accordingly, the signal range should be stretched so that full saturation of single colour component corresponds to full

saturation of the signal entering the ADC. In other words, the output signal must be amplified with gain enough to prevent the saturation of any colour component in CCD. The circuit with inverting preamplifier and microcontroller is shown in Fig. 10. Let us denote the CCD output voltage as  $V_{ccd}$ , the voltage reference from R1A,B as  $V_{ref} = R_{1A} / (R_{1A} + R_{1B}) \cdot 5 \text{ V}$  and the voltage at the output of the operational amplifier as  $V_{adc} = V_{adc}(V_{ccd}, V_{ref})$ . Taking into account that the operational amplifier inputs virtually no current, one obtains that

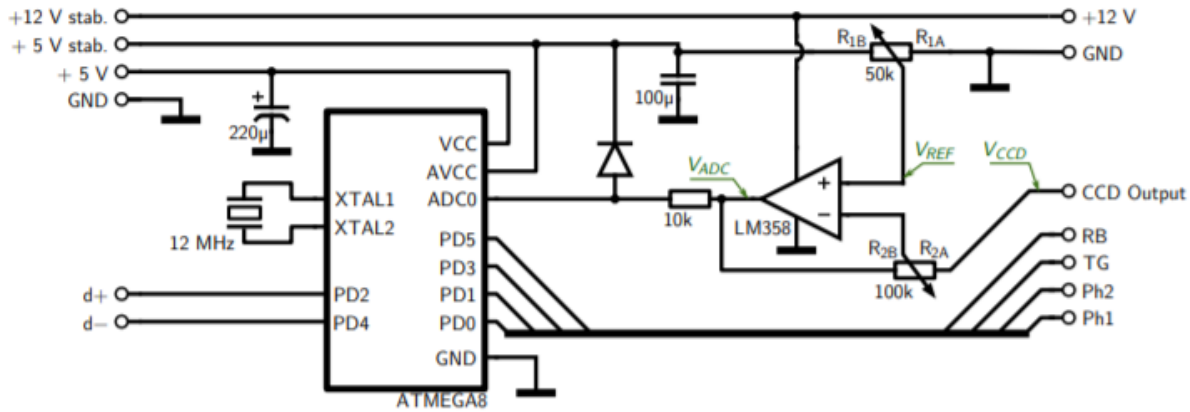


Figure 36: The microcontroller circuit. At its left side it is connected to the supply circuit, at right to the CCD detector

$$\frac{V_{ccd} - V_{ref}}{R_{2A}} = \frac{V_{ref} - V_{adc}}{R_{2B}}$$

and after simple arrangement

$$V_{adc} = \frac{R_{2A} + R_{2B}}{R_{2A}} \cdot V_{ref} - \frac{R_{2B}}{R_{2A}} \cdot V_{ccd}$$

This proves that if not saturated, the operational amplifier performs the desired linear transformation. The voltages do not have to be known precisely, as the potentiometers R1, R2 may be tuned depending on the waveform in computer. The amplification factor should be between 3 and 5. The operational amplifier supply voltage has to be 12 V, which presents a risk of destroying the ADC circuit by excess voltage, as the maximum input voltage of ADC is limited to 5.3 V in this case [3]. In order to prevent this, a 10 kΩ series resistor and a diode with low voltage drop limit the ADC input voltage, as shown at Fig. 10

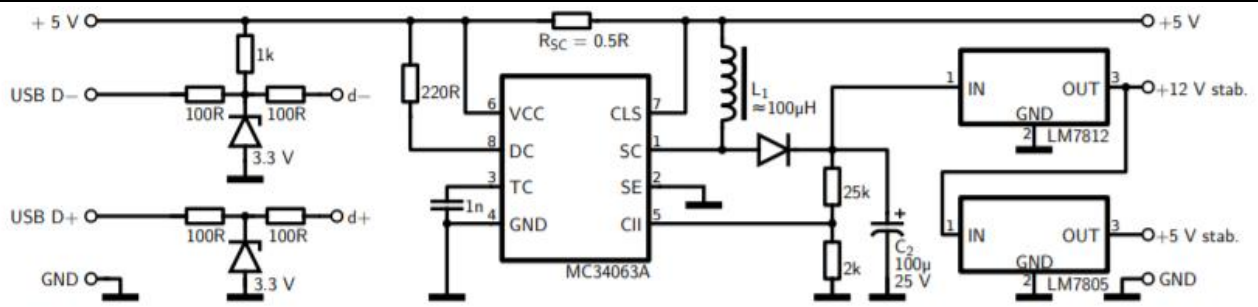


Figure 37: The supply circuit. At its left side it is connected to the computer via USB cable.

### 2.1.2 Supply circuit

The supply circuit converts the noisy 5 V USB voltage supply to stabilized 12 V required by the CCD detector and to additional stabilized 5 V for the ADC. Additionally, it limits the USB signalling levels to 3.3 V as required by the specification [16]. For the voltage conversion, a boost converter integrated circuit MC34063 was used. In short, the circuit senses the output voltage at the CII (comparator inverted input). When the voltage drops below 1.25 V, the SC (switch collector) shorts to ground, letting the current through the L1 coil and Rsc grow. The CLS (current limit sense) voltage drops as the current increases and when the voltage drop exceeds approximately 300 mV, the SC pin closes. The energy stored in the L1 coil creates an impulse of higher voltage that charges the C2 capacitor. The C1 capacitor determines the time interval of operation. The output voltage is given by the voltage divider parallel to the C2. The selected resistances of 25 k $\Omega$  and 2 k $\Omega$  set the minimum C2 voltage to 16 or 17 V. This voltage is limited by the LM7812 and LM7805 stabilizers to 12 V and 5 V, respectively. Reducing the C2 voltage would increase efficiency, but risk of negative ripple in the 12 V stabilized output would be present due to the voltage drop at LM7812. The USB signalling wires D+, D- are connected according to the figure 8.

### 2.1.3 Spectrometer casing

The spectrometer was cased in a black PVC box with dimensions 190  $\times$  90  $\times$  50 mm. About a half of the box is occupied by the optical mount, the rest contains the two circuits. The optical mount is fixed to the front panel by two M3 bolts with head containing a nut, which are common e. g. in older 17 computer connectors. This enables the user to fix some light source or cuvette in front of the input slit (or vice versa, attach the spectrometer onto a bigger device output) easily. These two bolts, as well as whole optical mount, were not connected to the USB ground to prevent accidental short-circuit or ground loop. Although the matt inner side of the plastic box has low reflection itself, the cylindrical mirror and CCD were additionally covered by a folded sheet of black paper to minimize the stray light coming directly from the input slit or any tiny hole left in the plastic case.

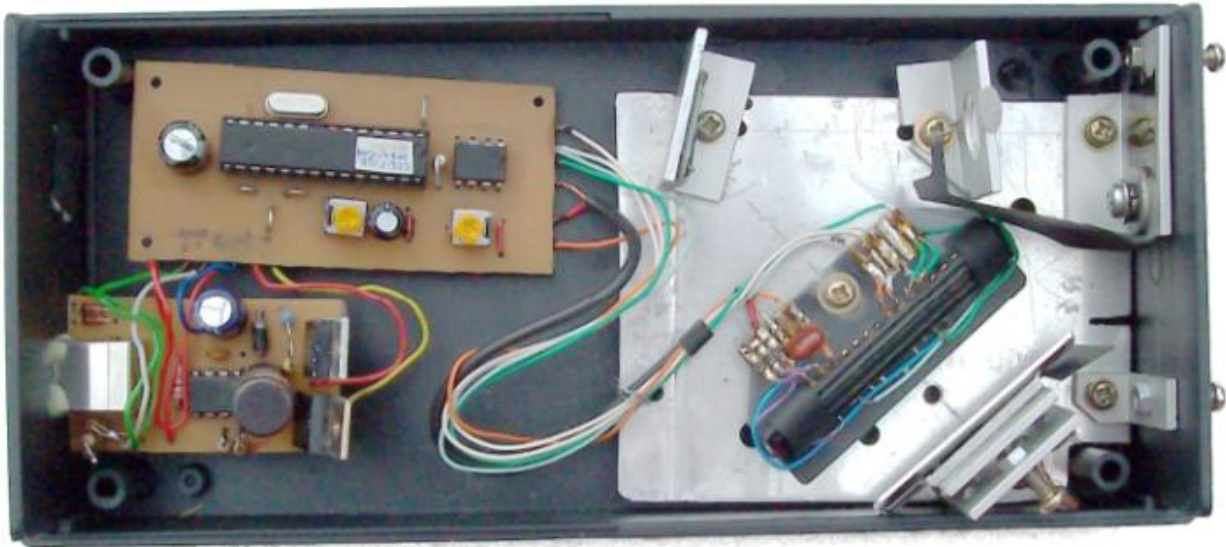


Figure 38: A view of the assembled spectrometer without top cover and paper light shielding. The light passes through the input slit at the top right and follows the path indicated at Fig. 5. At the left, there are the converter and microcontroller circuits and USB output.

Color	Wavelength	Frequency	Photon energy
Violet	380–450 nm	668–789 THz	2.75–3.26 eV
Blue	450–495 nm	606–668 THz	2.50–2.75 eV
Green	495–570 nm	526–606 THz	2.17–2.50 eV
Yellow	570–590 nm	508–526 THz	2.10–2.17 eV
Orange	590–620 nm	484–508 THz	2.00–2.10 eV
Red	620–750 nm	400–484 THz	1.65–2.00 eV

Figure 39:properties of colors

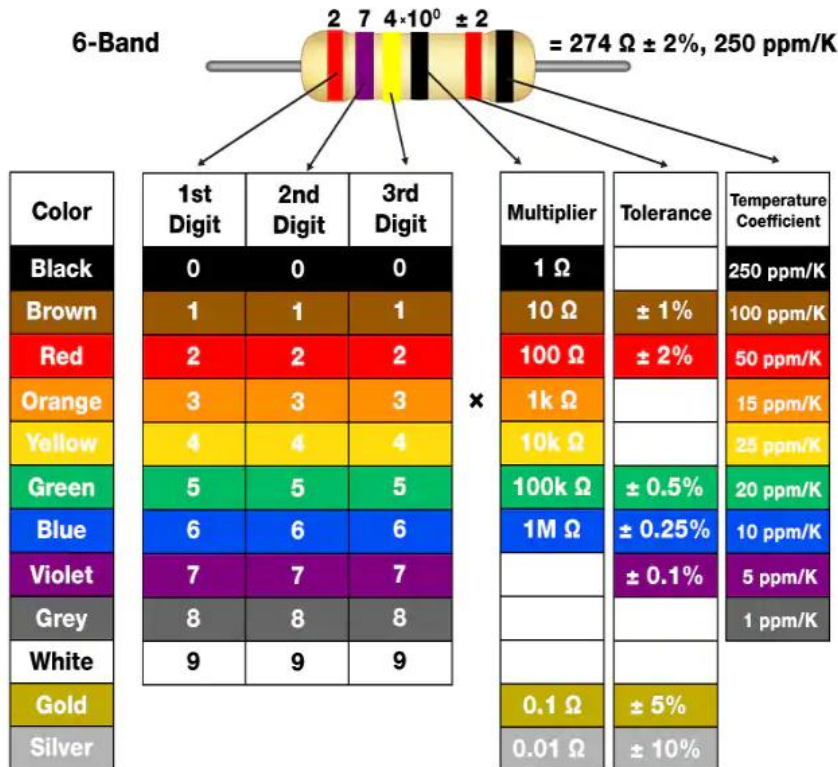
## 2.2 Minimal circuit between USB and microcontroller

1. 10-bit converter
2. microcontroller:ATmega8-16PU(1 kb)
3. Single USB cable :communication
4. converter circuit MC34063
5. 12.000 MHz quartz oscillator.

6. NEC  $\mu$ PD3799 CCD detector (four signal wires are needed: the phase 1 and phase 2 signals, the RB (reset gate) and the TG (transfer gate) signals): silicon CCD ,400-900 nm)
7. LM7812 and LM7805 stabilizers
8. Resistors :25 k $\Omega$  ,2 k $\Omega$ , 1 k $\Omega$  ,100 $\Omega$ (4) ,220  $\Omega$ ,0.5  $\Omega$ ,100k  $\Omega$  ,50 k $\Omega$ ,10k  $\Omega$
9. Capacitor: 100 microF,**100 nF**,220microF
10. Bobine:100microH
11. Zener diodes.:3.3 V(5V),nb=2
12. Circuit MC34063 w

Note :Yellow signifie that it is available in our lab.

### How to Read Resistor Color Codes



### 2.3 Microcontroller firmware

In this section, the full microcontroller firmware written in the C language (except for the USB driver) will be described, as it well illustrates the device function. The code comments were mostly maintained. The microcontroller was programmed via the serial programming interface using a USBAsp hardware programmer and the avrdude program. The firmware code was compiled on Linux (Ubuntu 10.04) in avr-gcc compiler and it was loaded into the microcontroller flash memory with commands:

```

1 avr-gcc -g -Wall -O1 -mmcu=atmega8 -c main.c -o main.o
2 avr-gcc -g -Wall -O1 -mmcu=atmega8 main.o -o main.elf
3 avr-objcopy -j .text -j .data -O ihex main.elf main.hex
4 sudo avrdude -p m8 -c usbasp -U flash:w:main.hex
    
```

To enable the 12 MHz clock, two reserved bytes in the persistent microcontroller memory, called fuses, must be set to hexadecimal values of 0xff for lfuse and 0xd9 for hfuse.

```
1 sudo avrdude -pm8 -c usbas -U lfuse:w:0xff:m -U hfuse:w:0xd9:m
```

During experiments, the fuses have been set wrong several times, which disabled also the serial programming needed to set fuses back. This was fixed by a parallel programming fuse resetting tool

General constants and procedures

**At the beginning, the essential header files from the avr-libc library are included.**

```
1 #include <avr/io.h>
2 #include <avr/wdt.h>
3 #include <avr/interrupt.h>
4 #include <util/delay.h>
5 #include <avr/eeprom.h>
6
7 #include <avr/pgmspace.h>
8 #include "usbdrv/usbdrv.h"
9 #include "usbdrv/oddebug.h"
```

To make the CCD driving routines clear, each CCD pin is referenced by its name from the datasheet instead of a simple port number. The CLB and SHB signals are predefined for the case that a CCD with more complicated driving signals is used. This definition enables to change the connection easily if needed.

```
1 // PORTD pins definition to comply with datasheet
2 #define PH1 BV (PD0)
3 #define PH2 BV (PD1)
4 #define TG123 BV (PD3) // Transfer gates (R+G+B)
5 #define RB BV (PD5) // Reset gate clock
6 #define CLB BV (PD6) // Reset feed-through level clamp clock (disabled)
7 #define SHB BV (PD7) // Sample and hold clock (disabled)
```

The following part contains the USB report descriptor, which is sent when the device is recognized by the computer. Further USB settings are set in the usbdrv.h file which is provided with the USB driver.

```
1 PROGMEM char usbHidReportDescriptor[22] = { /* USB report descriptor */
2     0x06, 0x00, 0xff, // USAGE PAGE (Generic Desktop)
3     0x09, 0x01, // USAGE (Vendor Usage 1)
4     0xa1, 0x01, // COLLECTION (Application)
5     0x15, 0x00, // LOGICAL MINIMUM (0)
6     0x26, 0xff, 0x00, // LOGICAL MAXIMUM (255)
```

```

7      0x75, 0x08, // REPORT SIZE ( 8 )
8      0x95, 0x80, // REPORT COUNT ( 128 )
9      0x09, 0x00, // USAGE ( U n d e f i n e d )
1     0x0b2, 0x02, 0x01, // FEATURE ( Data , Var , Abs , Bu f )
11     0xc0 // END COLLECTION
12 };

```

Here we define further constants: the number of all CCD pixels and the remaining space in memory to save the buffer. The full RAM size of Atmega8 is 1 kB, of which some bytes are occupied by variables and stack and other bytes are required for the USB driver. Approximately 920 bytes remain to store the data buffer in this configuration.

The BufMsrPos and BufBitPtr denote the position in the buffer to write the 10 bits measured by ADC. The latter variable points to the bit at which the value shall be written, as is described later.

The CCDMsrPos variable is incremented after measurement of each pixel to indicate when the CCD has been read out. The BufReadPos stores the position in the buffer which will the data transmission start from. Following variables will be described later.

```

1 # d e f i n e P I X E L S C O U N T 5400
2 # d e f i n e M S R B U F S I Z E 900
3 s t a t i c u n s i g n e d c h a r b u f [ M S R B U F S I Z E ] ;
4 s t a t i c i n t B u f M s r P o s ;
5 s t a t i c c h a r B u f B i t P t r ;
6 s t a t i c i n t C C D M s r P o s ;
7 s t a t i c i n t B u f R e a d P o s ;
8 s t a t i c u n s i g n e d i n t I n t e g r T i m e ;
9 s t a t i c c h a r S t a t u s ; // i n d i c a t e s t h e s t a t u s o f m e a s u r e m e n t o r t r a n s m i s s i o n

```

This procedure creates a short delay of approximately  $2 \mu\text{s} \cdot \text{num}$ . It is needed to hold the minimum timings when driving the CCD.

```

1 v o i d d e l a y ( u n s i g n e d i n t n u m )
2 {
3   u n s i g n e d i n t i , j ;
4   f o r ( j = 0 ; j < 2 ; j ++ )
5     f o r ( i = 0 ; i < n u m ; i ++ )
6 ;
7 }

```

## 2.4 CCD driving

Following three procedures are used to drive the CCD. They may need to be modified if different CCD is used. The first procedure performs one CCD register shift, It both begins and ends in the phase 1 state. A minimum delay of 110 ns is required for each phase [4].

```

1 v o i d C C D S h i f t R e g ( ) // e x p e c t s t h e C C D t o b e i n t h e p h i 2 s t a t e

```



```
2 {
3 PORTD = (PH1); // inverse RB strobe
4 PORTD = (PH1 | RB);
5 delay(0);
6 PORTD = (PH2 | RB);
7 delay(0);
8 }
```

The CCDTransferGate procedure initiates the CCD readout by transferring the charge from the photodiodes. When the transfer gate signal is activated, ten cycles of reset gate strobes are sent to the CCD, as is recommended [4].

```
1 void CCDTransferGate ()
2 {
3   int j;
4   PORTD = (PH1);
5   PORTD = (PH1 | RB);
6   delay(2);
7   for (j=0; j<10; j++) { // transfer gate
8     PORTD = (PH1 | TG123);
9     PORTD = (PH1 | TG123 | RB);
10    delay(1);
11  }
12  PORTD = (PH1 | RB);
13  delay(2);
14  PORTD = (PH2 | RB);
15  delay(1);
16 }
20
```

The FlushCCD procedure first performs several full readouts to drain all excess charge from the CCD (the more sensitivity was set, the more readouts are used). When the CCD was not used for a while, this does not drain the charge at once and several such cycles are needed.

After this, an integration period begins. Its duration is determined by the IntegrTime global variable, as the delay here is accomplished by running the ADC repeatedly each 32 CCD steps. The sampling speed is approximately 10,000 samples per second. Therefore, the IntegrTime value of 32 sets the integration time to half a second. Finally, the CCDTransferGate enables the measurement.

The sensitivity is roughly proportional to the integration time. However, two effects limit the integration time to approximately one second: first, the spectrometer does not respond to USB messages, causing USB timeouts when integrating too long, and secondly, the CCD charge volatility creates a significant background signal. To improve the sensitivity, the CCD would probably have to be cooled by a Peltier element and the integration should be controlled by asynchronous timer. The

best way to detect weak signals in the current setup is to set moderate sensitivity and average multiple spectral measurements.

```

1 void FlushCCD () {
2   int j, i, k;
3   PORTB |= BV (PB0);
4   CCDT ransfe rGate (); // read the CCD to drain all charge
5   for (i=0; i<IntegrTime; i++) {
6     for (j=0; j<PIXELS COUNT; j++) { CCDShi ftReg (); };
7     CCDT ransfe rGate ();
8   }
9   for (j=0; j<PIXELS COUNT; j++) {
10    for (i=0; i<IntegrTime; i++) { // delay loop
11      k++;
12      if (k%32 == 0) {
13        ADCSRA |= BV (ADSC);
14        while (!(ADCSRA & BV (ADIF)));
15        ADCSRA |= BV (ADIF);
16        k = 0;
17      }
18    }
19    CCDShi ftReg ();
20  };
21  CCDT ransfe rGate ();
22  PORTB &= ~ (BV (PB0));
23 }

```

### 2.4.1 USB communication

As noted above, the USB communication is ensured by a software driver by Hans Starkjohann (Objective Development GmbH) [13]. The USB driver has relatively low requirements, as it occupies no more than 1.5 kB of program code. These definition will be used later in the following routines.

```

1 //Spectrometer commands received via USB
2 #define COMMAND SET MEASURE 100
3 #define COMMAND READ CALIB AMPLI 101
4 #define COMMAND WRITE CALIB AMPLI 111
5 #define COMMAND READ CALIB LAMBDA 102
6 #define COMMAND WRITE CALIB LAMBDA 112
7
8 //Status
9 #define STATUS IDLE 0
10 #define STATUS CCD PENDING 1
11 #define STATUS CCD INTEGRATING 2
12 #define STATUS SAMPLING 3

```

```
12 #define STATUS_BUFFER_READY 4
13 #define STATUS_CALIB_READING 10
14 #define STATUS_CALIB_WRITING 11
15 // Room for calibration data in EEPROM
16 #define CALIB_BYTES_PER_POINT 4
17 // EEPROM bytes 9...410 reserved for amplitude calibration data
18 #define CALIB_AMPLI_POINT_NUMBER_MAX 100
19 #define CALIB_AMPLI_BUFPTR 9
20 // EEPROM bytes 411...511 reserved for lambda calibration data
21 #define CALIB_LAMBDA_POINT_NUMBER_MAX 25
22 #define CALIB_LAMBDA_BUFPTR 411
```

The `usbFunctionSetup` procedure is called by the driver always when a read or write packet arrives.

The type of packet can be obtained from the `rq->bRequest` structure.

```
1 usbMsgLen_t usbFunctionSetup(uchar data[8])
2 {
3     usbRequest_t *rq = (void *) data;
4     if ((rq->bmRequestType & USBRQ_TYPE_MASK) == USBRQ_TYPE_CLASS) {
5         if (rq->bRequest == USBRQ_HID_GET_REPORT) {
6             BufReadPos = 0;
7             return USB_NO_MSG; // use usbFunctionRead() to obtain data
8         }
9         else if (rq->bRequest == USBRQ_HID_SET_REPORT) {
10            return USB_NO_MSG; // use usbFunctionWrite() to receive data from host
11        }
12    } else {
13        // ignore vendor type requests, we don't use any
14    }
15    return 0;
16 }
```

The write packet contains data transmitted from the computer. Whereas the `usbFunctionSetup` is called once the packet arrives, the driver calls the following function `usbFunctionWrite` repeatedly, supplying the payload data in 8-byte chunks. All actions of the spectrometer are initiated by an incoming USB message from the computer. The first byte of the message describes the command, as is defined above in the `#define COMMAND...` block. Possible commands are to start spectral measurement, to read or write the wavelength or amplitude calibration. Once a `COMMAND SET MEASURE` message arrives, the spectrometer sets the integration time, flushes the CCD, starts the integration time, samples the data read from the CCD and stores the data in internal buffer. These steps can take up to several seconds and would cause USB timeout error if they were all done within the `usbFunctionWrite` procedure. Instead, only the Status variable is set here to `STATUS CCD PENDING` and all mentioned tasks are performed later in the main loop. The `COMMAND READ CALIB AMPLI` and `COMMAND READ CALIB LAMBDA` both set the Status variable into the

STATUS CALIB READING. The difference is in the initial EEPROM pointer value only.

```

1 static uchar   EEPROMPtr;
2 static uchar   CalibDataPointNumber;
3 static uchar   bytesRemaining;
4 uchar   usbFunctionWrite(uchar *data, uchar len)
5 { // Longer tasks may not be handled here. Instead, set the Status variable and
   // perform them in the main routine later.
6   if (Status == STATUS_CALIB_WRITING) {
7     if (bytesRemaining == 0)
8       return 1; // end of transfer
9     if (len > bytesRemaining) {
10      len = bytesRemaining;
11      Status = STATUS_IDLE;
12    }
13    eeprom_write_block(data, (uchar *)0 + EEPROMPtr, len);
14    EEPROMPtr += len;
15    bytesRemaining -= len;
16    if (bytesRemaining == 0) {
17      Status = STATUS_IDLE;
18      return 1; // return 1 if this was the last chunk
19    } else return 0;
20  }
21  // if first chunk of USB message, decide the command from the 1st byte
22  if (Status == STATUS_IDLE)
23    switch (data[0]) {
24      case COMMAND_SET_MEASURE: {
25        // if not zero, the two bytes set the sensitivity (integration time):
26        if (data[1]+data[2] != 0) {IntegrTime = data[1]*256 + data[2];};
27        Status = STATUS_CCD_PENDING;
28        return 1; // no additional data required
29        break;
30      }
31      case COMMAND_READ_CALIB_LAMBDA:
32      case COMMAND_READ_CALIB_AMPLI: {
33        // decide which memory location will be read
34        if (data[0] == COMMAND_READ_CALIB_AMPLI) {
35          EEPROMPtr = CALIB_AMPLI_BUFPTR;
36        } else {
37          EEPROMPtr = CALIB_LAMBDA_BUFPTR;
38        }
39        // number of points to be read
40        eeprom_read_block(&bytesRemaining, EEPROMPtr, 1);
41        bytesRemaining=bytesRemaining*CALIB_BYTES_PER_POINT+1;
42        Status = STATUS_CALIB_READING;
43        // no additional data required:
44        return 1;
45        break;
46      }
47      case COMMAND_WRITE_CALIB_LAMBDA:
48      case COMMAND_WRITE_CALIB_AMPLI: {
49        // number of points to be written
50        bytesRemaining = data[1]*CALIB_BYTES_PER_POINT;
51        if (data[0] == COMMAND_WRITE_CALIB_AMPLI) {
52          EEPROMPtr = CALIB_AMPLI_BUFPTR;
53        } else {
54          EEPROMPtr = CALIB_LAMBDA_BUFPTR;
55        }
56        // 1st byte of EEPROM block stores number of points:
57        eeprom_write_block(data+1, EEPROMPtr, 1);
58        EEPROMPtr++;
59        Status = STATUS_CALIB_WRITING;
60        // last 6 B of this chunk discarded, next chunk will contain data
61        return 0;
62        break;
63      }
64    }
65  }
66 }

```

The `usbFunctionRead` function is called when the computer asks the spectrometer for measured data. Naturally, the action depends on the `Status` variable: if the spectrometer finished the measurement recently, the spectral data are sent; if the microcontroller was requested for its calibration data, the corresponding EEPROM block is sent. Otherwise, no action is performed and the function returns 0 to indicate that no more data are available.

The USB specification limits the payload data length to 8 bytes for USB low-speed devices; however this would make the communication slow. Therefore, an extended length of packet up to the buffer size is used. This bigger size of packets is common for high-speed devices and it has been tested to work flawlessly, enabling to quickly transport the whole buffer in a single USB message.

```
1 uchar  usbFunctionRead(uchar *data, uchar len)
2 {
3     if (Status == STATUS_IDLE) {           // no command set
4         return 0;
5     }
6     if (Status == STATUS_BUFFER_READY) {   // Transmit the buffer with
7         spectrum to the computer.
8         if (len > (BufMsrPos - BufReadPos - 1)) { // buffer will be depleted, read
9             the left bytes
10            len = (BufMsrPos - BufReadPos);
11            if (CCDMsrPos < PIXELS_COUNT) {Status = STATUS_SAMPLING; BufBitPtr = 0;
12                BufMsrPos = 0;}
13            else {Status = STATUS_IDLE;};
14            BufMsrPos = 0;
15        }
16        int DataPos;
17        for (DataPos=0; DataPos<(len); DataPos++) {
18            data[DataPos] = buf[BufReadPos + DataPos];
19            buf[BufReadPos + DataPos] = SENT_BUF_STUFF;
20        };
21        BufReadPos += len;
22        return len;
23    }
24    if (Status == STATUS_CALIB_READING) {   // transmit the calibration data
25        from EEPROM
26        if (len > bytesRemaining) {
27            len = bytesRemaining;
28            Status = STATUS_IDLE;
29        }
30        eeprom_read_block(data, (uchar *)0 + EEPROMPtr, len);
31        EEPROMPtr += len;
32
33        bytesRemaining -= len;
34        return len;
35    }
36    return 0;
37 }
```

---

## 2.5 The main loop

This loop is called after the microcontroller starts and its clock stabilizes. During this loop the microcontroller continuously polls the USB driver for incoming packets, which is required to ensure reliable communication, and performs the action the `Status` variable describes. After the CCD readout is finished, the `Status` variable is finally set to the `STATUS_BUFFER_READY` value. In a consequent read request from computer, the spectrometer sends the data in one or more USB packets and `Status` is set back to `STATUS_IDLE`

```

1 int main(void)
2 {
3   DDRB |= _BV(PB0) | _BV(PB1); DDRD |= (TG123 | PH1 | PH2);   DDRD |= (RB | CLB |
4     SHB); // enable output pins
5   ADMUX = 0; ADCSRA |= _BV(ADEN) | _BV(ADPS2) | _BV(ADPS2); // A/D converter
6     settings
7   odDebugInit(); usblnit(); usbDeviceDisconnect(); // enforce re-
8     enumeration
9   unsigned char i; i = 0; while(--i){wdt_reset(); _delay_ms(5); } // fake USB
10    disconnect for > 250 ms
11   usbDeviceConnect(); sei();
12   IntegrTime = 1;
13   BufMsrPos = 0;
14   CCDMsrPos = 0;
15   Status = STATUS_IDLE;
16   for(;;){
17     usbPoll();
18     int j;
19     int MeasPerPoll = 1;
20     int PixPerMeas = 8; // buffer capacity: 900 B = 7200 b = 720 px; 5400 pix
21       /8 = 675 pix
22     if (Status == STATUS_CCD_PENDING) {
23       Status = STATUS_CCD_INTEGRATING;
24       // erase buffer
25       int i; for (i=0; i<MSR_BUF_SIZE; i++) {buf[i] = EMPTY_BUF_STUFF;};
26       FlushCCD();
27       BufBitPtr = 0;
28       CCDMsrPos = 0;
29       BufMsrPos = 0;
30       Status = STATUS_SAMPLING;
31     }
32     if (Status == STATUS_SAMPLING)
33       for (j=0; j<MeasPerPoll; j++)
34         if (CCDMsrPos < PIXELS_COUNT) {
35           if (BufMsrPos < (MSR_BUF_SIZE-1)) {
36             unsigned int value = 0;
37             for (i=0; i<PixPerMeas; i++) {
38               CCDSHiftReg(); CCDMsrPos += 1;
39
40               ADCSRA |= _BV(ADSC);
41               while (!(ADCSRA & _BV(ADIF)));
42               ADCSRA |= _BV(ADIF);
43               // 10 bits ADC input, always read ADCL first
44               value += ADCL + 256*(ADCH&3);
45             }
46             // average from several measurements
47             value = value / PixPerMeas;
48             char BitNumber = 10;
49
50             // remove leading zeros
51             unsigned int svalue = value << (16 - BitNumber);
52             int ValBitPtr = 0;
53             // compresses 4 pixels * 10 bits to 5 bytes
54             while (ValBitPtr < BitNumber) {
55               int ChunkLen = 8 - BufBitPtr;
56               if (ChunkLen > BitNumber - ValBitPtr) {ChunkLen = BitNumber -
57                 ValBitPtr;};
58               unsigned char Chunk = ((svalue << ValBitPtr) >> BufBitPtr) >>
59                 8;
60               unsigned char Mask = ~(0xFF >> BufBitPtr);
61               buf[BufMsrPos] = (buf[BufMsrPos] & Mask) | (Chunk & 0xFF);
62               ValBitPtr += ChunkLen; BufBitPtr += ChunkLen;
63               if (BufBitPtr >= 8) {BufBitPtr -= 8; BufMsrPos++;}
64             }
65           } else {
66             BufBitPtr = 0;
67             Status = STATUS_BUFFER_READY; // buffer full, wait until the
68               computer reads the data
69           }
70         } else {
71           Status = STATUS_BUFFER_READY; // whole CCD read, wait
72         }
73     }
74   }
75   return 0;
76 }

```

The used CCD detector had much more pixels than the microcontroller could hold in the buffer at once.

Although full CCD data could be read and transmitted sequentially, this was problematic due to the sawtooth bias. The need to fit the full CCD readout into the 7200 bits long buffer has lead to these two measures:

1. As the microcontroller has a 10-bit analog-to-digital converter, the measured values are compressed on the fly so that each value does not occupy 16 bits as in an integer, but only the significant 10 bits. Theoretically, the 7200 bit buffer can hold 720 measured points.
2. The total pixel number was 5400. Dividing this by 8 we obtain 675 measured points, which fits the buffer the best. Accordingly, eight pixels were read sequentially and then averaged.

This reduced the noise significantly, but did not spoil the spectral accuracy much, because the optical imprecision manifested even in the reduced pixel number.

## 2.6 Computer software

The software in computer was split into two programs:

1. the backend ensures communication with the spectrometer and transforms the data according to the wavelength and amplitude calibration,
2. and the frontend, which provides graphical user interface and, calling the backend repeatedly, presents the measured spectra in real time.

### 2.6.1 Command line backend for USB communication

The backend is written in C, compiled using the Gnu Compiler Collection (gcc, version 4.4.3). It was developed and tested under Linux 2.6, but it is designed to compile and run under Windows and other operating systems, too. Under Linux, the backend depends on libusb, on Windows it depends on the Driver Development Kit (DDK), which should be shipped along with MinGW compiler [13]. The full code is included in the attached CD and it will not be listed here. The commandline backend accepts several commands. The first parameter determines the action performed and optional parameters are in square brackets:

1. set measure [integration time] starts the measurement, integration time ranges from 1 to approx. 200
2. get spectrum receives, transforms and writes out the spectrum to the stdout
3. write calib ampli lambda1:amplitude1,[lambda2:amplitude2,...] write amplitude calibration to the EEPROM
4. write calib lambda pixel1:lambda1,[pixel2:lambda2,...] write wavelength calibration
5. read calib ampli [--short] reads amplitude calibration from the EEPROM
6. read calib lambda [--short] write wavelength calibration Usually the get spectrum command is called soon after the set measure was called. (These commands

do never have to be joint together into one command, as the spectrometer requires about half a second to measure the spectrum and much longer wait periods can occur if longer integration time is needed.

Such single command would halt the backend from responding. This would consequently either cause the frontend not to respond for a while or it would require to implement multiple threads.)

The calibration write commands use the second parameter to set the calibration points in the EEPROM. Each calibration point occupies 4 bytes in the EEPROM. See the README file for more information.

For wavelength calibration, pairs of pixel number and corresponding wavelength in picometers have to be input in the format of pairs of integers related by colon and separated by comma. First two bytes are the integer position of the pixel. Following two bytes are the wavelength divided by 32 pm. Therefore, the wavelength of  $221 = 2,097,152$  pm is encoded as the maximum integer value  $216 = 65,536$ .

For amplitude (i. e. sensitivity) calibration, the pairs of wavelength and corresponding coefficient are used, as the sensitivity curve mostly depends not on the optical geometry, but rather on the averaged spectral sensitivity of the three CCD channels. If the projected image moves slightly, only the wavelength calibration would have to be repeated. The wavelength and the coefficient are calculated similarly as above.

### 2.6.2 Data preprocessing according to calibration

Once the data are received in the compressed raw form, they are read sequentially to convert each 10 bits to a new integer that can be dealt with easier. For each measured point, the wavelength is calculated with spline interpolation of the calibration points.

Then, the calculated wavelength is input to the second spline interpolation, which calculates the sensitivity coefficient for the given wavelength and divides the measured data by this coefficient. The spectrum is output to stdout with two columns of tab-separated numbers, and usually this output is redirected into a file. This form of communication does not cause much holdup, because the file is stored in the disk cache and possibly does not get written to the disk until it is read by frontend and rewritten by new measurement.

### 2.6.3 Python module backend

Two versions of the backend were written: one as a standalone binary operated from command line, the second is a python module, which can be loaded dynamically into the running python program. The graphical user interface uses this module. The functions provided by the backend module are nearly the same, except for not existing equivalent for the get spectrum parameter. The SetMeasure function not only starts the measurement, but also receives the spectrum, performs calibration transformation and return it as two lists of wavelenghts and corresponding values.

### 2.6.4 Graphical user interface

Unlike the firmware and backend, the graphical frontend was written in the Python language with Gtk widgets. Python is an interpreted language with simple syntax and many advanced features. Its



great advantage is the number of additional modules, which facilitate various tasks. Among others, the numpy and scipy modules were included to perform mathematical operations, matplotlib to plot the interactive, antialiased graphs and gtk python module to build the graphical user interface. The gtk libraries are a widget toolkit often used to create multiplatform graphical applications. The gtk libraries are commonly installed on Linux desktops by default, under Windows, one has to download and install them. Both python and gtk are released under free licenses compatible with GPL [7], [15]. Thanks to this, all the software equipment of the spectrometer can be distributed without any license costs.

The graphical user interface provides only basic functions as for now (see next Fig). It allows to switch between manual spectral measurement and automatic measurement, which runs the spectrometer repeatedly when the previous spectrum was acquired and displayed. The Sensitivity slider at the top sets the integration time to be two on the power of the value set. The most practical values are between 2 and 5. Averaging can be set either to the moving average of 2 to 64 waveforms, or to average infinitely to suppress the sampling noise ppress the sampling noise. There is an option to calibrate the amplitude, which is the most important for measurement of a transmittance  $T(\lambda)$  of a sample. The calibration curves are stored in the computer memory. The spectrometer should be recalibrated always when the light source changes. It is recommended that

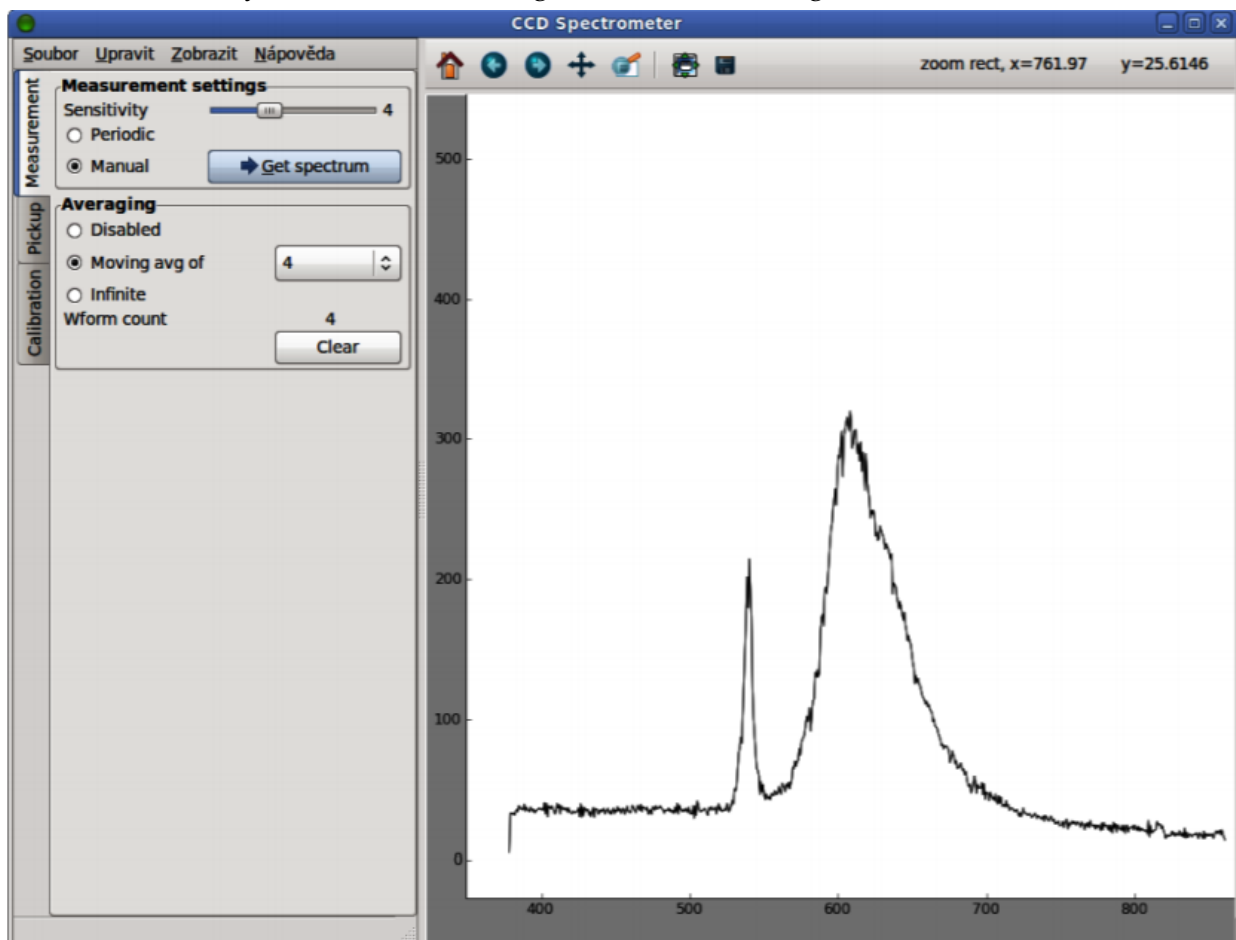


Figure 40: A screenshot of the graphical user interface, showing the orange-red fluorescence of a highlighter pen illuminated by a green laser pointer, whose reflection manifests as the narrow peak at 532 nm. Note also the weak component at  $\approx 810$  nm coming from the laser diode pumping the Nd:YVO<sub>4</sub> crystal

after several minutes of CCD warm up, the source is turned off and the dark signal calibration curve  $I_D(\lambda)$  is set, then the source is turned on again without the sample and the full signal curve  $I_F(\lambda)$  is set. Long averaging time improves accuracy. When the amplitude calibration is applied to the measured signal  $I_M(\lambda)$ , the transmission  $T(\lambda)$  is calculated the following way:

$$T(\lambda) = \frac{I_M(\lambda) - I_D(\lambda)}{I_F(\lambda) - I_D(\lambda)},$$

i. e., the dark signal curve  $I_D$  is subtracted first, then the remaining extra signal is divided by the source intensity at given wavelength. To suppress noise, an intensive and broadband source, such as focused halogen bulb, is needed.

Thanks to the interactive interface of the matplotlib package, the graph may be zoomed and panned, as well as easily exported into a bitmap file.

### 2.6.5 Calibration

The calibration procedure consists of two steps, that shall be done in the following order: the wavelength and the amplitude calibration.

For the wavelength calibration, a common compact fluorescent lamp (CFL) may be used. Such lamp contains diluted inert gas and mercury vapor and at the inner surface, a thin fluorescent layer of europium and terbium salts is sputtered. The output spectrum consists of many spectral lines

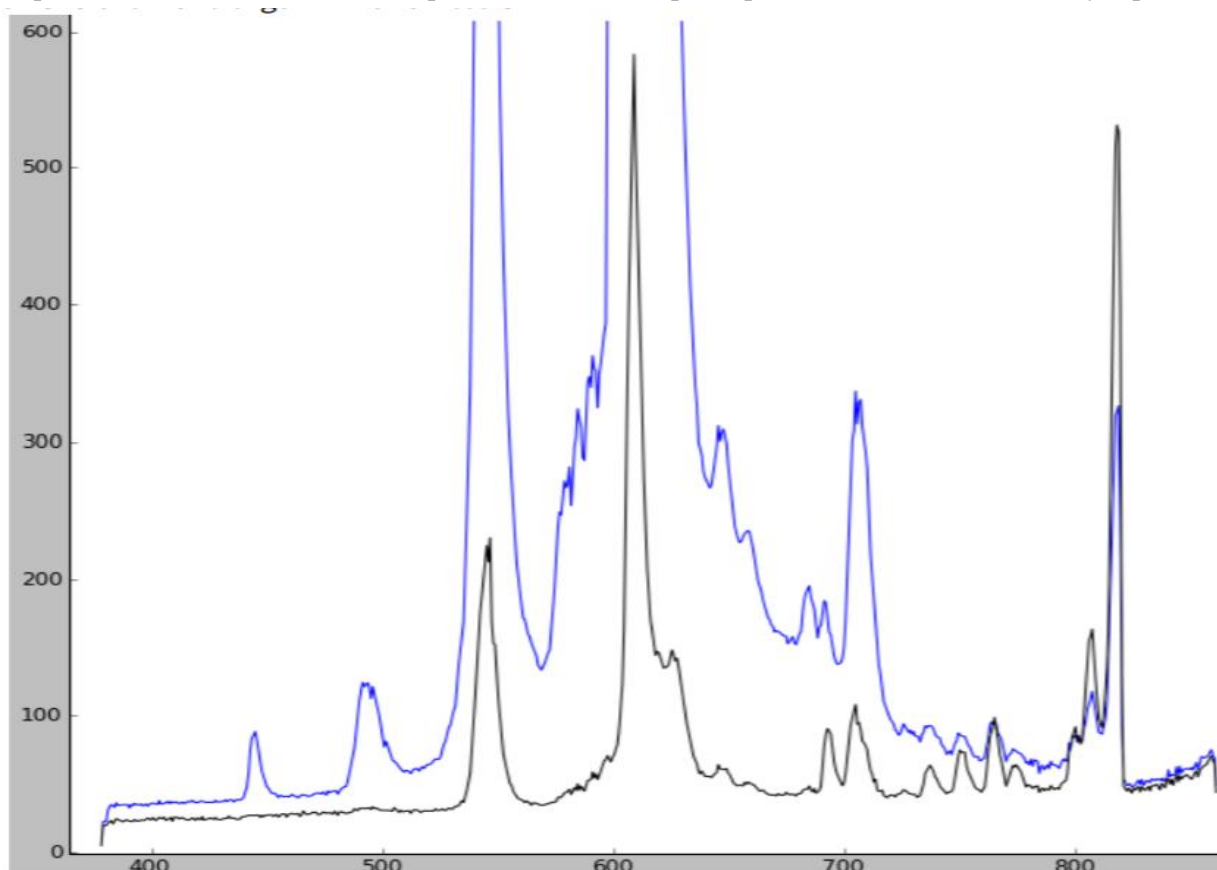


Figure 41: Emission of a compact fluorescent lamp, 5 s after cold start (black) and  $\approx 60$  s later (blue). The horizontal axis is the wavelength in nanometer

with different intensity and width, of which the most intensive are listed in the Table 2. The spectrum was first acquired without calibration, then the peaks were easily resolved and corresponding

calibration points were saved. As noted above, the backend uses spline interpolation/extrapolation and accordingly even for three distant enough calibration points it was possible to obtain reasonable spectral accuracy. The amplitude calibration requires a source of a broad and known spectrum. Possible candidates are a halogen bulb or common daylight. Similarly as for the wavelength calibration, several calibration points shall be calculated from the shape of uncalibrated spectrum. The value of each point is obtained as a ratio of the measured intensity to the expected real intensity of the source. It must be noted that the amplitude calibration does not take into account the linear background. This background depends on CCD temperature and sensitivity. Therefore, the background transforms to a curve that may not be easily visually subtracted without previous observation of its shape for zero input light. Additionally, it was observed that the spectrometer sensitivity varies by several percent from pixel to pixel. This can be accounted to irregularities of the cylindrical mirror or the CCD detector. Unfortunately, the corresponding compensation curves would not fit into the internal EEPROM of the microcontroller. Both unwanted effects must be compensated in the graphical user interface as the amplitude calibration curves for a particular device and light source.

*Table 2: List of the CFL spectral lines used for the wavelength calibration [17]*

Color	Origin	Peak wavelength [nm]
Dim violet	Mercury	404
Dim blue	Mercury	436
Turquoise	Terbium	485 to 490
Green doublet	Terbium and Mercury	544, 546
Red	Europium	611
Near infrared	Argon	811

## 2.7 Results

In this section, several measured spectra will be presented to illustrate the performance and shortcomings of the current design. In the Figure 11, the spectra of a starting 15 W IKEA compact fluorescent lamp is shown. This lamp was used to calibrate the spectrometer. The spectrum has been averaged from 16 measurements to suppress the noise and no amplitude calibration was used here. Initially, the argon filling emits mostly in the near infrared region. The slow start is probably caused by slow evaporation of the mercury filling, which manifests as growth of the spectral lines in visible region. Note that on the contrary, some lines intensity drops during the start. With longer averaging and proper zoom, several other lines may be resolved, such as the weak violet mercury line at 406 nm. Both the blue mercury line at 436 nm and the infrared argon line at 811 nm are emitted by diluted gas and are therefore narrow enough to assess the spectral resolution. The spectrometer measured their width at half maximum as 5 to 8 nm, which can be considered to be the maximum spectral resolution of the device. However, with proper zoom, the green peak at the 544 to 546 nm has a shallow, yet stable notch in its center. This may be accounted either to the nonuniformity of CCD response, or to the fine resolution of spectra. (Both is possible as the convolution function is probably not gaussian, but has a sharp peak instead.) The Figure 12 depicts three spectral curves measured by

passing an incandescent bulb light through a 10 mm long cuvette with pure water and two different concentrations of potassium permanganate ( $\text{KMnO}_4$ ). In low concentration, the very strong absorption in the green spectral region causes the pink tint of the solution. In higher concentration, broader spectral region from 450 to 650 nm gets absorbed. This explains the visible hue difference of different concentrations. The amplitude growth in unabsorbed regions is caused by the cuvette displacement. In this measurement, the amplitude calibration did not correct the pixel-to-pixel nonuniformity, although the spectrum was averaged from 16 measurements again. For practical application, the proper calibration for the particular source and fixed cuvette position is important.

## 2.8 Conclusion

In the above sections, a concept of a cheap, compact digital spectrometer was presented. If a CCD detector from an old scanner is used, the components cost less than 20 Euro. (A new suitable CCD can be obtained for under 10 Euro if a bigger package is requested.) The work per each next piece can be expected to be less than 5 hours, since the first prototype is tested and both the software and firmware are ready.

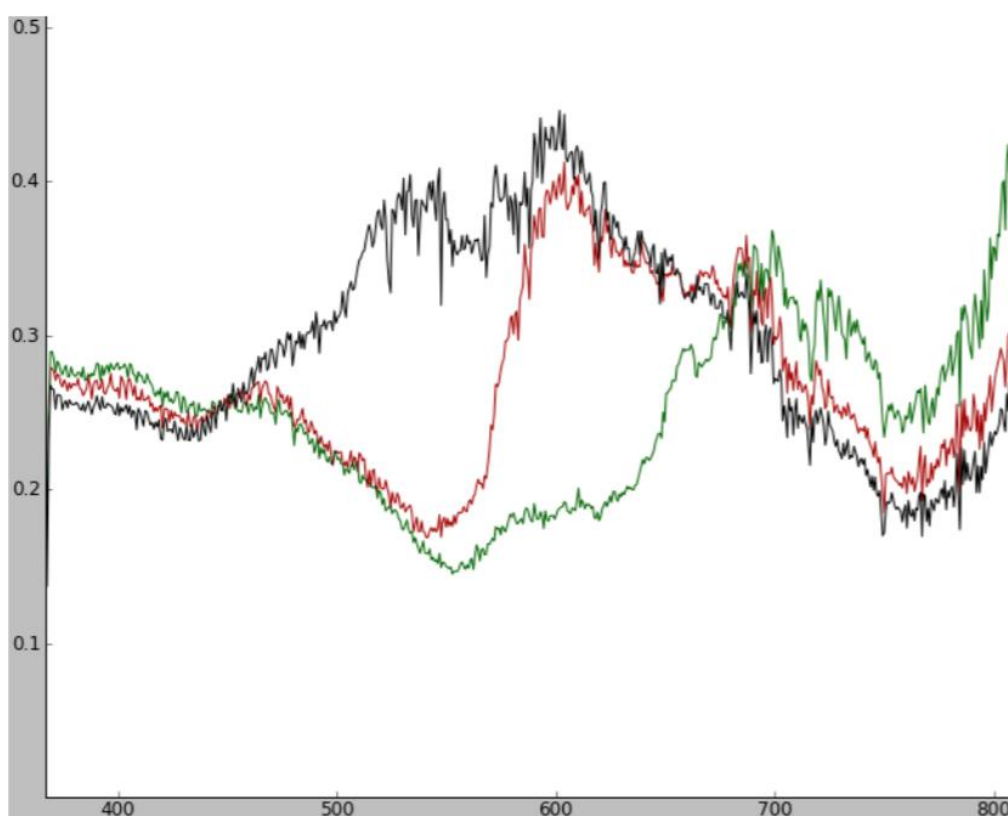
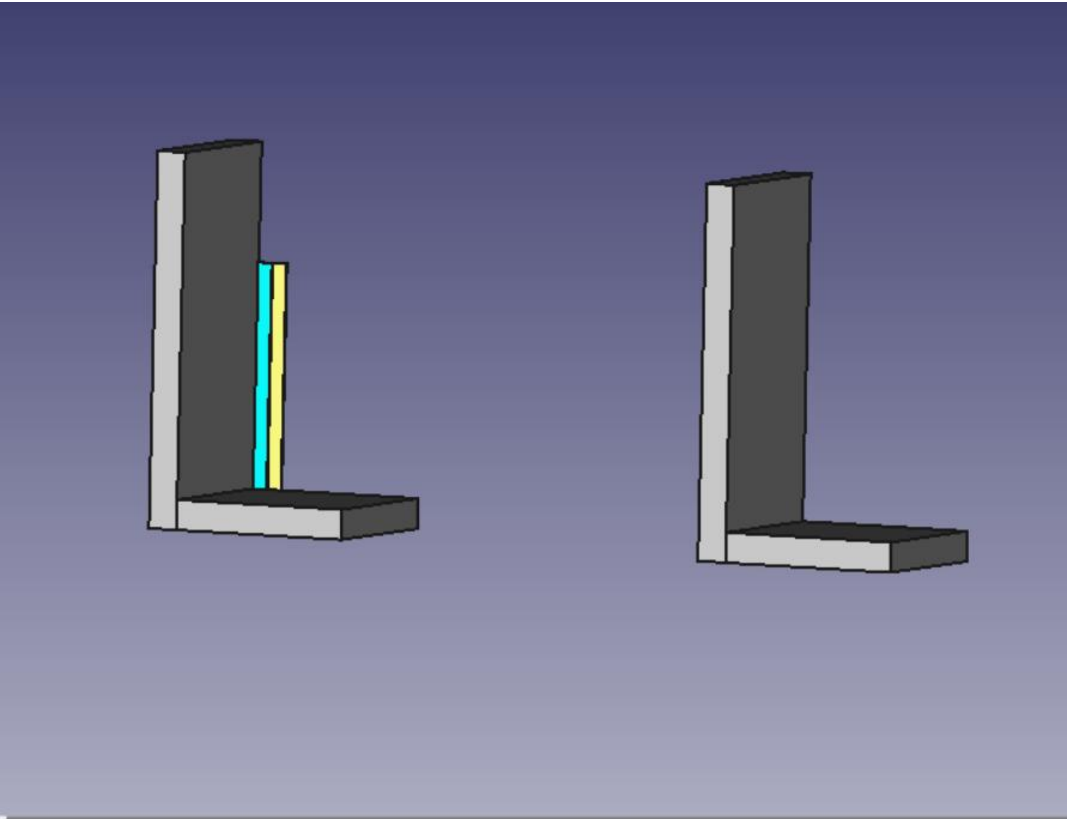
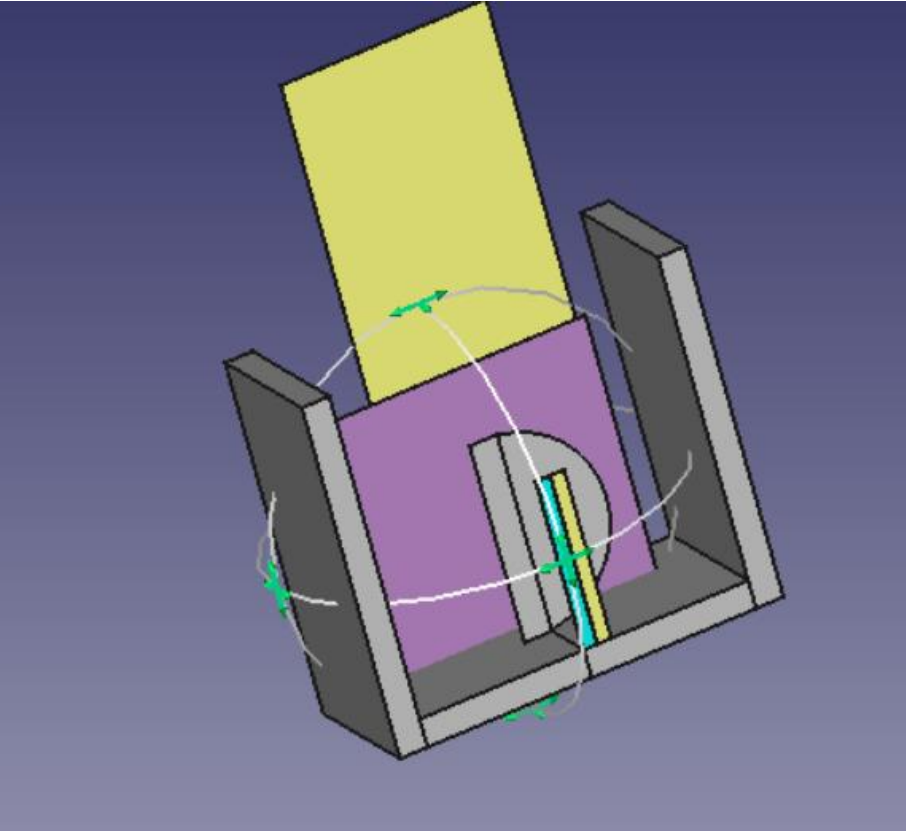


Figure 42: Transmission of pure water (black line); of water with  $\approx 10 \mu\text{mol/l}$  solution of  $\text{KMnO}_4$  (red line) and of water with  $\approx 100 \mu\text{mol/l}$  solution thereof (green line). The horizontal axis is the wavelength in nanometers

in the Results section it was shown that such device works with sensitivity and resolution acceptable for many tasks both in education and research. The graphical user interface makes the device relatively easy to work with. The main conclusion of this work is that it is possible to build a relatively usable, cheap and portable digital spectrometer.



# 3 Design of IAP-OSM

It was decided to use a already existing arduino kit for IAP-OSM.



بِسْمِ اللَّهِ الرَّحْمَنِ الرَّحِيمِ



## Spectroscopy for Visual Data

### 1-Definition of spectroscopy

Spectroscopy is the study of the interaction between matter and electromagnetic radiation. Historically, spectroscopy originated through the study of visible light dispersed according to its wavelength by a prism. Later the concept was expanded greatly to include any interaction with radiative energy as a function of its wavelength or frequency.



التحليل الطيفي هو دراسة التفاعل بين المادة والإشعاع الكهر ومغناطيسي. تاريخياً ، نشأ التحليل الطيفي من خلال دراسة الضوء المرئي المشتت وفقاً لطول الموجة ، بواسطة المنشور. في وقت لاحق تم توسيع المفهوم إلى حد كبير ليشمل أي تفاعل مع الطاقة الإشعاعية كدالة لطول الموجة.

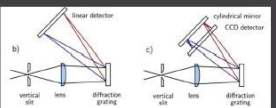
### 2-Spectrometer

A spectrometer is a scientific instrument used to separate and measure spectral components of a physical. The capability of spectroscopy to determine chemical composition drove its advancement and continues to be one of its primary uses. Much of our knowledge of the chemical makeup of the universe comes from astronomy.

المطياف هو أداة علمية تستخدم لفصل وقياس المكونات الطيفية. بمثابة قدرة التحليل الطيفي لتحديد التركيب الكيميائي الأساسية الكثير من معرفتنا للتركيب الكيميائي للكون يأتي من دراسة معرفة الأطياف.

### 3-Principle:

In the horizontal plane, the incoming light must be spatially limited by a vertical slit. Then the spatial limitation is converted to angular limitation using a concave mirror or a convex lens. Ideally, we obtain a parallel beam of white light. Its width is limited either by the size of the mirror or lens used, of by the angle of the beam passing through the slit. The light components of different wavelengths separate after being reflected into different angles by a diffraction grating, delivered to the CCD. Finally, the angular separation might be converted back to spatial separation using another lens or mirror. However, this would require a big lens with diameter similar to the length of CCD. The spatial difference would be proportional to its focal length, probably resulting in a small spatial separation.



### 4.The charge coupled device, CCD:

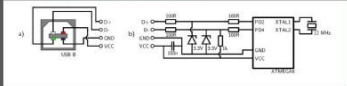
was originally designed not to be an optical detector, but a memory instead. It should work as an analog shift register, storing arbitrary charge in each of its cells and reading them sequentially. Soon it was discovered that illumination causes internal photoelectric effect in the silicon substrate and fills up each memory cell with additional charge proportional to the incident light intensity.



Although CCD was rarely used as a memory, it found widespread application as a sensitive optical detector both in consumer electronics and in high-end scientific instruments such as astronomical telescopes. It should use NEC µPD3799 CCD detector.

### 3-Electronic setup

A common microcontroller: The Atmega8-16PU version has 28 pins, of which 4 were occupied by DC supply, 2 by USB, 2 by oscillator, 4 by CCD driving signals and one for ADC input. The most demanding task is the USB communication.



The microcontroller should be equipped by a sufficient internal analog-to-digital converter (ADC). Many contemporary microcontrollers have an internal 10-bit converter able to perform at least 10,000 samples per second, which is sufficient for this application. The microcontroller was programmed via the serial programming interface using a USBasp hardware programmer and the avrdude program. The firmware code was compiled on Linux (Ubuntu 10.04) in avr-gcc compiler and it was loaded into the microcontroller flash memory with commands.

### Properties of colors

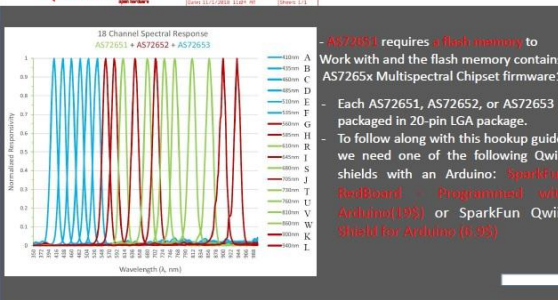
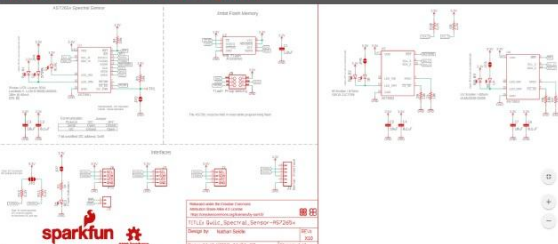
Color	Wavelength	Frequency	Photon energy
Violet	380-450 nm	668-789 THz	2.75-3.26 eV
Blue	450-495 nm	606-668 THz	2.50-2.75 eV
Green	495-570 nm	526-606 THz	2.17-2.50 eV
Yellow	570-590 nm	508-526 THz	2.10-2.17 eV
Orange	590-620 nm	484-508 THz	2.00-2.10 eV
Red	620-750 nm	400-484 THz	1.65-2.00 eV

### 6-Materials for optical setup

1. A standard aluminium L-profile 25 mm high, 2 mm thick and with 12 mm long foot.
2. The input slit was made of two razor blade segments, 15 mm long.
3. The collimating lens had 14 mm diameter, focal length  $f \approx 30$  mm, Plano-convex geometry.
4. The cylindrical mirror was obtained from a scrap photocopier. It is a polished metal rectangle, 42x15 mm in size. Its focal length is approximately 30 mm.
5. a blazed diffraction grating with 500-1000 grooves/mm, with size at least 8x8 mm.

### 7-Schematic of SparkFun Triad Spectroscopy Sensor - AS7265x (Qwiic)

AS7265x Multispectral Chipset consists of AS72651, AS72652, and AS72653 devices and each device has 6 optical filters so that AS7265x Multispectral Chipset have total 18 channels for spectral identification from 400nm to 1000nm with FWHM of 20nm. AS72651 is the main device with the smart interface to a microcontroller. The microcontroller gets the sensors data including AS72652 and AS72653 through AS72651 AT commands or I2C register.



- AS72651 requires a flash memory to work with and the flash memory contains AS7265x Multispectral Chipset firmware.
- Each AS72651, AS72652, or AS72653 is packaged in 20-pin LGA package.
- To follow along with this hookup guide, we need one of the following Qwiic shields with an Arduino: SparkFun RedBoard - Programmed with Arduino(195) or SparkFun Qwiic Shield for Arduino (p.95)

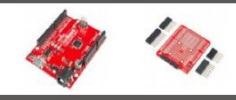
### 8-Software Design Considerations

In most of system designs, AS72651 is controlled by a microcontroller. With the UART interface, the controller could configure the devices and get the sensors data through some AT commands. The software of microcontroller design would be simple.

The following sections would focus on I2C interface and the software of microcontroller design should satisfy both I2C specification and AS7265x Multispectral Chipset register structure.



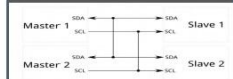
- Accessories:
- Qwiic Cable - Breadboard Jumper (4-pin) \$1.50
  - Qwiic Cable - 100mm \$1.50
  - SparkFun Qwiic Shield for Arduino \$6.95
  - SparkFun Qwiic HAT for Raspberry Pi \$5.95
  - SparkFun Qwiic Mux Breakout - 8 Channel (\$11.95)



### 9-Arduino

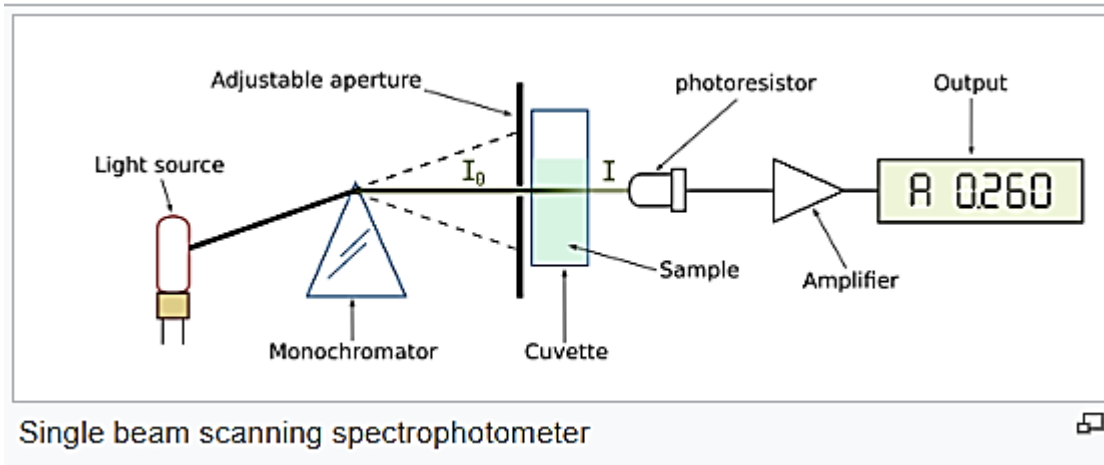
- A computer (Windows, Mac, or Linux)
- An Arduino-compatible microcontroller (anything from this guide should work)
- A USB A-to-B cable, or another appropriate way to connect your Arduino-compatible microcontroller to your computer
- I-installing Arduino IDE <https://www.sparkfun.com/blog/arduino-ide-installation>
- 2-The Inter-integrated Circuit (I2C) Protocol is a protocol intended to allow multiple "slave" digital integrated circuits ("chips") to communicate with one or more "master" chips. Like the Serial Peripheral Interface (SPI), it is only intended for short distance communications within a single device. Like Asynchronous Serial Interfaces (such as RS-232 or UARTs), it only requires two signal wires to exchange information.

AS7265x Qwiic Interface: The sensors are 3.3V compatible so don't use with a 5V Arduino Uno without proper conversion (use the Qwiic shield instead!). If you're using a 3.3V development platform that doesn't have a Qwiic connector, consider using the Qwiic Breadboard Cable.



### 3.1 Optical Setup

This project aims to design, develop and build a compact digital spectrometer. The spectrum is projected with a diffraction grating on a CCD detector, sampled in a 10-bit A/D converter to the microcontroller memory and finally transmitted to the computer via USB. In the computer it is digitally processed and displayed in a graphical user interface. The spectrometer operates in the optical and near-infrared region, approximately from 400 to 900 nm, which is given by the silicon CCD detector.



### 3.2 Materials for optical setup

1. A standard aluminium L profile 25 mm high, 2 mm thick and with 12 mm long foot
2. The input slit was made of two razor blade segments, 15 mm long
3. The collimating lens had 14 mm diameter, focal length  $f \approx 30$  mm, Plano convex geometry
4. The cylindrical mirror was obtained from a scrap photocopier. It is a polished metal rectangle, 42 × 15 mm in size. Its focal length is approximately 30 mm
5. a blazed diffraction grating with 500 - 1000 grooves/mm, with size at least 8 × 8 mm

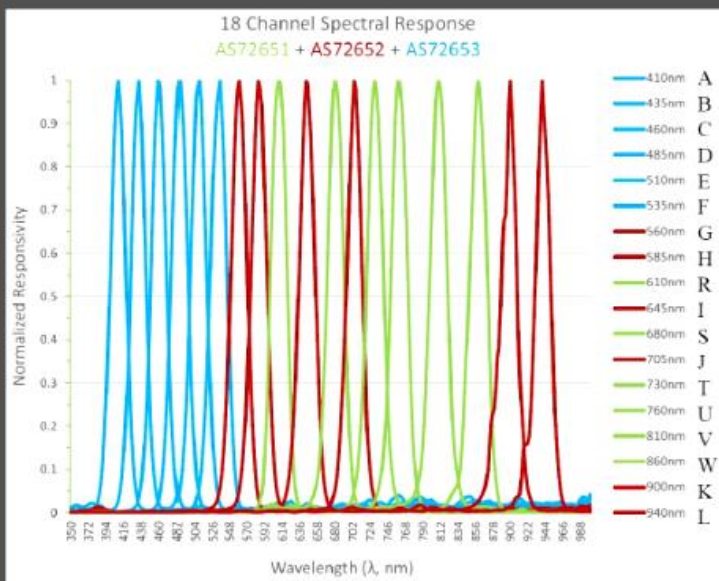
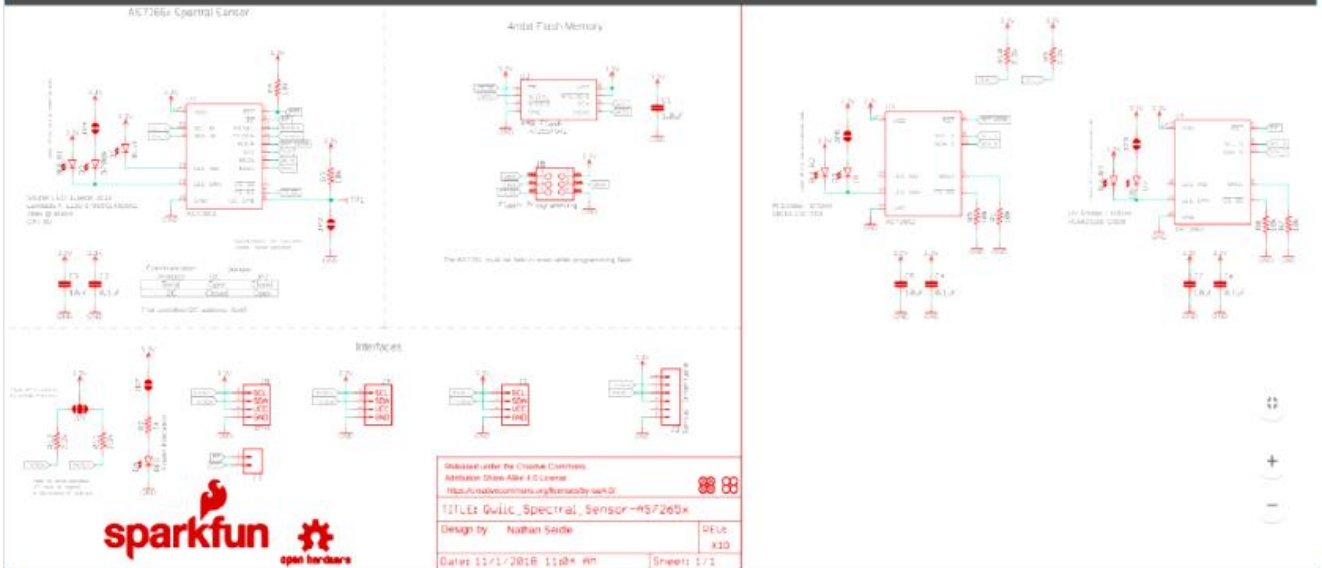
#### 6- Materials for optical setup

1. A standard aluminium L-profile 25 mm high, 2 mm thick and with 12 mm long foot.
2. The input slit was made of two razor blade segments, 15 mm long.
3. The collimating lens had 14 mm diameter, focal length  $f \approx 30$  mm, Plano-convex geometry
4. The cylindrical mirror was obtained from a scrap photocopier. It is a polished metal rectangle, 42×15 mm in size. Its focal length is approximately 30 mm
5. a blazed diffraction grating with 500 – 1000 grooves/mm, with size at least 8×8 mm .

### 3.3 Schematic of SparkFun Triad Spectroscopy Sensor - AS7265x (Qwiic)

#### 7-Schematic of SparkFun Triad Spectroscopy Sensor - AS7265x (Qwiic)

AS7265x Multispectral Chipset consists of AS72651, AS72652, and AS72653 devices and each device has 6 optical filters so that AS7265x Multispectral Chipset have total 18 channels for spectral identification from 400nm to 1000nm with FWHM of 20nm. AS72651 is the **main device with the smart interface to a microcontroller**. The **microcontroller** gets the sensors data including AS72652 and AS72653 through **AS72651 AT commands or I2C registers**.



- AS72651 requires a flash memory to work with and the flash memory contains AS7265x Multispectral Chipset firmware1.
- Each AS72651, AS72652, or AS72653 is packaged in 20-pin LGA package.
- To follow along with this hookup guide, we need one of the following Qwiic shields with an Arduino: **SparkFun RedBoard - Programmed with Arduino(19\$)** or **SparkFun Qwiic Shield for Arduino (6.9\$)**

### 3.4 Software Design Considerations and Arduino

In most of system designs, AS 72651 is controlled by a microcontroller with the UART interface, the controller could configure the devices and get the sensors data through some AT commands. The software of microcontroller design would be simple.



The following sections would focus on I<sup>2</sup>C interface and the software of microcontroller design should satisfy both on I<sup>2</sup>C specification and AS 7265 x Multispectral Chipset register structure.

### 8-Software Design Considerations

In most of system designs, AS72651 is controlled by a microcontroller. With the UART interface, the controller could configure the devices and get the sensors data through some AT commands. The software of microcontroller design would be simple.

The following sections would focus on I2C interface and the software of microcontroller design should satisfy both I2C specification and AS7265x Multispectral Chipset register structure.



#### Accessories:

Qwiic Cable - Breadboard Jumper (4-pin) \$1.50

Qwiic Cable - 100mm \$1.50

SparkFun Qwiic Shield for Arduino \$6.95

SparkFun Qwiic HAT for Raspberry Pi \$5.95

SparkFun Qwiic Mux Breakout - 8 Channel (\$11.95)

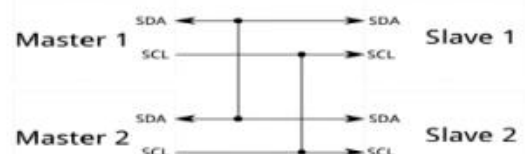


### 9-Arduino

- A computer (Windows, Mac, or Linux)
- An Arduino-compatible microcontroller (anything from this guide should work)
- A USB A-to-B cable, or another appropriate way to connect your Arduino-compatible microcontroller to your computer
- **1-installing Arduino IDE:** <https://learn.sparkfun.com/tutorials/installing-arduino-ide>
- **2-The Inter-integrated Circuit (I2C) Protocol** is a protocol intended to allow multiple "slave" digital integrated circuits ("chips") to communicate with one or more "master" chips. Like the Serial Peripheral Interface (SPI), it is only intended for short distance communications within a single device. Like Asynchronous Serial Interfaces (such as RS-232 or UARTs), it only requires two signal wires to exchange information.

#### I2C / Qwiic Interface:

The sensors are 3.3V compatible so don't use with a 5V Arduino Uno without proper conversion (use the Qwiic shield instead!). If you're using a 3.3V development platform that doesn't have a Qwiic connector, consider using the Qwiic Breadboard Cable.



### 3.5 References

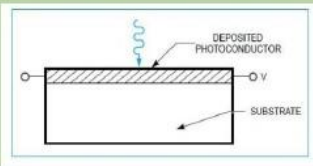
1. <https://en.wikipedia.org/wiki/Spectroscopy>
2. Czech Technical University in Prague, Faculty of Nuclear Sciences and Physical Engineering Department of Physical Electronics, "*Design and construction of a digital CCD spectrometer*", Research project, Author: Filip Dominec, Supervisor: Ing. Jaroslav Pavel, Academic year: 2009/2010  
([https://www.fzu.cz/~dominecf/electronics/usb-spect/usb\\_spectrometer\\_dominec.pdf](https://www.fzu.cz/~dominecf/electronics/usb-spect/usb_spectrometer_dominec.pdf)) Please note that this USB spectrometer project has a new HTML page, which may contain updates and further information: <http://www.fzu.cz/~dominecf/spek2/index.html>
3. Sparkfun - AS7265x (Qwiic)



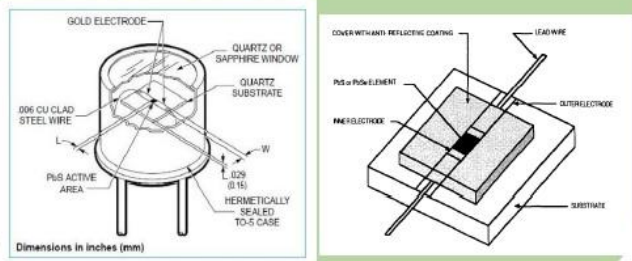
PbS cooled infrared detector (سنزور حراري)

A. Introduction

The electrical conductivity of photoconductive detectors is changed by the free-charge carriers generated by absorbed incident photons. A current starts flowing due to an applied voltage or bias. The current flow varies in proportion to the photon irradiance. Lead selenide and lead sulfide detectors fall into this category of detectors. This concept is shown in Figure .

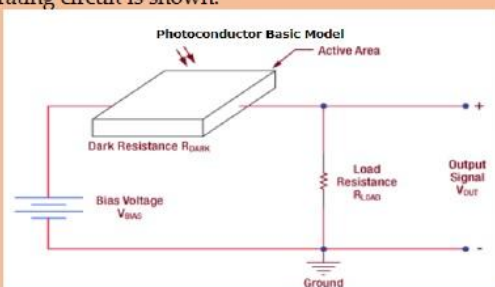


PbS and PbSe detectors are constructed through chemical deposition of polycrystalline film on a quartz substrate. Gold electrodes are plated to the film edges to provide electrical contact, and the entire assembly is sealed within a package with a suitable window, quartz or sapphire. A typical lead salt detector is depicted in Figure.



B. Theory of Operation

For photoconductive materials, incident light will cause the number of charge carriers in the active area to increase, thus decreasing the resistance of the detector. This change in resistance leads to a change in measured voltage, and hence, photosensitivity is expressed in units of V/W. An example operating circuit is shown.



The detection mechanism is based upon the conductivity of the thin film of the active area. The output signal of the detector with no incident light is defined by the following equation:

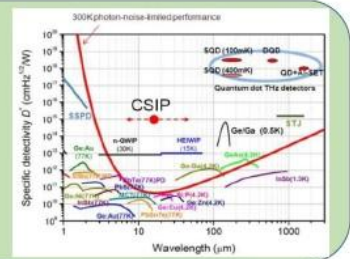
$$V_{OUT} = \frac{R_{LOAD}}{R_{DARK} + R_{LOAD}} * V_{BIAS}$$

A change  $\Delta V_{OUT}$  then occurs due to a change  $\Delta R_{Dark}$  in the resistance of the detector when light strikes the active area:

$$\Delta V_{OUT} = - \frac{R_{LOAD} V_{BIAS}}{(R_{DARK} + R_{LOAD})^2} * \Delta R_{DARK}$$

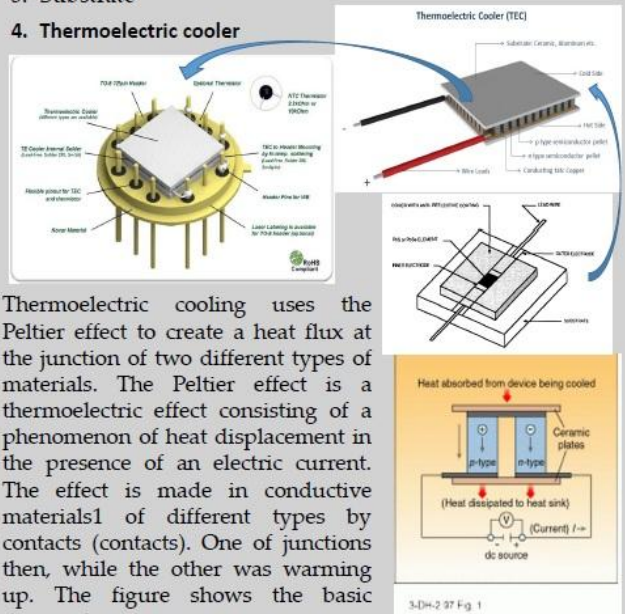
Spectral response characteristics of various infrared detectors.

(Lieda T. Komiya S, 2010, http://spinel.nim.nih.gov/dataset/result.php?img=3231243\_sensors-10-08411778req=4)

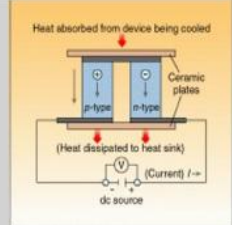


C. Material

1. Thin film of PbS
2. Electrical leads
3. Substrate
4. Thermoelectric cooler



Thermoelectric cooling uses the Peltier effect to create a heat flux at the junction of two different types of materials. The Peltier effect is a thermoelectric effect consisting of a phenomenon of heat displacement in the presence of an electric current. The effect is made in conductive materials of different types by contacts (contacts). One of junctions then, while the other was warming up. The figure shows the basic thermoelectric circuit.



Two conductive materials of different natures a and b are connected by two junctions in X and W. In the case of the Peltier effect, an electric current I is imposed on the circuit, by placing for example a source of electric current between Y and Z resulting in heat release Q at one junction and heat absorption at the other junction. The Peltier coefficient relative to the material pair a and b is defined as the thermal power P released or absorbed per unit of intensity of current I. It is expressed in volts.

$$\Pi_{ab} = \frac{P}{I}$$



If a current imposed in the direction  $Y \rightarrow W \rightarrow X \rightarrow Z$  causes a heat release in W and an absorption in X, then  $\Pi_{ab}$  is positive.

5. Sapphire window
6. Heat sink
7. Header is made of Kovar material (nickel-cobalt ferrous alloy)



Ras Masqa/Tripoli, Lebanon 06-11-2018

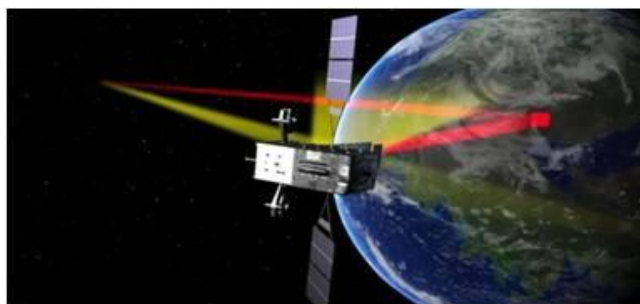
## Infrared Sensor System for IAP-SAT (IAP-IRS)

The IAP project aims to investigate a proper low cost platform to take interstellar data in IR and radio spectrum. There are the following working packages for 2018-2020:

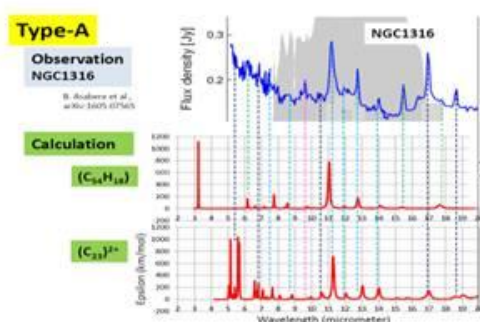
- Detailed space infrared sensor
- Detailed Mission Planning for bringing IAP-SAT into orbit
- Collect data from IAP-SAT



*Illustration 1: Caption: Black Widownebula captured by Spitzer's IRAC.  
Credit: NASA/NPL-Catech/E. Churchwell (University of Wisconsin-Madison) and the GLIMPSE Team*



*Illustration 2: The Space Based Infrared System can spot heat causing events across the world*



*Illustration 3: Type-A spectrum. Calculated spectrum of  $(C_{54}H_{18})$  and  $(C_{23})^{2+}$  are compared with observed one of NGC1316. Blue dashed lines coincident with both molecules, whereas green with only  $(C_{54}H_{18})$ , black with  $(C_{23})^{2+}$ , pink no coincidence with both molecules.*

### Tasks:

- Design of a proper infrared sensor.
- Collect IR data from satellite platform in Canopus Region.

### Contact:

Dr. Samir Mourad,  
Mob./WhatsApp +961 76 341526  
Email: samir.mourad@aecenar.com

# 1 Basics of infrared science & technology

## 1.1 Infrared Astronomy (Near Infrared, Mid Infrared, Far Infrared)<sup>5</sup>

Infrared is usually divided into 3 spectral regions: near, mid and far-infrared. The boundaries between the near, mid and far-infrared regions are not agreed upon and can vary. The main factor that determines which wavelengths are included in each of these three infrared regions is the type of detector technology used for gathering infrared light.

Near-infrared observations have been made from ground based observatories since the 1960's. They are done in much the same way as visiblelight observations for wavelengths less than 1 micron, but require special infrared detectors beyond 1 micron. Mid and far-infrared observations can only be made by observatories which can get above our atmosphere. These observations require the use of special cooled detectors containing crystals like germanium whose electrical resistance is very sensitive to heat.

Infrared radiation is emitted by any object that has a temperature (i.e. radiates heat). So, basically all celestial objects emit some infrared. The wavelength at which an object radiates most intensely depends on its temperature. In general, as the temperature of an object cools, it shows up more prominently at farther infrared wavelengths. This means that some infrared wavelengths are better suited for studying certain objects than others.



Visible (courtesy of Howard McCallon), near-infrared (2MASS), and mid-infrared (ISO) view of the Horsehead Nebula. Image assembled by Robert Hurt.

As we move from the near-infrared into mid and far-infrared regions of the spectrum, some celestial objects will appear while others will disappear from view. For example, in the above image you can see how more stars (generally cooler stars) appear as we go from the visible light image to the near-infrared image. In the near-infrared, the dust also becomes transparent, allowing us to see regions hidden by dust in the visible image. As we go to the mid-infrared image, the cooler dust itself glows. The table below highlights what we see in the different infrared spectral regions.

---

<sup>5</sup> <http://www.icc.dur.ac.uk/~tt/Lectures/Galaxies/Images/Infrared/Regions/irregions.html>

SPECTRAL REGION	WAVELENGTH RANGE (microns)	TEMPERATURE RANGE (degrees Kelvin)	WHAT WE SEE
Near-Infrared	(0.7-1) to 5	740 to (3,000-5,200)	Cooler red stars Red giants Dust is transparent
Mid-Infrared	5 to (25-40)	(92.5-140) to 740	Planets, comets and asteroids Dust warmed by starlight Protoplanetary disks
Far-Infrared	(25-40) to (200-350)	(10.6-18.5) to (92.5-140)	Emission from cold dust Central regions of galaxies Very cold molecular clouds

### 1.1.1 NEAR INFRARED

As we move away from visiblelight towards longer wavelengths oflight, we enter the infrared region. As we enter the near-infrared region, the hot blue stars seen clearly in visible light fade out and cooler stars come into view. Large red giant stars and low mass red dwarfs dominate in the near-infrared. The near-infrared is also the region where interstellar dust is the most transparent to infrared light.



Visible (left) and Near-Infrared View of the Galactic Center

Visible image courtesy of Howard McCallon. The infrared image is from the 2 Micron All Sky Survey (2MASS)

Notice in the above images how center of our galaxy, which is hidden by thick dust in visible light (left), becomes transparent in the near-infrared (right). Many of the hotter stars in the visible image have faded in the near-infrared image. The near-infrared image shows cooler, reddish stars which do not appear in the visible light view. These stars are primarily red dwarfs and red giants.

Red giants are large reddish or orange stars which are running out of their nuclear fuel. They can swell up to 100 times their original size and have temperatures which range from 2000 to 3500 K. Red giants radiate most intensely in the near-infrared region.

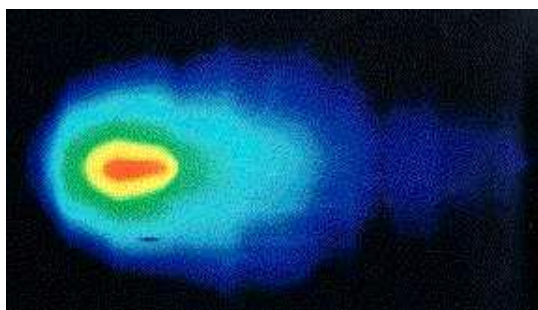
Red dwarfs are the most common of all stars. They are much smaller than our Sun and are the coolest of the stars having a temperature of about 3000 K which means that these stars radiate most strongly in the near-infrared. Many of these stars are too faint in visiblelight to even be detected by optical telescopes, and have been discovered for the first time in the near-infrared.

### 1.1.2 MID INFRARED

As we enter the mid-infrared region of the spectrum, the cool stars begin to fade out and cooler objects such as planets, comets and asteroids come into view. Planets absorb light from the sun and heat up. They then re-radiate this heat as infrared light. This is different from the visible light that we see from the planets which is reflected sunlight. The planets in our solar system have temperatures ranging from about 53 to 573 degrees Kelvin. Objects in this temperature range emit most of their light in the mid-infrared. For example, the Earth itself radiates most strongly at about 10 microns. Asteroids also emit most of their light in the mid-infrared making this wavelength band the most efficient for locating dark asteroids. Infrared data can help to determine the surface composition, and diameter of asteroids.



An infrared view of the Earth



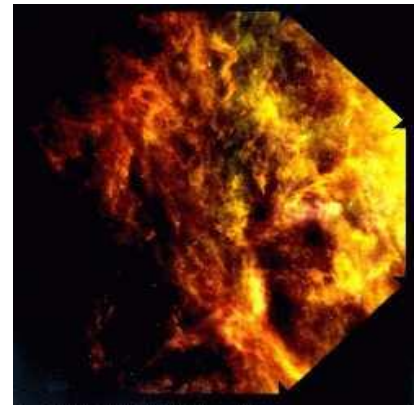
IRAS mid-infrared view of Comet IRAS-Araki-Alcock

Dust warmed by starlight is also very prominent in the mid-infrared. An example is the zodiacal dust which lies in the plane of our solar system. This dust is made up of silicates (like the rocks on Earth) and range in size from a tenth of a micron up to the size of large rocks. Silicates emit most of their radiation at about 10 microns. Mapping the distribution of this dust can provide clues about the formation of our own solar system. The dust from comets also has strong emission in the mid-infrared.

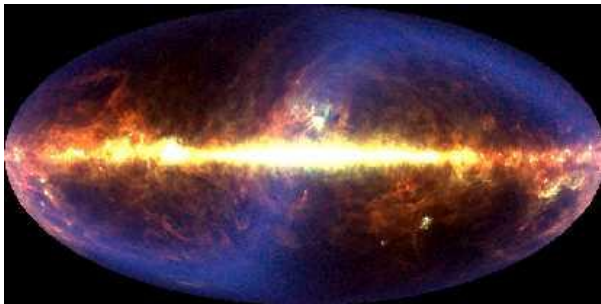
Warm interstellar dust also starts to shine as we enter the mid-infrared region. The dust around stars which have ejected material shines most brightly in the mid-infrared. Sometimes this dust is so thick that the star hardly shines through at all and can only be detected in the infrared. Protoplanetary disks, the disks of material which surround newly forming stars, also shines brightly in the mid-infrared. These disks are where new planets are possibly being formed.

### 1.1.3 FAR INFRARED

In the far-infrared, the stars have all vanished. Instead we now see very cold matter (140 Kelvin or less). Huge, cold clouds of gas and dust in our own galaxy, as well as in nearby galaxies, glow in far-infrared light. In some of these clouds, new stars are just beginning to form. Far-infrared observations can detect these protostars long before they "turn on" visibly by sensing the heat they radiate as they contract."



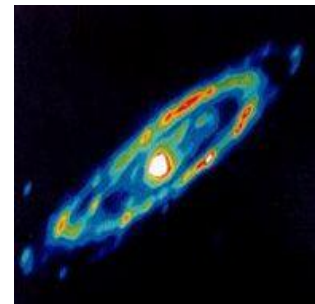
IRAS view of infrared cirrus - dust heated by starlight



Michael Hauser (Space Telescope Science Institute), the COBE/DIRBE Science Team, and NASA

The center of our galaxy also shines brightly in the far-infrared because of the thick concentration of stars embedded in dense clouds of dust. These stars heat up the dust and cause it to glow brightly in the infrared. The image (at left) of our galaxy taken by the COBE satellite, is a composite of far-infrared wavelengths of 60, 100, and 240 microns.

Except for the plane of our own Galaxy, the brightest far-infrared object in the sky is central region of a galaxy called M82. The nucleus of M82 radiates as much energy in the far-infrared as all of the stars in our Galaxy combined. This far-infrared energy comes from dust heated by a source that is hidden from view. The central regions of most galaxies shine very brightly in the far-infrared. Several galaxies have active nuclei hidden in dense regions of dust. Others, called starburst galaxies, have an extremely high number of newly forming stars heating interstellar dust clouds. These galaxies, far outshine all others galaxies in the far-infrared.



IRAS infrared view of the Andromeda Galaxy (M31) - notice the bright central region.

## 1.2 Definition of infrared and the origin of the infrared radiation<sup>6</sup>

### Table of Contents

#### 3.1 The definition of the infrared band

#### 3.2 The origin of infrared radiation

##### 3.2.1 Atomic transitions

##### 3.2.2 Molecular transitions

<sup>6</sup> <http://elte.prompt.hu/sites/default/files/tananyagok/InfraredAstronomy/ch03.html>



### 3.3 Radiation of molecules

#### 3.3.1 Molecular hydrogen

#### 3.3.2 Ices and other molecules

### 3.4 Radiation of dust

#### 3.4.1 Heating and cooling of dust

#### 3.4.2 Refractory dust

#### 3.4.3 Silicates

#### 3.4.4 Large dust grains

#### 3.4.5 Polycyclic Aromatic Hydrocarbons

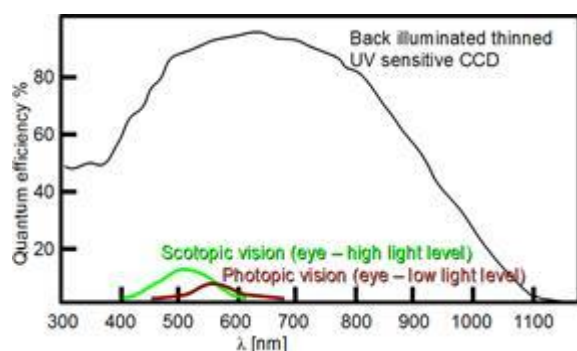
### References and further reading to the chapter:

In this chapter we describe the technological and observational justification of the infrared band. Atomic and molecular transitions are investigated as the origin of the infrared radiation.

**Electromagnetic radiation** is classified by wavelength into gamma rays, X-rays, ultraviolet, visible, infrared, microwave and radio, see on Figure 3.1. Infrared radiation lies between the visible and microwave part of the electromagnetic radiation.

#### 1.2.1 The definition of the infrared band

The quantum efficiency is a measure of a device's electrical sensitivity to light. It is the incident photon to converted electron ratio, i.e. the percentage of photons hitting the device's photoreactive surface that produce charge carriers. It is measured in electrons per photon or amps per watt. As we see in Figure 3.1 the quantum efficiency of the human eye is around 1% to 10%, over most conditions (see eg. <http://psych.nyu.edu/pelli/pubs/pelli1990efficiency.pdf>). It gets slightly better for red colour at low light levels (photopic vision), but our eyes lose all sensitivity beyond the red end of the visible spectrum ( $\lambda > 0.75 \mu\text{m}$ ).



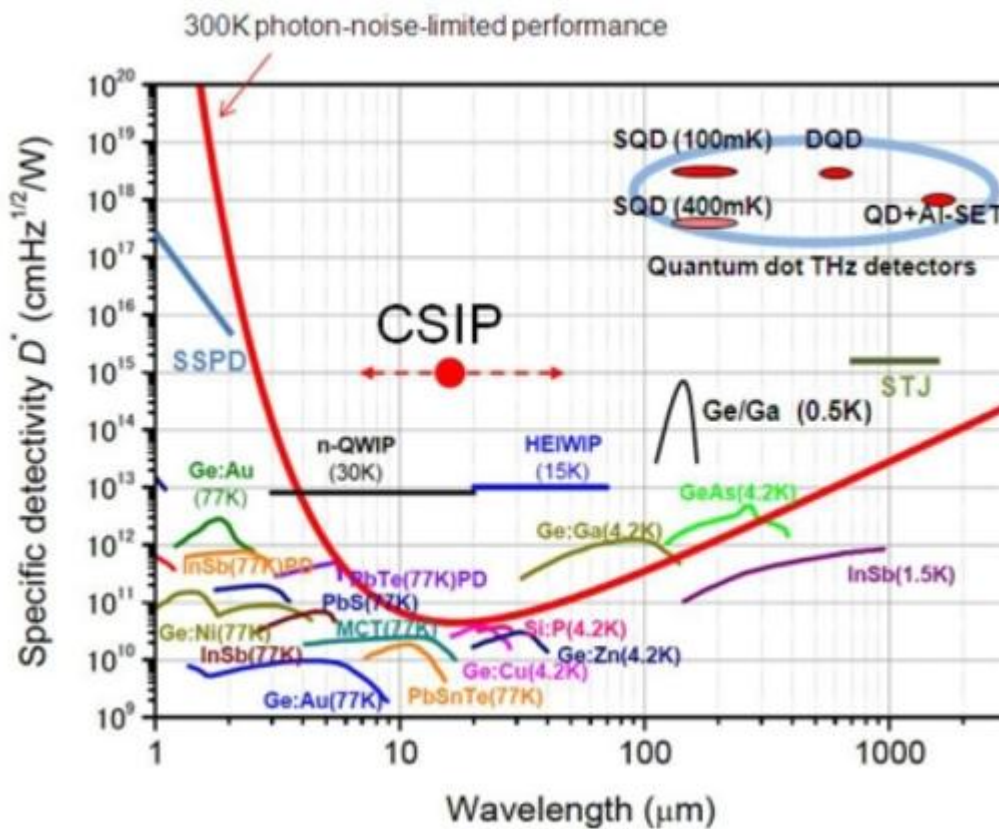
**Figure 3.1:** Quantum efficiency of human eye and CCD

The infrared quantum efficiency of typical photoemulsions is similar to the human eye, however infrared sensitive astrographic photo plates (Kodak IVN) were sensitive up to  $\lambda \approx 1 \mu\text{m}$ . We can not use any more most of the visible band technologies such as photography, CCDs and photocathodes

for  $\lambda > 1.1 \mu\text{m}$ , and that wavelength limit can be considered as a technical border of infrared at the short wavelength side. Referring to Figure 3.1 we note that the CCD surface has channels used for charge transfer that are shielded by polysilicon gate electrodes which absorb light (mostly blue). Such losses are eliminated in the back-illuminated CCD, where the light falls onto the back of the CCD in a region that has been thinned so it is transparent. The wavelength dependent specific detectivity  $D^*$  is defined as reciprocal of noise-equivalent power (NEP), normalized per unit area:

$$D^* = \frac{\sqrt{\text{Area}}}{\text{NEP}}, \quad (3.1)$$

where Area is the photosensitive region of the detector. The unit of  $D^*$  is:  $\text{cmHz}^{1/2}\text{W}^{-1}$ . Figure 3.1 shows the specific detectivity  $D$  of the most common compounds used as detectors which include: Gallium Arsenide – GaAs, Lead Sulfide – PbS, Indium Antimonide – InSb, Germanium doped with Copper - Ge:Cu, Germanium doped with Zinc - Ge:Zn, Germanium doped with Gold - Ge:Au, Germanium doped with Gallium - Ge:Ga, Lead Telluride – PbTe, phosphorus-doped silicon – Si:P.



**Figure 3.2:** Spectral response characteristics of various infrared detectors. (Ueda T, Komiyama S, 2010, [http://openi.nlm.nih.gov/detailedresult.php?img=3231243\\_sensors-10-08411f7&req=4](http://openi.nlm.nih.gov/detailedresult.php?img=3231243_sensors-10-08411f7&req=4))

The highest available frequency band of terrestrial sub-mm observatories is at 810GHz (0.37mm). The “end” of the infrared region is again technologically defined: it is the wavelength ( $\approx 350\mu\text{m}$ ) where radio techniques such as superheterodyne receivers tend to be used in preference to the “optical style” infrared approach and the incoming radiation tends to be thought of as waves rather than

individual photons. The region from 0.35mm to 1mm is referred to as the sub-millimeter region. It may be regarded as a subdivision of radio astronomy.

**Astronomical justification for the definition** is that already at 2.2 $\mu\text{m}$  the sky has a significantly different appearance from the visible one. The cooler end of the stellar population becomes predominant and some objects turn out to have infrared fluxes much higher than predicted from their visible spectra.

These infrared excesses can be due to cool dust shells surrounding them or to circumstellar free-free emission for example. The most important sources of the infrared photons are Solar system objects, stars and extended galactic objects, extragalaxies. The cosmic microwave background (CMB) is the relic of the Big Bang. It is characterized by a blackbody spectrum of temperature 2.73K. The rise of its spectrum marks the end of the infrared.

The vibrational transitions of molecules results infrared photons, whereas we observe their rotational transitions spectra in the sub-mm and radio region.

Infrared is divided into three parts: near, mid and far-infrared. Near-infrared refers to the part of the infrared spectrum that is closest to visible light and far-infrared refers to the part that is closer to the microwave region. Mid-infrared is the region between these two. The boundaries between these regions are not exact and can vary. (Table 3.1. shows the general properties of the infrared ranges.)

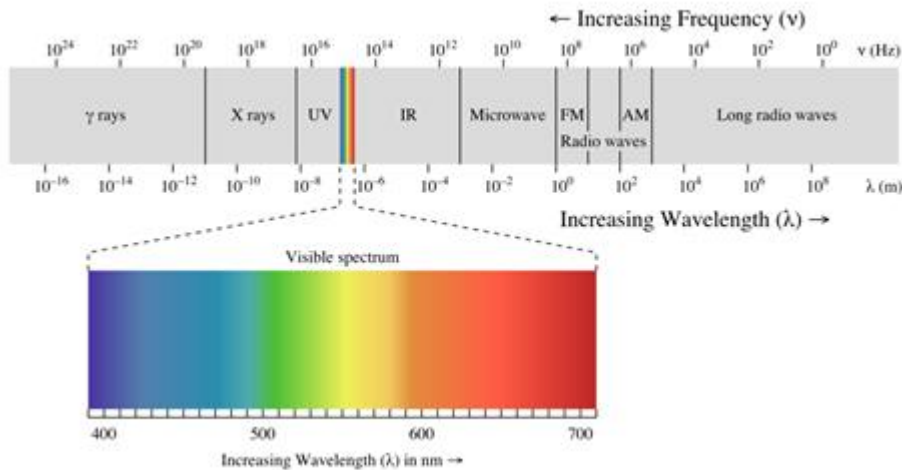
Infrared radiation	Wavelength range [ $\mu\text{m}$ ]	Astronomical objects
Near	1-5	Red giants Cooler red stars
Mid	5-30	Planets, comets and asteroids Protoplanetary disks
Far	30-400	Central regions of galaxies Emission from cold dust

**Table 3.1:** *Properties of the infrared ranges*

**A justification based on the observational conditions** can be made as well. Beyond 2.3 $\mu\text{m}$  blackbody radiation from the telescope and the atmosphere itself begins to dominate other sources of background. Measurements of faint astronomical objects have to be made by alternatively observing the field containing the source and a nearby "empty" one. This process is known as chopping. The signals are subtracted to eliminate the strong background. Alternatively the measurement is taken outside the atmosphere with a cooled observing system.

In the NIR, MIR and FIR the main sources of the background are terrestrial, Zodiacal light and galactic ISM radiation. From about 300 $\mu$ m CMB starts to dominate the background. Except bands in the NIR, the infrared sky is to be observed by air-borne or space-borne instruments.

The sub-millimeter region however can be accessed again in selected atmospheric windows by terrestrial telescopes located at high altitude, low precipitable water vapor (pww) sites like Mauna Kea or South Pole. Precipitable water is the measure of the depth of liquid water at the surface that would result after precipitating all of the water vapor in a vertical column over a given location, usually extending from the surface to 300 mb (<http://forecast.weather.gov/glossary.php?word=precipitable%20water>).



**Figure 3.3:** Electromagnetic spectrum ([http://en.wikipedia.org/wiki/File:EM\\_spectrum.svg](http://en.wikipedia.org/wiki/File:EM_spectrum.svg)) from  $10^{-16}$  to  $10^8$  m. The visible spectrum located in the middle, it covers only a small part of the spectrum.

Observations at different wavelengths reveal various pictures from astronomical objects. Figure 3.4 shows the M51 Spiral Galaxy at different wavelengths: from visible to far infrared. Observations of visible light show the stars that make up the galaxy. Infrared observations reveal the mixture of gas and dust from which new stars can be born.

**Figure 3.4:** Hubble, 2MASS, Spitzer Space Telescope, ISO and IRAS observations of M51 Spiral Galaxy. Shorter wavelengths show the star content of it, on longer wavelengths the radiation of gas and dust dominate. (<http://astromic.blogspot.de/2011/02/infrared-astronomy.html>)

Near-infrared observations have been made from ground based observatories since the 1960's. This part of the infrared radiation can be observed with similar technique as visible light, but it requires special infrared detectors. Mid and far-infrared observations, where the wavelength is longer than 20  $\mu$ m, can only be made by observatories which can get above our atmosphere. These observations require the use of special cooled detectors.

## 1.3 Instrumentation / Sensors Technology

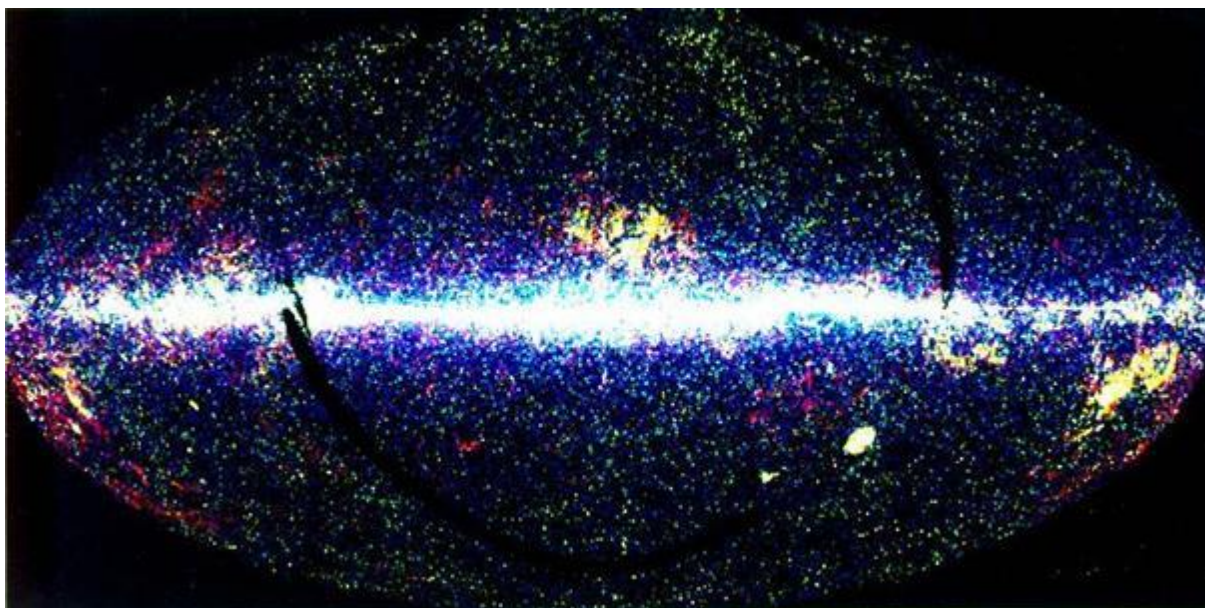
### 1.3.1 IRAS

The Infrared Astronomical Satellite (IRAS) was initiated in 1975, designed and constructed by NASA (USA), NIVR (the Netherlands), and SERC (UK), and launched by NASA (launcher: Delta 3910) on January 25, 1983. It was the first space-borne infrared observatory to scan the entire sky. During its ten months of operation, IRAS scanned more than 96 percent of the sky four times at four infrared

bands centered at 12, 25, 60 and 100 microns. Its main task was to discover and measure IR point sources. The IRAS mission has had a major impact on almost every area of astronomy.

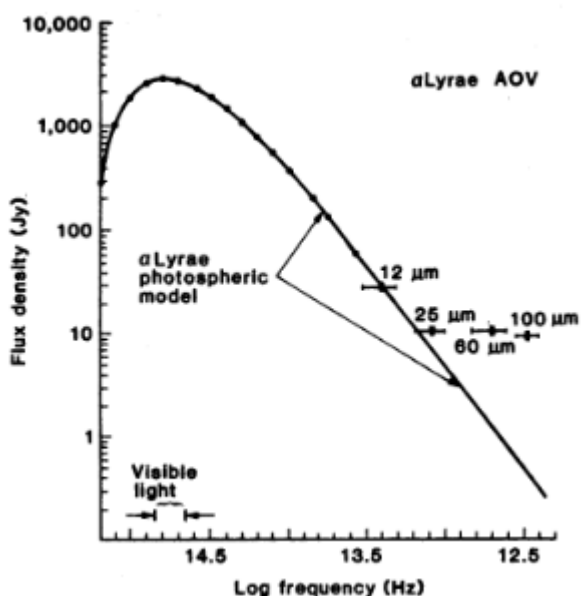
### 1.3.1.1 The most important results of IRAS

- Detected about 350,000 infrared sources (see Figure 6.1), increasing the number of cataloged astronomical sources by about 70%.



**Figure 6.1:** All sky map of IRAS sources (<http://www.iras.ucalgary.ca/~nkoning/irasDb/iras.html>)

- Discovered 6 new comets
- Found that comets are dustier than previously thought and that dust from comets fills the Solar System
- Detected useful infrared data for 2004 asteroids
- Detected the zodiacal dust bands - bands of infrared emission that girdle our solar system which are likely to be debris from asteroid collisions
- Found evidence of zodiacal dust bands around other stars
- Discovered a disk of dust grains around the star Vega, see Figure 6.2. The significant excess above the photospheric model indicates the presence of cold material around a star.



**Figure 6.2:** *Observed spectral energy distribution of Vega and photospheric stellar model (Neugebauer et al.).*

- Detected disks of material around several other stars.
- Detected several probable protostars embedded in clouds of gas and dust
- Found that some Bok globules contain protostars. e.g. Beichman (1984) showed that the Bok globule, Barnard 5 contains at least four protostars.
- Cataloged thousands of hot, dense cores within clouds of gas and dust which could be newly forming stars
- Cataloged over 12,000 variable stars, the largest collection known to date
- Revealed for the first time the core of our galaxy
- Found infrared cirrus (wisps of warm dust) in almost every direction of space
- Data from IRAS was used to show that our galaxy is a barred spiral galaxy - a galaxy which has an elongated central bar-like bulge from which its spiral arms unwind.
- Detected 75,000 starburst galaxies - galaxies which are extremely bright in the infrared due to intense star formation. It was found that many of these starburst galaxies have "superwinds" emerging from their centers due to the large number of supernova explosions which occur in these galaxies.
- Detected strong infrared emission from interacting galaxies
- First identified IRAS F10214+4724 - at the time, the most luminous object known in the Universe by a factor of 2. This object may be the best candidate for a forming spiral galaxy yet discovered.
- Instruments and observing strategy of IRAS

IRAS telescope system comprised the upper part of the satellite and was composed of a two mirror, Ritchey-Chretien telescope mounted within a toroidal superfluid helium tank, which in turn was mounted within the evacuated main shell. The optical system was protected from contamination before launch and during the first week of the mission by an aperture cover cooled with supercritical helium. After the cover was ejected, the sunshade limited heat flow to the aperture by blocking direct solar radiation and reflecting away terrestrial infrared radiation. The telescope orientation was constrained to prevent sunlight from striking the inner surface of the sunshade and radiation from the Earth from illuminating the radiators around the telescope aperture. The telescope was cooled by contact with the superfluid helium tank to temperatures ranging from 2 to 5 K. The surfaces of the sunshade which could be viewed by the telescope aperture were cooled by a three-stage radiator to about 95 K.

The focal plane assembly contained the infrared and visible detectors, cold electronics, and associated masks, filters and field optics. It consisted of 62 infrared channels and eight visible channels. The infrared channels were divided into eight modules, two for each color band with each module containing either seven or eight detectors. The detector masks were rectangular in aspect and infrared sources scanned across the focal plane parallel to the narrow dimension of the detectors in all observational modes.

## 1.4 Infrared satellite observatories

### Table of Contents

#### 7.1 Infrared Space Observatory (ISO)

##### 7.1.1 Scientific instruments and observing strategy

## 7.1.2 Most important results

## 7.2 Spitzer Space Telescope

### 7.2.1 Scientific instruments

### 7.2.1 Most important scientific results

## 7.3 Herschel Space Observatory

### 7.3.1 Scientific instruments

### 7.3.2 Most important scientific results

## References and further reading to the chapter:

In this chapter we give an overview of the observing strategy, scientific instruments and main scientific result of Infrared Space Observatory, Spitzer Space Telescope and Herschel Space observatory.

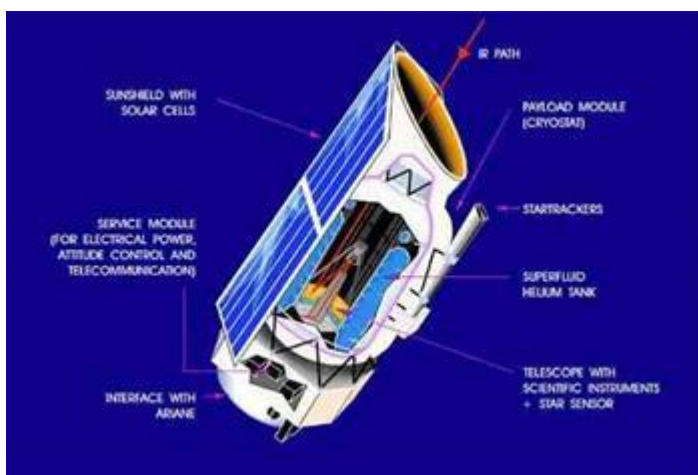
### **1.4.1 Infrared Space Observatory (ISO)**

ISO observed the infrared sky between February 1996 and April 1998. It was a European Space Agency (ESA) mission, launched in November 1995. The satellite weighed around 2500 kg and was launched with over 2000 litre of liquid helium coolant on board, which lasted for 29 months.

ISO was the first orbiting infrared observatory. It made during its lifetime more than 30 000 individual observations of all kind of astronomical objects: in the solar system and in the most distant galaxies.

The telescope operated between 2.5 and 240  $\mu\text{m}$ . Comparing to IRAS, at 12  $\mu\text{m}$  it was one thousand times more sensitive and had one hundred times better angular resolution.

Figure 7.1 shows ISO's two largely independent modules: the Payload Module and the Service Module. The Payload Module was a large cryostat containing super fluid helium which maintained the telescope and the scientific instruments at temperatures between 2 and 8 K. The Service Module contained the warm electronics of the scientific instruments and all the classical spacecraft subsystems, which are necessary to supply the basic functions. The sun-shield with solar cells always faced the Sun to provide electrical power and to protect the Payload Module from direct irradiation.



**Figure 7.1:** Schematic view of the ISO satellite, two largely independent modules are visible: the Payload Module and the Service Module

[http://vietsciences.free.fr/giaokhoa/vatly/thienvan/gsnnguyenquangrieu/images/iso\\_satellite.jpg](http://vietsciences.free.fr/giaokhoa/vatly/thienvan/gsnnguyenquangrieu/images/iso_satellite.jpg)

The ISO telescope was a 60 cm diameter Richey-Chrétien system with an overall focal ratio of  $f/15$ . This type of telescope is free from coma and spherical aberration, and they have larger field of view than the classical Cassegrain type telescopes. The optical quality of the primary and secondary mirrors provided diffraction limited performance at wavelengths beyond  $5 \mu\text{m}$ , also limited by pointing performance.

ISO had a high Earth orbit with a period of one-to-two days. It was accustomed by previous space observatories.

#### 1.4.1.1 Scientific instruments and observing strategy

ISO's four scientific instruments are the following: a camera, ISOCAM, an imaging photopolarimeter, ISOPHOT, and the two spectrometers, a long wavelength LWS and a short wavelength SWS.

The telescope and the scientific instruments operated at  $\sim 3\text{K}$ . Some of the infrared detectors were cooled down to  $1.8\text{K}$ . This low temperature enabled observations to be made at high sensitivities. Only one instrument was operational in prime mode at a time, but the camera was used in parallel mode to acquire extra astronomical data whenever it was possible. The long-wavelength channel of the photometer was used during satellite slews, this produced a partial sky survey, which covers  $\sim 15\%$  of the sky, at wavelengths around  $200 \mu\text{m}$ . After launch, a parallel/serendipity mode was added for the LWS, in which narrow-band data were obtained at 10 fixed wavelengths in parallel with the main instrument and also during slews.

New generations of space and air-borne integral field spectrometers required large format arrays of low noise equivalent power (NEP) detectors. NEP is the radiant power that produces a signal-to-noise ratio of unity at the output of a given detector at a given data-signaling rate or modulation frequency, operating wavelength, and effective noise bandwidth. In the FIR, photoconductors still offer the higher sensitivity under low background conditions in combination with moderately low operation temperatures ( $1.7\text{K}$  to  $4\text{K}$ ) when compared to bolometers. In the  $40$  to  $200 \mu\text{m}$  range, Gallium-doped germanium (Ge:Ga) photoconductors are commonly used because of their high sensitivity. Ge:Ga photoconductors which are mechanically stressed are used to cover the wavelength range from  $115$  to  $210 \mu\text{m}$ . Unstressed Ge:Ga detectors are used to cover the wavelength range from  $40$  to  $115 \mu\text{m}$ .

The ISO Camera instrument consisted of two optical channels, used one at a time, each with a  $32 \times 32$  element detector array, operated in the wavelength ranges  $2.5\text{-}5.5 \mu\text{m}$  and  $4\text{-}17 \mu\text{m}$ .

The ISOPHOT instrument consisted of three subsystems: ISOPHOT-C, ISOPHOT-P and ISOPHOT-S: ISOPHOT-C consists of two photometric far-infrared cameras, used one at a time, for the wavelength range  $50\text{-}240 \mu\text{m}$ . The 'C100' camera contained a  $3 \times 3$  array of Ge:Ga detectors, each with a pixel field of view of  $43.5''$ , and 6 filters covering wavelengths up to  $105 \mu\text{m}$ . The 'C200' camera used a  $2 \times 2$  array



of stressed Ge:Ga detectors with a pixel field of view of  $89''$  and had 5 filters covering wavelengths longwards of  $100\mu\text{m}$ .

ISOPHOT-P was a multi-band, multi-aperture photo-polarimeter for the wavelength range  $3\text{-}110\mu\text{m}$ . It contained 13 apertures ranging in size from  $5''$  to  $180''$  and 14 different filters. ISOPHOT-S was a dual grating spectrophotometer which provided a resolving power of  $\sim 90$  in two wavelength bands simultaneously ( $2.5\text{-}5\mu\text{m}$  and  $6\text{-}12\mu\text{m}$ ).

The ISO Long Wavelength Spectrometer covered the wavelength range  $43\text{-}196.7\mu\text{m}$  with a spectral resolving power of  $\sim 200$ . Using also the Fabry-Pérot (FP) etalons, the resolution could be increased to around 10,000.

The ISO Short Wavelengths Spectrometer covered the wavelength range  $2.38\text{-}45.2\mu\text{m}$  with a spectral resolving power of the order of 1000-2500. Using also the Fabry-Pérot (FP) etalons, the resolution could be increased to more than 25 000 for the wavelength range  $11.4\text{-}44.5\mu\text{m}$ .

ISO was operated in a pre-planned manner without any significant routine real-time interaction.  $\sim 45\%$  of the observing time was reserved for guaranteed time programmes. But as an observatory, ESO was open to the astronomical community including expert and non-expert users.

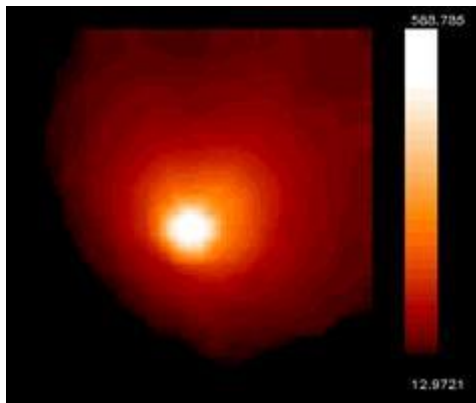
Each of the four instruments had a number of possible operating modes. To simplify the definition of an observation and to allow users to specify their observation in terms familiar to them, a set of astronomically-useful operating modes was defined and presented to users as a set of 'Astronomical Observation Templates' (AOTs). Each AOT was designed to carry out a specific type of astronomical observation.

$\sim 65\%$  of ISO's observing time was distributed to the general community via the traditional method of proposals and peer review. The scientific programme for ISO consisted of more than 1 000 individual proposals.. About 10% of ISO's time was used for Solar System studies, 23% for the Interstellar Medium (ISM), 29% on Stellar/Circumstellar topics, 27% for Extragalactic observations and 11% for Cosmology.

#### 1.4.1.2 Most important results

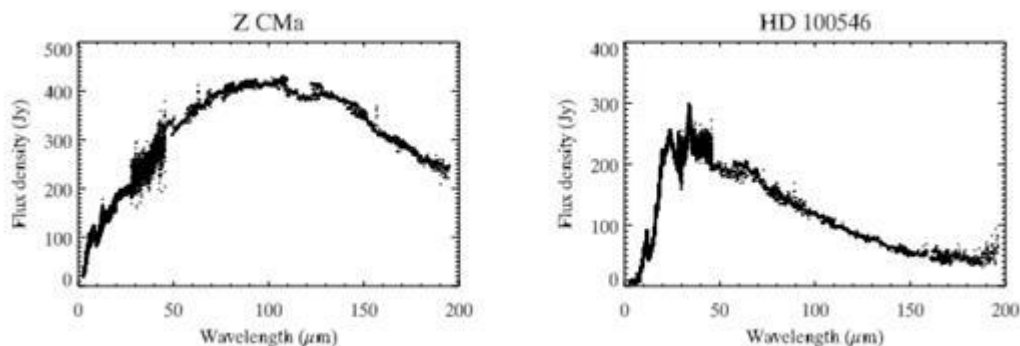
ISO has delivered important results in nearly all fields of astronomical research. Nearly 1400 papers have been published in the refereed literature on ISO results. A few example from ISO's most important scientific results:

- the discovery of crystalline silicates outside our own solar system, in the atmospheres of young and old stars and also in comet Hale-Bopp. Figure 7.2 show the ISOCAM image of Hale-Bopp comet at  $15\mu\text{m}$ . This discovery shows that water is ubiquitous in the cosmos.



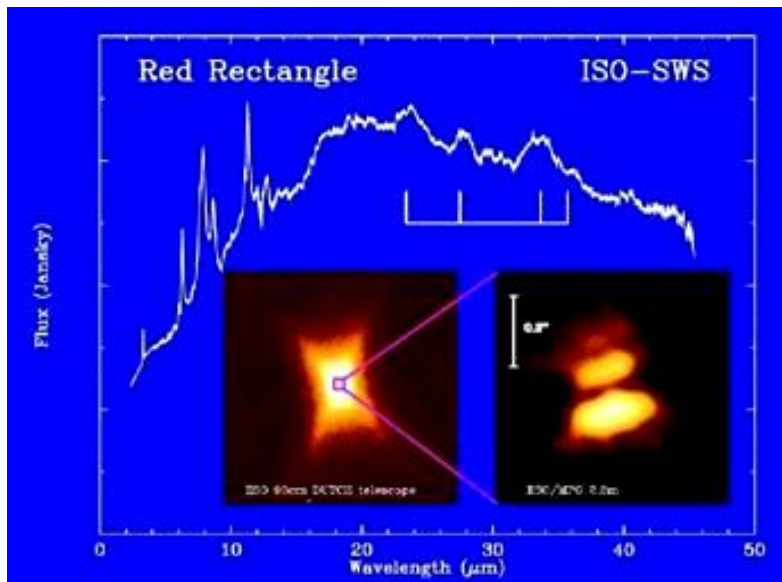
**Figure 7.2:** ISOCAM image of comet Hale-Bopp at 15  $\mu\text{m}$  (<http://iso.esac.esa.int/galleries/sso/halebopp.html>, Credit: ESA/ISO, ISOCAM, R. Walsh, B. Altieri, P. Lamy)

- a wealth of water vapour transitions were measured e.g. in Mars, Titan, the giant planets, comets including Hale-Bopp, in shocks, in the cold interstellar medium, in circumstellar envelopes and in the ultra-luminous galaxy Arp220. The spectral resolution of most water observations was limited, but the possibility to observe the full mid- and far-infrared spectrum has opened great possibilities.
- the first detections of the lowest pure rotational lines of  $\text{H}_2$  in young massive stars, HH-objects, the diffuse ISM, outer parts of edge-on galaxies. . Temperatures less than a few hundred K could be investigated.
- observing pre-main sequence stars with SWS and LWS spectrographs. These data were used for line detections and to reconstruct the spectral energy distributions. Figure 7.3 shows the spectral energy distribution of 2 Herbig Ae/Be stars. Very different SEDs were observed for Herbig Ar/Be stars, confirming the fact that these objects do not constitute a homogeneous class.



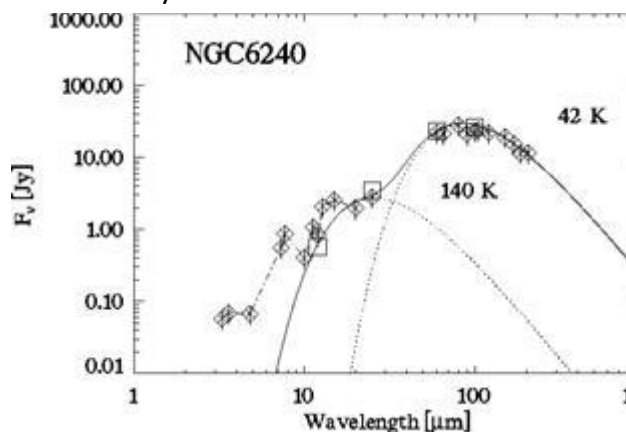
**Figure 7.3:** ISO spectra of two Herbig Ae/Be stars (Lorenzetti 2004).

- detecting planet formation around old, dying stars. E.g. in the vicinity of the Red Rectangle old binary star in the Monoceros constellation, a ring of matter constituting the first stage of planet formation was detected. This discovery contradicted theories that planet formation was only possible around young stars. Figure 7.4 shows two images in red light and the ISO LWS spectrum of the Red Rectangle. The left image was taken by H. van Winckel (Leuven) using the 90 cm Dutch telescope at the European Southern Observatory, La Silla, Chile. The right hand image was taken by G. Weigelt and R. Osterbart (Bonn) using the 2.2m Max Planck telescope, also at E.S.O.. A prominent dark lane is visible across the image, which is due to the disk surrounding the binary system. The tick marks on the spectrum indicate the position of the oxygen-rich olivine bands, suggesting that the disk contains oxygen-rich material. This disk may be the site of on-going planet formation.



**Figure 7.4:** Two images in red light and ISO LWS spectrum of Red Rectangle. ([http://coolcosmos.ipac.caltech.edu/image\\_galleries/ISO/sws/redrec.html](http://coolcosmos.ipac.caltech.edu/image_galleries/ISO/sws/redrec.html))

- ISO searched for, and found several protoplanetary disks: rings or disks of material around stars which are considered to be the first stage of planet formation.
- the detailed investigations of interstellar solid state features, e.g. CO<sub>2</sub> ices. It gives the possibility to have detailed interplay between observations and laboratory spectroscopy
- obtaining spectral energy distributions of extragalactic objects, which serve as templates for cosmological studies, helped to consolidate the unified scheme or to develop quasar evolutionary scenarios. ISOPHOT SED of NGC6240 are seen on Figure 7.5.



**Figure 7.5:** ISOPHOT spectral energy distribution of NGC6240. The SED is well fitted with two components: a 140 K and a 42 K blackbody radiation. (<http://iso.esac.esa.int/galleries/nor/ngc6240c.htm>, Credit: EAS/ISO, ISOPHOT, U. Klaas)

- making deep cosmological surveys at near- and far-infrared wavelengths. It resolved the part of the cosmic infrared background (CIB) into discrete sources and detected fluctuations in the CIB.

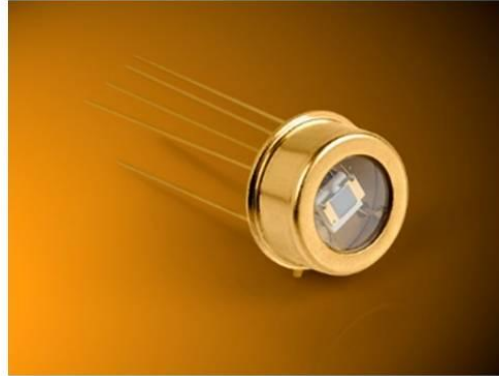
making the European Large Area ISO Survey to explore obscured galaxies and quantify the recent star-formation history of the Universe. This survey discovered 9 hyper luminous galaxies.

## 2 IAP-IRS Unit Design (PbS detector) Overview (Presentation)

SA, Last update: 25. Aug. 2019 / 1440، الأحد، 24 ذو الحجة،



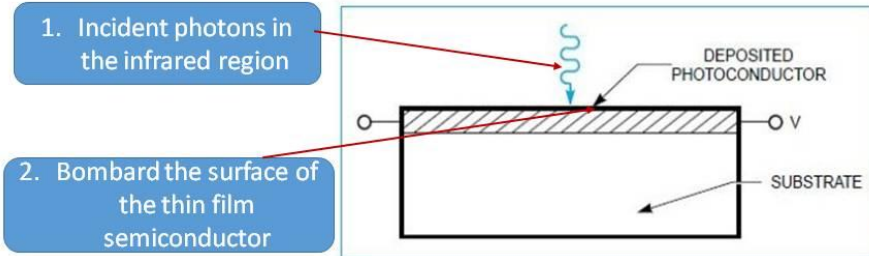
### PbS detector



Presented by: Siham Aisha

1

### Introduction



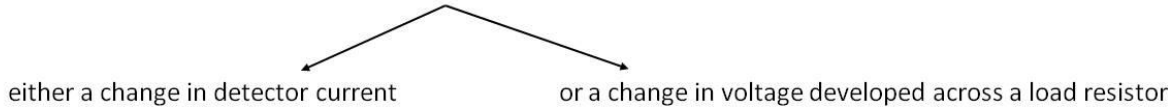
1. Incident photons in the infrared region

2. Bombard the surface of the thin film semiconductor

3. Collide with electrons residing within the valence band of the detector material

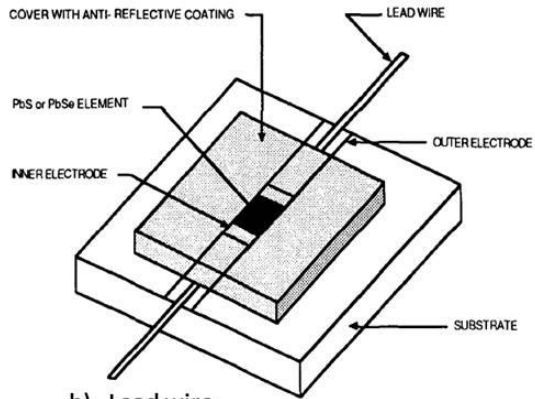
4. This interaction stimulates the generation of electron-hole pairs

Consequently, this results in an increase in the amount of current flowing through the device. The output signal of the detector circuit is:



2

## Structure



b) Lead wire



a) Substrate

AliExpress Lianyungang Hongan Technology Ltd. 100.0% Positive feedback 68 Followers

Thin transparent quartz glass plate 10\*10\*1.5mm quartz substrate

**US \$265 / lot** (200 pieces)

US \$3.00 New User Coupon Get coupons

Quantity: 1 1000 lots available

Shipping: US \$72.80 to Lebanon via EMS - Estimated Delivery: 5-17 days

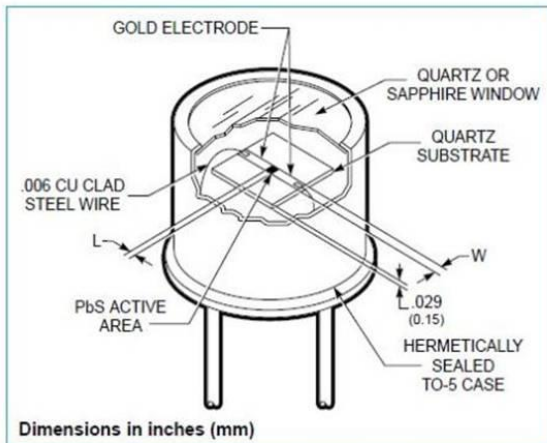
Buy Now Add to Cart

20-Day Buyer Protection Money back guarantee

c) Anti-reflective coating

An antireflective or anti-reflection (AR) coating is a type of optical coating applied to the surface of lenses and other optical elements to reduce reflection. In typical imaging systems, this improves the efficiency since less light is lost due to reflection

3



a) Sapphire window

OEM laser cutting Blank optical glass sapphire window

FOB Reference Price: Get Latest Price

**\$1.00 - \$100.00** / Pieces 1 Piece/Pieces (Min. Order)

Quantity(Pieces)	1 - 100	>100
Est. Time(days)	30	Negotiable

Contact Supplier

Chat Now!

Seller Support Trade Assurance - To protect your orders from payment to delivery

Payment: VISA T T Online Bank Payment Pay Later More

Shipping: Alibaba.com Ocean Shipping Service from China to U.S. Get shipping quote

b) Substrate

Thin transparent quartz glass plate 10\*10\*1.5mm quartz substrate

**US \$265 / lot** (200 pieces)

US \$3.00 New User Coupon Get coupons

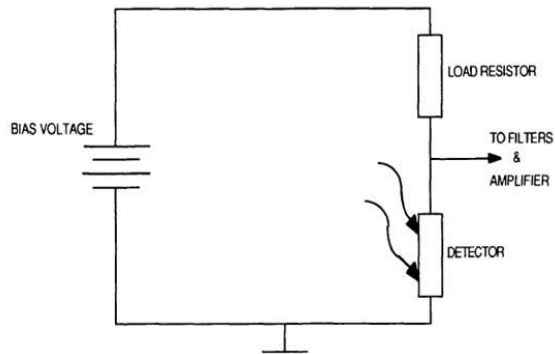
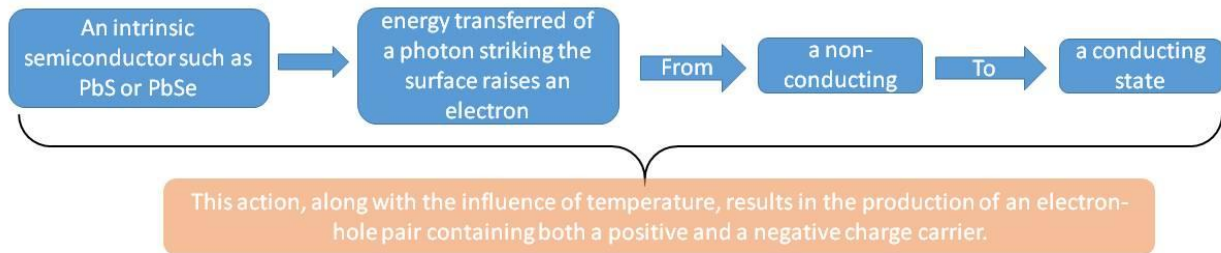
Quantity: 1 1000 lots available

Shipping: US \$72.80 to Lebanon via EMS - Estimated Delivery: 5-17 days

Buy Now Add to Cart

20-Day Buyer Protection Money back guarantee

## Theoretical background



If the detector is biased in a manner similar to that shown in figure, an electric field is developed which will increase the number of charge carriers. This phenomenon, known as the photoconductive effect, thus reduces the resistance of the device.

5

## PbS Detectors Cooled Ultimate PB30-Series

### Description

The PB30 series is a collection of TE cooled photoconductive single element PbS detectors that operate at  $-45^{\circ}\text{C}$  to  $-55^{\circ}\text{C}$  with a 20% cutoff of  $3.4\ \mu\text{m}$ . This series is widely used in analytic, safety and radiometric applications.

### Features

- Spectral range from 1 to  $3.4\ \mu\text{m}$
- State of the art performance
- 100% test data



### Applications

- Pulp and paper industry
- Non-contact temperature measurement
- Spark detection
- Flame control
- Moisture monitoring
- FTNIR

## PbS Detectors Cooled Standard PB27-Series

### Description

The PB27 series is a collection of TE cooled photoconductive single element PbS detectors that operate at  $-20^{\circ}\text{C}$  to  $-35^{\circ}\text{C}$  with a 20% cut-off of  $3.3\ \mu\text{m}$ . This series is widely used in analytic, safety and radiometric applications especially when large active areas are requested.

### Features

- Spectral range from 1 to  $3.3\ \mu\text{m}$
- State of the art performance
- 100% test data

### Applications

- Pulp and paper industry
- Non-contact temperature measurement
- Spark detection
- Flame control
- Moisture monitoring
- FTNIR



## PbS Detectors Uncooled PB25-Series

### Description

The PB25 series is a collection of uncooled photoconductive single element PbS detectors that operate at room temperature with a 20% cut-off of  $3.0\ \mu\text{m}$ . This series is widely used in analytic, safety and radiometric applications especially when large active areas are requested.

### Features

- Spectral range from 1 to  $3.0\ \mu\text{m}$
- State of the art performance
- 100% test data

### Applications

- Pulp and paper industry
- Non-contact temperature measurement
- Spark detection
- Flame control
- Moisture monitoring
- FTNIR



**PbS Photoconductor: 1.0 - 2.9  $\mu\text{m}$**



Zoom

- ▶ Good Performance for 1.0 - 2.9  $\mu\text{m}$  Range
- ▶ For Detection of CW Light We Recommend an [Optical Chopper](#)
- ▶ Also Comes as a Packaged, Amplified Detector, the [PDA30G](#)

Item # <sup>a</sup>	Info	Wavelength Range	Active Area	Package Type	Rise Time <sup>b</sup>	Peak Wavelength	Peak Sensitivity <sup>c</sup>	Specific Detectivity <sup>d</sup>	Dark Resistance	Compatible Sockets
FDPS3X3		1.0 - 2.9 $\mu\text{m}$	9 mm <sup>2</sup>	TO-5	200 $\mu\text{s}$	2.2 $\mu\text{m}$ (Typ.)	2 x 10 <sup>4</sup> V/W (Min) 5.0 x 10 <sup>4</sup> V/W (Typ.)	1 x 10 <sup>11</sup> cm <sup>2</sup> Hz <sup>1/2</sup> /W (Typ.)	0.25 - 2.5 MOhm	<a href="#">STO5S</a> <a href="#">STO5P</a>

a. All measurements performed with a 50 Ohm load unless stated otherwise.  
 b. Rise Time is measured from 0 to 63% of final value.  
 c. Measured at Peak Wavelength, Chopping Frequency of 600 Hz, and Bias Voltage of 15 V.  $R_{\text{DARK}} = R_{\text{LOAD}}$   
 d. Measured at Peak Wavelength and Chopping Frequency of 600 Hz

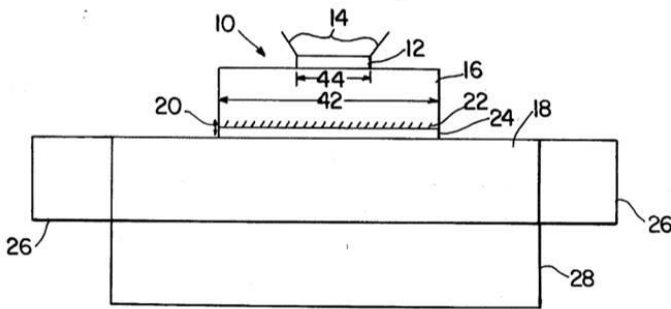
Based on your currency / country selection, your order will ship from Newton, New Jersey

+1	Qty	Docs	Part Number - Universal	Price	Available
	<input type="text"/>		<a href="#">FDPS3X3</a> PbS Photoconductor, 3 mm x 3 mm Active Area, 200 $\mu\text{s}$ Rise Time, 1.0 - 2.9 $\mu\text{m}$	\$191.21	Today

to extract a useful signal from these detectors, we can exploit this phenomenon. As the light falls on the detector, the electron flow increases, increasing the conductivity of the materials. and conversely, reducing its resistance. By using a load resistor (typically 1 Mohm, matching the black resistance of the detectors, the best detector will be obtained as a voltage divider, and a bias voltage is applied.) When the resistance of the detector changes, the electronic characteristics of a voltage divider are used for: The debate continues on whether this mode of operation is the most appropriate method of operation for PbS detectors, the community of FPA microbolometers discussing the advantages of the S / N ratio. current associated methods.

9

**patent**



- 12: thin film of PbS
- 14: electrical leads
- 16: substrate
- 18: heat buffer
- 20: interface
- 22: metal
- 24: bonding layer
- 26: surround
- 28 : heat sink

**16 Substrate**

Considering first the design of substrate 16, the thermal conductivity of the substrate, the thickness of the substrate, and the surface area of the substrate:

Conductivity: for applications where thin film photoconductors will be subject to intense radiation, the substrate should be fabricated from materials such as silicon or sapphire which have large thermal conductivities.

Thickness : It is noted that the substrate must be of sufficient thickness to supply mechanical stability for the thin films.

Surface area: The heat flow in the detector will also be improved if the substrate surface area, as indicated by 42 in FIG. 1, is made large compared to the absorbing detector area, as indicated by 44 in FIG.1. This will allow transverse heat flow within the substrate 16, as well as heat flow in the direction of optical radiation, to contribute to the power dissipation of the detector.

10



**20 interface**

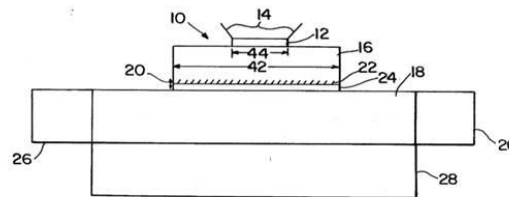
Considering now the design of the interface 20, if a thin highly-conductive material is used for the detector substrate 16, the interface 20 may become a thermal bottleneck (the thermal bottleneck is referred to the points where the temperature is excessively high mainly due to design flaws, the term being of primal importance in the Electronics Industry.)

**22 metal and 24 bonding layer**

In the preferred embodiment of detector 10, the back surface of the substrate 16 is metalized at 22 with a metal of high thermal conductivity, such as silver or copper, by conventional processes such as diffusion. This metalized surface has the effect of increasing the thermal conductivity at the back of the substrate 16, and also providing a metal layer so that a highly-thermally conductive material such as solder may be used as the bonding layer 24 between the substrate and the metal heat buffer.

It should be clear that if interface layer 20 has a higher thermal conductivity than substrate 16, the substrate should be as thin as possible considering requirements of mechanical support, electrical isolation, and formation of the metalized back surface.

Alternatively, if interface layer 20 has a lower thermal conductance than substrate 16, it is advantageous to have a substrate of a larger thickness so that the substrate may dissipate more heat itself.



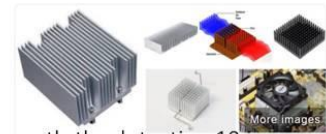
11

**18 heat buffer**

Heat buffer 18 is a high-thermal-conductivity, large-thermal mass in intimate thermal contact with the substrate 16 (via interface 20) and it has a two-fold function:

1. The first function is to remove heat from interface 20 as rapidly as possible and redistribute it throughout the entire buffer to eliminate any appreciable heat buildup in the region behind the interface.
2. The second function is to act as a high-specific-heat thermal reservoir until heat can be removed to the heat sink

Copper is a preferred material for use as the heat buffer 18.

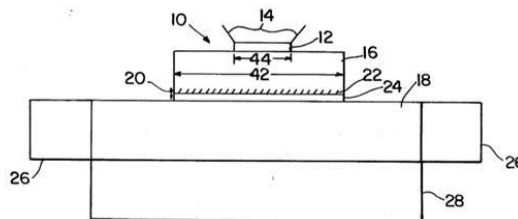


**26 surround**

The type of heat sink used with detector 10 will depend on the particular application. Frequently the detection 10 is surrounded circumferentially by a ring which acts as a heat sink as shown at 26.

**28 Heat sink**

Alternatively, the detector 10 may be mounted on a heat sink such as shown at 28. In that case, the heat sink 28 and the heat buffer 18 may be combined in a single piece of highly-thermally-conductive material such as copper.

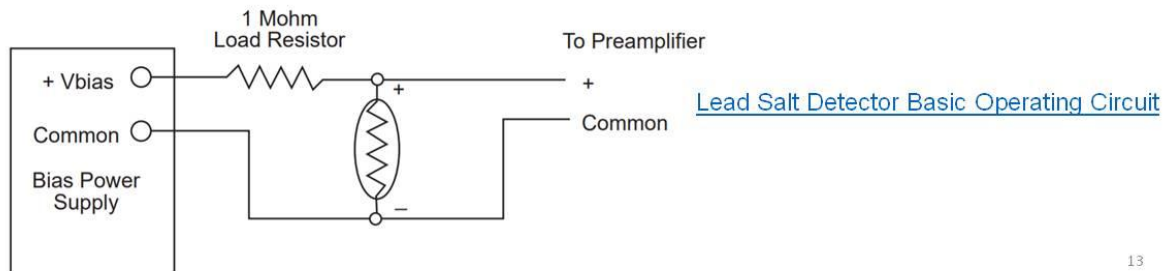


12

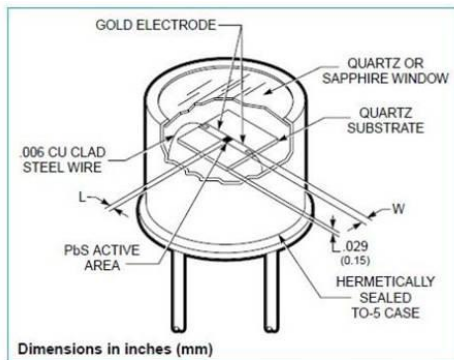
## Conclusion

A thin-film, photoconductive, infrared detector hardened against damage from laser irradiation comprising:

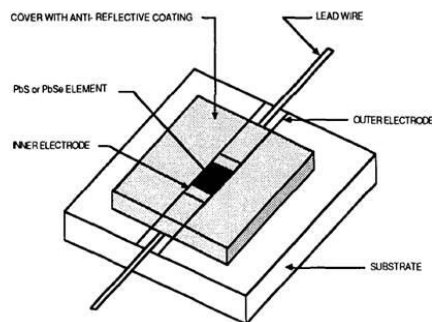
- a thin film of photoconductor material sensitive to infrared radiation;
- a thin substrate upon the front-surface of which said thin film is deposited,
- substrate having a high thermal conductivity to provide efficient heat flow from said thin film through said substrate
- substrate having a surface area that is large relative to the absorbing area of said thin film so that heat generated by said irradiation will be distributed transversely within said substrate,
- the back surface of said substrate being metallized with a metal of high thermal conductivity;
- a bonding layer of high thermal conductivity; and a heat buffer upon which said substrate is mounted, contact being made between said buffer and the metallized back surface of said substrate by said bonding layer said heat buffer having a high thermal conductivity to remove heat from said interface as rapidly as possible and redistribute it throughout the entire buffer to eliminate heat buildup in the region behind said interface, said heat buffer having a large thermal mass to act as a high-specific-heat thermal reservoir.



13



Dimensions in inches (mm)



## Material

1. Thin film of PbS
2. Electrical leads
3. Substrate:

Considering first the design of substrate 16, the thermal conductivity of the substrate, the thickness of the substrate, and the surface area of the substrate:

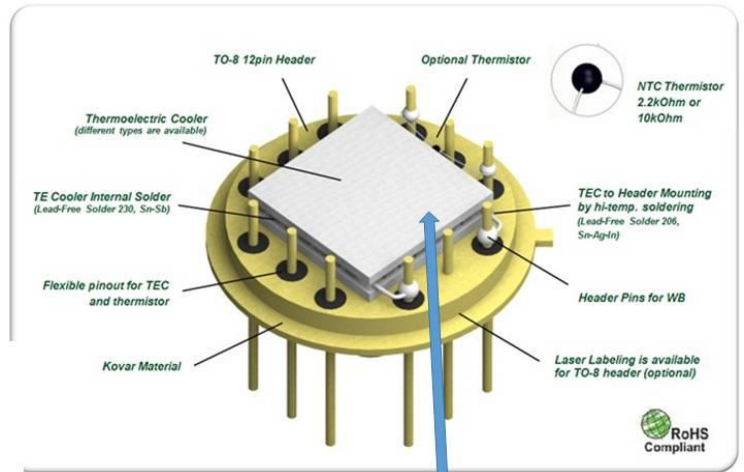
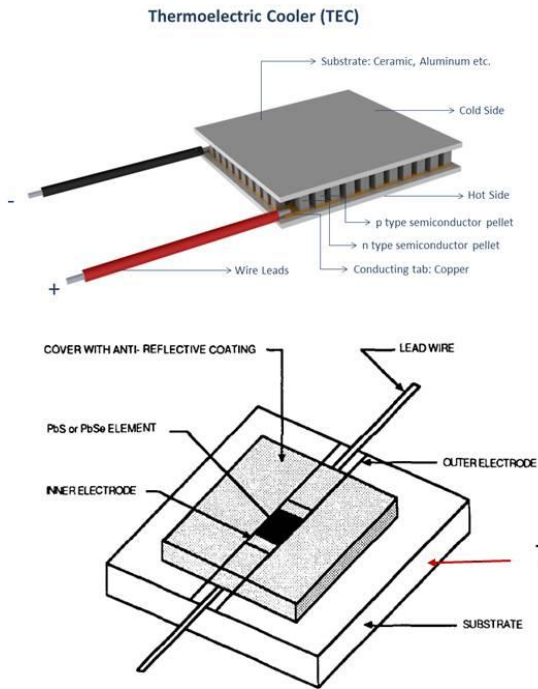
**Conductivity:** for applications where thin film photoconductors will be subject to intense radiation, the substrate should be fabricated from materials such as silicon or sapphire which have large thermal conductivities.

**Thickness:** It is noted that the substrate must be of sufficient thickness to supply mechanical stability for the thin films.

**Surface area:** The heat flow in the detector will also be improved if the substrate surface area, as indicated by 42 in FIG. 1, is made large compared to the absorbing detector area, as indicated by 44 in FIG.1. This will allow transverse heat flow within the substrate 16, as well as heat flow in the direction of optical radiation, to contribute to the power dissipation of the detector.

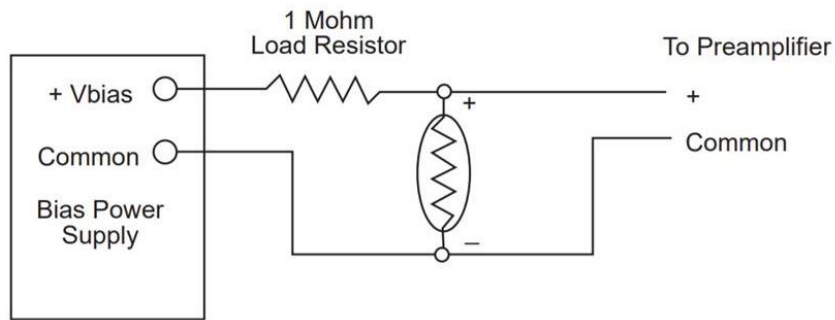
4. Thermoelectric cooler

# IAP-IRS Unit Design (PbS detector) Overview (Presentation)



This area it's put above the thermoelectric cooler

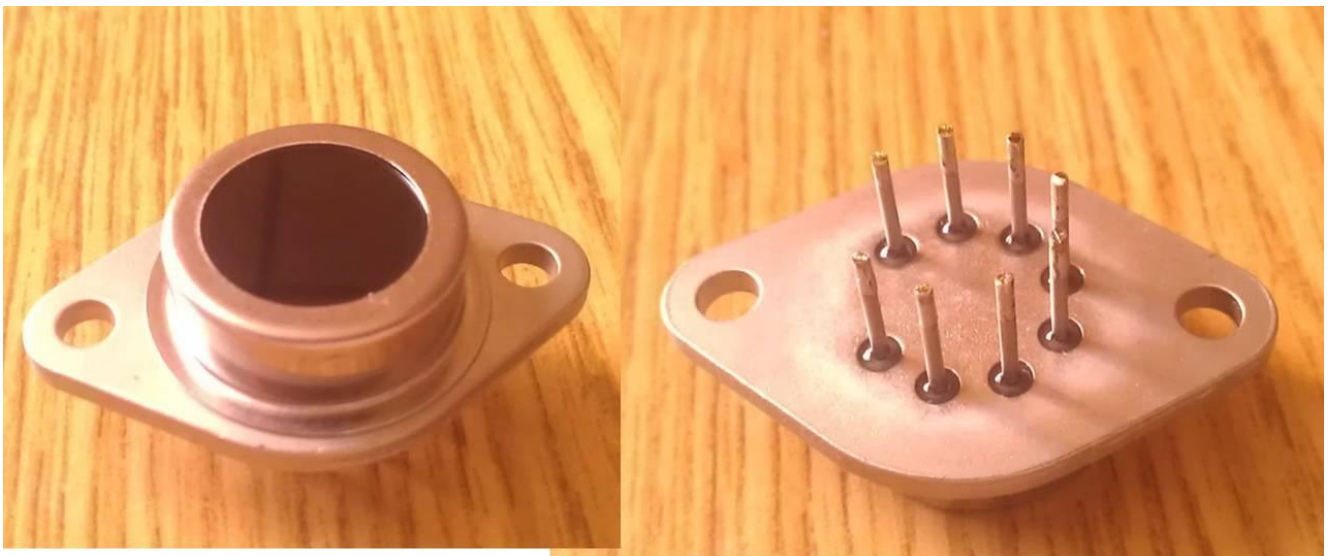
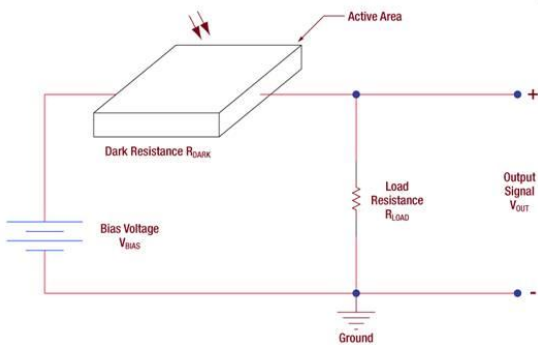
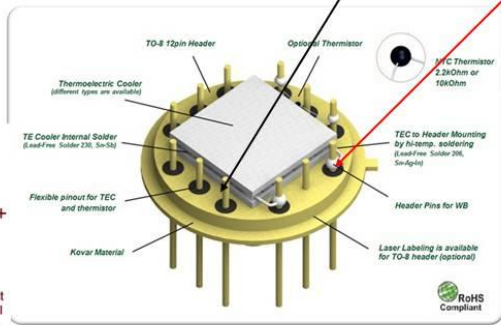




Questions:

يوجد في slide رقم 2 شكل ال detector و لديه عدة أرجل اثنين منها لل voltage and thermoelectric cooler كما موضح في الشكل أتناه و اثنين لنعطي current. لم أعلم لماذا تستخدم بقية الأرجل؟

كيف يتم توصيل ال detector على المخرج ليظهر signal ؟  
 ما هو preamplifier ؟  
 كيف أطبق Bias power supply ؟



**PbS Detector - 10X10 Thermoelectrically Cooled with an IR Filter - 1-3 Microns**

Condition: **New**  
 Quantity:  More than 10 available / 12 sold

Price: **US \$100.00**

[Buy It Now](#)  
[Add to cart](#)

Best Offer: [Make Offer](#)  
 Add to watch list

Longtime Member | 18 Watchers

Shipping: May not ship to Lebanon - Read item description or contact seller for shipping options. | See details  
 Item location: North, Massachusetts, United States  
 Ships to: United States

Delivery: Varies

Payments:

Returns: Seller does not accept returns | See details

**Specifications:**  
 $D^*(pk, 600, 1) - 1-2 \times 10^{11}$   
 Active Area - 10mm x 10mm  
 Cooler Power - 2.2V@1.2A  
 Thermistor - 1K @25C  
 Bias - 10 - 30VDC (MAX)  
 LR - 50-100% of Detector Res.

**NOTE:**  
 Improper heat sinking will cause permanent damage  
 Over bias will cause permanent detector damage.  
 Coolers and glass seals are FRAGILE. Do not drop, twist leads or otherwise use unnecessary force.

DO NOT SCALE DRAWING	DRAWN	DATE	NEW ENGLAND PHOTOCONDUCTOR			
	CHECKED	DATE	D-10-3			
MATERIAL:	DESIGNER	DATE				
	ENGINEER	DATE				
FINISH SPEC:	PROJECT ENGINEER	DATE	SIZE	CODE IDENT. NO.	TYPE	REV
	PROJECT APPROVAL	DATE	A		1412A	
PMB 7/21			SCALE	3-1	SHEET	

20

## Thermoelectric cooler (TE)



n/p type semiconductor element bismuth telluride pellet

FOB Reference Price: [Get Latest Price](#)

**\$150.00 - \$250.00** / Kilograms | 1 Kilogram/Kilograms (Min. Order)

[Contact Supplier](#)

[Leave Messages](#) [Request FREE Sample](#)

Seller Support: Trade Assurance - To protect your orders from payment to delivery

Payment:

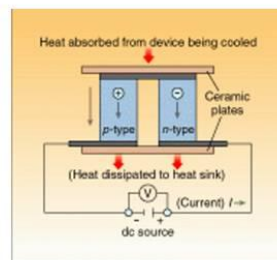
Shipping: Alibaba.com Ocean Shipping Service from China to U.S  
[Get shipping quote](#)



Thermoelectric materials on the basis of bismuth telluride  $Bi_2Te_3$

1. A single-stage TE cooler consists of a matrix of thermoelectric couples connected electrically in series, and thermally in parallel.
  - The couples themselves consist of bismuth telluride p- and n-type semiconductor material.
  - These couples are sandwiched between ceramic plates
2. When a positive dc voltage is applied to the n-type material, electrons pass from the p- to the n-type material
  - The temperature on the cold side decreases because heat is being absorbed from it
  - This heat pumped from the cold side plus the heat generated by the input power is conducted through to the hot side of the cooler, where it is dissipated by a heat sink
3. **Choosing a cooler**
  - the advantage of TE cooler is that you can integrate the detector and the cooler into one housing
  - The detector itself will generally be cooled below 0°C, so hermetic sealing is necessary to block out moisture that would otherwise precipitate and freeze on the cold detector surface.
4. The total heat load on the TE cooler stage plays a critical role in determining the minimum achievable temperature.
  - Gas convection inside the hermetic housing is a major source of heat-loading.
  - Convection can be reduced by filling the package with a high-molecular-weight gas (such as xenon) or by evacuating the package.
5. Finally, standard glass windows transmit wavelengths only to 2.5 μm.
  - For detectors that respond beyond this point, the package must incorporate sapphire windows or antireflection-coated germanium (Ge) windows, soldered or fused into the package cap.

- ❑ For detectors that respond beyond this point, the package must incorporate sapphire windows or antireflection-coated germanium (Ge) windows, soldered or fused into the package cap.
- ❑ Thermoelectrically cooled detectors are reliable and simple to operate
  - The most critical aspect of the design is proper heat-sinking, without which a cooler will be inefficient or may even be damaged by overheating



- For small two- and three-stage coolers, good thermal connection of the device to a metal plate with several square inches or more of surface area is usually sufficient; forced-air cooling is rarely needed

### 3 Basics<sup>7</sup>

The electrical conductivity of photoconductive detectors is changed by the free-charge carriers generated by absorbed incident photons. A current starts flowing due to an applied voltage or bias. The current flow varies in proportion to the photon irradiance. Lead selenide and lead sulfide detectors fall into this category of detectors. This concept is shown in Figure 43.

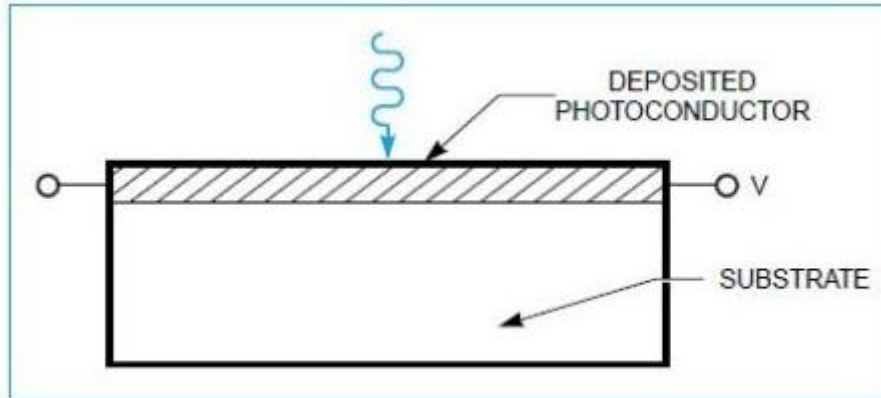


Figure 43: Schematic of a photoconductive detector

PbS and PbSe detectors are constructed through chemical deposition of polycrystalline film on a quartz substrate. Gold electrodes are plated to the film edges to provide electrical contact, and the entire assembly is sealed within a package with a suitable window, quartz or sapphire. A typical lead salt detector is depicted in Figure 44.

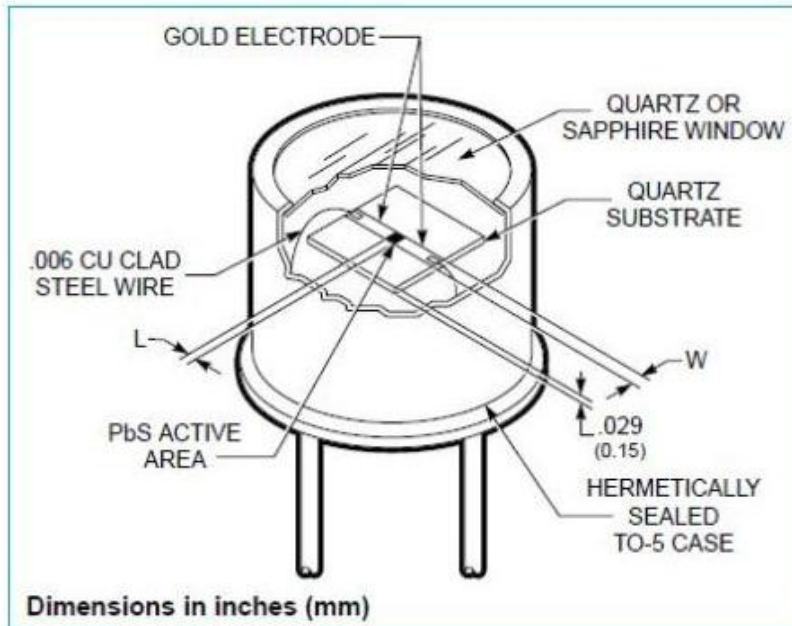


Figure 44: Typical lead salt detector

<sup>7</sup> <https://www.azooptics.com/Article.aspx?ArticleID=886>

### 3.1 Introduction to lead salt infrared detectors<sup>8</sup> (Kondas, February 1993)

Infrared detectors are generally classified as being either thermal or photon (quantum) detectors. Among the photon detectors there are two major types: photoconductors and photovoltaics (ref. 1). As shown in Figure 45, PbS and PbSe detectors are both members of the lead salt family of photoconductive infrared detectors. Photoconductive detectors are thin film semiconductor devices which undergo a change in conductivity when exposed to varying quantities of radiation. In the case of both detectors, incident photons in the infrared region bombard the surface of the thin film semiconductor and collide with electrons residing within the valence band of the detector material. This interaction stimulates the generation of electron-hole pairs. Consequently, this results in an increase in the amount of current flowing through the device. The output signal of the detector circuit is either a change in detector current or a change in voltage developed across a load resistor. Thus, when the device is incorporated as part of a sensor system, it is these current or voltage changes which are interpreted by the detector circuit processor as being the target of interest or not.

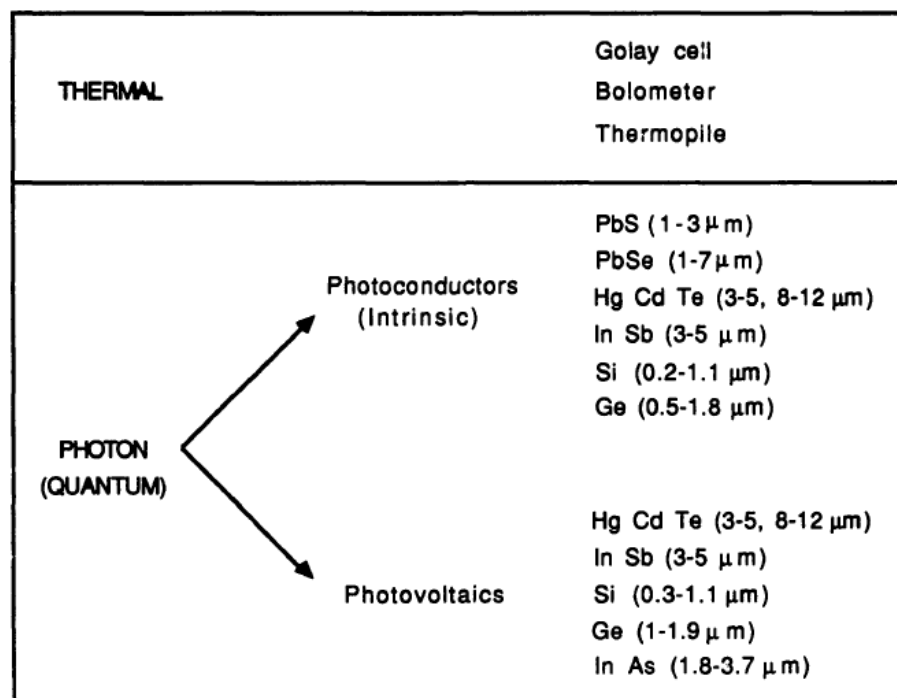


Figure 45: Types of infrared detectors

<sup>8</sup> <https://apps.dtic.mil/dtic/tr/fulltext/u2/a260781.pdf>



### 3.2 Structure

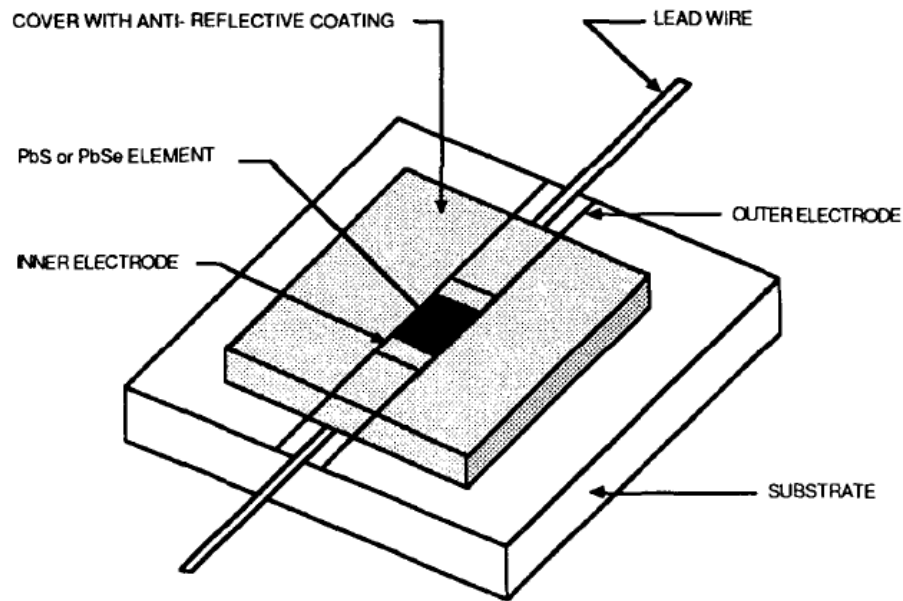


Figure 46: A single element lead salt detector

The structure of a lead salt infrared detector is that of a thin film semiconductor. These thin films are polycrystalline in nature, with individual PbS crystals ranging in size from 0.1  $\mu\text{m}$  to approximately 1.0  $\mu\text{m}$  in diameter, and PbSe crystals ranging in size from 0.2  $\mu\text{m}$  to 0.8  $\mu\text{m}$  in diameter. Lead salt detectors are manufactured as either single element detectors or multi-element detector arrays, the latter for which there are several array designs. A single element detector, which usually possesses the geometry of a thin plate, is shown in Figure 46. The fabrication and basic structure of both of these detector configurations have many similarities. Both configurations utilize chemical deposition techniques to precipitate photosensitive thin films on a flat, cylindrical or spherical substrate surface. However, the most widely used fabrication method is to chemically deposit a lead salt solution onto a flat surface substrate. The major differences between single element detectors and detector arrays are the overall detector sizes, patterns and overall complexity.

#### a) Substrate<sup>9</sup>



Thin transparent quartz glass plate 10\*10\*1.5mm quartz substrate

**US \$265 / lot** (200 pieces)

US \$3.00 New User Coupon [Get coupons](#)

Quantity:

– 1 + 1000 lots available

**Shipping: US \$72.80** to Lebanon via EMS  $\vee$

Estimated Delivery: 5-17 days  $\text{\textcircled{P}}$

Buy Now

Add to Cart

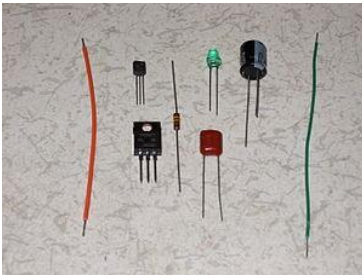
$\heartsuit$  2

$\checkmark$  **20-Day Buyer Protection**  
Money back guarantee

<sup>9</sup> <https://www.sumibe.co.jp/english/product/it-materials/package/prepreg/index.html>

The most widely used fabrication method is to chemically deposit a lead salt solution onto a flat surface substrate

### b) Lead wire

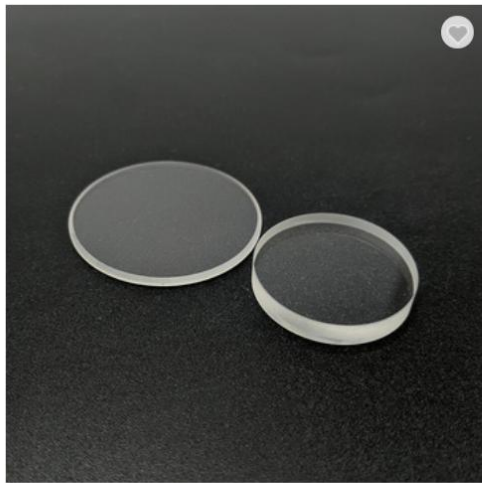


Several kinds of lead wires. A lead wire is a metal wire connected from the electric pole of an electronics part or an electronic component. The lead wire is a coated copper wire, a tinned copper wire or another electrically conductive wire used to connect two locations electrically.


### c) Cover with anti-reflective coating

An antireflective or anti-reflection (AR) coating is a type of optical coating applied to the surface of lenses and other optical elements to reduce reflection. In typical imaging systems, this improves the efficiency since less light is lost due to reflection. In complex systems such as telescopes and microscopes the reduction in reflections also improves the contrast of the image by elimination of stray light. This is especially important in planetary astronomy. In other applications, the primary benefit is the elimination of the reflection itself, such as a coating on eyeglass lenses that makes the eyes of the wearer more visible to others, or a coating to reduce the glint from a covert viewer's binoculars or telescopic sight.

### d) Sapphire window



[View larger image](#)



OEM laser cutting Blank optical glass sapphire window

FOB Reference Price: [Get Latest Price](#)

**\$1.00 - \$100.00** / Pieces | 1 Piece/Pieces (Min. Order)

Quantity(Pieces)	1 - 100	>100
Est. Time(days)	30	Negotiable

[Contact Supplier](#)

[Chat Now!](#)

Seller Support: Trade Assurance – To protect your orders from payment to delivery

Payment: [Online Bank Payment](#) [Pay Later](#) More

Shipping: Alibaba.com Ocean Shipping Service from China to U.S  
[Get shipping quote](#)

## 3.3 Theoretical background

As previously mentioned, the operation of a photoconductive lead salt detector relies heavily on the transfer of infrared energy from incoming photons to electrons residing within the detector material. This transfer results in an electronic reorganization within the atomic structure of the semiconductor. In the case of an intrinsic semiconductor such as PbS or PbSe, energy transferred from a photon striking the surface raises an electron from a non-conducting to a conducting state. This action, along with the influence of temperature, results in the production of an electron-hole pair containing both a

positive and a negative charge carrier. If the detector is biased in a manner similar to that shown in Figure 47, an electric field is developed which will increase the number of charge carriers. This phenomenon, known as the photoconductive effect, thus reduces the resistance of the device. Consequently, this will result in an increase in the amount of current flowing through the device. The measured output signal can be either the change in current through the detector or the change in voltage developed across the load resistor in series with the detector. In most cases, the signal detected is the change in voltage developed across the load resistance which is matched to the dark resistance of the detector.

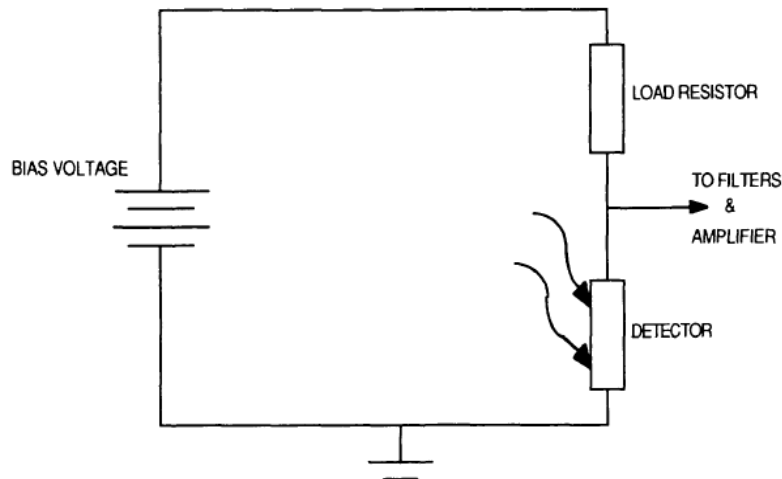


Figure 47: Photoconductive Detector Bias Circuit

### 3.3.1 Basic principle

To extract a useful signal from these detectors, we can exploit this phenomenon. As light falls on the detector the electron flow increases increasing the materials conductivity; and inversely, reducing its resistance. By using a load resistor (typically 1Mohm, as matching the detectors dark resistance will ensure the best detector as a voltage divider, and a bias voltage is applied. as the resistance of the detector changes, the electronic characteristics of a voltage divider are used to measure the "output". debate continues as to whether this mode of operation is the most suitable operation method for PbS and PbSe detectors, with the Microbolometer FPA community discussing the S/N ratio advantages of current related methods.

### 3.3.2 Biasing

our PbS and PbSe detectors are photoconductive and require a biasing voltage to operate, increasing the bias voltage increases signal and noise respectively. A minimum bias voltage is needed to overcome system noise and a maximum voltage cannot be exceeded due to runaway thermal effects. Historically the optimum biasing voltage has been 50V/mm with the maximum being roughly double, but progress in modern electronics means that lower voltages can now be used without making compromises in the performance. LASER COMPONENTS corporate research is looking into the trade-offs.

### 3.3.3 Noise

the two dominant types of noise in a PbS or PbSe detector are generation-recombination noise and 1/f noise, which is why historically detector specifications are given at 1 KHz to represent optimum

performance. However, we understand that more often than not these detectors are used at lower operation frequencies which is why LASER COMPONENTS lists  $D^*$  values for operation at 90 Hz as well. As a rule of thumb, you can expect a threefold increase in noise at 90 Hz when compared to 1 KHz.

## 4 Overview (William V. Cummings Jr., 1951)<sup>10</sup>

The infrared region of the spectrum was first discovered in 1800 by Sir William Herschel. While checking the heating power of the various colors in the solar spectrum, he found that the greatest heating effect was not inside the visible portion, but just beyond the red edge of the spectrum. Thus a simple heat detecting instrument, the thermometer, became the first infrared detector. (3) Sensitive heat detecting devices such as bolometers, thermocouples, and various other radiometers have been used as means of detecting and studying infrared radiation down to the present time. In fact, above 3.5 microns, thermal detection is used almost exclusively in infrared spectrometers.

For that part of the spectrum below 3.5 microns, other special techniques have been discovered and developed. Among these methods is the detection and measurement of spectra by photocells. Three types of photoelectric phenomena have been adapted to spectroscopy: (4) the photo emissive effect, which is the ejection of electrons from matter when energy is imparted to it by radiation; the photovoltaic effect, which is the generation of a potential difference between two electrodes when one of them is irradiated; and the photoconductive effect, which is the change of electrical conductivity of a material caused by radiation falling upon it. Cells incorporating these properties have been developed and used, but only the photoconductive cells have an appreciable response in the infrared. Detectors using various photoconductive materials have been developed, but at the present time those which have photosensitive elements composed chiefly of lead sulfide appear to be superior. Figure 48 illustrates the spectral sensitivities of various photocells and the visibility curve of the eye. (5) It should be pointed out that in this graph the maximum of sensitivity for each curve is arbitrarily set at 100. The two typical curves shown for lead sulfide surfaces indicates that the spectral response of cells of this type will vary somewhat in each individual case.

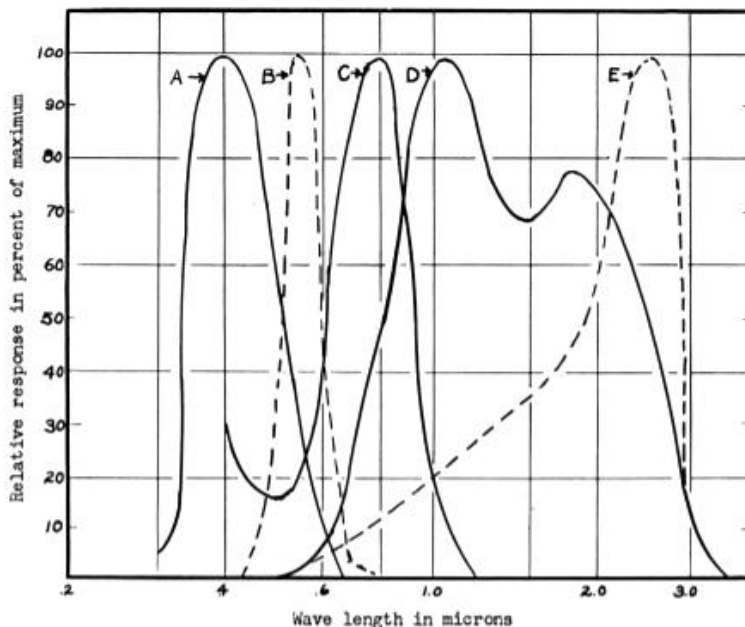
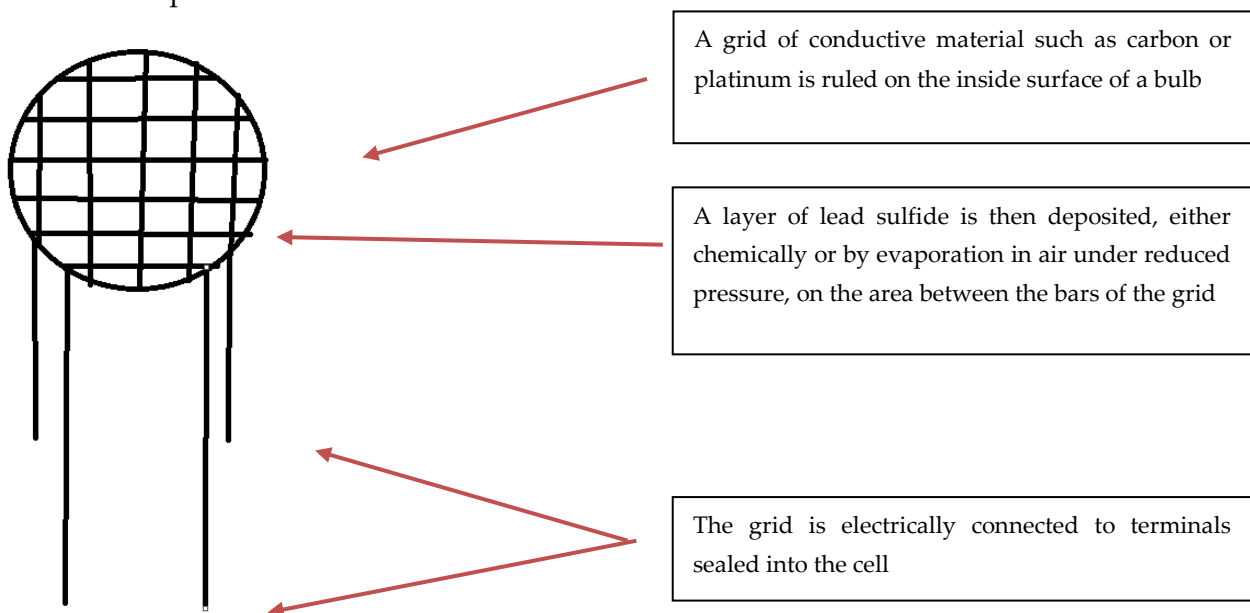


Figure 48: Spectral Response Curves of Various Photocells

<sup>10</sup> [https://scholarsmine.mst.edu/cgi/viewcontent.cgi?article=5150&context=masters\\_theses](https://scholarsmine.mst.edu/cgi/viewcontent.cgi?article=5150&context=masters_theses)

The photoconductive properties of lead sulfide when irradiated by wave lengths between 1 and 3.5 microns were first utilized by the Germans during world War II as a means of detecting infrared radiation. During the latter stages of the conflict PbS cells were developed by the United States and Great Britain, for it was noted that within their response range they were far superior to any other detector in speed of response and sensitivity. To the physicist, this indicated a powerful tool for infrared spectroscopy. Experiments by Sutherland and others (6) indicate that the signal-to-noise ratio for the PbS cell at its point of maximum sensitivity is increased to such an extent that slit widths can be reduced by a factor of 10 in going from thermocouple to lead sulfide detector. This, in turn, gives a corresponding increase in resolving power. Advantage is also derived from the exceptional speed of response of the lead sulfide detector which has a time constant of less than .001 sec. compared to times of about .1 sec. and .01 sec. for the thermocouple and bolometer, respectively. This permits the use of faster "chopping" rates for the incident radiation, which in turn simplifies the problem of amplification. <7>

The methods of manufacturing these cells are variable, but, all manufacturers seem to follow the same general procedure. A grid of conductive material such as carbon or platinum is ruled on the inside surface of a bulb and the grid is electrically connected to terminals sealed into the cell. A layer of lead sulfide is then deposited, either chemically or by evaporation in air under reduced pressure, on the area between the bars of the grid. (At the present time, the evaporation process seems to produce cells with more desirable characteristics.) A heat treatment then follows at determined temperature and pressure conditions. Finally, the activated surface is sealed off in vacuum or otherwise protected from the atmosphere.



As a result of this procedure, the original lead sulfide lattice has lost the sulfur in some small regions and consequently has an excess of lead. In other regions of the material, the sulfur has been replaced by oxygen, which had been contained in the lattice or absorbed interstitially, leaving as a final product a homogeneous mixture of both types. A layer of oxygen atoms also may be absorbed on the surface and barrier layers may be formed at the contact surface of the grid material. The characteristics of the cell will, to a great extent, depend upon this formation. [8]

## 5 IR photoconductive detectors<sup>11</sup>

- ▶ PbSe and PbS Photoconductive Detectors
- ▶ Linear Response for 1.0 - 2.9  $\mu\text{m}$  or 1.5 - 4.8  $\mu\text{m}$
- ▶ TO-5 Package Style



Lead Sulfide (PbS) and Lead Selenide (PbSe) photoconductors are widely used for the detection of infrared radiation from 1.0 to 4.8  $\mu\text{m}$ . Photoconductors detect light in a broader wavelength range, offer higher detection capability, and provide better linear response in the IR than typical PIN junction photodiodes.

### 5.1 Photoconductors vs. Photodiodes

Unlike PIN junction photodiodes, which generate a photocurrent when light is absorbed in the depleted region of the junction semiconductor, the photoconductive material in these devices exhibits a decrease in electrical resistance when illuminated with IR radiation. Photoconductive detectors typically have a very linear response when illuminated with IR radiation.

### 5.2 Usage Notes

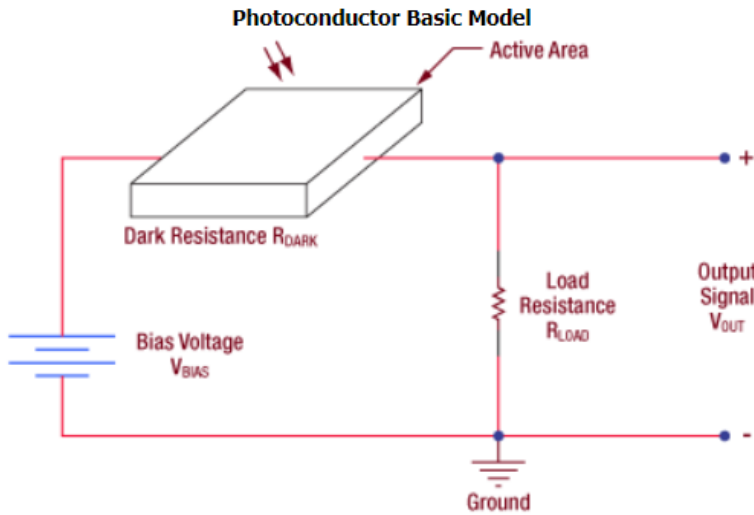
Photoconductors function differently than typical PIN junction photodiodes. We recommend that an optical chopper be employed when using these detectors with CW light, due to signal noise issues. PbS and PbSe detectors can be used at room temperature. However, temperature fluctuations will affect dark resistance, sensitivity, and response speeds (see the Temperature Considerations section in the Tutorial tab for details).

Theory

### 5.3 Theory of Operation

For photoconductive materials, incident light will cause the number of charge carriers in the active area to increase, thus decreasing the resistance of the detector. This change in resistance leads to a change in measured voltage, and hence, photosensitivity is expressed in units of V/W. An example operating circuit is shown. Please note that the circuit depicted is not recommended for practical purposes since low frequency noise will be present.

<sup>11</sup> [https://www.thorlabs.com/newgrouppage9.cfm?objectgroup\\_ID=6479](https://www.thorlabs.com/newgrouppage9.cfm?objectgroup_ID=6479)



The detection mechanism is based upon the conductivity of the thin film of the active area. The output signal of the detector with no incident light is defined by the following equation:

$$V_{OUT} = \frac{R_{LOAD}}{R_{DARK} + R_{LOAD}} * V_{BIAS}$$

A change  $\Delta V_{OUT}$  then occurs due to a change  $\Delta R_{Dark}$  in the resistance of the detector when light strikes the active area:

$$\Delta V_{OUT} = -\frac{R_{LOAD}V_{BIAS}}{(R_{DARK} + R_{LOAD})^2} * \Delta R_{DARK}$$

## 5.4 Frequency Response

Photoconductors must be used with a pulsed signal to obtain AC signals. Hence, an optical chopper (shown in Figure 49) should be employed when using these detectors with CW light. The detector responsivity ( $R_f$ ) when using a chopper can be calculated using the equation below:

$$f_c = \frac{1}{2\pi\tau_r}$$

Here,  $f_c$  is the chopping frequency,  $R_0$  is the response at 0 Hz, and  $\tau_r$  is the detector rise time.



Figure 49: The SR540 optical beam chopper from Stanford Research Systems

An optical chopper is a device that interrupts a light beam at periodic intervals. By varying the frequency of operation of the chopper it can be used for various applications. The first ever optical chopper was invented in the 1800s and was used to measure the speed of light.



The chopper consists of a mechanical disc that rotates at a certain speed. In order to improve the performance of the chopper high precision and stable mechanical components must be chosen. This worksheet will provide details on the working principle, construction and applications of optical beam choppers.

## 5.5 Temperature Considerations

These detectors consist of a thin film on a glass substrate. The effective shape and active area of the photoconductive surface varies considerably based upon the operating conditions, thus changing performance characteristics. Specifically, responsivity of the detector will change based upon the operating temperature.

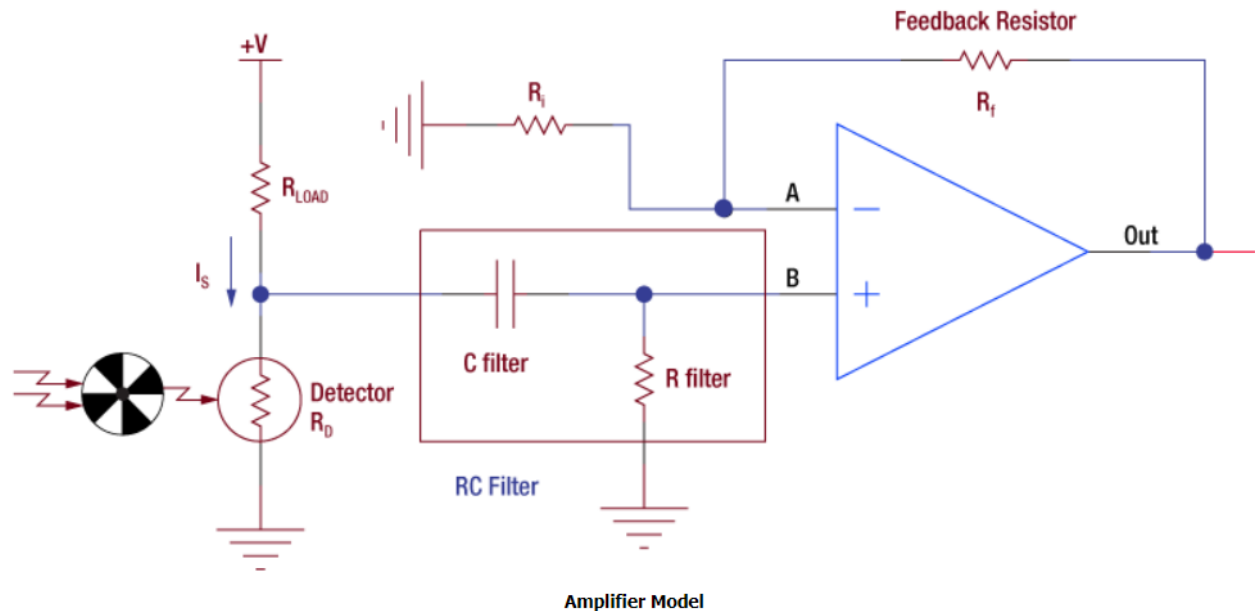
Temperature characteristics of PbS and PbSe bandgaps have a negative coefficient, so cooling the detector shifts its spectral response range to longer wavelengths. For best results, operate the photodiode in a stable controlled environment. See the Operating Manuals for characteristic curves of Temperature vs. Sensitivity for a particular detector.

## 5.6 Typical Photoconductor Amplifier Circuit

Due to the noise characteristic of a photoconductor, it is generally suited for AC coupled operation. The DC noise present with the applied bias will be too great at high bias levels, thus limiting the practicality of the detector. For this reason, IR detectors are normally AC coupled to limit the noise. A pre-amplifier is required to help maintain the stability and provide a large gain for the generated current signal.

Based on the schematic below, the op-amp will try to maintain point A to the input at B via the use of feedback. The difference between the two input voltages is amplified and provided at the output. It is also important to note the high pass filter that AC couples the input of the amplifier blocks any DC signal. In addition, the resistance of the load resistor (RLOAD) should be equal to the dark resistance of the detector to ensure maximum signal can be acquired. The supply voltage (+V) should be at a level where the SNR is acceptable and near unity. Some applications require higher voltage levels; as a result, the noise will increase. Provided in chapter 4 of the Operating Manual is a SNR vs. Supply Voltage characteristic curve to help determine best operating condition. The output voltage is derived as the following:

$$V_{out} = \left(1 + \frac{R_f}{R_i}\right) * I_s R_D$$



## 5.7 Signal to Noise Ratio

Since the detector noise is inversely proportional to the chopping frequency, the noise will be greater at low frequencies. The detector output signal is linear to increased bias voltage, but the noise shows little dependence on the bias at low levels. When a set bias voltage is reached, the detector noise will increase linearly with applied voltage. At high voltage levels, noise tends to increase exponentially, thus degrading the signal to noise ratio (SNR) further. To yield the best SNR, adjust the chopping frequency and bias voltage to an acceptable level.

## 5.8 Noise Equivalent Power

The noise equivalent power (NEP) is the generated RMS signal voltage generated when the signal to noise ratio is equal to one. This is useful, as the NEP determines the ability of the detector to detect low level light. In general, the NEP increases with the active area of the detector and is given by the following equation:

$$NEP = \frac{\text{Incident Energy} * \text{Area}}{\frac{S}{N} * \sqrt{\Delta f}}$$

Here,  $S/N$  is the Signal to Noise Ratio,  $\Delta f$  is the Noise Bandwidth, and Incident Energy has units of  $W/cm^2$ . For more information on NEP, please see Thorlabs' Noise Equivalent Power White Paper.

## 5.9 Dark Resistance

Dark Resistance is the resistance of the detector under no illumination. It is important to note that dark resistance will increase or decrease with temperature. Cooling the device will increase the dark resistance.

## 5.10 Detectivity (D) and Specific Detectivity (D\*)

Detectivity (D) is another criteria used to evaluate the performance of the photodetector. Detectivity is a measure of sensitivity and is the reciprocal of NEP.

$$D = \frac{1}{NEP}$$

Higher values of detectivity indicate higher sensitivity, making the detector more suitable for detecting low light signals. Detectivity varies with the wavelength of the incident photon.

NEP of a detector depends upon the active area of the detector, which in essence will also affect detectivity. This makes it hard to compare the intrinsic properties of two detectors. To remove the dependence, Specific Detectivity ( $D^*$ ), which is not dependent on detector area, is used to evaluate the performance of the photodetector. In the equation below,  $A$  is the area of the photosensitive region of the detector and  $\Delta f$  is the effective noise bandwidth.

$$D^* = \frac{\sqrt{A \cdot \Delta f}}{NEP}$$

**PbS Photoconductor: 1.0 - 2.9  $\mu\text{m}$**



Zoom

- ▶ Good Performance for 1.0 - 2.9  $\mu\text{m}$  Range
- ▶ For Detection of CW Light We Recommend an [Optical Chopper](#)
- ▶ Also Comes as a Packaged, Amplified Detector, the [PDA30G](#)

Item # <sup>a</sup>	Info	Wavelength Range	Active Area	Package Type	Rise Time <sup>b</sup>	Peak Wavelength	Peak Sensitivity <sup>c</sup>	Specific Detectivity <sup>d</sup>	Dark Resistance	Compatible Sockets
FDPS3X3	<a href="#">Info</a>	1.0 - 2.9 $\mu\text{m}$	9 mm <sup>2</sup>	TO-5	200 $\mu\text{s}$	2.2 $\mu\text{m}$ (Typ.)	2 x 10 <sup>4</sup> V/W (Min) 5.0 x 10 <sup>4</sup> V/W (Typ.)	1 x 10 <sup>11</sup> cm <sup>2</sup> Hz <sup>1/2</sup> /W (Typ.)	0.25 - 2.5 MOhm	<a href="#">STO5S</a> <a href="#">STO5P</a>

a. All measurements performed with a 50 Ohm load unless stated otherwise.  
 b. Rise Time is measured from 0 to 63% of final value.  
 c. Measured at Peak Wavelength, Chopping Frequency of 600 Hz, and Bias Voltage of 15 V,  $R_{\text{DARK}} = R_{\text{LOAD}}$   
 d. Measured at Peak Wavelength and Chopping Frequency of 600 Hz

Based on your currency / country selection, your order will ship from Newton, New Jersey

+1	Qty	Docs	Part Number - Universal	Price	Available
	<input type="text"/>		<a href="#">FDPS3X3</a> PbS Photoconductor, 3 mm x 3 mm Active Area, 200 $\mu\text{s}$ Rise Time, 1.0 - 2.9 $\mu\text{m}$	\$191.21	Today

## 6 Room-temperature, thin-fil, PbS photoconductive detector hardened against laser damage<sup>12</sup>

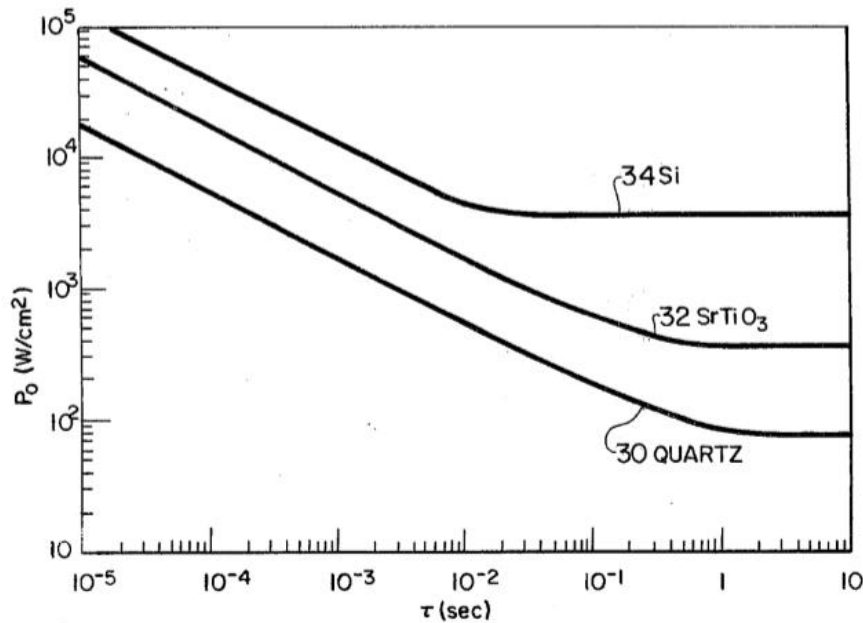
FIG. 1 shows a thin-film, photoconductive, infrared detector 10 incorporating the laser hardening techniques of the present invention. The active detecting layer is a thin film 12 of photoconductive material which is sensitive to infrared radiation at ordinary room temperatures (approximately 290 K. to 310 K.), such as a thin film of PbS, typically 1  $\mu\text{m}$  in thickness and 0.25-10mm in surface area. Electrical connection is made to the thin film in a conventional manner as indicated by electrical leads 14. The thin film 12 is deposited by conventional techniques on a substrate 16, which as previously noted, provides mechanical stability and electrical isolation for the thin film. The substrate 16 is mounted on a metal heat buffer 18 by means of an interface 20 of negligible thermal impedance. The interface 20 includes a metalized back-surface 22 of substrate 16 and a bonding layer 24. As will be described hereinafter, the characteristics of the substrate 16, the heat buffer 18, and the interface 20 are very important in hardening the detector against damage due to laser irradiation and constitute novel features of the present detector. The detector 10 (specifically heat buffer 18) is mounted on a conventional heat sink as shown conceptually at 26 and 28. Since laser irradiation may result in high thermal loading of thin-film detectors, the thermal configuration of a detector is important in determining its susceptibility to damage from optical radiation. To prevent irreversible detector damage, the heat generated by the laser irradiation must be dissipated so that the thin film does not reach the critical temperature where detector degradation begins. This is approximately 600 K. in a PbS detector. The detector of the present invention is designed to provide efficient heat flow from the thin film to prevent such detector degradation. Considering first the design of substrate 16, the thermal conductivity of the substrate, the thickness of the substrate, and the surface area of the substrate relative to the detector absorbing area are important factors in hardening the detector against laser irradiation. FIG. 2 shows the calculated power density  $P$  for heating thin films of PbS on substrates of quartz, strontium titanate and silicon (shown by curves 30, 32, and 34, respectively) from 300 K. to 600 K. (the damage threshold temperature) as a function of irradiation time  $t$ . The substrates are of the same thickness and have very good thermal contact with a heat sink so that heat flow within the detector is not limited by an interface layer which might confine the heat within the substrate. Further explanation of the calculations referred to herein may be found in "Thermal Analysis of Laser Damage in the Thin-film Photoconductors", Journal of Applied Physics, Vol. 47, No. 7, July 1976, authored by the inventors of the present application.

As shown in FIG. 2,  $P$  is strongly dependent on substrate material over a wide range of irradiation times. For times between 10 and 10-sec, the damage thresholds for detectors on silicon substrates are about seven times those for detectors on quartz and about two times those for detectors on strontium titanate. A comparison of the magnitudes of the damage thresholds for the different substrates at a specific irradiation time in this range indicates that  $P$  is approximately proportional to the square root of substrate thermal conductivity. (For example, the thermal conductivity of silicon is about 50 times that of quartz). For long times, the ratio of damage thresholds for silicon and quartz increases to 50 indicating the  $P$  is proportional to thermal conductivity. This analysis indicates that, for applications

---

<sup>12</sup> <https://patentimages.storage.googleapis.com/c5/3c/aa/789099fb49e8e4/US4117329.pdf>

where thin film photoconductors will be subject to intense radiation, the substrate should be fabricated from materials such as silicon or sapphire which have large thermal conductivities. The advantages of using a silicon or sapphire substrate over quartz become even greater for detectors operating at intermediate or low temperatures. For example, at 77 K., the thermal conductivity of silicon is three orders of magnitude greater than that of quartz, as compared to the factor of 50 at room temperature. Accordingly, materials that have high thermal conductivities such as silicon (1.5 W/cm K) and sapphire (0.33 W/cm-K) are preferred materials for use as substrate 16 in the present invention.



**FIG. 2**

The substrate thickness also has an effect on heat flow in the detector. Consider a detector on a quartz substrate which is bonded to a heat sink by an adhesive layer with a large thermal conductance per unit area ( $h = 10 \text{ W/cmK}$ ) so that the bonding layer does not limit heat flow. The calculated power density  $P$  required to heat a thin film from 300' to 600 K. is shown in FIG. 3 as a function of irradiation time for three different substrate thicknesses. The thicknesses used in the calculation to generate curves 36, 38 and 40 are 0.01 0.03 and 0.1 cm, respectively. For sufficiently short times ( $t(10 \text{ msec})$ ), heat does not diffuse to the rear of the substrate and  $P$  is independent of substrate thickness. The substrate thickness can have a large effect on  $P$  if the pulse duration is longer than 50 msec. For very large  $T$ , heat is conducted to the heat sink at the same rate it is deposited by the optical radiation. In this limit,  $P$ , asymptotically approaches a constant value independent of  $T$  and is inversely proportional to substrate thickness.

Therefore, decreasing the substrate thickness will improve detector resistance to laser irradiation if the thermal conductivity between the substrate and the heat sink is better than the thermal conductivity within the substrate. It is noted that the substrate must be of sufficient thickness to supply mechanical stability for the thin films.

The heat flow in the detector will also be improved if the substrate surface area, as indicated by 42 in FIG. 1, is made large compared to the absorbing detector area, as indicated by 44 in FIG.1. This will

allow transverse heat flow within the substrate 16, as well as heat flow in the direction of optical radiation, to contribute to the power dissipation of the detector.

Considering now the design of the interface 20, if a thin highly-conductive material is used for the detector substrate 16, the interface 20 may become a thermal bottleneck (the thermal bottleneck is referred to the **points where the temperature is excessively high mainly due to design flaws**, the term being of primal importance in the Electronics Industry.). This bottleneck becomes important at long times when heat has had time to diffuse to the rear of the substrate. FIG. 4 shows the calculated power density thresholds  $P_0$  for PbS thin films on silicon substrates assuming several values for the thermal conductance per unit area ( $h$ ) of the interface 20. The damage thresholds depicted by curves 46, 48, 50, and 52 were calculated using values of the  $h$  equal to 10, 1, 10, and 10 W/cm<sup>2</sup>K, respectively. For  $t < 10$  msec, the thermal conductance of the interface 20 is not important and the calculated threshold is the same for the four values of  $h$  used. For irradiation times  $t < 1$  sec, the above variation in  $h$  changes the calculated power density threshold  $P_0$  by several orders of magnitude.

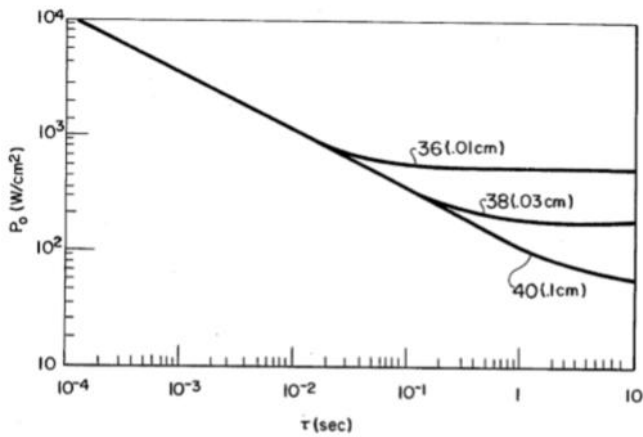


FIG. 3

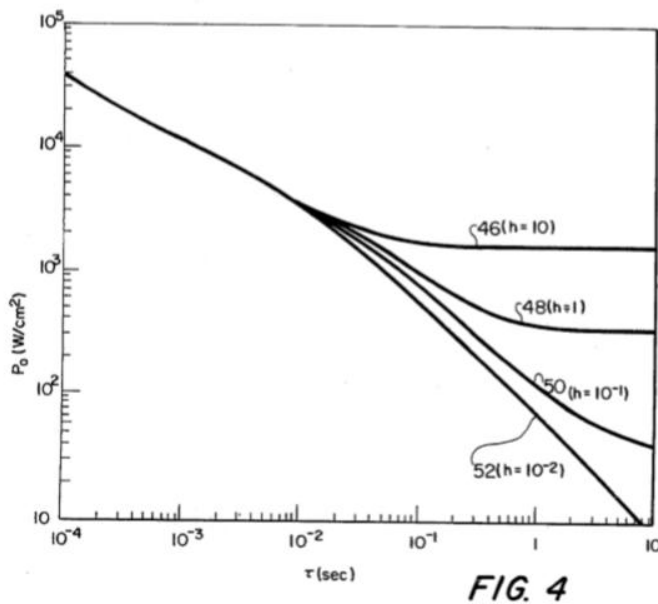
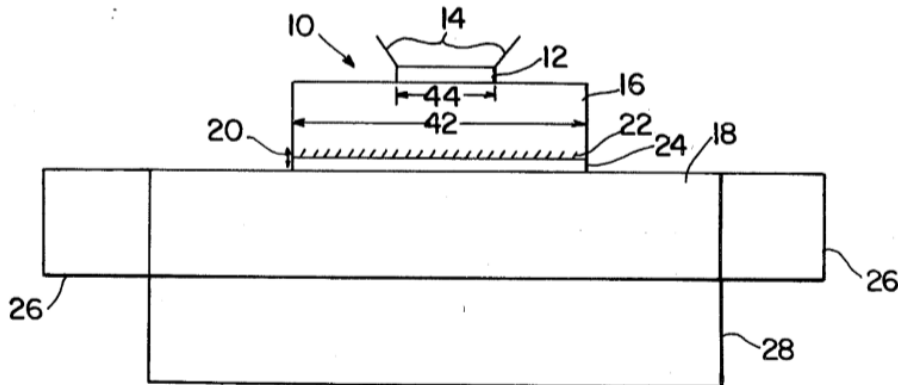


FIG. 4

In the preferred embodiment of detector 10, the back surface of the substrate 16 is metalized at 22 with a metal of high thermal conductivity, such as silver or copper, by conventional processes such as diffusion. This metalized surface has the effect of increasing the thermal conductivity at the back of

the substrate 16, and also providing a metal layer so that a highly-thermally conductive material such as solder may be used as the bonding layer 24 between the substrate and the metal heat buffer.

It can be seen that thermal conductance of the interface 20 is relatively more important if the substrate is efficient in transferring heat from the absorbing surface of the detector. If the interface layer 20 is less efficient in transferring heat than the substrate 16, the heat generated by the laser radiation will build up in the substrate.



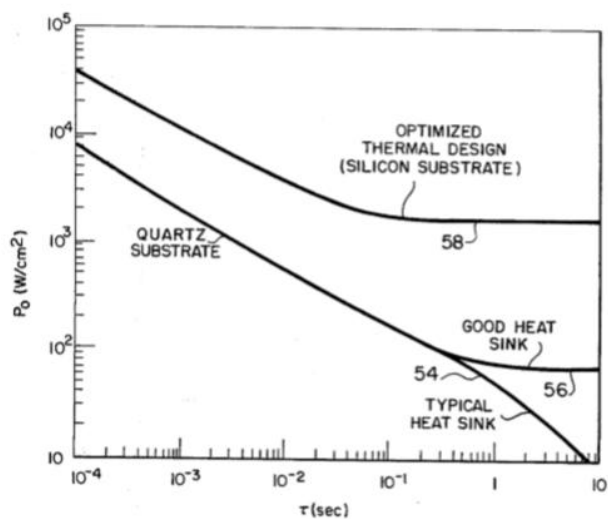
It should be clear that if interface layer 20 has a higher thermal conductivity than substrate 16, the substrate should be as thin as possible considering requirements of mechanical support, electrical isolation, and formation of the metalized back surface. These factors require a minimum substrate thickness of approximately 0.005 cm. Alternatively, if interface layer 20 has a lower thermal conductance than substrate 16, it is advantageous to have a substrate of a larger thickness so that the substrate may dissipate more heat itself.

The use of a heat buffer 18 is the final novel feature of a detector according to the present invention. Heat buffer 18 is a high-thermal-conductivity, large-thermal mass in intimate thermal contact with the substrate 16 (via interface 20) and it has a two-fold function. The first function is to remove heat from interface 20 as rapidly as possible and redistribute it throughout the entire buffer to eliminate any appreciable heat buildup in the region behind the interface. This requires a high thermal conductivity material. The second function is to act as a high-specific-heat thermal reservoir until heat can be removed to the heat sink. The large thermal mass of the heat buffer maintains the heat buffer (and therefore the detector) at a low temperature. For long optical irradiation times, heat can be effectively conducted into the heat sink and the function of the heat buffer becomes simply an effective conduit for heat transport. Copper is a preferred material for use as the heat buffer 18.

The type of heat sink used with detector 10 will depend on the particular application. Frequently the detector 10 is surrounded circumferentially by a ring which acts as a heat sink as shown at 26 in FIG. 1. Alternatively, the detector 10 may be mounted on a heat sink such as shown at 28. In that case, the heat sink 28 and the heat buffer 18 may be combined in a single piece of highly-thermally-conductive material such as copper.

The preceding analysis shows that thin-film photoconductors can withstand laser irradiation of much higher power if they are fabricated on thin, highly thermally conductive substrates which are efficiently coupled to heat sinks. These results are summarized in FIG. 5. Curve 54 is the threshold for onset of damage of PbS photoconductors on a quartz substrate assuming the thermal conductance per unit area of the bonding layer is 0.01 W/cmK. This thermal configuration is typical of that found in

many prior PbS applications. Curve 56 refers to thresholds for PbS detectors on quartz substrates with higher thermal conductance per unit area of the bonding layer. Curve 58 is the calculated threshold for a silicon substrate with a bonding layer having the same thermal conductance per unit area as the bonding layer in curve 56. These calculations show that an optimized thermal design can significantly increase the damage threshold for all irradiation times shown. In particular, for a 10-second irradiation time, the damage thresholds can be increased by more than two orders of magnitude. These considerations are particularly important for detectors exposed to chopped radiation or repetitively pulsed lasers where the energy of one pulse may not damage the detector but the integrated power may.



**FIG. 5**

Although the present invention has been described with application to room temperature PbS detectors, it is noted that other thin-film photoconductive detectors may be hardened against laser damage by using the techniques of the present invention. For example, a thin-film lead selenide (PbSe) detector (which operates at liquid nitrogen temperature) may be hardened against laser irradiation by fabrication on a thin, highly-conductive substrate which is mounted on a heat buffer by means of a highly-conductive interface. The heat sink in this case must be capable of maintaining the required operating temperature in the liquid-nitrogen Dewar.

It is also noted that when the word "high" is used to describe the thermal conductivity of the substrate 16 in the present specification, a thermal conductivity of approximately 0.25W/cm-K to 15 W/cm-K is denoted. When the term "high" is used to describe the thermal conductivity of the heat buffer 18 or the bonding layer 24, a thermal conductivity of approximately 0.5 W/cm K to 20 W/cm-K is denoted. For example, silicon would be a material having a thermal conductivity within the former range and copper would be a material within the latter range. It is further noted that when the word "thin" is used to describe the substrate 16, a substrate of approximately 0.005 cm to 0.025 cm in thickness is denoted.

Obviously, many modifications and variations of the present invention are possible in light of the above teachings. It is therefore to be understood that within the scope of the appended claims, the invention may be practiced otherwise than as described.

What is claimed and desired to be secured by Letters Patent of the United States is:



1. A thin-film infrared detector hardened against damage from laser irradiation comprising: a thin film of material sensitive to infrared radiation; a thin substrate upon the front-surface of which said
2. thin film is deposited, said substrate having a high thermal conductivity to provide efficient heat flow from said thin film through said substrate, said substrate having a surface area that is large relative to the absorbing area of said thin film so that heat generated by irradiation will be distributed transversely within said substrate; a heat sink; and an interface of negligible thermal impedance between said substrate and said heat sink for removing heat from said substrate.
3. The detector of claim 1 wherein said thin film comprises lead sulfide.
4. The detector as recited in claim 1, wherein said interface of negligible thermal impedance comprises: a metalized back surface of said substrate, said back surface being metallized with a metal of high thermal conductivity; and a bonding layer of high thermal conductivity between said back-surface and said heat sink.
5. The detector of claim 3 wherein said bonding layer comprises solder.
6. The detector of claim 3 wherein said thin substrate is sapphire.
7. The detector of claim 3 wherein said thin substrate is silicon.
8. A thin-film, photoconductive, infrared detector hardened against damage from laser irradiation comprising: a thin film of photoconductor material sensitive to infrared radiation; a thin substrate upon the front-surface of which said thin film is deposited, said substrate having a high thermal conductivity to provide efficient heat flow from said thin film through said substrate, said substrate having a surface area that is large relative to the absorbing area of said thin film so that heat generated by said irradiation will be distributed transversely within said substrate, the back surface of said substrate being metallized with a metal of high thermal conductivity; a bonding layer of high thermal conductivity; and a heat buffer upon which said substrate is mounted, contact being made between said buffer and the metalized back surface of said substrate by said bonding layer said heat buffer having a high thermal conductivity to remove heat from said inter face as rapidly as possible and redistribute it throughout the entire buffer to eliminate heat buildup in the region behind said interface, said heat buffer having a large thermal mass to act as a high-specific-heat thermal reservoir.
9. The detector of claim 7 further comprising a heat sink in good thermal contact with said heat buffer for removing heat from said heat buffer.
10. The detector of claim 7 wherein said thin substrate is sapphire.
11. The detector of claim 7 wherein said thin film comprises lead sulfide.
12. The detector of claim 10 wherein said heat buffer comprises copper.
13. The detector of claim 10 wherein said thin substrate is silicon.
14. A thin-film, photoconductive, infrared detector hardened against damage from laser irradiation comprising: a thin film of photoconductor material sensitive to infrared radiation; a thin substrate upon the front-surface of which said thin film is deposited, said substrate having a high thermal conductivity to provide efficient heat flow from said thin film through said substrate, said substrate having a surface area that is large relative to the absorbing area of said thin film so that heat generated by said irradiation will be distributed transversely

- within said substrate; an interface of negligible thermal impedance located on the back-surface of said substrate; and a heat buffer upon which said substrate is mounted, contact being made with said buffer by said inter face, said heat buffer having a high thermal conductivity to remove heat from said interface as rapidly as possible and redistribute it throughout the entire buffer to eliminate heat buildup in the region behind said interface, said heat buffer having a large thermal mass to act as a high-specific heat thermal reservoir.
15. The detector of claim 13 further comprising a heat sink in good thermal contact with said heat buffer for removing heat from said buffer.
  16. The detector as recited in claim 13 wherein said interface of negligible thermal impedance comprises: a metalized back-surface of said substrate, and a bonding layer of high thermal conductivity between said back-surface and said heat sink.
  17. A detector of claim 15 wherein said bonding layer comprises solder.

## 7 PbS Synthesis<sup>13</sup>

### 7.1 Prepare Reactants

Prepare reaction mixture with 14 g of octadecene, 1.4 grams of oleic acid, 450 mg of lead oxide. When it mixes up it is murky yellow at first and then becomes clear when it is heated up.

### 7.2 Degas the mixture

The Schlenk line is used to degas the reaction mixture. Remove the nitrogen bubbler and replace with a pipette bulb. Slowly turn the stopcock from nitrogen flow to vacuum. First watch the pipette bulb when it collapses vacuum is being pulled on the solution. Now slowly turn the stopcock while watching the reaction mixture making sure not over-boil. Once the boiling mixture has stabilized fully-open the vacuum valve. Leave the mixture under vacuum for approximately 1 hour. Slowly turn the stopcock back to nitrogen while holding a finger over the bubbler to prevent pulling the silicon fluid into the Schlenk line. Remove the pipette bulb and replace the nitrogen bubbler. Increase the reaction mixture to 180 degrees

### 7.3 Injection

Prepare the injection mixture from 4 gms of octadecene in 210 mL of hexylmethylidisilazane (HMDS). Once the reaction mixture has stabilized purge a syringe with nitrogen. Draw up the injection mixture and quickly insert it into the reaction vessel. Within second the mixture should turn a turbid black color. Let it react for 5 minutes and then quench the reaction in an ice bath. After it comes to room temperature transfer it to a separatory funnel.

### 7.4 Cleaning

After the synthesis is quenched it is necessary to remove excess oleic acid and other impurities. Two methods are shown:

A) Separatory Funnel:

1. pour PbS QDs (dissolved in minimal amount of hexanes) into sep. funnel
2. precipitate with methanol (MeOH)
3. Add back small amounts of hexanes and shake funnel vigorously between additions. If there is still precipitated product clinging to the walls of the funnel between hexanes additions, continue to add more hexanes. Once the product stops sticking to the walls, let the funnel sit for a minute or so to see if any phase separation occurs. If not, continue adding small amount of hexanes until it does. Note that only a small amount of separation will be seen at the bottom of the funnel at first, and the mixture will have to sit for at least 30 mins to fully separate. If no phase separation is observed after a few additions, the funnel can be placed in the freezer to speed the process.
4. Drain off the clear bottom MeOH layer into the waste
5. Drain small amounts (~1 or 2 mL portions) of PbS into a centrifuge tube.

---

<sup>13</sup> <https://youtu.be/bKLDkjV6Mbc>

6. Precipitate by filling the tube with MeOH
7. Centrifuge the tube (5 min, 3000 RPM), and pour off clear MeOH layer
8. Pour another addition of PbS into the same tube and repeat steps 6) and 7). Note: for the first two cycles, multiple tubes can be used rather than just one, but on the third (last) cleaning step, it is generally preferred to use a single tube to consolidate product.
9. Dissolve the product in minimal amount of hexanes, vortex, sonicate (5 mins, or until dissolved) and add PbS back to the separatory funnel. Repeat the above steps for the first two cleaning cycles.

B) Simply use multiple centrifuge tubes:

- (1) Dissolve the product in small amount of hexanes, then vortex and sonicate until QDs dissolve.
- (2) Precipitate by filling each centrifuge tube with MeOH
- (3) Centrifuge each tube (5 min, 3000 RPM)
- (4) Discard clear supernatant
- (5) For the first two cleaning cycles, repeat the above steps

To consolidate into a single tube, just choose one tube to keep and repeat step 1) above for the other tubes. Then successively add the dissolved QDs of ONE of the other tubes to to the dry product in the tube you chose to keep and repeat steps 2-4 above until all tubes have been combined into one (only add the contents of one tube for each step precipitation-centrifuge cycle-do not combine the contents of all remaining tubes at once)

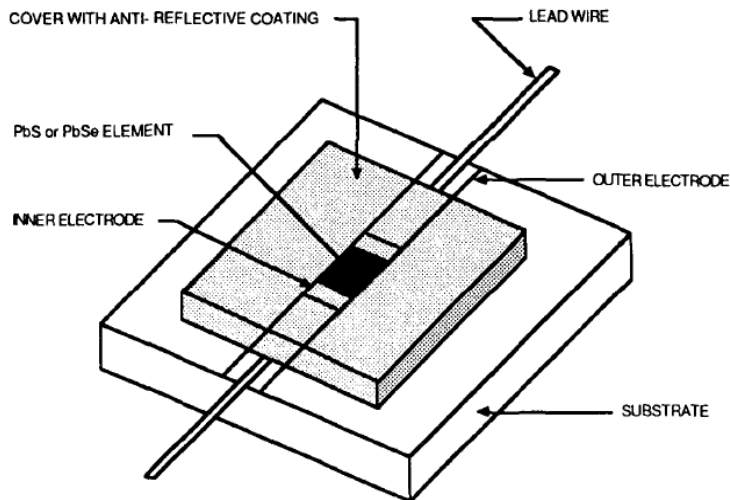
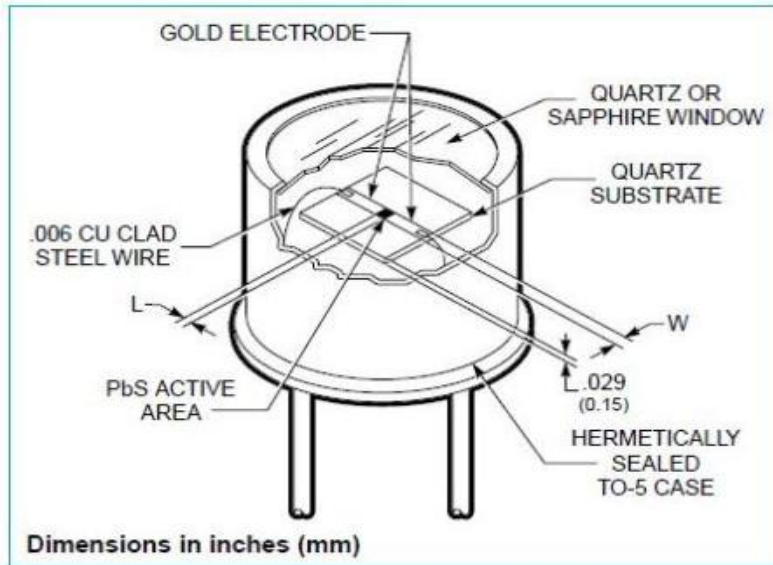
In both cases, once the cleaning cycles are complete, the QDs can be dissolved in hexanes or toluene and left to sit. Alternatively, a septum cap can be placed on the centrifuge tube which can then be placed on the Schlenk line to dry.

## 7.5 PbS/Polymer Nanocomposite Optical Materials with High Refractive Index

High refractive index nano-PbS/polymer composites were fabricated from reactive lead-containing precursors and polythiourethane (PTU) oligomer terminated with isocyanate group, followed by in situ gas/solid reaction. The lead-containing precursor with a chemical formula of  $\text{Pb}(\text{SCH}_2\text{CH}_2\text{OH})_2$  was synthesized in water phase at  $\text{pH} = 5.9$  and exhibited an absorption at 317 nm in dimethyl sulfoxide (DMSO) in UV-vis spectra. PbS nanoparticles can be formed in DMSO after treatment with  $\text{H}_2\text{S}$ . TEM studies indicated that the PbS nanoparticles were smaller than 10 nm and aggregated seriously in DMSO. After the precursors were incorporated into PTU oligomer, the obtained composite films were treated with  $\text{H}_2\text{S}$  to obtain PbS nanoparticles/PTU nanocomposite films. TEM showed that the nanocomposites exhibited interesting phase behaviors depending on the precursor content in films. A uniform spherical aggregate of PbS nanoparticles (nanospheres) with a size smaller than 100 nm formed in the nanocomposite films below 26.3 wt % of lead-containing precursors. When the precursor content was larger than 59.3 wt %, the PbS.

## 8 Conclusion

### PbS detector design



### Material

1. **Thin film of PbS**
2. **Electrical leads**
3. **Substrate:**

Considering first the design of substrate 16, the thermal conductivity of the substrate, the thickness of the substrate, and the surface area of the substrate:

Conductivity: for applications where thin film photoconductors will be subject to intense radiation, the substrate should be fabricated from materials such as silicon or sapphire which have large thermal conductivities.

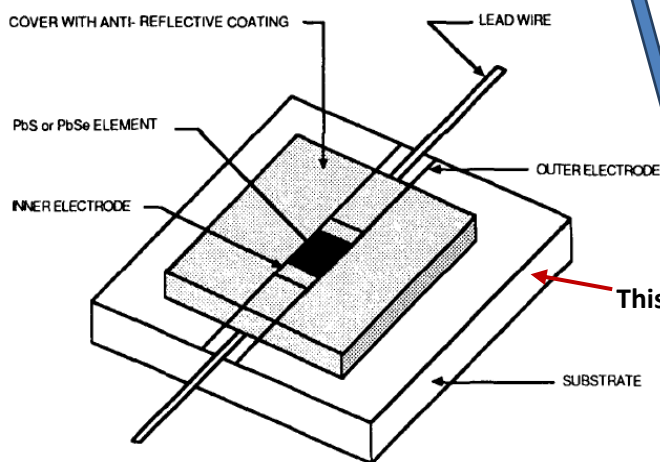
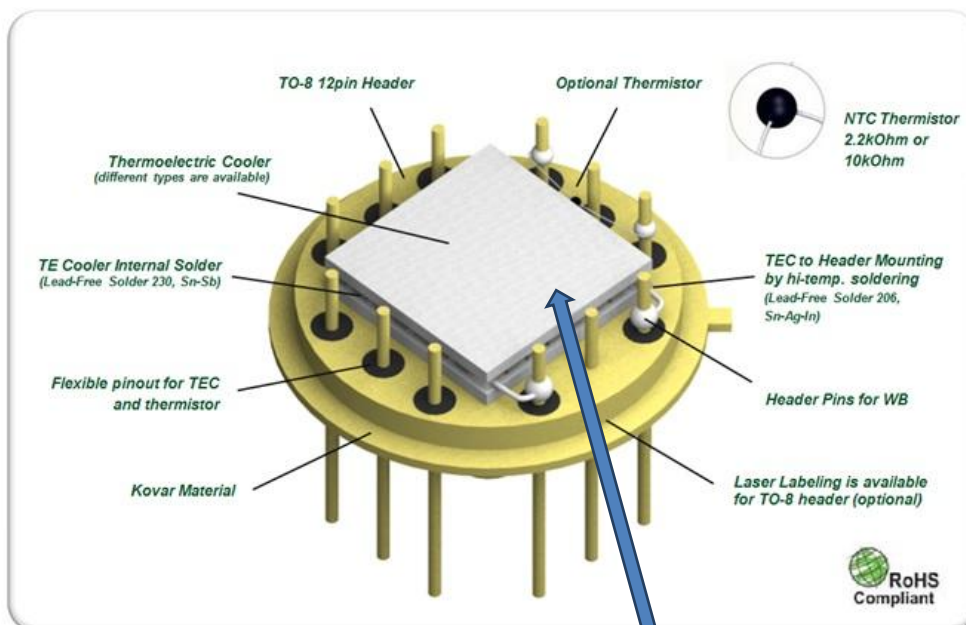
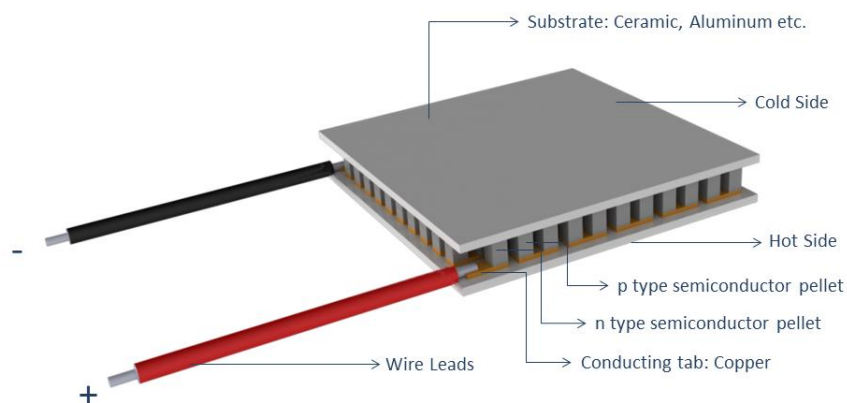
Thickness: It is noted that the substrate must be of sufficient thickness to supply mechanical stability for the thin films.

Surface area: The heat flow in the detector will also be improved if the substrate surface area, as indicated by 42 in FIG. 1, is made large compared to the absorbing detector area, as indicated by 44 in

FIG.1. This will allow transverse heat flow within the substrate 16, as well as heat flow in the direction of optical radiation, to contribute to the power dissipation of the detector.

4. Thermoelectric cooler

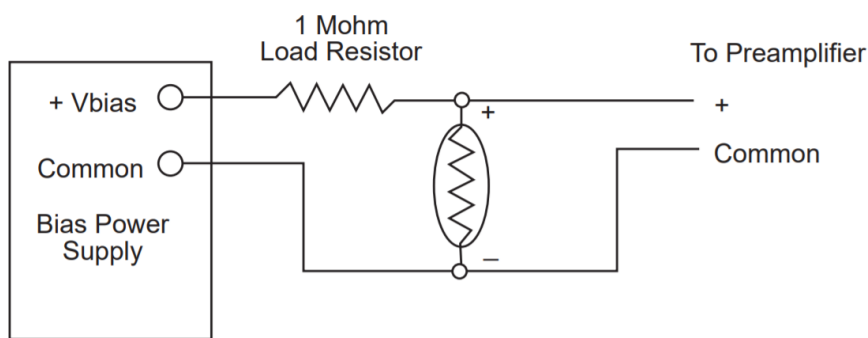
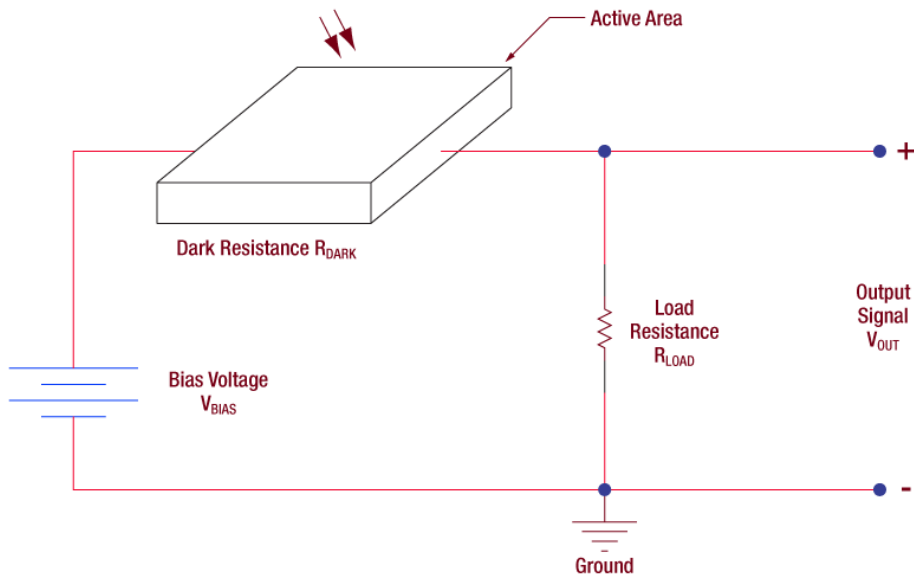
Thermoelectric Cooler (TEC)



This area it's put above the thermoelectric cooler


Finally, the detector will be supplied power

## Conclusion



Material	Supplier
PbS thin element film	
Thermoelectric cooler	<p style="text-align: right;"><a href="http://www.ekt2.com">www.ekt2.com</a> قطرنجي</p> <p style="text-align: center;"><a href="http://www.ekt2.com/products/productdetails/14_SENSOR_PELTIER_TEC1-12706">http://www.ekt2.com/products/productdetails/14_SENSOR_PELTIER_TEC1-12706</a></p> <p>Alibaba</p> <p><a href="https://www.alibaba.com/product-detail/Multistage-Peltier-Thermoelectric-Cooler-TEC2-127_1968756161.html?spm=a2700.7724838.2017115.26.11a72476ZW5aqT&amp;s=p">https://www.alibaba.com/product-detail/Multistage-Peltier-Thermoelectric-Cooler-TEC2-127_1968756161.html?spm=a2700.7724838.2017115.26.11a72476ZW5aqT&amp;s=p</a></p>
Substrate quartz	<p>Alibaba</p> <p><a href="https://www.alibaba.com/product-detail/SUCCESS-Polished-Quartz-Slides-Clear-Optical_60697516047.html?spm=a2700.galleryofferlist.normalList.69.2be0ffc5HIpEP3">https://www.alibaba.com/product-detail/SUCCESS-Polished-Quartz-Slides-Clear-Optical_60697516047.html?spm=a2700.galleryofferlist.normalList.69.2be0ffc5HIpEP3</a></p>
Sapphire window	<p>Alibaba</p> <p><a href="https://www.alibaba.com/product-detail/25-4mm-Anti-Reflection-Coated-Optical_60830570102.html?spm=a2700.7724838.2017115.25.4b4d6ebe2KQix&amp;s=p">https://www.alibaba.com/product-detail/25-4mm-Anti-Reflection-Coated-Optical_60830570102.html?spm=a2700.7724838.2017115.25.4b4d6ebe2KQix&amp;s=p</a></p>
Heat sink	<p style="text-align: right;"><a href="http://www.ekt2.com">www.ekt2.com</a> قطرنجي</p> <p style="text-align: center;"><a href="http://www.ekt2.com/products/productdetails/412_3D_PRINTER_EXTRUDER_HEAT_SINK">http://www.ekt2.com/products/productdetails/412_3D_PRINTER_EXTRUDER_HEAT_SINK</a></p>
Kovar material	

### Heat sink:







## 412 3D PRINTER EXTRUDER HEAT SINK

40x40x11 Aluminum Radiator Black

Original No:  
In Stock: confirmed after order

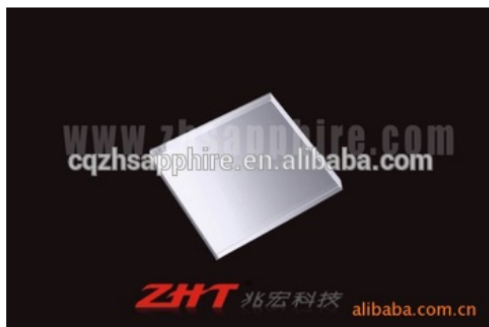
Quantity:  Price 3.30627 USD

[Buy Now](#)

### Sapphire window overview:

[https://www.alibaba.com/product-detail/square-sapphire-window\\_60473688791.html?spm=a2700.7724838.2017115.66.7003110fs2bxd2](https://www.alibaba.com/product-detail/square-sapphire-window_60473688791.html?spm=a2700.7724838.2017115.66.7003110fs2bxd2)



[View larger image](#)



[Add to Compare](#)  [Share](#)

square sapphire window

FOB Reference Price: [Get Latest Price](#)

**\$1.00 - \$15.00** / Pieces | 1 Piece/Pieces (Min. Order)

[Contact Supplier](#)

[Leave Messages](#)

Seller Support:  Trade Assurance protect your orders from payment to delivery

Payments:    [Online Bank Payment](#) [Pay Later](#) [More](#) 

Shipping: Alibaba.com Ocean Shipping Service from China to U.S  
[Get shipping quote](#)



# Conclusion

## Quick Details

Place of Origin:	Chongqing, China (Mainland)	Brand Name:	ZHT
Model Number:	ZHT-Round Sapphire Window	Material:	Synthetic Sapphire Optical Grade
Usage:	Infrared, optical, UV	Structure:	Round
Shape:	Plano	Product name:	sapphire window
Description:	optical grade	Surface Quality:	S/D 10/5, 20/10, 40/20, 80/50

## Supply Ability

Supply Ability: 50000 Piece/Pieces per Month

## Packaging & Delivery

Packaging Details ZHT sapphire products are packed within vacuumed plastic bag.  
ZHT packing is anti-dust. And, more customized packing demand can be met.

Port Chongqing, China

## Product Description

Sapphire possesses nice light transmission in 0.20-5.50um wave band, and its infrared ray transmission is hardly influenced by temperature, so the optical components made of sapphire are fully applied to infrared equipments, low-temperature laboratory viewing aperture, and high precise apparatus of navigation and aviation, etc.

We can fabricate miniature size as well as super large size: diameter 1mm to 300mm, with thickness 0.2mm to 200mm.

## Substrate quartz:

[https://www.alibaba.com/product-detail/Polishing-thin-optical-clear-quartz-substrate\\_60729729793.html?spm=a2700.galleryofferlist.normalList.64.144867c876zxgm](https://www.alibaba.com/product-detail/Polishing-thin-optical-clear-quartz-substrate_60729729793.html?spm=a2700.galleryofferlist.normalList.64.144867c876zxgm)



[View larger image](#)



[Add to Compare](#) [Share](#)

Polishing thin optical clear quartz substrate

FOB Reference Price: [Get Latest Price](#)

**\$3.00 - \$50.00** / Pieces | 5 Piece/Pieces (Min. Order)

[Contact Supplier](#)

[Chat Now!](#)

Seller Support: [Trade Assurance](#) protect your orders from payment to delivery

Payments: [VISA](#) [MasterCard](#) [TT](#) [Online Bank Payment](#) [Pay Later](#) [More](#)

Shipping: [Alibaba.com Ocean Shipping Service from China to U.S](#)  
[Get shipping quote](#)

Value-added services: [Production View](#)

## Overview

### Quick Details

Type:	Clear Quartz Plate	Application:	semiconductor material
Thickness:	1-3mm	Shape:	Square
Place of Origin:	Jiangsu, China (Mainland)	Brand Name:	HIGHBORN
Model Number:	HBC	Material:	Fused Quartz Glass/JGS1/JGS2/JGS3/GE
purity:	99.99%	density:	2.2kg/cm3
working temperatur...	1100 degree celsius	annealing point:	1180 degree celsius
softening point:	1680 degree celsius	process:	polishing or grind
Keywords:	optical quartz substrate	kaywords 2:	Clear quartz substrate

### Supply Ability

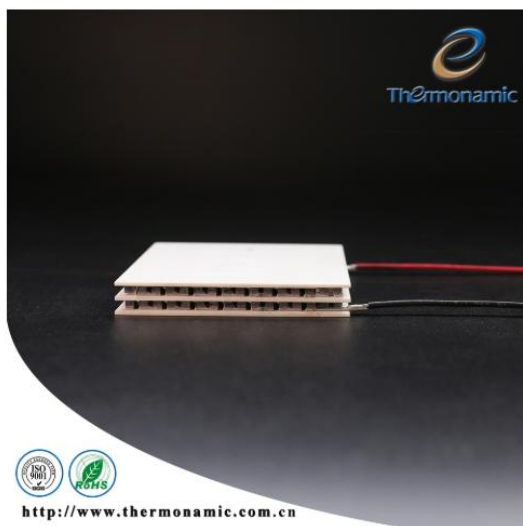
Supply Ability: 500 Kilogram/Kilograms per Month

### Packaging & Delivery

Packaging Details 1.pearl cotton 2.bubble pad 3.carton 4.standard wooden case

Port Shanghai,Qingdao,Ningbo,Shenzheng,Tianjin

## Thermoelectric cooler



[View larger image](#)



### Multistage Peltier Thermoelectric Cooler TEC2-127-127-06

FOB Reference Price: [Get Latest Price](#)

**\$10.00 - \$100.00** / Pieces | 1 Piece/Pieces (Min. Order)

[Contact Supplier](#)

[Chat Now!](#)

Payments: [VISA](#) [MasterCard](#) [TT](#) [Online Bank Payment](#) [Pay Later](#) [More](#) ∨

Shipping: Alibaba.com Ocean Shipping Service from China to U.S  
[Get shipping quote](#)

## Overview

### Quick Details

Place of Origin:	Jiangxi, China (Mainland)	Brand Name:	Thermonamic
Model Number:	TEC2-127-127-06	Couples:	127+127
DTmax:	93	Umax (Voltage):	14.6
Imax (amps):	6.5	QCmax (Watts):	40.6
AC resistance (oh...):	2.1~2.4	Size (mm):	40*40(top) /40*40 (bottom).
Appearance:	Cube and White	Certification:	ROHS, REACH, SGS, A&V, ISO9001

### Supply Ability

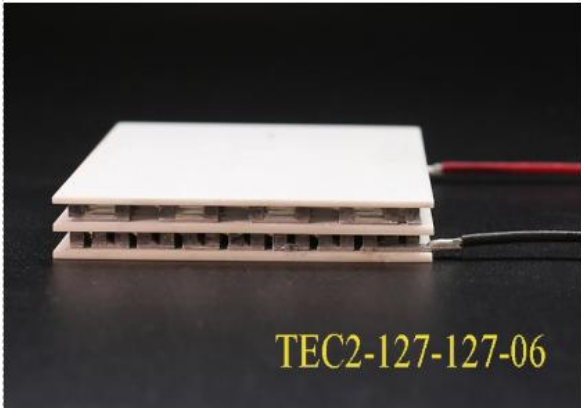
Supply Ability: 100000 Piece/Pieces per Month

### Packaging & Delivery

Packaging Details Inner packing: hard foam box, Outer packing: carton  
Port Shanghai, Guangzhou

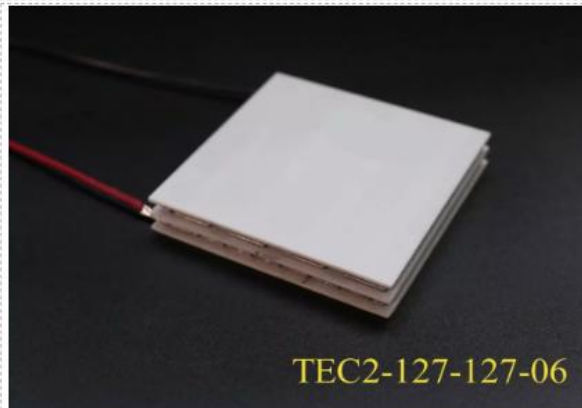
## DESCRIPTION

*Thermonic Electronics(Jiangxi) Corp., Ltd.*



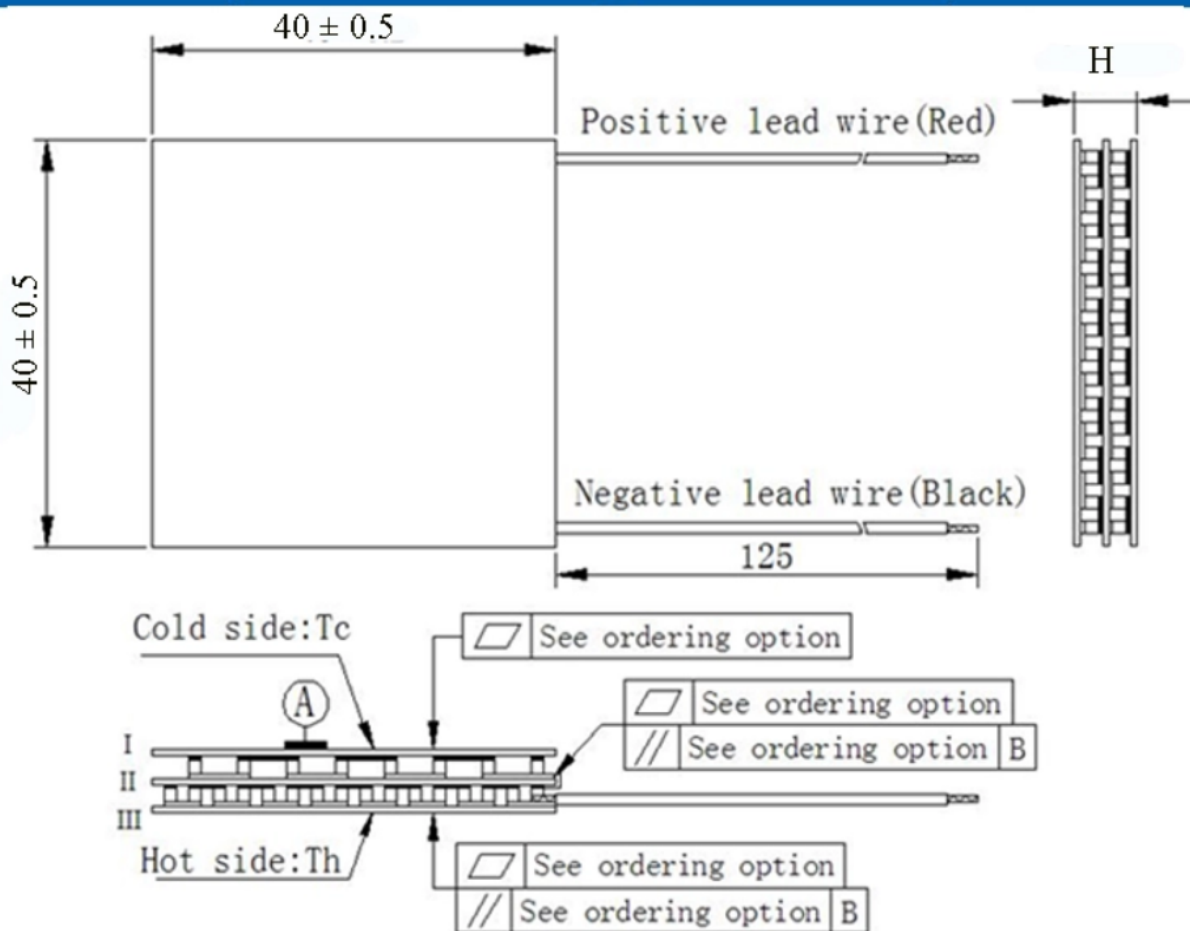
The TEC2-127-127-06 is a multistage module designed for greater temperature differential cooling, good for cooling and heating up to 100 °C applications. It is a 127-127 couples module in size of 40mm×40mm (top)/40mm ×40mm (bottom). If higher operation or processing temperature is required, please specify, we can design and manufacture according to your special requirements.

- Environmental friendly
- RoHS compliant
- Precise temperature control
- Exceptionally reliable in quality
- High performance
- High Temperature Differential
- No moving parts, no noise, and solid-state
- Compact structure
- Small in size, light in weight



**GEOMETRIC CHARACTERISTICS**

*Thermonamic Electronics(Jiangxi) Corp., Ltd.*



## Specification of Thermoelectric Module

TEC2-127-127-06

## Description

The TEC2-127-127-06 is a multistage module designed for greater temperature differential cooling, good for cooling and heating up to 100 °C applications. It is a 127-127 couples module in size of 40 mm × 40 mm (top) / 40 mm × 40 mm (bottom). If higher operation or processing temperature is required, please specify, we can design and manufacture according to your special requirements.

## Features

- High Temperature Differential
- No moving parts, no noise, and solid-state
- Compact structure, small in size, light in weight
- Environmental friendly
- RoHS compliant
- Precise temperature control
- Exceptionally reliable in quality, high performance

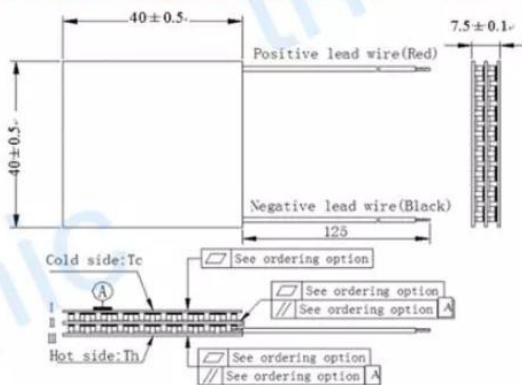
## Application

- Infrared (IR) Sensors
- CCD Sensor
- Gas Analyzers
- Calibration Equipment
- CPU cooler and scientific instrument
- Photonic and medical systems
- Guidance Systems

## Performance Specification Sheet

Th (°C)	27	50	Hot side temperature at environment: dry air, N <sub>2</sub>
DT <sub>max</sub> (°C)	93	104	Temperature Difference between cold and hot side of the module when cooling capacity is zero at cold side
U <sub>max</sub> (Voltage)	14.6	16.4	Voltage applied to the module at DT <sub>max</sub>
I <sub>max</sub> (amps)	6.5	6.5	DC current through the modules at DT <sub>max</sub>
Q <sub>Cmax</sub> (Watts)	40.6	42.2	Cooling capacity at cold side of the module under DT=0 °C
AC resistance (ohms)	2.25	2.45	The module resistance is tested under AC
Tolerance (%)	± 10		For thermal and electricity parameters

## Geometric Characteristics Dimensions in millimeters



## Ordering Option

Suffix	Thickness (mm)	Flatness/ Parallelism (mm)	Lead wire length(mm) Standard/Optional length
TF	0: 7.5±0.1	0: Face II 0.010/0.010, Face III 0.015/0.015	125±1/Specify
TF	1: 7.5±0.08	1: Face II 0.008/0.008, Face III 0.01/0.01	125±1/Specify

Eg. TF0: Thickness 7.5±0.1(mm) and Face II 0.008/0.008, Face III 0.01/0.01

## Manufacturing Options

## A. Solder:

1. T100: BiSn (Melting Point=138°C)
2. T200: CuSn (Melting Point= 227 °C)

## B. Sealant:

1. NS: No sealing (Standard)
2. SS: Silicone sealant
3. EPS: Epoxy sealant
4. Customer specify sealing

## C. Ceramics:

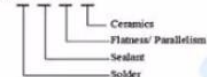
1. Alumina (Al<sub>2</sub>O<sub>3</sub>, white 96%)(AlO)
2. Aluminum Nitride (AlN)

## D. Ceramics Surface Options:

1. Blank ceramics (not metalized)
2. Metalized (Copper-Nickel plating)

## Naming for the Module

TEC2-127-127-06-X-X-X-X



TEC2-127-127-06-T100-NS-TF01-ALO

T100: BiSn(Tmelt=138°C)

NS: No sealing

AlO: Alumina white 96%

TF01: Thickness ±0.2(mm) and Face II 0.008/0.008, Face III 0.01/0.01

Creative technology with fine manufacturing processes provides you the reliable and quality products  
Tel: +86-791-88198288 Fax: +86-791-88198308 Email: [sales@thermonamic.com.cn](mailto:sales@thermonamic.com.cn) Web Site: [www.thermonamic.com.cn](http://www.thermonamic.com.cn)

Or other supplier [www.ekt2.com](http://www.ekt2.com)





### 14 SENSOR PELTIER TEC1-12706

Thermoelectric Cooler Senso

4.32 USD

Quantity:

 Add To Cart

 Details

## 9 Thermoelectrically cooled IR detectors beat the heat<sup>14</sup>

High-performance solid-state infrared (IR) detectors are at the heart of a wide variety of military, industrial, and medical electro-optical systems. As in visible-wavelength-sensitive silicon photodetectors, IR detectors can be made from semiconductor materials. To absorb IR photons, the detector material must have band-gap energy less than the energy of the incoming photon; thus, sensing longer wavelengths requires the use of small band gap materials. Such materials yield devices sensitive to low-energy IR photons, but the electron carriers are then more easily generated in the semiconductor from random thermal excitation, and this degrades performance through increased dark current and noise.

One way to reduce these effects is to reduce the operating temperature of the detector, for example by thermoelectric (TE) cooling. Thermoelectric coolers are simply low-power, miniature heat pumps that are small enough to be easily integrated into compact optical systems. When properly packaged, TE coolers can efficiently cool small detector chips (3, 3 mm) to temperatures below -70°C. Thermoelectric coolers can provide temperature control to better than 0.1°C, ensuring stable detector performance. The devices operate under direct current (dc), minimizing electrical noise, and can be used for heating or cooling by reversing the direction of current flow. Because both the detector and cooler are solid-state components, operating lifetimes are greater than 10 years.

Thermoelectric coolers have not entirely replaced cryogenic coolers for IR applications. Background-limited performance in the mid- or long-wave IR spectral regions still requires operating temperatures of 100 K or less, which can be attained only by liquid-nitrogen-filled Dewars or closed-cycle refrigerators. But for many applications at near- and mid-IR wavelengths, thermoelectric cooling is appropriate.

### 9.1 Thermoelectric coolers

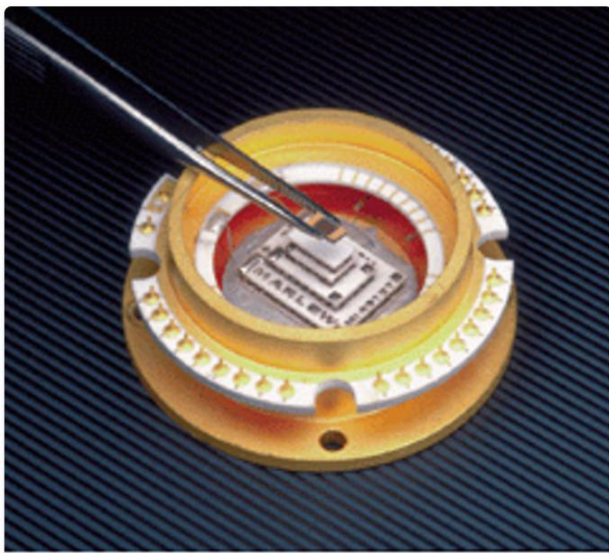
The development of thermoelectric (TE) cooling can be traced back to the early 1800s when Jean Peltier noted a heating or cooling effect when electrical current passed through two conductors. Thomas Seebeck later found that two dissimilar conductors at different temperatures created a voltage. William Thomson (Lord Kelvin) concluded that over a temperature gradient, a single conductor with current flow will demonstrate reversible heating and cooling. Based on these principles and the development of certain semiconductor materials in the late 1950s, thermoelectric cooling has developed into a viable technology for many IR detector applications.

A single-stage TE cooler consists of a matrix of thermoelectric couples connected electrically in series, and thermally in parallel (see Fig. 1). The couples themselves consist of bismuth telluride p- and n-type semiconductor material. Depending on performance requirements, a TE cooler incorporates anywhere from one to several hundred couples. These couples are sandwiched between ceramic plates, which provide structural integrity as well as electrical insulation between the heat sink and the object being cooled.

---

<sup>14</sup> <https://www.laserfocusworld.com/detectors-imaging/article/16550903/thermoelectrically-cooled-ir-detectors-beat-the-heat>





When a positive dc voltage is applied to the n-type material, electrons pass from the p- to the n-type material. The temperature on the cold side decreases because heat is being absorbed from it. This heat pumped from the cold side plus the heat generated by the input power is conducted through to the hot side of the cooler, where it is dissipated by a heat sink. The degree of cooling achieved is proportional to the current and the number of thermoelectric couples. For more extensive cooling requirements, multiple cooler assemblies can be stacked to accommodate additional heat pumping for both active and passive heat loads. Thermoelectric coolers with as many as four stages are typically used in many IR detector applications.

## 9.2 Choosing a cooler

One of the main advantages of TE coolers compared to bulk liquid nitrogen or mechanical refrigerators is their small size, which allows the detector and cooler to be incorporated in a single housing (see bottom photo on p. S15). Selecting the proper package for TE-cooled IR detectors requires some special considerations. The detector chip itself will generally be cooled below 0°C, so hermetic sealing is necessary to block out moisture that would otherwise precipitate and freeze on the cold detector surface. This is especially critical for near-IR spectroscopy in the 3- $\mu\text{m}$  wavelength region, where ice has a strong absorption band. Proper cleaning and bake out of the coolers and packages eliminate moisture that might introduce this spurious absorption feature.

The colder the operating temperature desired, the more TE cooler stages are required. This increases the size of the device and hence the housing; power consumption also rises. For single-element detectors in the near-IR spectral region, TO-37 or TO-8 headers are sufficient to accommodate small two-stage TE coolers. Array detectors require larger coolers with more complex packages.

The total heat load on the two cooler stage plays a critical role in determining the minimum achievable temperature. Gas convection inside the hermetic housing is a major source of heat-loading. Convection can be reduced by filling the package with a high-molecular-weight gas (such as xenon) or by evacuating the package.

Finally, standard glass windows transmit wavelengths only to 2.5  $\mu\text{m}$ . For detectors that respond beyond this point, the package must incorporate sapphire windows or antireflection-coated germanium (Ge) windows, soldered or fused into the package cap.

### 9.3 Near-infrared detectors

Over the spectral range from 0.8 to 3.0  $\mu\text{m}$ , IR detectors are used for applications as diverse as fiber optic communications, agricultural sorting, environmental monitoring, chemical analysis, and Fourier-transform spectroscopy. Typical photovoltaic detector materials are germanium for the 0.8- to 1.6- $\mu\text{m}$  wavelength region, indium gallium arsenide (InGaAs) for the 1- to 2.5- $\mu\text{m}$  region, and indium arsenide (InAs) for the 1- to 3.4- $\mu\text{m}$  region. For wavelengths up to 1.6  $\mu\text{m}$ , cooling is often unnecessary. Both germanium and InGaAs offer high shunt resistance, low dark currents, and stable response at 25°C (see Fig. 2). However, dark currents are higher for detectors sensitive to longer wavelengths. Detectors are often cooled for wavelengths beyond 2  $\mu\text{m}$ .

Indium arsenide has the longest wavelength response in the near-IR spectral range. With TE cooling, InAs exhibits dark currents below 10 nA, with noise-equivalent powers (NEPs) of less than 1 pW. InAs offers linear performance from the Pico watt to the mill watt regime, response times below 1  $\mu\text{s}$ , dc response stability, and good uniformity of response. Lead sulfide (PbS) detectors are also available for near-IR wavelengths, but these devices operate in the photoconductive mode and can suffer from poor response stability, high bias voltages, and slow response times.

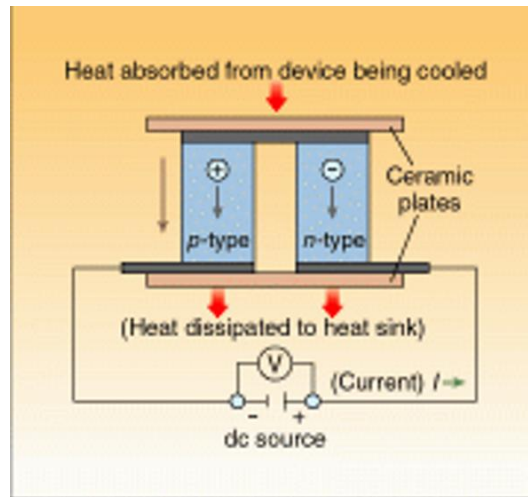
Further into the IR region (from 2 to 5  $\mu\text{m}$ ), applications for IR detectors include noncontact temperature sensing, thermal imaging, and gas analysis for pollution control. Indium antimonide (InSb) is the highest-performance detector for this region, but unfortunately, InSb cannot be used with TE coolers because the large number of thermally generated carriers shorts out the p-n junction in InSb.

Photoconductive devices do not incorporate a p-n junction and can operate successfully over a wider temperature range. Lead selenide (PbSe) and mercury cadmium telluride (HgCdTe) photoconductive detectors are widely used in industrial and medical instruments. When mounted on two-stage thermoelectric coolers, PbSe detectors are economical alternatives to InSb and offer sufficient performance for many applications. For high-performance applications such as thermal imaging and radiometry, photoconductive HgCdTe provides better sensitivity, faster response, and lower bias voltage. Three-stage or even four-stage cooling is used for maximum performance.

The long-wave IR spectral region spans the wavelength range from 8 to 13  $\mu\text{m}$ , which corresponds to a peak for thermal emission at ambient temperature. The 8-13- $\mu\text{m}$  range also has high transmission through the atmosphere. This spectral region is thus optimal for such applications as thermal imaging, noncontact temperature sensing, security sensing, and environmental monitoring. Photoconductive HgCdTe detectors can provide background-limited performance at these wavelengths, but only at operating temperatures below 100 K.

Thermoelectrically cooled HgCdTe photoconductive detectors for the 8- to 12- $\mu\text{m}$  region do not necessarily offer better sensitivity than low-cost thermal detectors (thermopiles, pyroelectrics, or bolometers) that convert heat energy to an electrical signal. Such devices require no cooling and can achieve NEPs of 100 pW/ $\sqrt{\text{Hz}}$ . The major drawbacks of pyroelectrics and thermopiles are the slow response time and reduced sensitivity at higher frequencies. Thermoelectrically cooled HgCdTe detectors maintain their sensitivities up to very high frequencies (10 MHz), making them suitable for fast-pulsed applications such as CO<sub>2</sub> laser detection.

Thermoelectrically cooled detectors are reliable and simple to operate. The most critical aspect of the design is proper heat-sinking, without which a cooler will be inefficient or may even be damaged by overheating (see Fig.). For small two- and three-stage coolers, good thermal connection of the device to a metal plate with several square inches or more of surface area is usually sufficient; forced-air cooling is rarely needed. Once properly integrated into an electro-optical system, TE-cooled IR detectors should give years of continuous, maintenance-free operation.



3-DH-2 97 Fig. 1

## 9.4 Principle of thermoelectric cooling

Thermoelectric cooling uses the Peltier effect to create a heat flux at the junction of two different types of materials. A Peltier cooler, heater, or thermoelectric heat pump is a solid-state active heat pump which transfers heat from one side of the device to the other, with consumption of electrical energy, depending on the direction of the current. Such an instrument is also called a Peltier device, Peltier heat pump, solid state refrigerator, or thermoelectric cooler (TEC). It can be used either for heating or for cooling, [1] although in practice the main application is cooling. It can also be used as a temperature controller that either heats or cools.

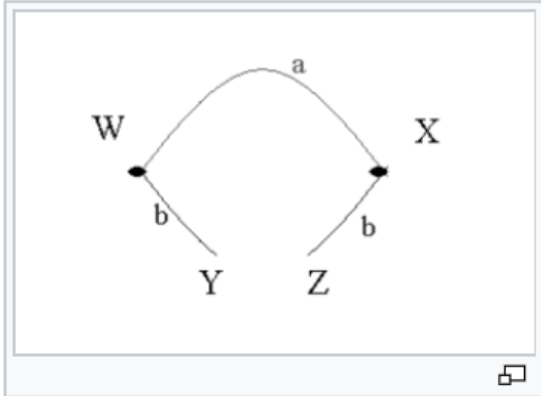
This technology is far less commonly applied to refrigeration than vapor-compression refrigeration is. The primary advantages of a Peltier cooler compared to a vapor-compression refrigerator are its lack of moving parts or circulating liquid, very long life, invulnerability to leaks, small size, and flexible shape. Its main disadvantages are high cost and poor power efficiency. Many researchers and companies are trying to develop Peltier coolers that are cheap and efficient. (See Thermoelectric materials.)

A Peltier cooler can also be used as a thermoelectric generator. When operated as a cooler, a voltage is applied across the device, and as a result, a difference in temperature will build up between the two sides. When operated as a generator, one side of the device is heated to a temperature greater than the other side, and as a result, a difference in voltage will build up between the two sides (the Seebeck effect). However, a well-designed Peltier cooler will be a mediocre thermoelectric generator and vice versa, due to different design and packaging requirements.

### 9.4.1 Peltier effect

The Peltier effect is a thermoelectric effect consisting of a phenomenon of heat displacement in the presence of an electric current. The effect is made in conductive materials<sup>1</sup> of different types by contacts (contacts). One of junctions then, while the other was warming up. This effect was discovered in 1834 by physicist Jean-Charles Peltier.

The figure shows the basic thermoelectric circuit.



Two conductive materials of different natures a and b are connected by two junctions in X and W. In the case of the Peltier effect, an electric current  $I$  is imposed on the circuit, by placing for example a source of electric current between Y and Z resulting in heat release  $Q$  at one junction and heat absorption at the other junction<sup>2</sup>. The Peltier coefficient relative to the material pair a and b is defined as the thermal power  $P$  released or absorbed per unit of intensity of current  $I$ . It is expressed in volts.

$\Pi_{ab}$  is then defined by:

$$\Pi_{ab} = \frac{P}{I}$$

If a current imposed in the direction  $Y \rightarrow W \rightarrow X \rightarrow Z$  causes a heat release in W and an absorption in X, then  $\Pi_{ab}$  is positive.

## 10 Lead Sulfide Quantum Dots Synthesis

### 10.1 Overview

Quantum dots are semiconductor nanocrystals on the scale of a few nanometers, or several hundred atoms. At this size quantum effects dominate and the electrons are quantum confined to narrow energy levels determined by the size of the particle. This means that the absorption wavelength the light can be fine-tuned and that quantum dots can be used to adjust the bandgap of the materials they are associated with. Quantum dots being explored for use in photovoltaics and in signal processing.

### 10.2 Significance

Quantum dots can be used increase the efficiency of solar cells by tapping different portions of the spectrum and by increasing the number of excitons that be formed per photon, resulting in higher quantum efficiency.

### 10.3 Procedure

**Link:** <https://youtu.be/bKLdkjV6Mbc>

- **Prepare Reactants:**

Prepare reaction mixture with 14 g of octadecene, 1.4 g of oleic acid, 450 mg of lead oxide. When it mixes up it is murky yellow at first and then becomes clear when it is heated up.

- **Degas the mixture:**

The Schlenk line is used to degas the reaction mixture. Remove the nitrogen bubbler and replace with a pipette bulb. Slowly turn the stopcock from nitrogen flow to vacuum. First watch the pipette bulb when it collapses vacuum is being pulled on the solution . Now slowly turn the stopcock while watching the reaction mixture making sure not over-boil. Once the boiling mixture has stabilized fully-open the vacuum valve. Leave the mixture under vacuum for approximately 1 hour. Slowly turn the stopcock back to nitrogen while holding a finger over the bubbler to prevent pulling the silicon fluid into the Schlenk line. Remove the pipette bulb and replace the nitrogen bubbler. Increase the reaction mixture to 180 degrees

- **Injection**

Prepare the injection mixture from 4 gms of octadecene in 210 mL of hexylmethylidisilazane (HMDS).

Once the reaction mixture has stabilized purge a syringe with nitrogen. Draw up the injection mixture and quickly insert it into the reaction vessel. Within second the mixture should turn a turbid black color. Let it react for 5 minutes and then quench the reaction in an ice bath. After it comes to room temperature transfer it to a separatory funnel.

- **Cleaning**

After the synthesis is quenched it is necessary to remove excess oleic acid and other impurities. Two methods are shown.

### **I. Separatory Funnel:**

1. pour PbS QDs (dissolved in minimal amount of hexanes) into sep. funnel
2. precipitate with methanol (MeOH)

Add back small amounts of hexanes and shake funnel vigorously between additions. If there is still precipitated product clinging to the walls of the funnel between hexanes additions, continue to add more hexanes. Once the product stops sticking to the walls, let the funnel sit for a minute or so to see if any phase separation occurs. If not, continue adding small amount of hexanes until it does. Note that only a small amount of separation will be seen at the bottom of the funnel at first, and the mixture will have to sit for at least 30 mins to fully separate. If no phase separation is observed after a few additions, the funnel can be placed in the freezer to speed the process.

3. Drain off the clear bottom MeOH layer into the waste
4. Drain small amounts (~1 or 2 mL portions) of PbS into a centrifuge tube.
5. Precipitate by filling the tube with MeOH
6. Centrifuge the tube (5 min, 3000 RPM), and pour off clear MeOH layer
7. Pour another addition of PbS into the same tube and repeat steps 6) and 7). Note: for the first two cycles, multiple tubes can be used rather than just one, but on the third (last) cleaning step, it is generally preferred to use a single tube to consolidate product.
8. Dissolve the product in minimal amount of hexanes, vortex, sonicate (5 mins, or until dissolved) and add PbS back to the separatory funnel. Repeat the above steps for the first two cleaning cycles.

### **II. Simply use multiple centrifuge tubes:**

1. Dissolve the product in small amount of hexanes, then vortex and sonicate until QDs dissolve.
2. Precipitate by filling each centrifuge tube with MeOH
3. Centrifuge each tube (5 min, 3000 RPM)
4. Discard clear supernatant
5. For the first two cleaning cycles, repeat the above steps

To consolidate into a single tube, just choose one tube to keep and repeat step 1) above for the other tubes. Then successively add the dissolved QDs of ONE of the other tubes to to the dry product in the tube you chose to keep and repeat steps 2-4 above until all tubes have been combined into one (only add the contents of one tube for each step precipitation-centrifuge cycle-do not combine the contents of all remaining tubes at once)

In both cases, once the cleaning cycles are complete, the QDs can be dissolved in hexanes or toluene and left to sit. Alternatively, a septum cap can be placed on the centrifuge tube which can then be placed on the Schlenk line to dry.

## **10.4 PbS/Polymer Nanocomposite Optical Materials with High Refractive Index**

High refractive index nano-PbS/polymer composites were fabricated from reactive lead-containing precursors and polythiourethane (PTU) oligomer terminated with isocyanate group, followed by in situ gas/solid reaction. The lead-containing precursor with a chemical formula of  $\text{Pb}(\text{SCH}_2\text{CH}_2\text{OH})_2$

was synthesized in water phase at pH = 5–9 and exhibited an absorption at 317 nm in dimethyl sulfoxide (DMSO) in UV–vis spectra. PbS nanoparticles can be formed in DMSO after treatment with H<sub>2</sub>S. TEM studies indicated that the PbS nanoparticles were smaller than 10 nm and aggregated seriously in DMSO. After the precursors were incorporated into PTU oligomer, the obtained composite films were treated with H<sub>2</sub>S to obtain PbS nanoparticles/PTU nanocomposite films. TEM showed that the nanocomposites exhibited interesting phase behaviors depending on the precursor content in films. A uniform spherical aggregate of PbS nanoparticles (nanospheres) with a size smaller than 100 nm formed in the nanocomposite films below 26.3 wt % of lead-containing precursors. When the precursor content was larger than 59.3 wt %, the PbS nanoparticles about 3 nm dispersed uniformly in the whole polymer matrix. Ellipsometric measurement indicated that the precursors/PTU composite films before being treated with H<sub>2</sub>S had a refractive index in the range 1.57–1.665 and after reaction with H<sub>2</sub>S, the obtained PbS/PTU nanocomposite films had a higher refractive index in the range 1.57–2.06 with the varied content of precursors from 0 to 67 wt %.

## 11 Synthesis and Optical Properties of the Semiconductor PbS Nanobelts

### 11.1 Introduction

Due to its unique structure and superior optoelectronic properties, nanobelts have surpassed nanowires and nanotubes and attracted a lot of interest in nanomaterials research. The controlled synthesis of no-defective, oxide nanobelts under high temperature and the solid gas phase method was first described by Pan et al. Since the one-dimensional nanobelts with wide band gap were expected to have vital applications in areas such as high-efficiency electricity transmission, a series of nanobelts have been fabricated, most of which were oxides, such as ZnO, SnO<sub>2</sub>, GaO<sub>2</sub>, MoO<sub>3</sub>, etc. There have also been a lot of interests in making nanobelts with non-oxide materials and potentially utilizing them in areas such as electronics, biology, pigment and pharmaceuticals. The most commonly study of nonoxide semiconductors focus on sulfides, such as CdS, ZnS, Bi<sub>2</sub>S<sub>3</sub>, Ti<sub>2</sub>S, etc. However, synthesis of nanobelts has proven to be difficult because reactions are often performed at very high temperature and require the addition of catalysts. Therefore, it is important to explore the simple and mild methods to achieve the controlled synthesis of nanobelts, preferably under room temperature.

As typical narrow band gap semiconductors, PbS nanomaterials possess special optoelectronic properties, which have vital applications in optical information storage, optical communication apparatus, radioactivity detector, etc. A number of PbS nanomaterials with different morphologies and structures such as nanoparticles, nanorods, nanowires, nanoflakes, and nanocubes have been synthesized. However, so far there is no report so far on the synthesis of nanobelts by employing using the reverse micelles under a mild chemical reaction condition and at room temperature.

The reverse micelle soft-template method represents a simple and unique way to make nanomaterials with desired nano-sizes and two- or three-dimensional tropism. Compared with nanomaterials obtained from physical-chemical methods, the products prepared in reverse micelles are widely considered to show superior structures and physical properties. Herein, this paper describes a successfully selfcontrolled synthesis of PbS nanobelts in a reverse micelle system by employing the surfactant of C<sub>12</sub>E<sub>9</sub> as the soft template. The optical properties of PbS nanobelts are investigated and the potential mechanism of reaction is also proposed.

### 11.2 Experimental Section

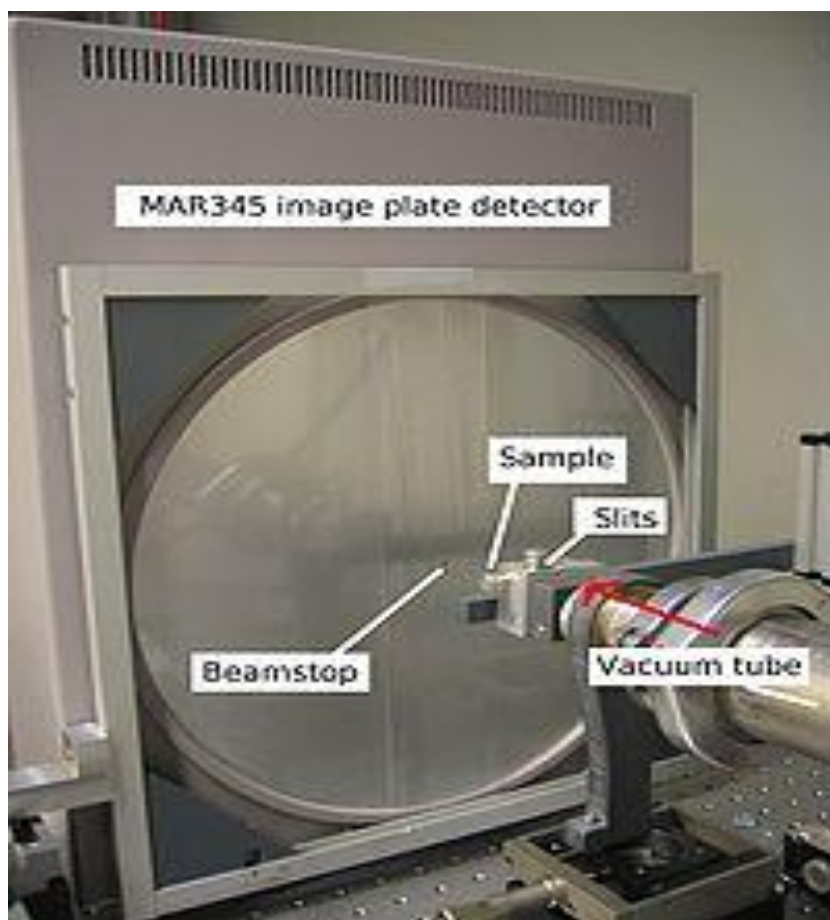
#### 11.2.1 Reagents & Equipments:

C<sub>12</sub>E<sub>9</sub> [polyoxyethylene (9) dodecy ether], cyclohexane, absolute ethanol, n-pentanol, Na<sub>2</sub>S·9H<sub>2</sub>O and Pb(CH<sub>3</sub>COO)<sub>2</sub>·3H<sub>2</sub>O were purchased from Shanghai Chemical Reagent Factory, China. All the reagents are of analytical grade.

The morphologies of the products were observed through transmission electron microscopy (TEM). The crystal phase and structure of the products were determined by X-ray powder diffraction (XRD) using Hitachi-800 diffractometer with graphite monochromatized Cu-K $\alpha$  radiation ( $\lambda = 0.15418$  nm, 50 kV, 100 mA). Optical properties of products were studied by Agilent 8453 UV-Visible spectrophotometer, Perking Elmer LS-55 fluorescent spectroscopy.



A **diffractometer** is a measuring instrument for analyzing the structure of a material from the scattering pattern produced when a beam of radiation or particles (such as X-rays or neutrons) interacts with it.



### **Preparation of PbS Nanobelts:**

The reverse micelle system was prepared by adding into a 250 mL volumetric glass in sequence of 28 mL cyclohexane, 3 mL  $C_{12}E_9$ , 1 mL of 0.1 mol/L aqueous  $Pb(CH_3COO)_2 \cdot 3H_2O$  and 1 mL n-pentanol.

The same experiment was also performed in parallel by adding into another 250 mL volumetric glass in sequence of 28 mL cyclohexane, 3 mL  $C_{12}E_9$  and 1 mL of 1.0 mol/L aqueous  $Na_2S \cdot 9H_2O$ .

Both solutions were mixed vigorously at approximately 3000 rpm for 15 minutes, and kept at room temperature for another five minutes.

After that an equal volume of two microemulsions, one containing  $S^{2-}$  and the other containing  $Pb^{2+}$ , was mixed together followed by gentle shaking for another 5 to 10 minutes. The final solution was kept at room temperature for 12 hours to result in the formation of nanobelts.

A volume of 3 mL acetone was then added to the solution to break up the micelles.

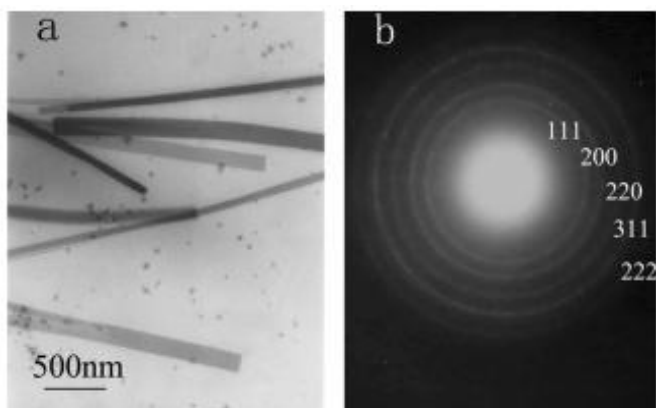
Finally, the supernatant was removed from the solution described above, the bottom solution was centrifuged at 2000 rpm for 10 minutes, washed sequentially with acetone, ethanol and water 2-3 times each.

The final product should be black precipitate insoluble in water and ethanol.

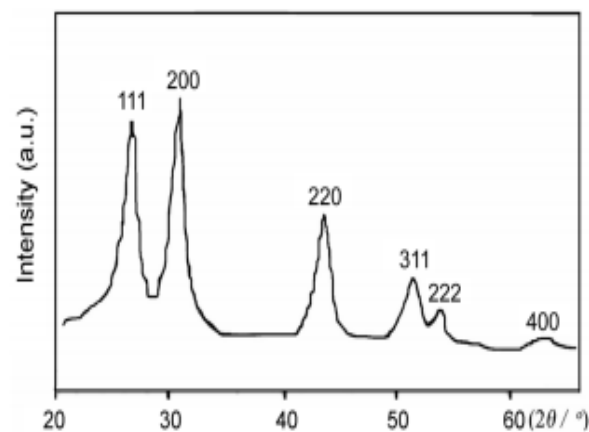
The morphology of the final product was observed using TEM. One to two drops of the microemulsion solutions containing the PbS products were transferred onto a copper grid that was placed on filter paper followed by air-drying. The structure of the final product was studied using X-ray diffraction, while the optical properties of the product was determined by photoluminescence (PL) and UV-Vis spectrophotometers.

### 11.3 Results and Discussions

**Morphologies and Structures.** The TEM micrograph and electron diffraction of the PbS nanoproducts formed are shown in Figure 1. The products have belt shape (Figure 1a). The single layer nanobelts were very thin and nearly transparent. There were also some other nanobelts shown in Figure 1a, which were likely made of a few overlapping layers. The width of the nanobelt was found to be between 50 and 120 nm and the length over 3  $\mu\text{m}$ . The exact thickness of the nanobelts can't be easily measured. However, it was concluded that nanobelts should be approximately 3 nm thick based on: (1) As pointed in the arrow in Figure 1a, the particles were still visible even when they were underneath the nanobelt. This has clearly demonstrated the transparent nature of the nanobelt and subsequently shown the thickness of the nanobelt was under 5 nm. (2) As shown in Figure 1b, the nanobelts could be penetrated by 100 kv electron beam. This has proven the nanobelt was less than 20 nm in thickness. (3) "Blue Shift" was observed on the UV-Vis absorption spectrum of the PbS nanobelts (in Figure 3). The thickness of the nanobelts was thus determined to be around 3 nm based on literature report. (4) As shown in Figure 5, the gap between different layers of micelles was normally 1- 4 nm. This has in turn limited the nanobelt thickness to 1-4 nm.

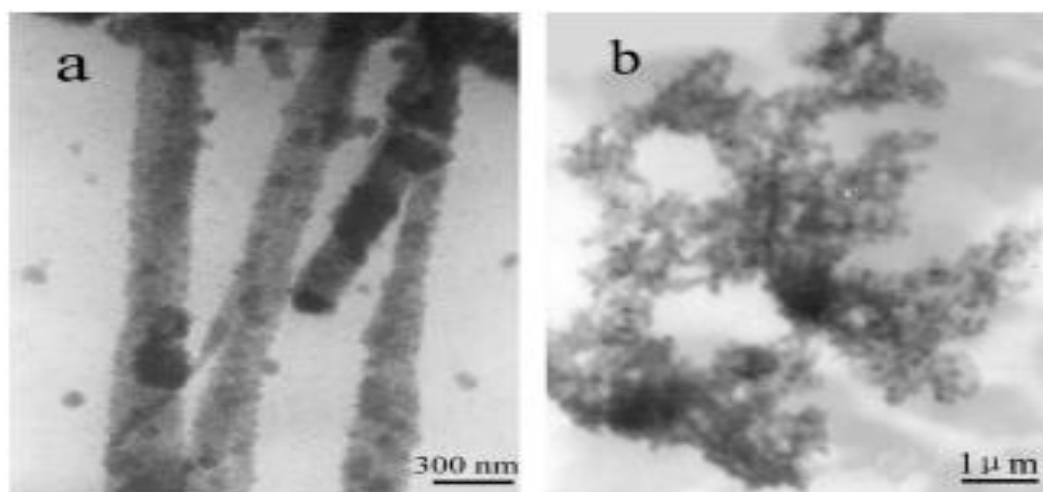


**Figure 1.** The TEM micrograph (a) and ED image (b) of PbS nanobelts.



**Figure 2.** The XRD pattern of the PbS nanobelts.

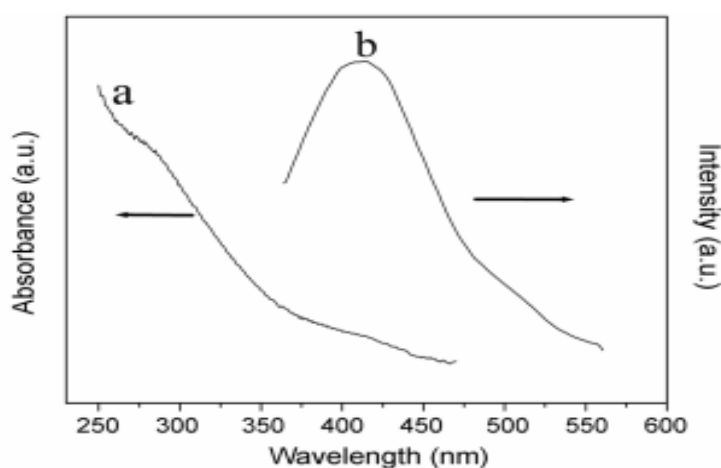
The corresponding electron diffraction pattern has shown the presence of clear diffraction circles, indicative of polycrystal structure. No impurity peaks were observed from the XRD spectral of the nanobelts (Figure 2). All the peaks found in Figure 2 matched with the ones listed in JC-PDS file (No: 5-592) for the cube galena structure. The lattice constant was then calculated to be 5.9378 Å, close to the JCPDS file. Therefore, it was concluded that very pure PbS nanobelts were synthesized in this experiment and the nanobelts possessed cube galena polycrystal structure.



**Figure 3.** The TEM micrograph of PbS products (When the concentration of  $\text{Pb}^{2+}$  and  $\text{S}^{2-}$  were a 0.1 mol/L; b When the concentration of  $\text{Pb}^{2+}$  and  $\text{S}^{2-}$  were 1.0 mol/L)

**Experimental Conditions.** Experimental conditions have been optimized in order to produce the PbS nanomaterial with the desired dimension, morphologies and structures. (1) It was found that the concentrations of reactant have influence on morphologies and structures of the products. When the concentration of  $\text{Pb}^{2+}$  and  $\text{S}^{2-}$  were 0.1 mol/L respectively, the products were nanorods (shown in Figure 3a), not nanobelts. When the concentration of  $\text{Pb}^{2+}$  and  $\text{S}^{2-}$  were 1.0 mol/L respectively, the products were large particulates (shown in Figure 3b), not nanorods or nanobelts. The excess amount of  $\text{S}^{2-}$  was important. It not only improved the morphologies of the final nanobelts, but also ensured the complete depletion of  $\text{Pb}^{2+}$  to avoid the environmental pollutions from heavy metal waste. In this paper the concentration ratio of  $\text{S}^{2-}$  to  $\text{Pb}^{2+}$  was 10. A concentration of 0.1 mol/L for  $\text{Pb}(\text{CH}_3\text{COO})_2 \cdot 3\text{H}_2\text{O}$  and that of 1.0 mol/L of  $\text{Na}_2\text{S} \cdot 9\text{H}_2\text{O}$  were used in the experiments described in this paper. (2) Molar ratio of the water to the surfactant was ten on the experiments described in this paper. Theoretically, surfactant to n-pentanol volume ratio ( $\delta$ ) had no effect on the reverse micelle system containing  $\text{C}_{12}\text{E}_9$ . However, a  $\delta$  value of three was selected here for the solution containing  $\text{Pb}(\text{CH}_3\text{COO})_2 \cdot 3\text{H}_2\text{O}$  to improve emulsion, and no n-pentanol was added to the solution containing  $\text{Na}_2\text{S} \cdot 9\text{H}_2\text{O}$  as determined to be unnecessary.

**Optical Properties.** As shown in the UV-Vis absorption spectra in Figure 3, a strong absorption peak was observed at the wavelength about 347 nm for the PbS nanobelts. Due to its semiconductor nature, the PbS nanobelts have demonstrated excellent photoluminescence (PL) properties. When excited at 390 nm, nanobelts have shown a significant “blue shift” with the new emission wavelength



**Figure 4.** The UV-Vis spectra (a) and PL spectra (b) of the PbS nanobelts.

peaking at 423 nm. Unlike the bulk materials,<sup>23</sup> the PbS nanobelts have shown narrow gap band (0.41 eV) and large Bohr exciton radius. This has resulted in strong quantum confinement effect, unique three stage non-linear optical properties and properties of optical band restriction found on the PbS nanobelts.

**Formation Mechanism of Nanobelts.** The process of nanobelts synthesis is relatively complexed. A microemulsion template based mechanism is proposed below to explain the formation process of nanobelts in the reverse micelle system containing C12E9. It has been reported previously that different surfactants or even the same surfactant at different concentrations may have provided different microemulsion soft templates that resulted in the formation of nanomaterials with different morphologies and structures, such as spheres, rods, layers, etc. The surfactant of C<sub>12</sub>E<sub>9</sub> is a relatively simple and symmetric molecule (Figure 4). The hydrophilic oxy-ethylene chain tended to arrange along the surface and formed the colloids of layer shape. This has subsequently provided the microemulsion template leading to the directional aggregation of PbS colloid nanoparticles. PbS nucleuses were formed as soon as the reverse micelles containing S<sup>2-</sup> and Pb<sup>2+</sup> were mixed. The nucleuses would penetrate each other and amalgamate; the PbS nanoparticles were then produced. Guided by the microemulsion soft template, the nanoparticles aligned along the plane surface. The gap between different layers would shrink due to the interaction between the hydrophilic groups of C12E9 molecules. Finally, a very thin layer of nanobelt was obtained after removing template (Figure 5).

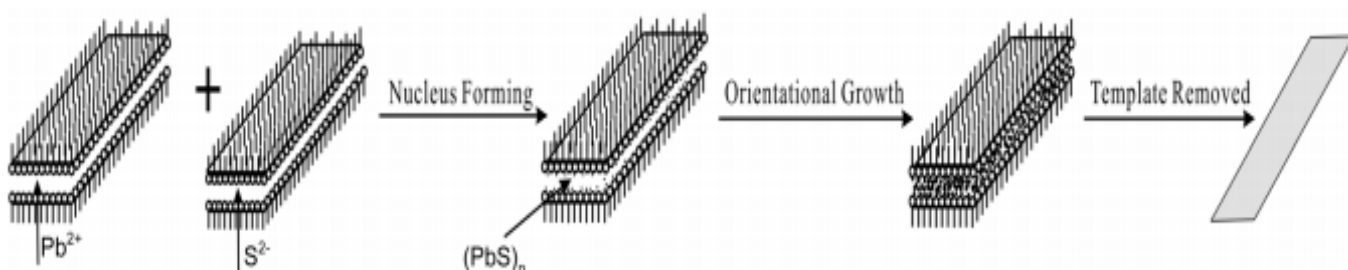


Figure 6. The proposed formation mechanism of PbS nanobelts.

## 11.4 Conclusion

The synthesis of the non-oxide nanobelts is traditionally considered to be technically very challenging. Although the reverse micelle systems have been employed to prepare nanomaterials with various morphologies and structures, the synthesis of the nanobelts using the reverse micelles isn't still reported. As described in this paper, PbS nanobelts were formed at the room temperature using the reverse micelles technique that included the surfactant of C<sub>12</sub>E<sub>9</sub>. The method used is simple, easy, mild and controllable.

Significant “blue shift” was observed on the PbS nanobelts when analyzed by photoluminescence and UV-Vis spectroscopy. Nanobelts have thus demonstrated even more superior optoelectronic properties than nanowires and nanotubes. Therefore, they are expected to show vital applications in many important areas. A microemulsion templates based assembling process was proposed as the mechanism of synthesis. However, a lot more studies are still needed in order to fully understand the mechanism for the formation of nanobelts in the reverse micelle systems containing the surfactant of C12E9.

**Acknowledgements.** The authors are grateful to the financial support of the National Natural Science Foundation of China (Grant No: 20471042 and 20571051); NanoFoundation of Shanghai in China (Grant No: 0452nm075) and the Doctoral Program Foundation of the Ministry of Education (Grant No: 20040247045).

## 12 Materials

قد استحصلت اليوم على:

Acetate plomb كمية قليلة

Poudre

وعلى haxane ربع ليتر

بسعر اجمالي \$68 ثمن المادتان

منى ترغب استلامها

## 13 References to IAP-IRS

### 13.1 References and further reading to the 2.6

- Beichman, C. A. et al.** 1984, "*The formation of solar type stars - IRAS observations of the dark cloud Barnard 5*", ApJ, 278, 45
- Cohen, M., Walker, R. G., Carter, B., Hammersley, P., Kidger, M., Noguchi, K.,** 1999: "*Spectral Irradiance Calibration in the Infrared. X. A Self-Consistent Radiometric All-Sky Network of Absolutely Calibrated Stellar Spectra*", AJ, 117, 1864
- Cohen, M., Megeath, S. T., Hammersley, P. L., Martin-Luis, F. & Stauffer, J.,** 2003a: "*Spectral Irradiance Calibration in the Infrared. XIII. ``Supertemplates'' and On-Orbit Calibrators for the SIRTf Infrared Array Camera*", AJ, 125, 2645
- Cohen, M., Wheaton, W. A., Megeath, S. T.,** 2003b: "*Spectral Irradiance Calibration in the Infrared. XIV. The Absolute Calibration of 2MASS*", AJ, 126, 1090
- Cutri R. M. et al.,** 2012: "*WISE All-Sky Data Release*", NASA/IPAC Infrared Science Archive , 2012yCat,2311,0C
- Hauser, M. G. et al.** 1998: "*The COBE Diffuse Infrared Background Experiment Search for the Cosmic Infrared Background. I. Limits and Detections*", ApJ, 508, 25
- Kataza, H. et al.,** 2010: "*AKARI/IRC All-Sky Survey Point Source Catalogue Version 1.0- Release Note (Rev.1)*"
- Kawada, M., Baba, H., Barthel, P.D., et al.,** 2007: "*The Far-Infrared Surveyor (FIS) for AKARI*", PASJ, 59, S389
- Kim, H.-J. et al.** 2012: „*Star Formation in the Long Filamentary Infrared Dark Cloud at  $l \sim 53^\circ.2$* ", Proceedings of the International Astronomical Union, Symposium 292, Volume 8, pp 46
- Kim, H.-J. et al.** 2013: „*Star Formation Activity in the Long Filamentary Infrared Dark Cloud IRDC G53.2*", poster at Protostars and Planets VI, Heidelberg, July 15-20, 2013, <http://www.mpi-hd.mpg.de/homes/ppvi/posters/1S015.pdf>
- Müller, T. G., & Legerros, J. S. V.,** 1998: "*Asteroids as far-infrared photometric standards for ISOPHOT*", A&A, 338, 340
- Müller, T. G.; Lagerros, J. S. V.,** 2002: "*Asteroids as calibration standards in the thermal infrared for space observatories*", A&A, 381, 324
- Murakami, H., Baba, H., Barthel, P. et al.,** 2007: "*The Infrared Astronomical Mission AKARI*", PASJ, 59, S369
- Nakagawa, T. et al.** 2007: "*Flight Performance of the AKARI Cryogenic System*" PASJ, 59, 377
- Neugebauer, G. et al.** "*Early Results from the Infrared Astronomical Satellite*", (<http://www.sciencemag.org/content/224/4644/14.long>)

**Planck Collaboration**, 2011: “*Planck early results. I. The Planck mission*”, A&A, 536, A1

**Schlegel, D. J., Finkbeiner, D.P., & Davis, M.**, 1998: “*Maps of Dust Infrared Emission for Use in Estimation of Reddening and Cosmic Microwave Background Radiation Foregrounds*”, ApJ, 500, 525

**Schulz, B., et al.** 2002: “*ISOPHOT - Photometric calibration of point sources*”, A&A, 381, 1110

**Simon, R., et al.**, 2006: “*A Catalog of Midcourse Space Experiment Infrared Dark Cloud Candidates*”, ApJ, 639, 227

**Wright, E.L., Eisenhardt, P.R.M., Mainzer, A.K. et al.**, 2010: “*The Wide-field Infrared Survey Explorer (WISE): Mission Description and Initial On-orbit Performance*”, AJ, 140, 1868

**Yamamura, I., Makiuti, S., Ikeda, N. et al.**, 2010, “*AKARI/FIS All-Sky Survey Point Source Catalogues*”, 2010yCat,2298,0Y

<http://astron.berkeley.edu/davis/dust/index.html>

<http://irsa.ipac.caltech.edu/Missions/msx.html>

<http://lambda.gsfc.nasa.gov/product/cobe/>

## 13.2 For PbS Sensor

Kondas, D. A. (February 1993). *INTRODUCTION TO LEAD SALT INFRARED DETECTORS*. U.S.: ARMY ARMAMENT RESEARCH, DEVELOPMENT AND.

William V. Cummings Jr. (1951). *A lead sulfide near infrared detection system*. U.S.: missouri university of science and technology.

<https://cdn.embedded.com/contentetimes/images/My%20Pictures/>



## Suppliers Data

### Electronics, Control

- CNCLab
- قطرنجي للإلكترونيات EKT Beirut
  - Number: 01 820020
  - Website: www.ekt2.com
- البشير للإلكترونيات - Bashir electronics



### Satellite Parts

Specification form © Surrey Satellite Technology Ltd., Tycho House, 20 Stephenson Road, Surrey Research Park, Guildford, Surrey, GU27YE, United Kingdom, Tel: +44(0)1483803803 | Fax: +44(0)1483803804 | Email: info@sstl.co.uk | Web: www.sstl.co.uk

Remark: No answer to email has come.

### CNC Fine Mechanics (2D)

**HI-TECH FABRICATION**  
Where Quality is Priority

**Hard Steel Digits**  
Hi-Tech Fab is specialized in manufacturing brass and hardened steel stamps. We make various types of marking heads for food packing and pharmaceutical industries.

We use the most advanced CAD/CAM software with our CNC milling machines. Our state of the art CNC machines enable us to produce quality parts with utmost precision.

We also manufacture custom parts that are designed according to customer's drawings. We carry printing heads that fit on Markem, Imaje, and Allen coding printers (Rotary and flat holders).

In the case of difficult jobs our clients are supported by qualified engineers to develop a solution and satisfy their needs. Our facilities are prepared for delivering large custom jobs in a timely manner.

**Brass Digits**

**HI-TECH FABRICATION**  
Mahjar Suhi  
P.O. Box 1274  
Tripoli, Lebanon  
Tel 00961-6-442787  
www.hitechfabrication.com  
info@hitechfabrication.com  
sirfawaz@yahoo.com

"You will find our products in every packing factory"

**HI-TECH FABRICATION**  
Precision Mechanical Parts Manufacturing  
Brass & Steel Marking Heads Maker

**M. Fawaz Adul Hadi**  
Mechanical Engr

Mahjar Suhi  
P.O. Box 1274  
Tripoli, Lebanon  
Tel/Fax 00961-6-442787  
www.hitechfabrication.com  
info@hitechfabrication.com  
sirfawaz@yahoo.com

The company HI-TECH Facrification takes CAD Data (in .dxf format) -> Changing to CAM Data.

Satellite Parts are in Alluminium Alloy.

### 3D Printing (Plastics)

<http://www.cnclablb.com/>

### CNC

Company	Phone number	Description	Address	E-mail web site
CNC LAB	06 412 895 03 476 916	Manufacture 3D design in plastic & open source hardware	Tripoli, Lebanon Bahsas, Behind Haykalieh Hospital, Harba Bld.	<a href="http://www.cnclab.com">www.cnclab.com</a> <a href="mailto:info@cnclablb.com">info@cnclablb.com</a>
Hasan Al Baba	03 828 256	Manufacture and casting	Tripoli, Lebanon Mina, Industry and Commerce street	
HI-Tech fabrication Fawaz Abdel Hadi	06 442 787 70 751 522	Precision mechanical parts manufacturing brass & steel marking heads maker	Tripoli, Lebanon Mahjar suhi P.O. Box 1274	<a href="http://www.hitechfabrication.com">www.hitechfabrication.com</a> <a href="mailto:info@hitechfabrication.com">info@hitechfabrication.com</a> <a href="mailto:sirfawaz@yahoo.com">sirfawaz@yahoo.com</a>
Hannuf mechanical 'Corporation for casting and art construction	06 387 723 03 717 107	Manufacture and casting	Tripoli, Lebanon Al Badawi	
GPS Steel	03 196 225	Uses electric discharge machining process to shape any metal material rapidly by using desired modeled electrodes	Beirut, Lebanon Burj Hammoud	<a href="mailto:Gps.steel.co@gmail.com">Gps.steel.co@gmail.com</a>
Riyako factory	79 118 779	3D CNC machine, manufacture cupboard for cars	Tripoli, Lebanon Badawi, behind Al Ridani bakery	